LIGHT MANAGEMENT IN SOLAR CELLS WITH PLANAR STRUCTURES AND SCATTERING MEDIA

A THESIS SUBMITTED TO
THE GRADUATE SCHOOL OF NATURAL AND APPLIED SCIENCES
OF
MIDDLE EAST TECHNICAL UNIVERSITY

BY

MEHMET KOÇ

IN PARTIAL FULFILLMENT OF THE REQUIREMENTS
FOR
THE DEGREE OF DOCTOR OF PHILOSOPHY
IN
MICRO AND NANOTECHNOLOGY

APRIL 2020

Approval of the thesis:

LIGHT MANAGEMENT IN SOLAR CELLS WITH PLANAR STRUCTURES AND SCATTERING MEDIA

submitted by **MEHMET KOÇ** in partial fulfillment of the requirements for the degree of **Doctor of Philosophy in Micro and Nanotechnology Department, Middle East Technical University** by,

Prof. Dr. Halil Kalıpçılar
Dean, Graduate School of **Natural and Applied Sciences**

Prof. Dr. Almıla Yazıcıoğlu
Head of Department, **Micro and Nanotechnology**

Assist. Prof. Dr. Selçuk Yerci
Supervisor, **Micro and Nanotechnology, METU**

Assoc. Prof. Dr. Özgür Ergül
Co-Supervisor, **Electrical-Electronics Eng., METU**

Examining Committee Members:

Prof. Dr. Raşit Turan
Physics, METU

Assist. Prof. Dr. Selçuk Yerci
Micro and Nanotechnology, METU

Prof. Dr. Hamza Kurt
Electrical and Electronics Engineering, TOBB ETU

Assist. Prof. Dr. Emre Yüce
Physics, METU

Assist. Prof. Dr. Bülend Ortaç
UNAM, Bilkent University

Date: 09.04.2020

I hereby declare that all information in this document has been obtained and presented in accordance with academic rules and ethical conduct. I also declare that, as required by these rules and conduct, I have fully cited and referenced all material and results that are not original to this work.

Name, Surname: Mehmet Koç

Signature:

ABSTRACT

LIGHT MANAGEMENT IN SOLAR CELLS WITH PLANAR STRUCTURES AND SCATTERING MEDIA

Koç, Mehmet
Doctor of Philosophy, Micro and Nanotechnology
Supervisor: Assist. Prof. Dr. Selçuk Yerci
Co-Supervisor: Assoc. Prof. Dr. Özgür Ergül

April 2020, 184 pages

Photovoltaics is a prime interest for not only developed but also developing countries considering its historically-low efficiency/cost ratio. Further development of solar cells necessitates the maximum utilization of available light, which has to be done by taking the multi-physics nature of the solar cells and the fabrication constraints to maintain its competitive price into account. In this thesis, we explore light management strategies to improve the overall performances of various solar cells. First, light management is exploited to eliminate the reflection, and at the same time to increase the trapping of the non-reflected light within the active layer in the thin-film solar cells. Using optical simulation methods, transfer matrix method (TMM), finite-difference time-domain approach (FDTD), and ray-tracing, as well as analytical approaches, material independent optical optimization guidelines are provided for achieving higher optical absorption under ideal and practical conditions. Simple and effective empirical algorithms are developed to replace simulations. Developed algorithms are applied to various thin-film solar cell technologies; particularly, perovskite, organic, and CdTe solar cells. Besides, optoelectronic effects of transparent conductive oxides in thin-film solar cells are discussed. Using the simultaneous optimization of optoelectronic properties of cell geometries, we develop a roadmap for the perovskite solar cells that can increase their efficiency and at the same time decrease the fabrication costs. Secondly, we have presented a low-cost rear reflector material for silicon solar cells to eliminate the metal parasitic absorption. Using a combination of three different optical simulations methods (TMM, Ray Tracing, and FDTD), optical interaction mechanisms are quantized. Lastly, using a combination of thin-film and silicon solar cell technologies, we provide a detailed investigation of CdZnTe-Si tandem solar cells. We present theoretical limits of CdZnTe-Si tandem solar cells using a combined optical and electrical simulations environment. We investigate the effect of the top cell absorber bandgap on the optimum optical and electrical trends. Light management strategies provided in this thesis can be beneficial for researchers developing various types of solar cells, not necessarily skilled in optics.

Keywords: Light Management, Anti-Reflection, Thin-Film, Light Trapping, Optics, Solar Cell, Tandem Solar Cells

ÖZ

DÜZ YAPILAR VE SAÇICI ORTAMLAR İLE GÜNEŞ HÜCRELERİNDE IŞIK YÖNETİMİ

Koç, Mehmet
Doktora, Mikro ve Nanoteknoloji
Tez Danışmanı: Dr. Öğr. Üyesi Selçuk Yerci
Ortak Tez Danışmanı: Doç. Dr. Özgür Ergül

Nisan 2020, 184 sayfa

Fotovoltaik tarihteki en düşük verim/maliyet oranına ulaşarak artık sadece gelişmiş değil gelişmekte olan ülkelerin de yoğun ilgisini çekmektedir. Daha üstün güneş hücrelerinin geliştirilmesi için güneşten gelen ışığın tamamına yakınının hücre tarafında kullanılması gerekmektedir. Bunu yaparken ise güneş hücrelerinin çoklu fizik yaklaşımlarına ihtiyaç duyduğu ve rekabetçi fiyatını korumak için üretim kısıtlamalarının bulunduğu göz önünde bulundurulmalıdır. Bu doğrultuda, bu tezde güneş hücrelerindeki verimi artırmak için ışık yönetim stratejileri incelenmiştir. İlk olarak ince-film güneş hücrelerinde, ışık yönetimi; yansımayı engellemek ve aynı zamanda yansıma yapmayan ışığın aktif katmanda hapsolmasını sağlamak için kullanılmıştır. Optik benzetim metodları; taşıma matris yöntemi (TMM), zaman-uzayı sonlu-farklar yaklaşımı (FDTD), ve ışın izleme ile analitik yöntemler kullanılarak, optik soğurmayı ideal ve gerçekçi koşullar altında geliştirmek için malzemeden bağımsız optik optimizasyon ilkeleri verilmiştir. Basit ama etkili, ampirik algoritmalar benzetimlerin yerini almak üzere geliştirilmiştir. Bu geliştirilen algoritmalar perovskit, organik ve CdTe ince-film güneş hücrelerine uygulanmıştır. Öte yandan geçirgen iletken oksitlerin ince-film güneş hücrelerindeki optoelektronik etkileri incelenmiştir. Optoelektronik özelliklerin hücre geometrisi üzerindeki etkisinin optimizasyonu yapılarak, perovskit güneş hücrelerinde aynı anda verim artışı elde etmek ve üretim maliyetini düşürmek için bir yol haritası verilmiştir. İkinci olarak, silisyum güneş hücrelerinde parazit soğurmayı engellemek için düşük maliyetli bir arka yüzey yansıtıcı katmanı gösterilmiştir. Optik etkileşimler üç farklı algoritmanın; TMM, FDTD ve ışın takibinin bir birleşimi kullanılarak hesaplanmıştır. Son olarak, ince-film ve silisyum güneş hücrelerinin birleşimi kullanılarak CdZnTe/Si tandem güneş hücrelerinin detaylı bir incelemesi verilmiştir. Optik ve elektronik benzetim yöntemlerinin bir birleşimi kullanılarak CdZnTe-Si tandem güneş hücrelerinin teorik limitleri verilmiştir. Bu tezde verilen ışık yönetim stratejileri ve analitk hesaplamalar farklı güneş hücreleri üzerinde çalışan araştırmacılara optik alanındaki deneyimlerinden bağımsız olarak daha verimleri güneş hücreleri tasarlamak için yol gösterici olacaktır.

Anahtar Kelimeler: Işık Yönetimi, Yansıma Önleme, İnce Film, Işık Hapisleme, Optik, Güneş Hücresi, Tandem Güneş Hücresi

To my beloved family

ACKNOWLEDGEMENTS

I wish to express my deepest appreciation to my supervisor, Asst. Prof. Dr. Selçuk Yerci, who persistently and patiently guided me. He has always encouraged me to take part in different projects, especially in experimental researches. His unlimited help, kind understandings, outstanding attention to details, enthusiasm in research, and critical thinking provided me priceless guidance.

I would like to pay my special regards to Prof. Dr. Hamza Kurt and Asst. Prof. Dr. Emre Yüce for their crucial feedbacks and kindly offering their deep insights into my research.

I would like to express my very great appreciation to Dr. Giray Kartopu for his invaluable and meticulous comments and suggestions at all stages of this study. His willingness to offer his help so generously has been very much appreciated.

I would particularly like to thank Assoc. Prof. Dr. Görkem Günbaş, who offered support and encouragement at all stages.

I would like to offer my special thanks to Prof. Dr. Raşit Turan. His trust in researchers, professional and scientific guidance, valuable support, sustaining a superb research infrastructure encouraged me in my studies.

I would like to thank Assoc. Prof. Dr. Özgür Ergül for his valuable comments and excepting to be my co-advisor.

My sincere thanks also go to Asst. Prof. Dr. Bülend Ortaç for his insightful suggestions during my thesis defense and PhD qualification exam.

I would like to extend my sincere thanks to Prof. Dr. Henk J. Bolink for his valuable suggestions and support.

Many thanks to all the past and current members of APP team including Can Özcan, Arman Ayan, Mehmet Cem Şahiner, Necati Işık, İlker Yıldız, Kerem Artuk, Umut

Bekci, Amir Zarean, Çağıl Köroğlu, Dr. Hava Kaya, Dr. Şerife Özdemir, Naser Beyraghi, Wisnu Hadibrata, Afnan Ansari, Bahri Eren Uzuner, Buse Ünlü, Elif Cüce, Esra Bağ, and Gülsüm Güneş.

Massive thanks to my close friend Dr. Wiria Soltanpoor. His dedication to the research, profound knowledge and unlimited energy make him one true scientist. He is an excellent researcher and a great friend who radiates happiness.

I am deeply grateful to my friend Gence Bektaş who is not only a dedicated researcher but also a great friend. He was instrumental in NiO_x sputtering.

I would like to thank Deniz Türkay for his valuable comments, fruitful discussions, and excellent cooperation. He taught me a lot about device physics.

I would like to thank Milad Ghasemi for his kind supports and efforts in thin-film studies. He trained me in the spin-coating of various materials, and he provided thin SiO_2 films.

I am grateful to Damla Koçak who fabricated aerogel samples and carried out comprehensive experiments with a great deal of speed.

I would like to acknowledge the assistance of Dr. Mohsen Ameri for proofreading and valuable comments.

I would like to thank Muhammet Mustafa Çodur, who extended a great amount of effort in helping with NiO_x sputtering.

I am thankful to Konstantin Tsoi who helped with simulations of charge transport mechanisms.

I would like to thank my friends Levent Yıldız, Salar Sedani, Mona Borra, Dr. Mete Günöven, Kaan Kirdeciler, Melda İşler Binay.

I gratefully acknowledge the assistance of Hisham Nasser for ellipsometry, Hande Emine Çiftpınar for textured silicon samples, and Gamze Kökbudak for reflection-transmission measurements.

I very much appreciate the assistance of Yeliz Galioğlu Özkan and Fulya Karahan Dağ.

The financial support was received from the Scientific and Technological Research Council of Turkey (TÜBITAK) under contract numbers of 315M360 and 118M981.

And, I am extremely grateful to my parents Filiz and Erol for their unlimited support and unconditional love. They kept me going on and this thesis work would not have been possible without them. Massive thanks to my brothers, Mustafa and Furkan. You are the best. I am deeply grateful to my wife Meryem and daughter Elif, Without them, I would not have had the courage to embark on this journey.

TABLE OF CONTENTS

CHAPTERS

LIST OF TABLES

TABLES

LIST OF FIGURES

FIGURES

LIST OF ABBREVIATIONS

ABBREVIATIONS	
AFM	Atomic Force Microscopy
EQE	External Quantum Efficiency
ETL	Electron Transport Layer
FTL	Front Transport Layer
FTO	Flourine-doped Tin Oxide
FA	Formamidinium
FF	Fill Factor
FWHM	Full Width at Half Maximum
HTL	Hole Transport Layer
ITO	Tin-doped Indium Oxide
J-V	Current Density-Voltage
Jph	Photocurrent
J_{SC}	Short Circuit Current
MA	Methylammonium
MAPC	Maximum Achievable Photocurrent
MAPI	Methylammonium Lead Iodide
Poly-TPD	Poly(N,N'-bis-4-butylphenyl-N,N'-bisphenyl)benzidine
PV	Photovoltaics

QCM	Quartz Crystal Microbalance
RF	Radio-Frequency
RMS	Root Mean Square
RTL	Rear Transport Layer
SEM	Scanning Electron Microscopy
Spiro-OMeTAD	2,20,7,70-tetrakis-(N,N-dip-methoxyphenylamine)-9,9′-spirobifluorene
SQ	Shockley-Quiesser
TCO	Transparent Conductive Oxide
V_{OC}	Open Circuit Voltage

LIST OF SYMBOLS

SYMBOLS	
Ag	Silver
Ar	Argon
CdS	Cadmium Sulphide
CdTe	Cadmium Telluride
q	Elemental charge
ε_0	Vacuum Permitivity
ε	Relative Dielectric Constant
μ	Micro
λ	Lambda
MgF_2	Magnesium Fluoride
MoO_x	Molybdenum Oxide
NiO_x	Nickel Oxide
Ω	Ohm
Si	Silicon
SiO_2	Silicon Dioxide
θ	Theta (degree)
TiO_2	Titanium Dioxide

CHAPTER 1

INTRODUCTION

Every second, a photon flux of 5.23×10^{21} photons/m^2 reaches the Earth from the Sun. These quantized particles of light carry enormous amounts of energy regarding their massive numbers. More precisely, every second approximately ~340 W/m^2 of solar radiation is estimated to be reaching the Earth. Approximately 30% of this flux reflected without being absorbed on the surface, while about 5-6% is absorbed by greenhouse gases (e.g. carbon dioxide, methane) dispersed in the atmosphere. Therefore, these gases trap the light from the Sun in the atmosphere, which in turn results in heating up of the Earth's climate, as known as the Greenhouse effect. This thermodynamic phenomenon has long been providing the Earth's inhabitable climate, that is by keeping the average surface temperature at 298 K since the ratio of the greenhouse gases at the atmosphere has been in a balance. However, atmospheric levels of carbon dioxide have been at the highest ever recorded, which is considered to be the result of human-related actions. The excess amounts of greenhouse gases affect our planet's weather and climate systems not only as rising average temperatures, which is referred to as global warming but also as extreme weather events such as glacier and sea ice melting, desertification. Aftermaths of global warming cause even propelled warming rates, which in turn end up being trapped in a vicious circle.

Fossil fuels (e.g. coal, oil, natural gas) have been and continue to be the main source of global energy demand. They provide more than 80% of global energy consumption at the time of writing (2020). Burning of fossil fuels results in the release of carbon dioxide and other carbon-rich gasses which adds up to other greenhouse gases in the atmosphere which has been long considered the primary reason for the increased carbon dioxide levels in the atmosphere.

While the sun is the primary reason behind this greenhouse effect, it can also be the main actor of the solution to being free from fossil fuels. To employ solar energy efficiently, solar cells should be tailored to exploit the maximum of the incoming flux. The solar radiation flux can be described with the blackbody radiation of the Sun which is propelled by high energy internal nuclear fusion reactions. The spectral irradiance of the solar flux can be described with Planck's law of Blackbody radiation:

$$F(\lambda, T) = \frac{2\pi hc^2}{\lambda^5} \frac{1}{e^{hc/\lambda kT} - 1} \qquad \text{Equation 1}$$

where F is the spectral irradiance in W m^{-2} μm^{-1}, c is the speed of light in vacuum, h is the Planck's constant, k is the Boltzmann constant, λ is the wavelength of the radiation and T is the absolute surface temperature of the blackbody. The substances at the surface and the bulk of the Sun blocks blackbody radiation from the core therefore the emission is a result of surface temperatures.

The Earth receives this solar flux density as a function of its distance from the Sun, and the net radiative flux, which can be described as the balance of incident and escaped photons, defines its climate. The amount of the solar radiation incident on the Earth's surface varies with geographical location, time of the year, momentary weather conditions, and time of the day. Yet a standard measurement, called Air Mass (AM), is taken as reference illumination among the literature.[1] The Air Mass Zero (AM0) is used for the solar spectrum at the top of the earth's atmosphere and the Air Mass 1.5 Global (AM1.5G) is used to describe the solar spectrum reaching the earth's surface after passing through 1.5 times a standard air mass. The AM0 and AM1.5G spectra are presented in Figure 1 along with the Planck's blackbody radiation model.

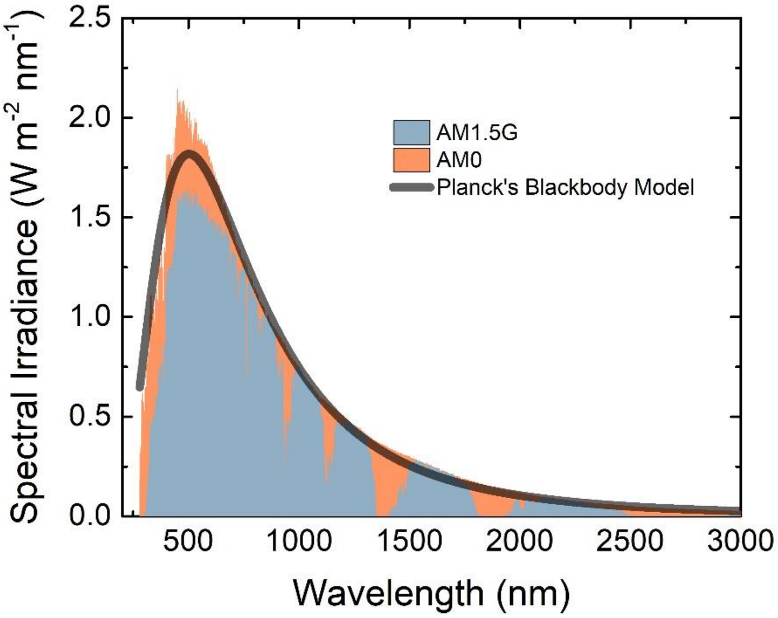

Figure 1 The solar spectral irradiance at the top of the Earth's atmosphere (AM 0) and surface (AM1.5G) along with the Planck's blackbody model at T = 5800 K.

With its enormous available power of 89,300 terawatts, solar energy has the highest potential to be the main source of energy among all the candidates as it provides more than 5200 times the global demand (17 terawatts as of 2019).

1.1. **Fundamentals of Solar Cells**

The working principle of solar cells is based on the photovoltaic effect in which a potential difference is generated as a result of photon absorption. To absorb incident light and generate a potential difference, the presence of an electron at the lower energy level and a vacancy at the higher energy level are required in the absorber. Moreover, the incident photon should have energy larger than the absolute energy difference of vacancy and initial energy level of the electron. The energy of a photon can be presented as:

$$E = h\nu \quad \textit{Equation 2}$$

where ν is the frequency of the photon. In semiconductors, the energy difference of conduction band minimum and valence band maximum is called the bandgap energy

(E_g). Only incident photons with energies larger than the bandgap of the semiconductor can create a band-to-band electron excitation in which every electron leaves a hole (vacancy) behind. This hole is considered as a virtual positively charged particle. To complete a full solar cell working cycle, generated electron-hole pairs should be collected in different polar electrodes. Even though it is demonstrated as a very simple process, to successfully generate photocurrent, absorption of the incident light should be fulfilled, and excited electrons should be collected before they recombine.

Some key parameters to evaluate the performance of the solar cells are developed, such as external and internal quantum efficiencies. The external quantum efficiency (EQE) is the spectral distribution of the ratio of the number of electrons/holes collected to the number available incident photons. The internal quantum efficiency (IQE) is the spectral distribution of the ratio of the number of electrons/holes collected to the number of absorbed photons. The illuminated current-voltage (I-V) characteristics of a solar cell between the points of maximum voltage (V_{OC}) and maximum current (I_{SC}) is used to evaluate the performance under normal and dark operation conditions. V_{OC} is the open-circuit voltage which is the maximum voltage across the cell when there is no current flow and I_{SC} is the short-circuit current which is the maximum current through the cell when there is no voltage difference across the cell. The short-circuit current density (J_{SC}) which equals to I_{SC} divided by the cell area, is also employed as a performance monitor. The conversion efficiency of a solar cell (η) is defined as the ratio of power output from the solar cell to input power from the sun (P_{solar}) and can be expressed as:

$$\eta = \frac{V_{OC} I_{SC} FF}{P_{solar}} \quad \text{Equation 3}$$

where FF is the fill-factor which is defined as the ratio of maximum power from the solar cell to the multiplication of I_{SC} and V_{OC}.

Early designs of solar cells have an efficiency of around 6%,[2] while it can be seen in the best research-cell efficiency chart of the status of different types of solar cells that there has been an outstanding progress for the last 44 years. Recently, CdTe cells with 22.1%, silicon cells with 27.6%, perovskite cells with 25.2%, organic cells with 17.4%, and two-junction tandem cells with 32.9% efficiencies are presented, and it is still increasing in a continuous progressive manner.[3]

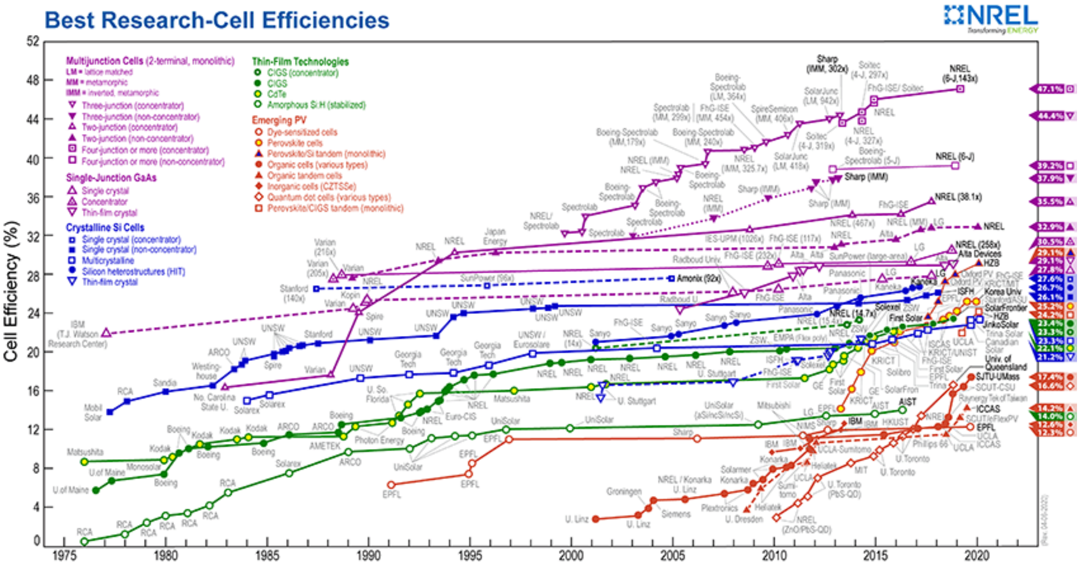

Figure 2 The highest verified efficiencies for research type solar cells for various photovoltaic technologies.[3]

In order to define a landmark for maximum efficiency, a thermodynamic limit is introduced which is based on the Carnot cycle model with idealization assumptions such as monochromatic absorption and emission (no thermalization loss), only radiative recombination, no carrier collection loss, and a unity absorption are assumed.[4] It is shown that maximum efficiencies are 67% for non-concentrated and 86% for concentrated cell structures with these overidealized assumptions.

William B. Shockley and Hans-Joachim Queisser demonstrated that when the spectral mismatch combined with radiative recombination losses are taken into account, the maximal energy conversion of the single-junction solar cell is 33.7 %, which is significantly below the thermodynamic limit.[5] The spectral mismatch can be briefly described with two main loss mechanisms, transparency to photons below bandgap energy and relaxation of the excess energy of photons above bandgap energy. Typically, a photogenerated electron relaxes to the lowest level conduction band in much shorter lifetimes compared to the recombination and carrier collection rate at the contacts in a typical semiconductor. Therefore, the excess energy of the incident light generally results in thermal relaxation. If the bandgap of the semiconductor is large, the number of available photons with energies above the bandgap is lower regarding the spectral distribution of solar flux, while if the bandgap is narrow, a higher fraction of excess energy of the excited electrons is lost by thermalization.

1.2. **Light Management**

Up to this point, an ideal absorption mechanism is discussed which is based on complete utilization of the incident light, however, most of the instances light is underutilized. Solely, high enough energy of the incident photons was considered as a requirement for the absorption. Another important aspect that affects the absorption rate is the available states, which is the density of the occupied states in the valence band (electrons) and the unoccupied states in the conduction band (vacancies). The larger the number of available electrons in the valence and the vacancies in the conduction bands, the higher the probability of the absorption.

Moreover, the absorption mechanism is intensely affected by the band structure which can be either direct or indirect band type. When the lowest energy level of the conduction band of the material has the same crystal momentum with the highest energy level of the valence band, the electron can be excited to the conduction band if the incident photon has enough energy. While the excitation of the electron strongly depends on an external momentum transfer in indirect bandgap materials. Thus, regarding its lower-order interaction mechanism, direct bandgap materials have much higher absorptivity compared to their indirect counterparts.

To quantize absorptivity, a statistical term, the absorption coefficient (α) that corresponds to the absorption probability of the incident photon within the medium is defined. It is a material-dependent and wavelength dispersive parameter. The unit of absorption coefficient parameter is per length which quantifies the rate of absorption. The absorption coefficient is related to the extinction coefficient of the material by the following formula:

$$\alpha(\lambda) = \frac{4\pi k(\lambda)}{\lambda} \qquad \text{Equation 4}$$

where λ is the wavelength of the incident photon and k is the extinction coefficient of the material. The absorption, *A*, can be defined in the Beer-Lambert formalism:

$$A = 1 - e^{-\alpha(\lambda)t} \qquad \text{Equation 5}$$

where *t* is the path length of the photon in the medium.

The required thicknesses to suffice large absorption is significantly smaller when a direct bandgap material is employed as the absorber layer in solar cells. For instance, perovskite is a direct bandgap material and perovskite solar cells are considered as thin-film solar cells regarding their active layer thicknesses in the range of a few hundreds of nanometers. While, silicon solar cells, regarding the indirect bandgap of silicon, have thicknesses ranging from tens to a few hundred micrometers to sufficiently absorb incident photons. Since solar cells are based on the maximum utilization of the incident photons, higher absorption typically results in higher overall solar cell efficiency. One way of increasing the absorption is increasing the absorption coefficient. The absorption coefficient is dependent on the multi-dimensional physical parameters of the material and increasing the absorption coefficient is a research field of material science. Naturally, the thickness is another primary parameter affecting the absorption of the incident photon. Although absorption of the incident photons increases with the thickness of the absorber, this comes with some inevitable penalties such as increased material cost, fabrication challenges, poor extraction efficiency. Moreover, decreasing the active layer thickness while increasing the absorption is required for superior solar cells. Light trapping can address both issues sufficiently with path length enhancement of the incident photons while decreasing the active layer thickness. To exemplify, light trapping features in silicon solar cells support the elimination of the reflection in the front surface and preventing the escape of the light until it becomes fully absorbed with a path length enhancement compared to a planar silicon solar cell with the same thickness.

Besides, optical interaction mechanisms differ with increasing thickness. For instance, one of the most important aspects of optics is coherence. Coherence can be defined as preserving a phase-sensitive interaction mechanism in the medium and coherence length can be used to measure the degree of spatial coherence of the light. Photons can make multiple reflections within a medium until they become fully extinct. The phase relation between reflecting photons and the next incident photon becomes important if the thickness of the layer is of the order of coherence length or smaller. Hence, interference mechanisms can cancel out the incoming or outgoing radiation. While, if the thickness of the layer is much larger than the coherence length, phase interaction mechanisms can be neglected.

Considering poor absorptivity of the indirect bandgap absorbers, typically they are being used with thicknesses beyond the coherence length which yields weakened interference effects. Conversely, direct bandgap absorbers are employed with thicknesses below coherence length, therefore absorption and reflection are dominated by interference mechanisms that can completely cancel or boost with varying the phase relation. Investigation of direct bandgap solar cells is mainly a field of thin-film optics.

The reflection at an interface of two media scales with their refractive index difference where the refractive index is a unitless, dispersed, material-dependent parameter that describes the ratio of the velocity of the light within the medium to its velocity in the air. Hence, reflection can be expressed with the Fresnel equations at the normal incidence:[6]

$$R = \left(\frac{n_1(\lambda) - n_2(\lambda)}{n_1(\lambda) + n_2(\lambda)} \right)^2 \qquad \textit{Equation 6}$$

where λ is the wavelength, n_1 and n_2 are wavelength-dependent refractive indices of both media. For example, in the case of the silicon/air interface ($n_1 \cong 3.95$ and $n_2 = 1$ at $\lambda = 600$ nm), the approximate reflection can be as high as 35% at the normal incidence which calls for the requirement the light management solutions. The surface texturing and anti-reflective coatings (ARC) are among the widely-utilized approaches to eliminate the large reflections. The surface texture can function as an ideal light-trapping structure and increase the chance of coupling of light inside the active medium by refracting the transmitted light with oblique angles as well as eliminating the reflection. On the other hand, anti-reflection coatings provide a smoother transition with homogenous or inhomogeneous coatings and decrease the refractive index contrast at the interface.

The light-surface interaction mechanism varies with the feature size (Λ) of the surface texture. When the feature size is much larger than the wavelength of the incident light ($\Lambda \gg \lambda$), the propagation directions of the reflected and transmitted light change due to diffraction within the geometrical optics formalism. The change in the propagation direction of the transmitted light yields enhanced optical paths due to oblique angles. In the case of reflection, the redirection of the incident light allows multiple reflections in which overall transmission at the surface towards the substrate increases.

In the case of the similar sizes of feature size and wavelength ($\Lambda \approx \lambda$), more defined diffraction orders happen due to a combination of interference and waveguide effects. Suppressed reflection and increased optical path can be achieved with careful optical engineering.

When textured features are much smaller than the wavelength of the incident light ($\Lambda \ll \lambda$), the interaction can be described using the effective medium approach since the effective refractive index of the textured region becomes sensitive to the topology while the change in the propagation direction is none or less pronounced. As a result, incident light experiences a gradual transition of refractive indices as a function of topology which in turn decreases reflection and increases the absorption.

Another light management application is the utilization of a scattering medium. For instance, utilization of randomly dispersed, nano-sized particles presents diffused reflection and transmission where the ratio of the reflected and transmitted light can be optically engineered to enhance overall transmission to the substrate.

Next, light-trapping can be utilized to eliminate parasitic absorption. For instance, a metal layer is typically utilized as the contact and they can present parasitic absorption in the spectrum of interest which in turn decreases the overall absorption of the active layer. Rear reflectors are widely used among the literature to eliminate parasitic absorption within the metal layer through a phenomenon called total internal reflection (TIR) which incident light elastically back-reflected to the incidence medium without having an intensity change.

Interference management can be an alternative way of light management. Regarding the phase relation of the incident electromagnetic waves, the interaction of multiple waves can result in destructive or constructive interference to some degree at the interfaces. Hence, light management can be realized with the vertical-cavity design approach which is based on tuning optical paths within the comprising layers to induce appropriate interferences leading to enhanced absorption and reduced reflection. The optical path is associated with the refractive index, the incidence angle, and the thickness of the layer.

For instance, in the simplest case, a single-layer, homogeneous anti-reflection coating (SLARC) can be utilized to suppress the reflection. The refractive index of the SLARC (n) should be equal to $\sqrt{n_{substrate} \times n_{medium}}$. Reduced reflections through destructive interferences can be attained when the thickness of SLARC fulfills the quarter-wave optical thickness (QWOT) condition which is odd multiples of the wavelength of the light within the layer (λ/4n). On the other hand, the constructive interference condition is satisfied when the thickness of the layer satisfies half-wave optical thickness (HWOT) which is even multiples of the wavelength within the layer (λ/2n). Employing a SLARC provides zero reflection for a single wavelength at the normal incidence and typically it has a narrow band response.

Similarly, the double-layer anti-reflective coating (DLARC) can be used if the refractive indices satisfy the following equation to maintain minimum reflectance at the normal incidence:

$$\frac{n_2}{n_1} = \sqrt{\frac{n_{substrate}}{n_{medium}}}$$ *Equation 7*

Thicknesses are equal to QWOT for both coatings. This design is also called V-coating, regarding the V-shape observed in the reflection spectrum. Alternatively, the high refractive index material can be coated with an HWOT which results in slightly higher reflection at the central wavelength, but a relatively broader low reflectance is obtained. Yet, single- and double-layer coating approaches suffer from poor broadband reflectance performances. Besides, λ/4 or λ/2 thicknesses can be perturbed so that broader low reflectance is achieved with a cost of non-zero reflection at the central wavelength. The solutions are based on iterative numerical approaches where an analytical formula has not yet been developed.

An alternative way of suppressing the reflection is using an inhomogenous, graded refractive index (GRIN) layer. GRIN ARCs have varying refractive indices in the propagation direction of the light so that incident light experiences a smoother transition which leads to reduced reflections.

1.3. Contributions to the Literature

This thesis aims to provide a recipe for the photovoltaic society to boost the optical performance of three solar cell technologies: thin-film, silicon, and tandem solar cells. Some of these optical investigations have been published.[7,8]

In thin-film solar cells, we engineer the individual layers that comprise a cell using their refractive indices and thicknesses. Using the vertical-cavity design approach, we maximize the absorption of the incident light within the absorber layer. Within this context, the FTL is designed as an ARC in a perovskite solar cell with a semi-infinite thick perovskite layer. A hypothetical layer with a constant refractive index is assumed in place of the FTL to investigate the effects of thickness and refractive index of the FTL on light trapping in a broad parameter range. Later, three commonly-used FTLs (PEDOT:PSS, NiO_x, and TiO_2) with distinguishing refractive index spectra are surveyed in coherence with the hypothetical FTL case. A guide to predict the optimum thicknesses of each layer of a perovskite solar cell is provided with sets of semi-empirical and analytical formulations. Although the case study is based on the utilized exemplary ITO and perovskite refractive index spectra from the literature,[9] the effects of the use of various TCO materials and perovskites with different refractive indices are also elucidated. Next, the developed models are validated by fabricating perovskite solar cells in collaboration with Prof. Henk J. Bolink at the University of Valencia with various perovskite thicknesses supporting QWOT and HWOT settings at long wavelengths. Finally, the guidelines are extended for organic and CdTe solar cells to present their applicability for other thin-film solar cells.

In silicon solar cells, we develop an alternative, low cost, and superior rear reflector material to improve the most widely used silicon solar cell technologies. We develop a calculation technique to quantize optical interaction mechanisms. Finally, we present how to improve parasitic absorption elimination. The effect of the silica aerogel as a rear reflector layer in the silicon solar cells is investigated. Aerogel is fabricated using the spray pyrolysis method which is a low-cost and scalable method. Furthermore, it is presented that the aerogel layer has a very low refractive index throughout the spectrum of interest which is around 1.1 and it is tunable. Regarding its low-cost fabrication, being upscalable, and low refractive index, it is shown that aerogel is a strong candidate to replace available rear reflectors. Moreover, a hybrid simulation environment is developed to quantize the loss mechanisms within the silicon solar cells which takes porosity, the surface roughness of the individual layers, texturing, and interdiffusion of the evaporated metal into account. It is shown that compare to the SiN_x rear reflectors with smooth surfaces, a rear reflection improvement more than 10% can be achieved with proposed designs in the case of screen-printed Al metal layers and double side textured silicon substrates.

In tandem solar cells, we analyze optical and electrical loss mechanisms of CdZnTe/c-Si tandem solar cells. Using a combination of optical and electrical simulations, we provide a guideline to improve tandem solar cells. We present alternative solutions to optoelectronic loss mechanisms such as alternative functional materials and structural changes in collaboration with Dr. Giray Kartopu at the University of Swansea. In this context, an optical optimization analysis of $Cd_{1-x}Zn_xTe$ (denoted $C_{1-x}Z_xT$ hereafter) top cells in tandem with an interdigitated back contact (IBC) c-Si rear cell build on various practical thickness and material combinations are carried out. To explicate the effect of the top cell bandgap, several absorber compositions were investigated: CdTe, $C_{0.8}Z_{0.2}T$, $C_{0.6}Z_{0.4}T$, $C_{0.4}Z_{0.6}T$, $C_{0.2}Z_{0.8}T$, and ZnTe. Optical loss mechanisms are examined and addressed. Moreover, alternative functional (buffer and contact) materials are investigated. The optimum thicknesses determined from optical investigations are utilized to carry out electrical simulations. Substantial improvements at conversion efficiencies have been shown by fine-tuning the material parameters and types.

1.4. **Organization of the Thesis**

Chapter 2 summarizes the computational and experimental methods used in this thesis. We characterize various thin-films using spectroscopic ellipsometry, provide details of the fitting methodology, and details of the experimental setup. We present specific aspects of the measurement setups such as reflection-transmission spectrometer, scanning electron microscope, and atomic force microscopy. We discuss the fundamentals of both utilized and developed simulation methods: finite-difference time-domain (FDTD), transfer matrix method (TMM), and 1D drift-diffusion & Poisson’s Equation solver.

Chapter 3 introduces the optimization methodology we applied for the thin-film solar cells. We investigate the anti-reflective properties of the front functional layers of the solar cells based on strong absorbers (i.e. perovskite, organic, and CdTe) using a semi-infinite absorber and their light-trapping properties in their full device configurations.

Chapter 4 presents an industry-applicable, low-cost, high-performance rear reflector layer based on aerogel for silicon solar cells to mitigate the parasitic absorption in the metal layer. We present the quantization of the loss mechanisms using a TMM/FDTD/ray tracing hybrid simulation environment. We demonstrate a recipe to surpass the performance of state-of-the-art SiN_x rear reflectors.

Chapter 5 presents a detailed investigation of CdZnTe/c-Si tandem solar cells. We analyze the effect of the bandgap of the top cell and we present optimum bandgap condition for various electrical parameters. We provide optical and electrical optimization guidelines of CdZnTe/c-Si tandem solar cells. We present alternative fabrication routes and materials to reduce optical and electrical losses.

In Chapter 6, we give our concluding remarks and perspectives on future directions.

CHAPTER 2

COMPUTATIONAL AND EXPERIMENTAL DETAILS

2.1. **Computational Details**

A computer *code* for optical analysis based on the transfer matrix method (TMM) is developed to compute the reflection and absorption of layers in the third chapter. Finite-difference time-domain (FDTD) simulations, performed using LUMERICAL^{TM}, are used in roughness calculations. The relatively-thick glass layer is treated as incoherent (i.e. the interference is neglected).

A rapid, and computationally low cost hybrid optical calculation method is developed and utilized in the fourth chapter (Figure 3). Since silicon substrates are of the order of a few hundred microns, while the typical thickness of rear reflectors is around a few hundred nanometers, the calculation of electromagnetic interaction of the full stack becomes a large matrix problem. Considering this, optical calculations are carried out by transferring internal transmission and reflection of each interface. The ray-tracing method is employed for the thick silicon substrate with and without texture. Both FDTD and TMM are utilized for calculation of internal reflection of the rear reflector interface.

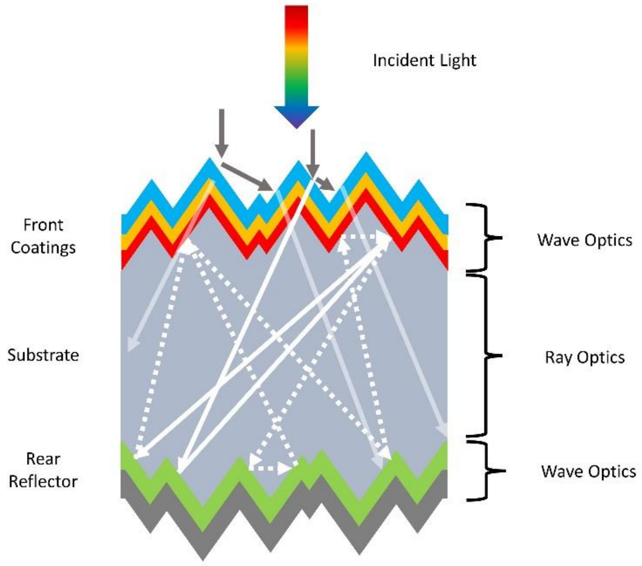

Figure 3 Scheme of the combined ray-wave optics simulation method.

TMM is employed in reflection, transmission, and absorption simulations of the top cell in the fifth chapter. The Lambertian scattering profile is assumed for the incident light at the silicon interface. The ray-tracing method is employed to calculate the scattered light paths until full attenuation.

Complex refractive index spectra of materials, obtained either by spectroscopic ellipsometry or adapted from the literature, are used as input in the optical simulations. Reflection, transmission, and absorption results are reported for the unpolarized light which is calculated as the average of *s*- and *p*-polarizations considering the unpolarized illumination of the solar flux.

The maximum achievable photocurrent (MAPC) is used in the thesis as a bench for the evaluation of the optical designs leading to the minimum loss mechanisms, reflection, and parasitic losses, thus the highest anticipated short circuit current. MAPC can be expressed as:

$$MAPC = J_{ph} \cong q \int_{\lambda} \varphi\,(\lambda) A(\lambda) d\lambda \quad \text{Equation 8}$$

where φ is the photon flux of the A.M. 1.5 spectrum, q is the unit charge, A is the absorption spectrum of the absorber layer. Hence, MAPC indicates the photogenerated electrons are collected without any recombination losses. The unity charge collection efficiency approximation is employed for all of the optical simulation environments, TMM, FDTD, and ray-tracing.

SCAPS-1D is used for optoelectrical investigation of the CZT solar cells which is comprised of a glass/ITO/CdS/CZT/ITO structure. The rear transparent conductive oxide layer is treated as a metal with high transparency. Transmission spectra of both TCOs are computed in optical simulations using TMM and imported to the SCAPS-1D. In addition to that, the generation profiles of the absorbers are calculated with TMM. The solar cell simulation parameters utilized in SCAPS-1D are obtained from the literature[10–12] and manifested in Table 1. The four-terminal design (4T) is chosen as the structure types for the tandem solar cell, by which $C_{1-x}Z_xT$ and IBC c-Si are utilized as top and rear solar cells, respectively.

Table 1 Simulation parameters of solar cells used in SCAPS 1-D.

	CdTe	$C_{0.8}Z_{0.2}T$	$C_{0.6}Z_{0.4}T$	$C_{0.4}Z_{0.6}T$	$C_{0.2}Z_{0.8}T$	ZnTe	CdS	MZO	ITO
E_g (eV)	1.45	1.54	1.69	1.85	2.03	2.19	2.4	3.6	3.72
χ (eV)	4.28	4.23	4.03	3.87	3.69	3.53	4.3	4.2	4.5
CB eff. DOS (cm^{-3})	1.5×10^{18}	1.5×10^{18}	1.5×10^{18}	1.5×10^{18}	1.5×10^{18}	1.5×10^{18}	2.1×10^{18}	2.1×10^{18}	4×10^{19}
VB eff. DOS (cm^{-3})	1.8×10^{19}	1.8×10^{19}	1.8×10^{19}	1.8×10^{19}	1.8×10^{19}	1.8×10^{19}	1.7×10^{19}	1.7×10^{19}	1×10^{18}
V_{te} (cm/V.s)	1×10^7	1×10^7	1×10^7	1×10^7	1×10^7	1×10^7	1×10^7	1×10^7	1×10^7
V_{th} (cm/V.s)	1×10^7	1×10^7	1×10^7	1×10^7	1×10^7	1×10^7	1×10^7	1×10^7	1×10^7
M_e (cm^2/V.s)	700	700	700	700	700	700	70	70	30
M_h (cm^2/V.s)	60	60	60	60	60	60	20	20	5
N_A (cm^{-3})	1×10^{16}	1×10^{16}	1×10^{16}	1×10^{16}	1×10^{16}	1×10^{16}	-	-	-
N_D (cm^{-3})	-	-	-	-	-	-	1.2×10^{18}	1.2×10^{18}	1×10^{21}

E_g: bandgap; χ: electron affinity, DOS: density of states; V_{te}: electron velocity; V_{th}: hole velocity; M_e: electron mobility; M_h: hole mobility; N_A: acceptor density; N_D: donor density.

2.1.1. **Transfer Matrix Method**

TMM is a widely used tool in numerical studies in various application areas such as acoustics, astronomy, statistical mechanics, and optics.[13] In this thesis, TMM is used to calculate the reflection and transmission terms of individual layers of a multi-layered structure. The s- and p-polarized reflections at an interface of two semi-infinite media can be described by the Fresnel equations:[13]

$$R_s = \left| \frac{n_1 \cos\theta_i - n_2 \sqrt{1 - (\frac{n_1}{n_2}\sin\theta_i)^2}}{n_1 \cos\theta_i + n_2 \sqrt{1 - (\frac{n_1}{n_2}\sin\theta_i)^2}} \right|^2 \qquad \text{Equation 9}$$

$$R_p = \left| \frac{n_1 \sqrt{1 - (\frac{n_1}{n_2}\sin\theta_i)^2} - n_2 \cos\theta_i}{n_1 \sqrt{1 - (\frac{n_1}{n_2}\sin\theta_i)^2} + n_2 \cos\theta_i} \right|^2 \qquad \text{Equation 10}$$

where R_s and R_p are reflection terms for the s- and p-polarized incident light, n_1, and n_2 are refractive indices of media, θ_i is the angle of incidence. However, in the case of multilayered structures, light undergoes an infinite number of internal reflections. TMM method models these reflection terms according to Maxwell's equations. TMM is based on exploiting the continuity of the electric field within the structure. Since the incident light is independent of the structure, the electric field components at any point in the structure can be normalized to the incident light.

Layers are assumed as homogenous and isotropic. Incident light is assumed as monochromatic and coherence of the incident light is conserved. The size of the illumination source is assumed as infinite.

Reflected and transmitted light in the case of a single layer coating is presented in Figure 4. Light propagating from the first interface to the second is illustrated as black, the opposite case is presented as blue. Internal reflections and incident light are also demonstrated. In addition to that, the electric field as a function of depth is given in atop. TMM is based on equating the electric and magnetic fields at the interface. Hence, the electromagnetic relation at the two interfaces can be described with a 2x2 transfer matrix as:[14]

$$\begin{bmatrix} E_1 \\ B_1 \end{bmatrix} = \begin{bmatrix} cos\delta & \dfrac{i\ sin\delta}{\gamma} \\ i\gamma\ sin\delta & cos\delta \end{bmatrix} \begin{bmatrix} E_2 \\ B_2 \end{bmatrix} \quad \text{Equation 11}$$

where E_1 and B_1 are electric and magnetic fields at the first interface and E_2 and B_2 are electric and magnetic fields at the second interface, respectively. γ can be described as $n_{layer}\, cos\ \theta_t/c$ for *s*-polarized and $n_{layer}/cos\ \theta_t c$ for *p*-polarized light. The angle θ_t is the refraction angle of the light within the layer, and n_{layer} is the refractive index of the layer. Here δ is the phase difference in a single traverse in the thin-film can be described as:

$$\delta(\lambda) = \frac{2\pi}{\lambda_o} n_{layer}(\lambda) t_{layer} cos\theta_t \quad \text{Equation 12}$$

where λ_o is the vacuum wavelength of the incident light, t_{layer} is the thickness of the layer.

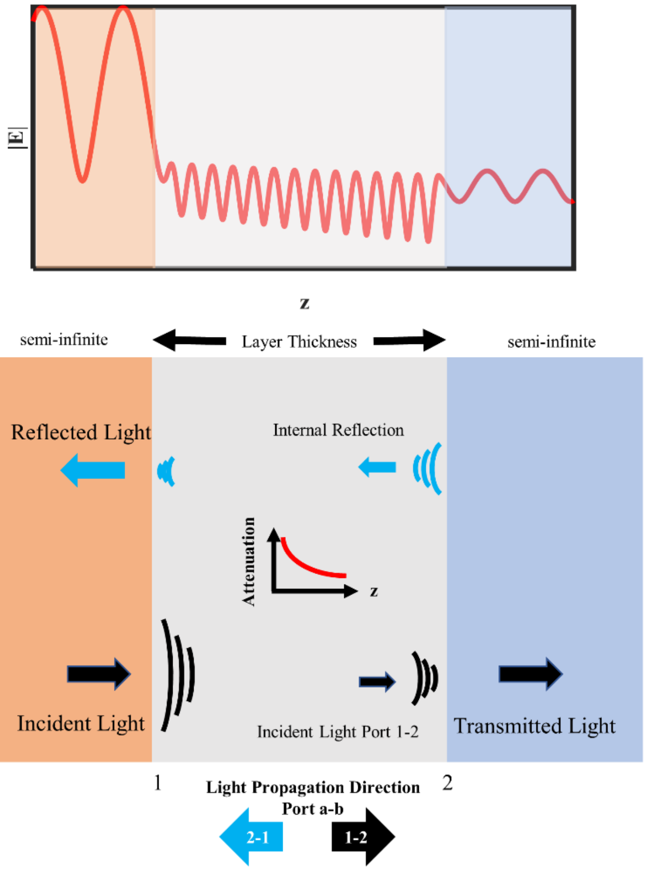

Figure 4 Reflection and transmission of light from a single layer. |E| as a function of depth is presented atop.

For a configuration with N layers, each layer has its transfer matrix (M) based on its optical properties and thickness can system transfer matrix can be written as:

$$\begin{bmatrix}E_1\\B_1\end{bmatrix} = M_1 M_2 M_3 \ldots M_N \begin{bmatrix}E_2\\B_2\end{bmatrix}$$

Equation 13

Since tangential components of electric and magnetic fields are continuous at the boundaries, reflection and transmission terms can be found by rearranging the electromagnetic fields at the interfaces. To determine the total absorption within each layer, the Poynting vector is computed using previously-determined electric field components at each interface.

2.1.2. **Finite-Difference Time-Domain Method**

The FDTD method is used for computation of the electromagnetic interactions in the time-domain. Since it is a time-domain approach, a broad range of wavelengths can be simulated in a single simulation run. Electromagnetic problems for the three-dimensional structures can be solved using the FDTD method. The illustration of the 3D Yee Cell is presented in Figure 5.

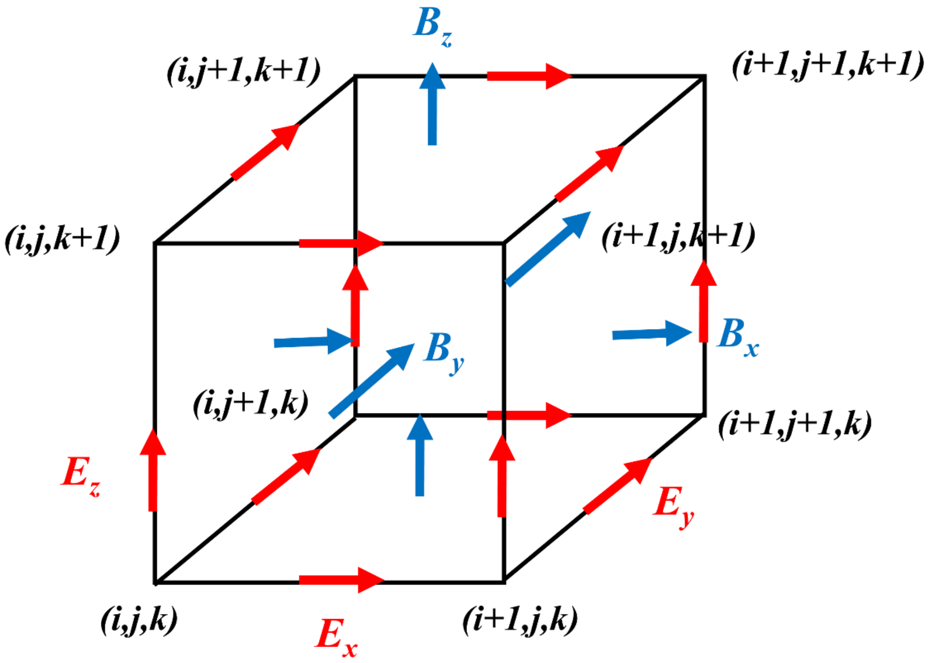

Figure 5 Illustration of a Yee cell used in the FDTD method.[15]

Electric and magnetic fields are solved with the leapfrog integration method which is based on solving the electric field vector components at a given instant time step, and magnetic field vector components of the same coordinates in the next time step alternatively. The new values are obtained using the values of electric and magnetic fields of the last steps. This process is repeated until the desired convergence is achieved.

FDTD is a precise and versatile method to model the electromagnetic behavior of complex geometries. However, it has some challenges among them computation cost is considerable. Since it is based on the discretization of the real geometry with a grid approach, the mesh size is of great importance. Unlike the TMM approach, media are modeled with complex refractive index mapping. In complex geometries with small feature sizes, ultra-fine mesh sizes are required for accurate simulations. Yet, it is a very capable and powerful tool for electromagnetic researches.

FDTD Solutions which is developed by Lumerical, a company headquartered in Vancouver, Canada, is utilized as the FDTD solver for the design, analysis, and optimization of nanophotonic devices, processes, and materials.[16]

2.1.3. 1D Semiconductor Simulations

Solar Cell Capacitance Simulator ($SCAPS$) – developed at the University of Gent – is a freely available, one-dimensional simulation program for modeling planar solar cells.[17] Simulation setup is based on the solution of the Poisson equation, and the continuity equations for charge carriers which can be expressed as:[18]

$$\frac{\partial}{\partial x}\left(\epsilon(x)\frac{\partial\psi}{\partial x}\right) = -\frac{q}{\epsilon_0}\left[-n(x) + p(x) - N_A^-(x) + N_D^-(x) + \frac{1}{q}\rho_{defects}(n,p)\right] \quad \text{Equation 14}$$

$$-\frac{\partial J_n}{\partial x} + G - U_n(n,p) = \frac{\partial n}{\partial t} \quad \text{Equation 15}$$

$$-\frac{\partial J_p}{\partial x} + G - U_p(n,p) = \frac{\partial p}{\partial t} \quad \text{Equation 16}$$

where p and n are free carrier concentrations, $N_{D,A}^{\pm}$ is the concentration of the dopants, $\rho_{defects}(n,p)$ is the defect distribution, $J_{n,p}$ is the electron/hole current density, $U_{n,p}$ is the net recombination rates, and G is the generation rate.

The device and semiconductor parameters can be used in simulations for each layer are thickness, bandgap, electron affinity, electron and hole mobilities, electron and hole thermal velocities, effective masses of electrons and holes, intrinsic carrier concentration, doping density, and optical properties. Various defect mechanisms can be introduced to interfaces and layers such as band-to-band, Auger, and Shockley Read Hall-type recombinations with a broad degree of freedom. There exist dark and under pre- or user-defined illumination operation modes.

2.2. **Characterization**

Optical coefficients (n and k) of glass, perovskite, PEDOT:PSS, NiO_x, TiO_2, Ag, Si,PTB7:PCBM, and ITO used in these calculations are taken from literature.[9,19–22] The optical constants, the refractive index and the extinction coefficient, of $Mg_xZn_{1-x}O$ (MZO)[23], $C_{1-x}Z_xT$[24], ethylene/vinyl acetate (EVA)[25], $Cd_xZn_{1-x}O$ (CZO)[26], and cadmium sulfide (CdS)[27] used in the computations are adapted from the literature. Refractive index spectra of MgF_2 and materials used in the experimental section (perovskite, MoO_x, ITO, C_{60}, SiN_x, SiO_2 and aerogel, and NiO_x) are obtained by Spectroscopic ellipsometry measurements (SOPRA GES-5E) with a spectral range from 1.23 to 5.00 eV on c-Si at 70^o incidence angle and on glass at 57^o incidence angle.

Here, experimental methods are briefly described, key parameters and metrics are mentioned.

2.2.1. **Atomic Force Microscopy**

The correlation length and the root mean squared roughness data of the surface metrology of planarized aerogel samples are measured with tapping mode AFM (Veeco Nanoscope5). Measured surfaced dimensions are $4.97x4.37\ \mu m^2$.

2.2.2. **Scanning Electron Microscopy**

Samples surface topographical images are obtained using a Scanning Electron Microscope, SEM (FEI, Model Quanta400 F) located at the central laboratory, METU.

This technique provides information about surface topography and morphology. A beam of electrons is generated using a field emission gun under vacuum operation conditions. Using electromagnetic lenses, the beam of electrons is collimated and focused. To obtain a conductive layer atop a thin layer of gold/palladium alloy is sputtered on the top surface of the samples. This coating helps to reduce beam damage and sample charging while improves secondary electron emissions to obtain high-resolution SEM images.

SEM is used to provide thickness and surface morphology data of perovskite solar cells in this thesis.

2.2.3. **Spectroscopic Ellipsometry**

Spectroscopic ellipsometry measurements are carried out using a SOPRA GES-5E. Spectroscopic ellipsometry is a non-destructive measurement technique that determines the optical parameters, refractive index *n* and extinction coefficient *k*, of samples, bandgap, surface roughness, and thickness of samples based on the change in the polarization of the light upon the reflection or transmission. Samples are illuminated with a superposition of *s*- and *p*- polarized light. The amplitudes of the *s*- and *p*-polarized reflected waves differ with the polarization of the incident light as a function of refractive index, extinction coefficient, and thickness. The resultant reflection (or transmission) presents an elliptical polarization due to asynchronous peaks and valley positions of reflection amplitudes.

Figure 6 presents the working principle of a typical spectroscopic ellipsometer. Incident light is produced with a Xenon lamp, collimated with lenses, and finally linearly polarized with polarizers before reaching the surface of the sample.

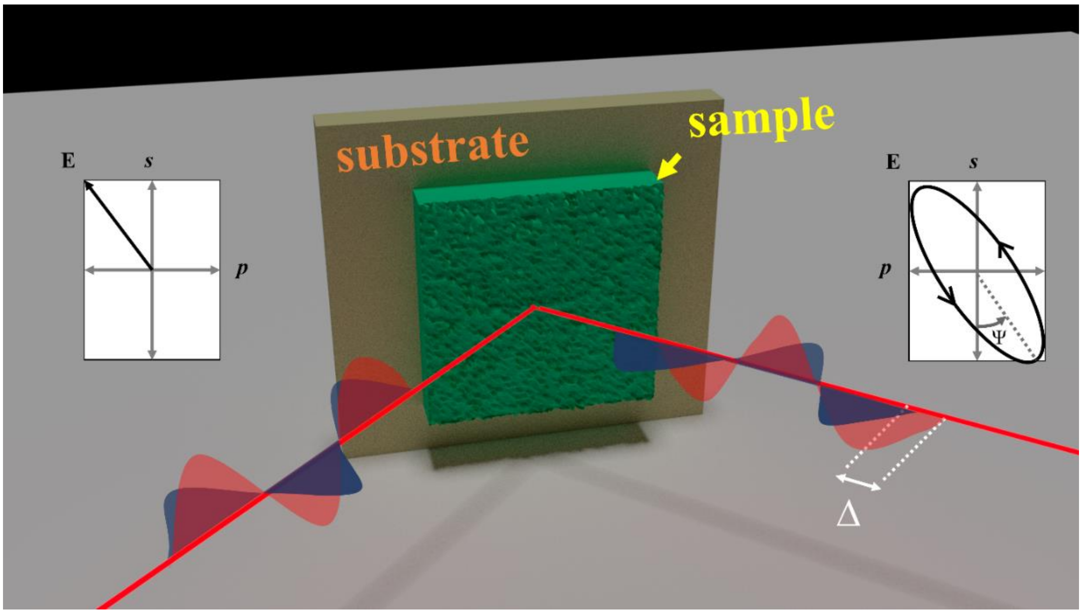

Figure 6 Illustration of a typical spectroscopic ellipsometry measurement.

Samples are illuminated with a polarized Xenon lamp is collimated and then passed through a polarizer to produce a linearly polarized light. After interacting with the sample surface, the linearly polarized light becomes elliptically polarized. The main measurement parameters of the spectroscopic ellipsometer are $tan\ \psi$ and $cos\ \Delta$ which are the relative reflection ratio and phase difference of both polarizations, respectively. They can be expressed as:

$$tan\,\psi = \frac{|\widehat{r_p}|}{|\widehat{r_s}|} \quad \text{Equation 17}$$

$$\Delta = \delta_p - \delta_s \quad \text{Equation 18}$$

where $\widehat{r_s}$ and $\widehat{r_p}$ are complex reflection terms and δ_s and δ_p are the phase terms of *s*- and *p*-polarized light, respectively. The optical properties, refractive index n and extinction coefficient k, are determined by fitting tan(ψ) and cos(Δ) with the proper physical oscillator models.

Typical analysis steps of a spectroscopic ellipsometry characterization are presented in Figure 7. First, the ellipsometry measurement of the sample is carried out. The substrate can be selected among the known materials or it can also be part of the fitting procedure. Typically, to enhance the sensitivity, the incidence angle is selected close to the Brewster angle (θ_B), which is the angle where the reflection of the *p*-polarized light at the uncoated substrate surface vanishes. Since it varies with the wavelength, the central wavelength of the spectrum of interest can be considered. For instance, in the majority of instances, the incidence angles of 70° ($\theta_B \cong 76^\circ$) and 57° ($\theta_B \cong 56^\circ$) are utilized for the silicon and glass substrates, respectively. Next, the optical model is constructed including introducing the thicknesses and appropriate physical oscillation models for each layer constituting the stack. Here, if required, proper adjustments such as surface roughness and additional oscillator models are also introduced. Later, parameters of the optical and oscillator models are swept using fitting algorithms to achieve minimum error between measured and simulated $\tan\psi$ and $\cos\Delta$ spectra within the physical constraints. The root means squared error (RMSE) and R^2 are used to evaluate the quality of the regression. R^2 is a statistical measure that represents the variance rate of the dependents which is explained by the independent variable(s) in the regression model. RMSE and R^2 can be expressed as:

$$RMSE = \sqrt{\frac{1}{n}\sum_{i=1}^{n}(\mathcal{Y}_i - \hat{\mathcal{Y}}_i)^2} \qquad \textit{Equation 19}$$

$$R^2 = 1 - \frac{SSE}{TSS} \qquad \textit{Equation 20}$$

where *SSE* is the sum of squared errors or $SSE = \sum_{i=1}^{n}(\mathcal{Y}_i - \hat{\mathcal{Y}}_i)^2$ and *TSS* is the total sum of squares and is equal to $\sum_{i=1}^{n}(\mathcal{Y}_i - \bar{\mathcal{Y}})^2$, where $\bar{\mathcal{Y}} = \frac{1}{n}\sum_{i=1}^{n}\mathcal{Y}_i$. Here $\mathcal{Y}_i$ and $\hat{\mathcal{Y}}_i$ are measured and fitted data. In most instances, the Levenberg-Marquardt algorithm (LMA) is used for curve fitting. Finally, obtained physical properties such as surface roughness, bandgap, thickness, and dielectric constant can be verified with other characterization methods.

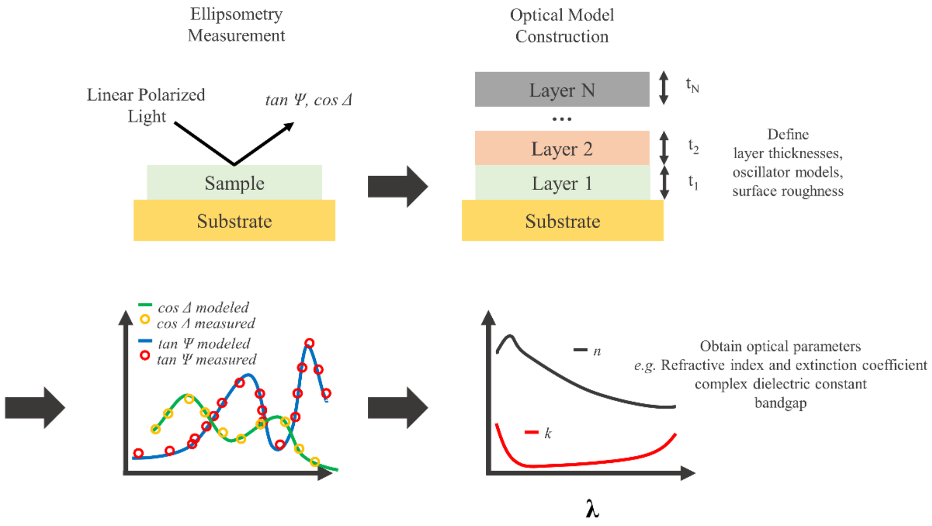

Figure 7 Data acquisition steps for a typical spectroscopic ellipsometry measurement.

Since spectroscopic ellipsometry is based on the measurement of relative intensities of polarization, it is more tolerant of the measurement errors and imperfections than optical characterization techniques which based on absolute intensity measurements such as the reflection-transmission spectroscopy. Hence, spectroscopic ellipsometry can be considered as one of the most reliable and practical techniques for the determination of the optical properties.

In this thesis, the optical constants of MgF_2, NiO_x, MoO_x, ITO, perovskite, C_{60}, aerogel, ITO, LiF, TiO_2, SiO_2, and SiN_x are obtained with the spectroscopic ellipsometer. Corresponding optical models of each material are provided in the Appendix A including the dielectric models, obtained optical parameters, fitted and measured *tan* ψ and *cos* Δ spectra.

2.2.3.1. Dispersion Laws

Here, details of the dispersion laws used in this thesis are briefly presented. Fitting results are manifested in the Appendix A.

2.2.3.1.1. Sellmeier Model

Typically, the Sellmeier model is used to model the optical properties of transparent materials such as glass. The real part of the dielectric function can only be described by the Sellmeier model and it can be expressed as:

$$\epsilon_1(\lambda) = \frac{B\lambda^2}{\lambda^2 - \lambda_0^2} \quad \text{Equation 21}$$

where λ is the wavelength, λ_0 is the resonance wavelength and B is the oscillator strength.

2.2.3.1.2. Lorentz Model

The Lorentz oscillator model is based on modeling vibration of strongly bounded electrons with a harmonic dipole oscillator equations, and best demonstrates the insulators at their interband absorption region.[28] The Lorentz model for complex dielectric functions can be expressed as:

$$\epsilon_1(E) = \frac{fE_0(E_0^2 - E^2)}{(E_0^2 - E^2) + \Gamma^2 E^2} \quad \text{Equation 22}$$

$$\epsilon_2(E) = \frac{fE_0^2 \Gamma E}{(E_0^2 - E^2) + \Gamma^2 E^2} \quad \text{Equation 23}$$

where f is the oscillator strength, E_0 is the peak energy of the oscillator, and Γ is the oscillator width.

2.2.3.1.3. Drude Model

The Drude model is used to describe the free carriers in metals and highly doped semiconductor materials.[29] The Drude model for complex dielectric functions can be expressed as:

$$\epsilon_1(E) = -\frac{(\frac{E_P}{E})^2}{1+(\frac{\Gamma}{E})^2} \quad \text{Equation 24}$$

$$\epsilon_2(E) = \frac{\Gamma}{E}\frac{(\frac{E_P}{E})^2}{1+(\frac{\Gamma}{E})^2} \quad \text{Equation 25}$$

where E_P is the plasma energy, and Γ is the broadening of the oscillation at the plasma energy.

2.2.3.1.4. Tauc Lorentz Model

The Tauc-Lorentz (TL) model well demonstrates the behavior of semiconductor and insulator materials in their interband transition energy region. An approach based on the combination of the Tauc joint density of states of interband absorption at the band edge[30], and the classical Lorentz oscillation model is employed with the TL oscillator model. In the scheme of the Kramers-Kronig (KK) equations, imaginary and real parts of dielectric constants are connected and can be expressed as:[31]

$$\epsilon_1(E) = \epsilon_\infty + \frac{2}{\pi}P\int_{E_g}^{\infty}\frac{x\epsilon_2(x)}{x^2-E^2}dx \quad \text{Equation 26}$$

$$\epsilon_2(E) = -\frac{2}{\pi}P\int_{E_g}^{\infty}\frac{x\epsilon_1(x)}{x^2-E^2}dx \quad \text{Equation 27}$$

where ϵ_1 and ϵ_2 are the real and imaginary part of the dielectric constant, E_g is the bandgap of the material, ϵ_∞ is the offset dielectric constant, P is the Cauchy principal value. Equation 26 and Equation 27 are modified versions of the first proposed KK relation. In the TL Model, the imaginary part of the dielectric constant is taken as zero for the energy values below the interband transition. Hence, the lower limit of the equation is taken as bandgap energy. In theory, it is possible to fully extract real part of dielectric constant, if the imaginary part is known for all energy levels, and vice versa. However, in practical cases conducted measurements are constrained with the limits of the experimental setup. Therefore, the KK relation provides a general shape for the fittings. The offset dielectric constant value, ϵ_∞, defined in Equation 26 accounts for the anomalous dispersions caused by the absorptions which are beyond the spectral range of measurement. Dielectric properties of the films can be expressed analytically by a combination of the TL and KK equations[32]

$$\epsilon_1(E) = \tau_0(E)[\alpha_1(E)\tau_1 - \alpha_2(E)\tau_2 - \alpha_3(E)\tau_3 - \tau_4(E)] \tag{Equation 28}$$

$$\alpha_1(E) = \frac{\left(E_g^2 - E_0^2\right)E^2 + E_g^2 C^2 - E_0^2(E_0^2 + 3E_g^2)}{E_0^2} \tag{Equation 29}$$

$$\alpha_2(E) = \frac{(E^2 - E_0^2)\left(E_0^2 + E_g^2\right) + E_g^2 C^2}{E_0^2} \tag{Equation 30}$$

$$\alpha_3(E) = 2E_g(E^2 - \gamma^2) \tag{Equation 31}$$

$$\tau_0(E) = \frac{ACE_0}{\pi\zeta^4(E)} \tag{Equation 32}$$

$$\tau_1 = \begin{cases} \dfrac{1}{\alpha C}\dfrac{E_g^2 + E_0^2 + \alpha E_g}{E_g^2 + E_0^2 - \alpha E_g}, & \alpha^2 > 0 \\ \dfrac{E_g}{E_g^2 + E_0^2}, & \alpha^2 = 0 \\ \dfrac{1}{\alpha} arg(E_g^2 + E_0^2, \alpha E_g), & \alpha^2 < 0 \end{cases} \tag{Equation 33}$$

$$\tau_2 = \frac{1}{C}\arg\left(4\frac{E_g^2 - E_0^2}{C^2}, \frac{4E_g}{C}\right) \tag{Equation 34}$$

$$\tau_3 = \begin{cases} \dfrac{1}{\alpha C}\left[\pi - 2\tan^{-1}\left(2\dfrac{E_g^2 - \gamma^2}{\alpha C}\right)\right], & \alpha^2 > 0 \\ \dfrac{1}{E_g^2 - \gamma^2}, & \alpha^2 = 0 \\ \dfrac{1}{\alpha C}\left[\ln\left|1 + 2\dfrac{E_g^2 - \gamma^2}{\alpha C}\right| - \ln\left|1 - 2\dfrac{E_g^2 - \gamma^2}{\alpha C}\right|\right], & \alpha^2 < 0 \end{cases} \tag{Equation 35}$$

$$\tau_4(E) = \begin{cases} 2E_g \ln\dfrac{4E_g^2}{\sqrt{(E_0^2 - E_g^2)^2 + E_g^2 C^2}}, & E = E_g \\ 2E_g \ln\dfrac{(E + E_g)^2}{\sqrt{(E_0^2 - E_g^2)^2 + E_g^2 C^2}} - \dfrac{(E - E_g)^2}{E}\ln\dfrac{\left|E - E_g\right|}{E + E_g}, & E \neq E_g \end{cases} \tag{Equation 36}$$

$$\zeta^4(E) = (E^2 - \gamma^2)^2 + \frac{\alpha^2 C^2}{4}$$ Equation 37

$$\gamma = \sqrt{E_0^2 - \frac{C^2}{2}}$$ Equation 38

$$\alpha^2 = 4E_0^2 - C^2, \alpha := \sqrt{|\alpha^2|}$$ Equation 39

where E_g is the bandgap, E_0 is the peak energy of the Lorentz oscillator, A is the oscillator strength and C is the oscillator width. The imaginary part of the dielectric constant can be expressed as

$$\epsilon_2(E) = \begin{cases} \frac{AE_0C(E-E_g)^2}{(E^2-E_0^2)^2 + C^2E^2}\frac{1}{E}, & E > E_g \\ 0, & E \leq E_g \end{cases}$$ Equation 40

2.2.3.1.5. Cauchy Model

The Cauchy Model is an empirical method to describe the complex refractive index of insulators and semiconductors in their transparent spectrum.[33] The refractive index and extinction coefficient can be expressed as:

$$n(\lambda) = n_\infty + \frac{B}{\lambda^2} + \frac{C}{\lambda^4}$$ Equation 41

$$k(\lambda) = D + \frac{E}{\lambda^2} + \frac{F}{\lambda^4}$$ Equation 42

where B, C, D, E, and F are empirical fitting parameters, and n_∞ is the offset refractive index at the infinity.

2.2.3.1.6. Forouhi-Bloomer Model

The Forouhi-Bloomer model can be utilized to describe the optical properties of crystalline and amorphous semiconductors and dielectrics which is based on a quantum mechanical dispersion model.[34,35] The optical band gap is assumed without defect electronic states and band structures are assumed to have a parabolic energy dispersion. In conjunction with the KK relation, the corresponding dispersion model can be expressed as:

$$n(E) = n_\infty + \frac{B_0 E + C_0}{(E - B)E + C}$$ Equation 43

$$k(E) = \frac{A(E - E_g)^2}{(E - B)E + C}$$ Equation 44

where E_g is the bandgap of the material and n_∞ is the offset refractive index. Here, B_0 and C_0 are defined as:

$$B_0 = \frac{A}{Q}[-\frac{B^2}{2} + E_g B - E_g^2 + C]$$ Equation 45

$$C_0 = \frac{A}{Q}\left[\frac{B}{2}(E_g^2 + C\right) - 2E_g C]$$ Equation 46

and

$$Q = \frac{1}{2}(4C - B^2)^{0.5}$$ Equation 47

where A, B, and C are positive non-zero fitting parameters. In some cases, materials can have multiple peaks in their spectra, therefore the dispersion can be extended as a sum of individual Forouhi-Bloomer oscillators for each peak which have their own fitting parameter sets. For instance, in this thesis complex refractive index of perovskite is modeled using three Forouhi-Bloomer oscillators. Details of the fittings are provided in the Appendix A.

2.2.4. Reflection-Transmission Spectrometer

The PVE300 Photovoltaic quantum efficiency system is used to carry out reflection and transmission spectra measurements. It is a production line quality measurement setup, utilized in the accurate determination of the spectral response of samples. The system brings together a dual Xenon/quartz halogen source, a monochromator, and detection units to gather reflected and transmitted light in an integrating sphere. Measurement can be carried out under specular only and diffusion and specular combined operation modes. The angle of incidence is 8°.

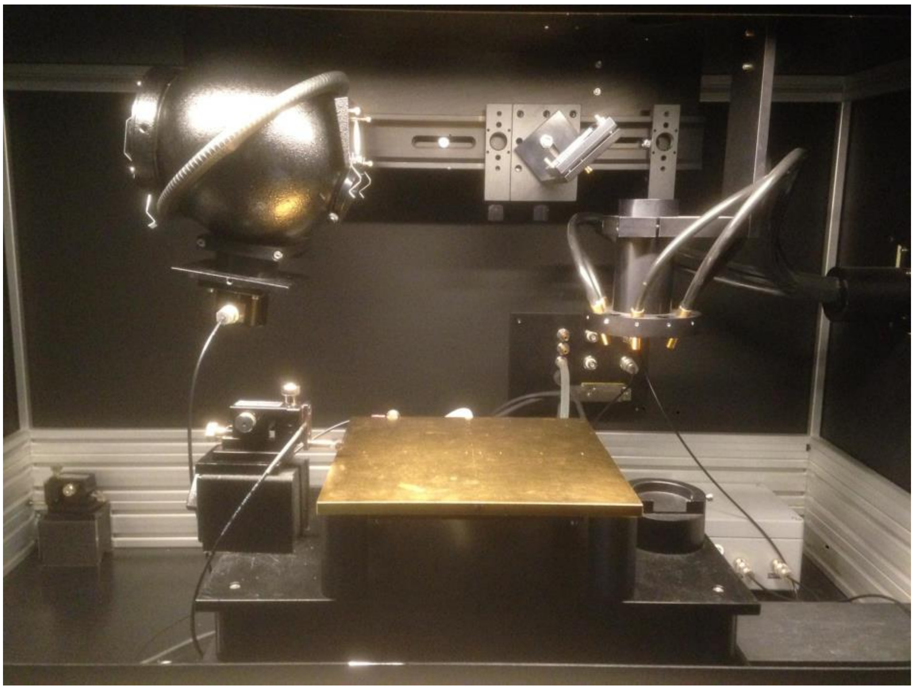

Figure 8 Photograph of the reflection-transmission measurement setup.

The reflection and transmission spectra of the fabricated structures are measured with BENTHAM PVE300.

2.3. **Fabrication**

Photolithographically patterned ITO coated glass substrates were purchased from Naranjo Substrates. NiO_x sputtering target was purchased from Kurt J. Lesker. PbI_2 and CH_3NH_3I (MAI) were purchased from Tokyo Chemical Industry CO. (TCI) and Lumtec, respectively. Fullerene (C_{60}) and 2,9-Dimethyl-4,7-diphenyl-1,10-phenanthroline (BCP) were purchased from Sigma Aldrich.

ITO coated substrates were cleaned deionized water for 10 min. The substrates were further treated by UV-ozone plasma cleaner for 10 min before transferring to a vacuum chamber with a base pressure of 6×10^{-7} Torr. NiO_x target was sputtered at RF power of 150 W and Ar-partial pressure of 6×10^{-3} Torr to deposit 33 nm of compact NiO_x film as HTL. Later, the NiO_x coated substrates were transferred to a vacuum deposition chamber which was evacuated to 2×10^{-6} Torr. $CH_3NH_3PbI_3$ was formed by coevaporating PbI_2 and CH_3NH_3I explained in the study of Pérez-del-Rey et al.[36] Briefly, CH_3NH_3I was evaporated with a temperature of 70 °C and PbI_2 at 250 °C. The thickness of the MAPI was monitored by two quartz crystal microbalance (QCM) sensors. After forming the MAPI layer (310, 370, and 460 nm), C_{60} (25 nm) and BCP (7 nm) were consecutively evaporated to deposit ETL. The substrates were later transferred to the metal evaporation chamber at 1×10^{-6} Torr to deposit 100 nm of silver as the top electrode.

MoO_x, NiO_x, LiF_x, aerogel, and SiO_2 samples were fabricated on c-Si for spectroscopic ellipsometry measurements. MoO_x, LiF, and MgF_2 samples were deposited by using the thermal evaporation technique. Samples were evaporated under 1×10^{-6} torr pressure. The SiO_2 sample was deposited by the spin-coating method with a 3000 rpm spin rate. Aerogel samples were fabricated with the methyltrimethoxysilane (MTMS) precursor solution.

CHAPTER 3

LIGHT MANAGEMENT IN THIN-FILM SOLAR CELLS

Planar thin-film structures are getting popular among solar cell researches and various other optical applications regarding their ease of fabrication, compatibility with industrial processes and high-quality outputs. In this chapter, perovskite, organic and CdTe thin-film solar cells are investigated from a light management perspective. Simple yet effective guidelines are provided, and the proposed methodology is generalized to be material independent. Along with the optical point of view, the charge transport properties of TCOs are also discussed.

Part of the material presented in this chapter has been published in *Adv. Optical Mater.* **2019**, *1900944.*[7]

Typical thin-film solar cells in superstrate configuration consist of glass/transparent conductive oxide (TCO)/front transport layer (FTL)/absorber/rear transport layer (RTL)/metal. The illustration of this structure is given in Figure 9. The glass layer is utilized with a thickness beyond its coherence length which mitigates any interferences. ITO is utilized as an exemplary TCO layer in this chapter. MAPI (or $CH_3NH_3PbI_3$) is used as the absorber in the first part of this chapter and later it is extended for PTB7:PCBM and CdTe. Moreover, the effects of various materials and electrical properties of TCOs are also discussed. Transparency and light trapping properties of FTL are of great importance regarding being part of window layers of solar cell design. Silver (Ag) is used as an exemplary metal layer with a thickness larger than its skin depth. Typically, the reflection is the primary loss mechanism in the thin-film solar cells. In addition to reflection losses, transparency of the window layers should be improved to enhance overall absorption. Both challenges require a careful refractive index and thickness selection.

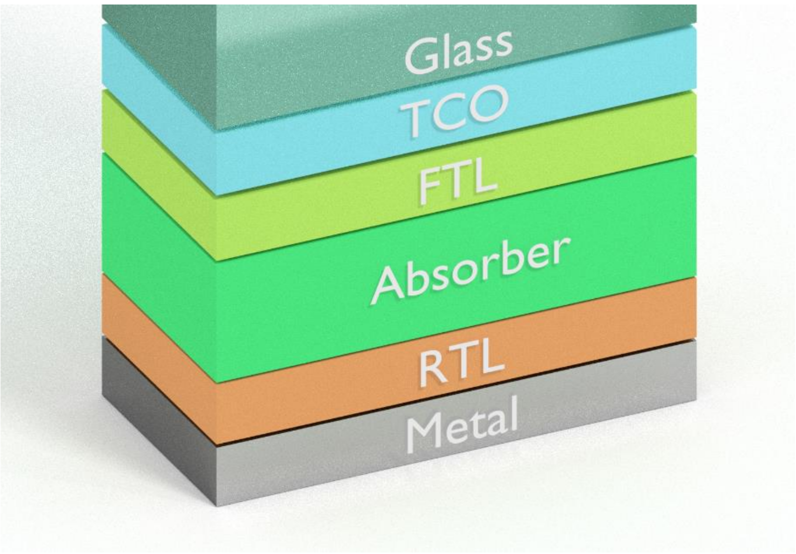

Figure 9 Illustration of the typical thin-film planar solar cell structure investigated in this thesis.

An uttermost absorption of incident light is the most important optical aspect in the design of solar cells. This is possible with arranging layers to focus absorption inside the absorber layer and eliminating reflectance. A thin-film solar cell is typically fabricated on a TCO coated glass substrate where the sunlight is incident on it (Figure 9). An FTL that allows the transport of one type of the carriers (i.e. electrons or holes) only is placed between the TCO and the absorber. This structure optically resembles a double-layer coating where the refractive index of air needs to be replaced by that of the glass. Therefore, the investigation of the optical interaction mechanism within a thin-film solar cell is approached using a two-step analysis method starting with isolating the window layers from the rest of the structure to analyze their anti-reflective trends, and later investigating the full device structure as an optical cavity analysis to enhance the total light-trapping with careful adjustment of refractive indices and thicknesses of the individual layers.

3.1. **Guideline for Optical Optimization of Perovskite Solar Cells**

Excellent optoelectronic properties of perovskites such as high carrier mobilities and absorption coefficients and long minority carrier lifetimes enable reports of new record efficiencies on average twice a year since 2013.[37–40] A massive number of surveys have been conducted on enhancing stability and improving the efficiency of perovskite solar cells. One way of the maximization of the photocurrent generation can be sustained by the light trapping. Light trapping in perovskite solar cells can be sustained by vertical-cavity design,[9,41–47] plasmonics,[48–50] external anti-reflective films,[51,52] photon recycling,[53,54] and surface texturing.[55–62] The vertical-cavity design among all other light-trapping approaches is much more attractive since it can be realized by adjusting the optical thicknesses of the layers used to fabricate a perovskite solar cell. In conjunction with that, the planar vertical-cavity designs based on simple vacuum fabrication steps that guarantee the low-cost of the perovskite solar cell.

An optical simulation analysis of glass/FTO/TiO_2/$CH_3NH_3PbI_3$/Spiro-OMeTAD/Au solar cell stack is reported by Ball et al. where they have presented local maxima in the modeled short circuit current at perovskite thicknesses of ~190 nm, ~320 nm, ~470 nm, and ~630 nm regarding the interference settings.[42] Nevertheless, their simulations were not extended to include various transport materials (TLs) with altering refractive indices. A more inclusive optical simulation investigation on perovskite/c-Si tandem solar cells using the FEM was published by Grant et al.[46] They have investigated the optimum refractive index of an ideal FTL of the perovskite-based top cell which two distinct regions are reported as, ones smaller and larger than the perovskite refractive index at a wavelength of 1000 nm since the focus of the study is the optimization of the tandem structure. Nevertheless, this division is incomplete in the elucidation of the single-junction perovskite solar cells utilizing shorter wavelengths than a perovskite/c-Si tandem cell. Vertical-cavity designs to improve 2T and 4T based perovskite/silicon tandem solar cells in which, perovskite solar cell consists of ITO coated glass, Spiro-OMeTAD, $CH_3NH_3PbI_3$, TiO_2, and rear ITO layers is documented by Filipic et al.[44] It is noteworthy that the optimum thickness of a transport layer depends on the configuration type, 2T or 4T. For instance, a structure with non-optimum layer thicknesses can lead to an underutilized perovskite photocurrent value while a higher tandem efficiency in the 2T configuration. Thus, optical cavity design of a single-junction perovskite solar cell is more similar to that of perovskite top cell in a 4T tandem cell configuration, however, it is still not enough to compare them regarding the fact that utilizing a planar metal mirror at the rear side in the case of single-junction optically differs from the transparent conductive electrode of the tandem solar cell substantially. Even though there exist reports recommending the usage of FTL with a refractive index (n_{FTL}) contiguous to the refractive index of perovskite,[9,46] the optical mechanism of this recommendation is not fully elucidated.

V- and W-coating approaches can be applied to perovskite structure with the selection of proper wavelengths to minimize the integrated reflection. In addition to that, the optimum optical thicknesses can be found iteratively. Also, an analytical approach based on the first derivate test method is developed to obtain optimum parameters. Performance comparison of these approaches is presented later in this chapter.

The effect of the refractive indices and thicknesses of the window layers on perovskite absorption is investigated. Perovskite thickness is used as semi-infinite to isolate the window layers and to investigate the reflection and parasitic absorption losses specific to these layers, and thus to elucidate the anti-reflective effect of them. The illustration of this structure is given in Figure 10.

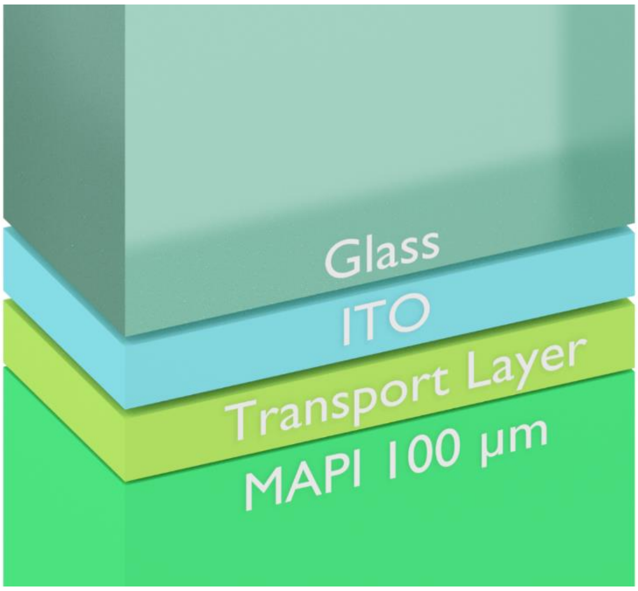

Figure 10 Illustration the structure used to probe anti-reflection of FTL and ITO layers on a very think perovskite

MAPC as a function of the thickness and refractive index of a hypothetical FTL is demonstrated in Figure 11. The refractive index of the FTL is used as constant and the extinction coefficient is omitted to present a direct guideline to optimize the FTL, leading to superior ARC performance in perovskite solar cells. The ITO layer thickness is taken as 70 nm which corresponds to the QWOT condition at a wavelength of 525 nm. Since the majority of the common TCO materials (i.e. ITO, AZO, FTO, IO:H) have refractive indices satisfying the SLARC condition ($n_{TCO} = \sqrt{n_{perovskite} \times n_{glass}}$) in a glass/TCO/perovskite structure, reflection elimination in the QWOT condition is obtained in the case of no FTL. In particular, ITO fulfills this principle in the UV-Visible part of the spectrum which yields a peak MAPC for QWOT of ITO at this range. For longer wavelengths, ITO has a gradually decreasing refractive index and converges to the one of glass, therefore QWOT condition weakens. The higher the ITO thickness, the lower the MAPC values, and this can be attributed to the pronounced parasitic absorption in ITO with increasing its thickness. Refractive index and thickness dependence of the hypothetical FTL changes negligibly with ITO thickness as revealed in Figure 12a, b.

There exist three prominent regions in Figure 11 and Figure 12 where MAPC has distinct behaviors:

1) n_{FTL} ranging between approximately 1.8 and 2.8 is optimum irrespective of its thickness.

2) The optimum refractive index window broadens for thinner FTLs. In particular, MAPC becomes insensitive to n_{FTL} for the thickness values below 15 nm.

3) MAPC intensively depends on the FTL thickness when n_{FTL} is not within the optimum range, which yields definite interferences inside the FTL.

In the case of n_{FTL} larger than 2.8 or smaller than 1.8, low and high reflections are attained for thickness values corresponding to the HWOT and QWOT values, respectively. For example, HWOT behavior is accomplished for FTL thickness ranges of 70-100 nm and 200-300 nm in the case of large and small n_{FTL}, respectively. On the contrary, the selection of FTL within thickness ranges of 60-130 nm and 30-60 nm for small and large n_{FTL} satisfies the QWOT condition, respectively, hence reflection increases which in turn, decreases the MAPC. The broadband nature of the solar spectrum is considered for the given thickness ranges. If not, QWOT and HWOT behaviors should coincide with a single wavelength. Consequently, the optimum FTL thickness is as thin as possible for an n_{FTL} that is larger than 2.8 and smaller than 1.8 as shown by the solid line in Figure 12b. The optimum FTL thickness value shifts to ~16 nm from ~97 nm with increasing n_{FTL} from 1.8 to 2.8.

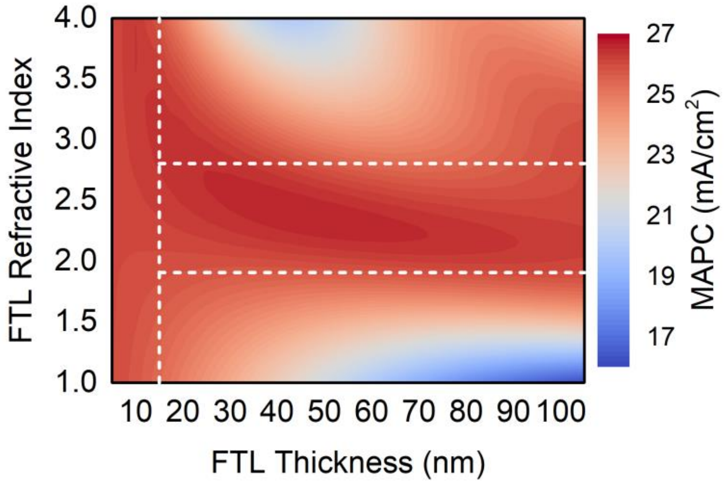

Figure 11 MAPC of semi-infinite perovskite as a function of the thickness and refractive index of a hypothetical FTL upon a 70 nm-thick ITO (a). Dashed lines separate three regions with distinct behaviors.

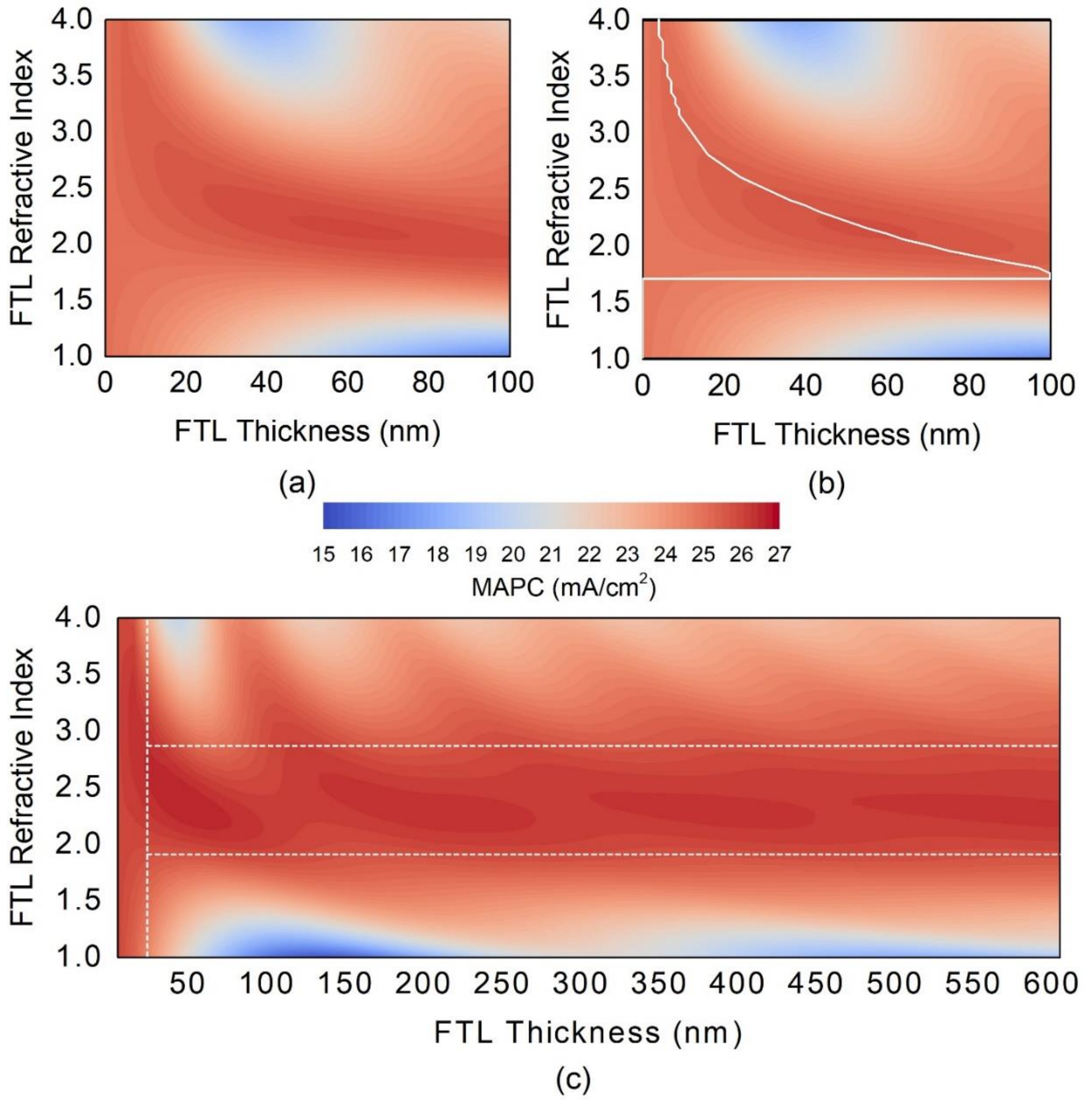

Figure 12 MAPC for a semi-infinite perovskite as a function of FTL thickness and refractive index for ITO thicknesses of (a) 150 nm, (b) 210 nm, and (c) 70 nm (extended). The white solid line in (b) indicates the optimum FTL thickness for FTL refractive index calculated with Equation 56. White dashed lines in (c) separate three regions with distinct behaviors.

3.1.1. An Analytical Approach for the Double-Layer AR Stack with an Ideal FTL and ITO atop Semi-Infinite Perovskite

This strategy provides a straightforward guideline of the TL choice in perovskite solar cells. Double-Layer analytical reflection atop a semi-infinite substrate can be expressed as:

$$R=\frac{\left(n_0\left(A-\frac{B\,n_2}{n_1}\right)-n_3\left(A-\frac{B\,n_1}{n_2}\right)\right)^2+\left(C\,n_2+D\,n_1-n_0\,n_3\left(\frac{C}{n_2}+\frac{D}{n_1}\right)\right)^2}{\left(n_0\left(A-\frac{B\,n_2}{n_1}\right)+n_3\left(A-\frac{B\,n_1}{n_2}\right)\right)^2+\left(C\,n_2+D\,n_1+n_0\,n_3\left(\frac{C}{n_2}+\frac{D}{n_1}\right)\right)^2}$$

Equation 48

where A = cos(β$_1$) cos(β$_2$), B = sin(β$_1$) sin(β$_2$), C = cos(β$_1$) sin(β$_2$), and D = sin(β$_1$) cos(β$_2$), and t_1 and t_2 are thicknesses of ITO and FTL layer, and n_0, n_1, n_2, and n_3 are refractive indices of glass, ITO, FTL, and perovskite, respectively. The term β$_1$ and β$_2$ are defined as the phase difference related to optical path length that forms as one passage through the ITO and FTL layers, respectively. They can be given by $2\pi n_1 t_1/\lambda$ and $2\pi n_2 t_2/\lambda$ at normal incidence. The extended version of the formula can be given as:

$$R=\frac{A^2(n_0-n_3)^2+B^2\left(\frac{n_0n_2}{n_1}-\frac{n_3n_1}{n_2}\right)^2-2AB(n_0-n_3)\left(\frac{n_0n_2}{n_1}-\frac{n_3n_1}{n_2}\right)+C^2\left(n_2-\frac{n_0n_3}{n_2}\right)^2+D^2\left(n_1-\frac{n_0n_3}{n_1}\right)^2+2CD\left(n_2-\frac{n_0n_3}{n_2}\right)\left(n_1-\frac{n_0n_3}{n_1}\right.}{A^2(n_0+n_3)^2+B^2\left(\frac{n_0n_2}{n_1}+\frac{n_3n_1}{n_2}\right)^2-2AB(n_0+n_3)\left(\frac{n_0n_2}{n_1}+\frac{n_3n_1}{n_2}\right)+C^2\left(n_2+\frac{n_0n_3}{n_2}\right)^2+D^2\left(n_1+\frac{n_0n_3}{n_1}\right)^2+2CD\left(n_2+\frac{n_0n_3}{n_2}\right)\left(n_1+\frac{n_0n_3}{n_1}\right.}$$

Equation 49

When ITO thickness equals QWOT, reflection can be simplified since sin(β$_1$) is equal to one and cos(β$_1$) is equal to zero:

$$R\cong\frac{sin(\beta_2)^2\left(\frac{n_0n_2}{n_1}-\frac{n_3n_1}{n_2}\right)^2+cos(\beta_2)^2\left(n_1-\frac{n_0n_3}{n_1}\right)^2}{sin(\beta_2)^2\left(\frac{n_0n_2}{n_1}+\frac{n_3n_1}{n_2}\right)^2+cos(\beta_2)^2\left(n_1+\frac{n_0n_3}{n_1}\right)^2}$$

Equation 50

As shown in Figure 11 and Figure 12, the optimum window widens for thinner layers as optical path length shortens suppressing the interferences within the FTL and the resultant reflection. When FTL thickness is smaller than 20 nm, from an optical point of view, MAPC becomes independent of the FTL refractive index. This can be sought given the extended relationship for reflection as given in Equation 50.

Low reflections with very thin FTL, that satisfy the $n_{FTL}t_{FTL}<\lambda/10$ condition, can be explained with the diminished sin(β$_2$) term. Eventually, reflection for thin FTLs can be written as

$$R \cong \frac{\left(n_1 - \frac{n_0 n_3}{n_1}\right)^2}{\left(n_1 + \frac{n_0 n_3}{n_1}\right)^2} \ (6) \qquad \textit{Equation 51}$$

Since the refractive index of ITO fulfills the SLARC criteria, low reflection can be achieved. The refractive index range between 1.8 and 2.8 is optimum for any FTL thickness. This can be ascribed to the fact that when the refractive index of FTL is chosen within the range of $\sqrt{\mathrm{n}_3\mathrm{n}_0} < \mathrm{n}_2 < \mathrm{n}_1\sqrt{\mathrm{n}_3/\mathrm{n}_0}$, the reflection term caused by the refractive index of the FTL vanishes, hence FTL functions as a perfect matching layer. Eventually, total reflection can be expressed as:

$$R \cong \frac{cos(\beta_2)^2\left(n_1 - \frac{n_0 n_3}{n_1}\right)^2}{sin(\beta_2)^2\left(\frac{n_0 n_2}{n_1} + \frac{n_3 n_1}{n_2}\right)^2 + cos(\beta_2)^2\left(n_1 + \frac{n_0 n_3}{n_1}\right)^2} \qquad \textit{Equation 52}$$

and it can be seen that regardless of the thickness of FTL, reflection is suppressed. When FTL thickness equals to QWOT, further reflection suppression is possible with n_{FTL} falling into the optimum FTL refractive index range. For a non-optimum refractive index range of FTL, which is above 2.8 or below 1.8, overall reflection is substantially affected by the thickness of FTL. In this refractive index range, the refractive index difference term is significantly pronounced, and the reflection losses increase which can be expressed by Equation 50. Therefore, reflection and MAPC, strongly depend on the thickness of the FTL. High MAPC zones in Figure 11 and Figure 12, correspond to the HWOT condition. In this case, phase terms are canceled, and reflection term reduces to Equation 51. For instance, if $n_2 < \sqrt{\mathrm{n}_3\mathrm{n}_0}$, regarding the relatively small refractive index of FTL, HWOT conditions that exploit phase cancellations can be satisfied if TL is as thick as 150-200 nm as shown in Figure 12c. Similarly, if $n_2 > \mathrm{n}_1\sqrt{\mathrm{n}_3/\mathrm{n}_0}$, the FTL thickness range of 70-100 nm corresponds to the HWOT value and presents higher MAPCs, as shown in Figure 11 and Figure 12. When

QWOT values are selected for the FTL thickness outside the optimum refractive index window, reflection can be expressed as:

$$R \cong \frac{\left(\frac{n_0 n_2}{n_1} - \frac{n_3 n_1}{n_2}\right)^2}{\left(\frac{n_0 n_2}{n_1} + \frac{n_3 n_1}{n_2}\right)^2} \quad \text{Equation 53}$$

since the refractive index difference is large, resultant reflection becomes high which in turn reduces the MAPCs.

The reflection spectrum of an exemplary stack consists of glass/ITO/FTL/perovskite with simplified equations and optical TMM simulations are calculated to evaluate the accuracy of the analytical equations. Figure 13a shows the simulated reflection spectrum of the mentioned stack when NiO_x is selected as 15 nm to fulfill the thin FTL condition, along with the reflection spectrum calculated with the corresponding formula (Equation 51). It can be seen that for wavelengths longer than 450 nm, Equation 51 and simulation results are identical. Figure 13b shows the reflection spectra of glass/ITO/TiO_2/perovskite stack calculated with Equation 52 and optical simulations. A 30 nm-thick TiO_2 is used as an FTL due to the fact that its refractive index falls into the optimum refractive index window. Figure 13c presents the comparison of the analytical approach and simulation for an FTL with non-optimum refractive index and thickness satisfying QWOT, PEDOT:PSS is used as an FTL with a thickness of 80 nm to satisfy QWOT condition at 500 nm wavelength. Since PEDOT:PSS has a refractive index of 1.48 which is below the optimum refractive index window and a thickness value of QWOT, an increased reflection is obtained in both simulation and analytical approaches. Simulation and analytical methods are in good agreement for wavelengths longer than 400 nm. It should be noted that the refractive index spectrum of perovskite has a sharp change in the 300-400 nm wavelength range which causes analytical approaches to diverge in this range. However, the photon flux in this range is limited, therefore the discrepancy within this region is sustainable.

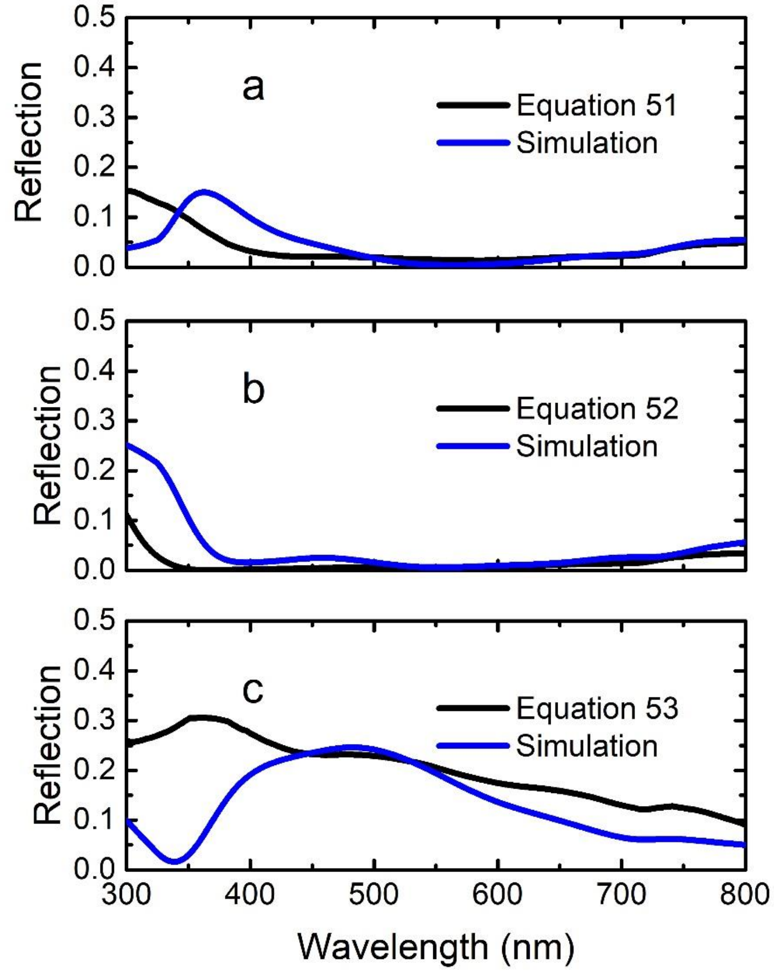

Figure 13 Reflection spectra of glass/ITO/NiO/perovskite stack with QWOT ITO for 15 nm NiO_x FTL (a), 30 nm TiO_2 FTL (b) and 80 nm PEDOT:PSS FTL (c) calculated with analytical (black) and simulation (blue).

Considering the higher photon density of the solar flux at the visible and longer wavelengths, the weighted reflection spectrum minimizes the reflection difference, especially in the UV part of the spectrum. To demonstrate a comparative investigation of the proposed analytical approach and simulations, photocurrent equivalents of the reflection spectra calculated with both methods are presented as a function of the FTL thickness and refractive index. For the analytical approach, reflections are calculated with: (i) Equation 51 if the thickness of the FTL is smaller than 20 nm, (ii) Equation 52 if the n_{FTL} falls into the optimum index range, and (iii) Equation 50 if the n_{FTL} is outside the optimum window, and results are presented in Figure 14.

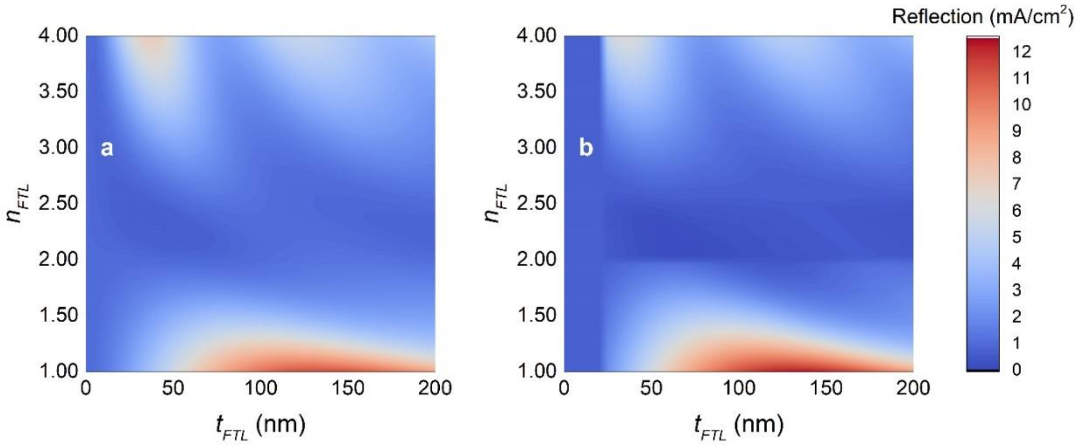

Figure 14 Comparison of weighted reflections obtained by simulations (a) and analytical calculations (b). Reflection losses are presented as current flux as a function of the thickness and refractive index of FTL.

The optimum refractive index spectra of the FTL is calculated using the first derivative test. The derivative of Equation 49 is taken with respect to the refractive index of the FTL. The obtained first derivative of the reflection equation is given in Appendix C. The derived optimum refractive index spectrum by the first derivative test is presented in Figure 15 along with the optimum refractive index spectrum by the iterative optical simulation. The calculated optimal refractive indices using both methods are in good agreement. The slight difference arises from neglecting the extinction coefficients in the first derivative test. It is worth mentioning that if the optimal refractive index profile is used, absorptions of more than 97% within the active layer can be achieved. An absorption of more than 99% can be achieved for wavelengths longer than 380 nm when the reflection of the air-glass interface is ignored.

The constant refractive index approach is congruent with most of the transport materials such as NiO_x, TiO_2, and PEDOT:PSS whose refractive index spectra are shown in Figure 116 (see Appendix B). An FTL refractive index of 1.6 in the UV region of the spectrum is ideal as presented in Figure 15. Approaching to longer wavelengths (the near IR part of the spectrum of interest) the ideal FTL refractive index becomes ~2 where refractive indices of ITO and perovskite are ~1.6 and ~2.7, respectively. Lastly, the ideal FTL refractive index is ~2.5 in the visible part of the spectrum regarding the larger refractive index of the ITO and extinction coefficient of perovskite in comparison with their values in the IR part of the spectrum. The calculated ideal FTL refractive index spectrum is presented in Figure 15 for a 30 nm-thick FTL and 70 nm-thick ITO providing a weighted reflection below 4.1% and this value is lower than 0.6% when the reflectance at the air/glass interface is omitted. Beyond this point in this chapter, three commonly-used transport layers in perovskite solar cells: PEDOT:PSS, NiO_x, and TiO_2, having distinguishing refractive indices from each other are analyzed as demonstrated in Figure 116 (see Appendix B).[63–65] In the case of the TiO_2 FTL, the TiO_2 refractive index (n_{TiO2}) is within the optimal refractive index range (Figure 11), for nearly all the implicated spectrum, that of PEDOT:PSS ($n_{PEDOT:PSS}$) is mostly away from the mentioned range. Alternatively, the NiO_x refractive index (n_{NiOx}) is close to the lower bounds of the optimum refractive index window for a broad range of the interested spectrum. It is noteworthy that the refractive indices of PEDOT:PSS and ITO, and of TiO_2 and perovskite pairs are analogous, the NiO_x refractive index is sandwiched by those of ITO and perovskite at long wavelengths.

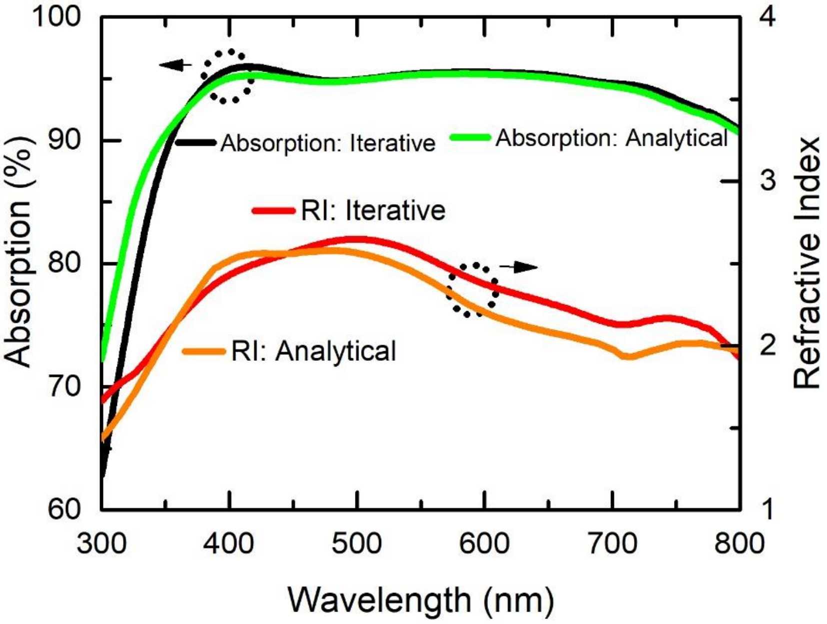

Figure 15 Absorption spectra of computed champion refractive index profile, optimum thicknesses (40nm TL and 70nm ITO) are given with numerically and iteratively found champion refractive index profiles.

3.1.2. **Double-Layer AR Approach for Practical FTL Materials**

Figure 16 shows the differences in MAPCs of a semi-infinite perovskite as a function of ITO and FTL thicknesses for PEDOT:PSS, NiO_x and TiO_2 as the FTL. In the absence of an FTL, the optimum ITO thickness range is found at a 50-70 nm range (Figure 16),[44,47,58] supporting the QWOT behavior in line with Equation 50. Furthermore, MAPC steadily decreases with increasing the ITO, PEDOT:PSS, TiO_2 and NiO_x thicknesses due to the parasitic absorptions in these layers regarding their non-zero extinction coefficients, especially at short wavelengths. The decreasing the PEDOT:PSS thickness yields an increase in the MAPC and MAPC maximizes in the absence of PEDOT:PSS as shown in Figure 16a, and as recommended in Figure 11. Furthermore, a local maximum around a PEDOT:PSS thickness of 160 nm is found due to the supported HWOT behavior at a central wavelength around 500 nm. Notably, a PEDOT:PSS thickness of 160 nm is beyond the limits of efficient carrier transport. Alternatively, MAPC does not change considerably with varying the TiO_2 thickness since the TiO_2 refractive index is similar to that of perovskite particularly for wavelengths longer than 475 nm (Figure 116, see Appendix B) . Hence, the TiO_2 and perovskite layers function as a joint optical layer, and the resultant reflection from the TiO_2/perovskite interface becomes negligible. Also, the TiO_2 refractive index is considerably larger than the one of perovskite and its extinction coefficient is highest at short wavelengths, driving higher reflections and parasitic absorption losses in the UV part of the spectrum. Consequently, a local maxima zone in MAPC arises at a TiO_2 thickness around 25 nm (Figure 16b), which serves a superior ARC at wavelengths around 400 nm - 600 nm as presented in Figure 17. The dependency the MAPC on the thickness of NiO_x is relatively weaker (Figure 16c) since the NiO_x refractive index falls within the optimum refractive index range across the absorption spectrum of perovskite as presented in Figure 11. MAPC presents a local maxima trend in the case of the 60 nm joint thickness of the ITO and NiO_x layers (Figure 16c), manifesting an absorption maximum primarily at long wavelengths (>600 nm) as presented in Figure 17b. A broad thickness range of NiO_x allows high MAPC due to its refractive index being in proximity to the one of ITO, particularly in the visible region of the spectrum, which brings on a low reflection at the interface of NiO_x and ITO. Notably, the 60 nm-thick NiO_x and 25 nm-thick TiO_2 are optimum thicknesses that perfectly aligned with those found from the constant refractive index analysis, as shown by the solid line in Figure 16c and Figure 17b, presenting an endorsement of this concept for metal oxides.

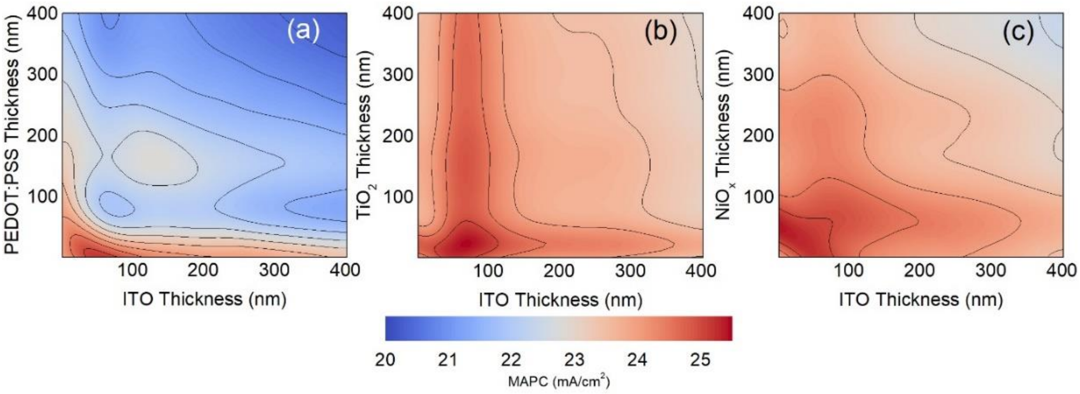

Figure 16 MAPC of semi-infinite perovskite at various thicknesses of ITO and (a) PEDOT:PSS, (b) TiO_2, (c) NiO_x.

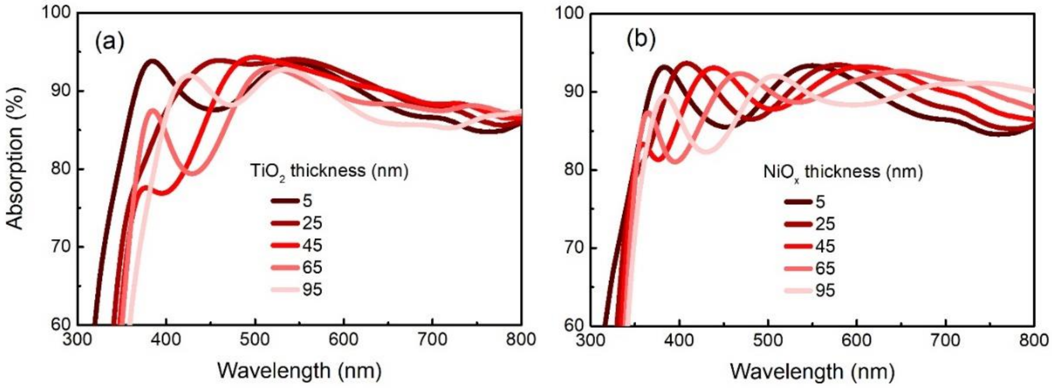

Figure 17 Absorption spectra of semi-infinite perovskite for various TiO_2 and NiO_x thicknesses.

The semi-infinite perovskite absorption spectra calculated for the 30 nm-thick PEDOT:PSS, TiO_2 and NiO_x FTLs are presented in Figure 18 together with the AM1.5G photon flux spectrum. The perovskite absorption maximizes for

PEDOT:PSS in the UV, and for NiO_x and TiO_2 in the visible and IR regions of the spectrum. Considering the fact that there is a higher photon flux at longer wavelengths of AM 1.5G photon flux spectrum, absorptions in the cases of NiO_x and TiO_2 mostly superior to that of PEDOT:PSS leaving the UV part of the spectrum. The perovskite absorption drops found in wavelengths shorter than 350 nm for NiO_x and TiO_2 is primarily due to more distinct refractive indices of the FTLs and perovskite, and larger FTL parasitic absorptions as presented in Figure 116 (see Appendix B). The local drop in the absorption spectrum in the case of NiO_x around 480 nm wavelength can be ascribed to the fact that the joint optical thickness of NiO_x and ITO is an integer multiple of HWOT which leads to increased reflection for the mentioned region. In the case of PEDOT:PSS, this drop moves to the 470 nm wavelength on account of smaller optical thickness of PEDOT:PSS through its smaller refractive index for that wavelength. Furthermore, the drop is more intense for the PEDOT:PSS case regarding the higher index contrast result of larger refractive index difference between PEDOT:PSS and perovskite compared to the case of NiO_x. For the TiO_2 FTL case, the perovskite absorption spectrum is considerably enhanced for 420-600 nm wavelength range result of superior ARC behavior of the 30 nm-thick TiO_2 in good agreement with Figure 16b and Figure 17a.

Selecting the thickness of the ITO layer is critical also from the electrical perspective along with the optical point of view due to the fact that it should be sufficiently thick to support the required lateral conductivity. Therefore, a 210 nm-thick ITO with a corresponding typical sheet resistance of approximately 10 $\Omega/\square$, is selected in Figure 18 and the rest of the chapter unless otherwise stated.

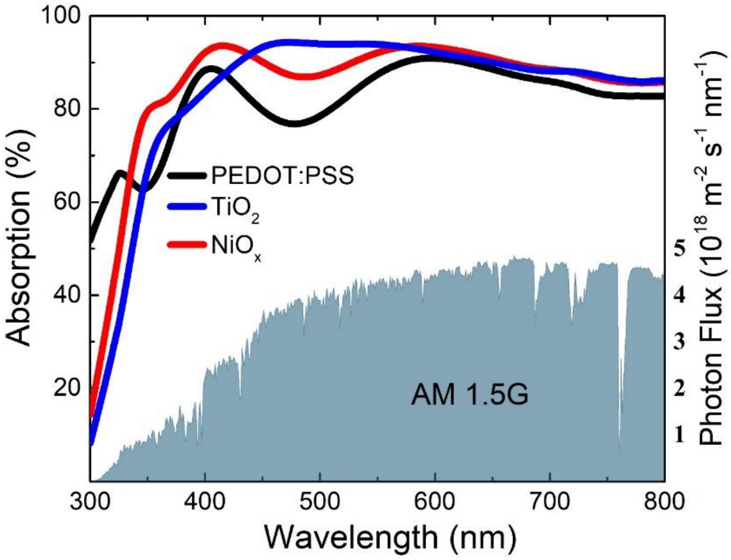

Figure 18 Absorption spectra of semi-infinite perovskite when a 30 nm TL and 210 nm ITO are used (d) together with the AM 1.5G spectrum for the photon flux (green shaded area). The simulated structure (e).

When PEDOT:PSS or NiO_x hole transport layers are used at the front side of a perovskite solar cell (Figure 9), PCBM is commonly chosen as the electron transport layer at the rear side. Likewise, Spiro-OMeTAD is a common hole transport layer when TiO_2 is used at the front side as an electron transport layer. The absorption spectra of 445 nm- and 510 nm-thick perovskites are shown in Figure 19 for ITO, NiO_x, PCBM and Ag thicknesses of 210, 30, 50 and 100 nm, respectively. The semi-infinite perovskite (i.e. 100 µm) absorption spectrum with 30 nm-thick NiO_x and 210 nm-thick ITO atop is also demonstrated for comparison reasons. The perovskite extinction coefficient maximizes at the 350 nm wavelength, and it reduces gradually with wavelength as presented in Figure 116 (see Appendix B). Therefore, the incident light at short wavelengths is mainly absorbed in a single-pass completely before reaching the rear side of the solar cell depending on the perovskite thickness. While, the incident light with longer wavelengths is mainly absorbed in distinct fringes due to interferences, as shown in the inset of Figure 19. Thus, the region shorter and longer than a threshold wavelength, which corresponds to the dominant absorption mechanism change, are called Beer-Lambert and interference regions of the spectrum, respectively, as presented in Figure 19.[41] When typical perovskite thickness is varied from 250 to 800 nm, the onset of the interference region changes from a threshold wavelength of 420 nm to 630, respectively, as presented in Figure 20. The mentioned onset threshold wavelength around 550 nm is prominent in Figure 19 for a ~500 nm-thick perovskite thickness.

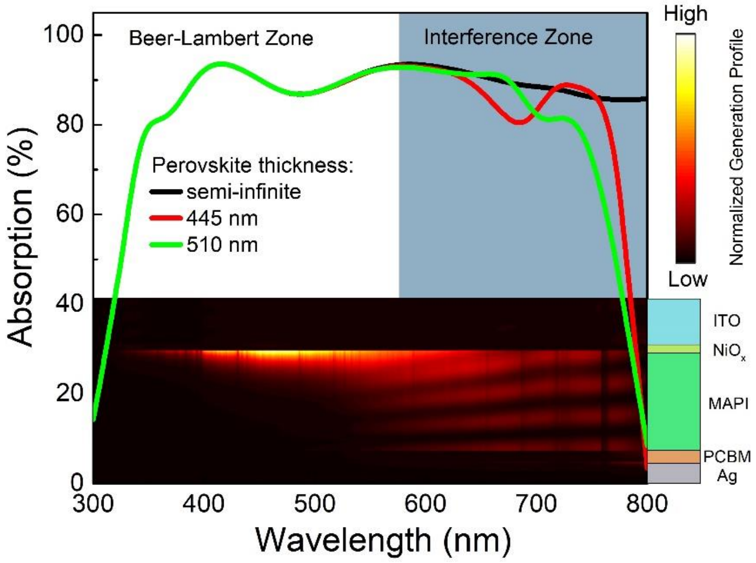

Figure 19 Absorption spectra of perovskite at thicknesses of semi-infinite, 445 nm and 510 nm for NiO$_x$, PCBM and Ag thicknesses of 30 nm, 50 nm, 100 nm, respectively. Inset: The weighted spectral absorption rate of photon profile within the depth of 445 nm perovskite.

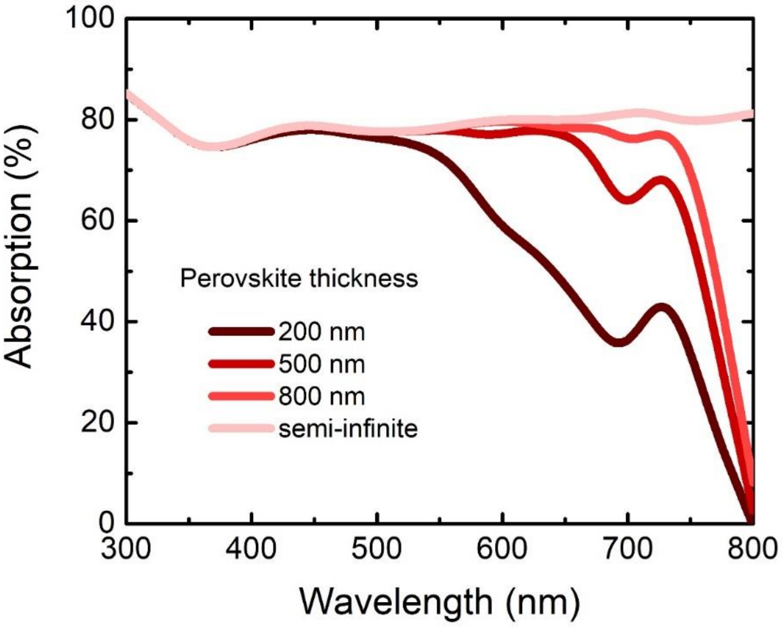

Figure 20 Absorption spectra of 200 nm-, 500 nm- and 800 nm-thick perovskite along with semi-infinite 100 μm perovskite for a NiO_x thickness of 30 nm. The thickness of PCBM is 50 nm in the case of finite perovskite layers.

Destructive and constructive interferences in perovskite have a principal consequence on the MAPC making it minimum and maximum, respectively.[9,42] For instance, a 445 nm-thick perovskite supports the constructive interferences, and a 510 nm-thick one supports destructive interferences at long wavelengths (i.e. around 700-750 nm). Thus, a 445 nm-thick perovskite leads to a 0.5 mA/cm^2 higher MAPC than the MAPC of the 510 nm-thick one in the given cell structure with a NiO_x FTL. Notably, in the case of PEDOT:PSS and TiO_2 FTLs, a 0.5 mA/cm^2 improvement in MAPCs by utilizing a thinner perovskite layers, 455 nm vs. 525 nm for PEDOT:PSS and 435 nm vs. 510 nm for TiO_2, can also be attained as presented in Figure 21. Evidently, the perovskite absorption is weak at wavelengths longer than 780 nm, which almost corresponds to its band edge, due to the small perovskite extinction coefficient.

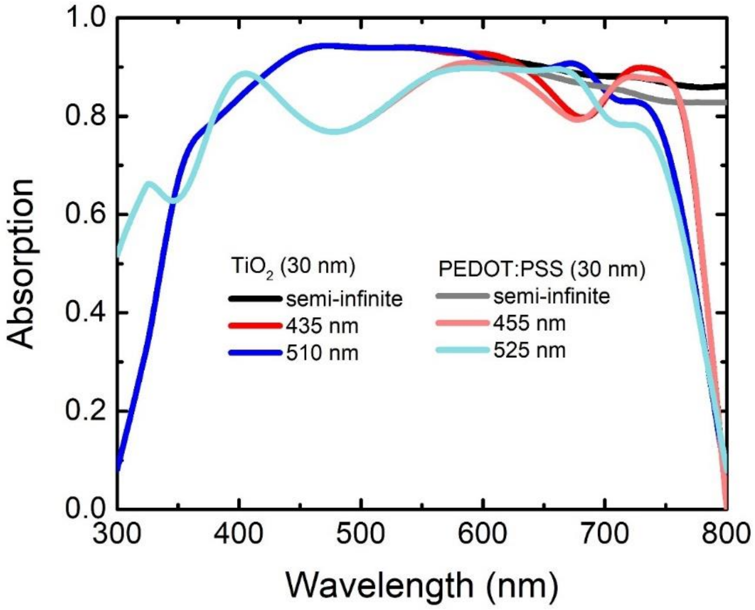

Figure 21 Absorption spectra of perovskite for perovskite thickness leading to local maxima and minima, and for semi-infinite perovskite. The thicknesses of TiO2 and PEDOT:PSS are 30 nm. The thickness of PCBM is 50 nm in the case of finite perovskite layers.

The effects of the thicknesses of the rear transport layer (RTL) and perovskite on MAPC is presented in Figure 22a, Figure 22b, and Figure 22c for 30 nm-thick PEDOT:PSS, NiO_x and TiO_2 FTLs. Furthermore, the effects of FTL and perovskite thicknesses on MAPC is demonstrated in Figure 23a, Figure 23b, and Figure 23c for a 50 nm-thick RTL. Light trapping (circular arrows) and ARC (vertical arrows) mechanisms in perovskite solar cells are presented in Figure 24.

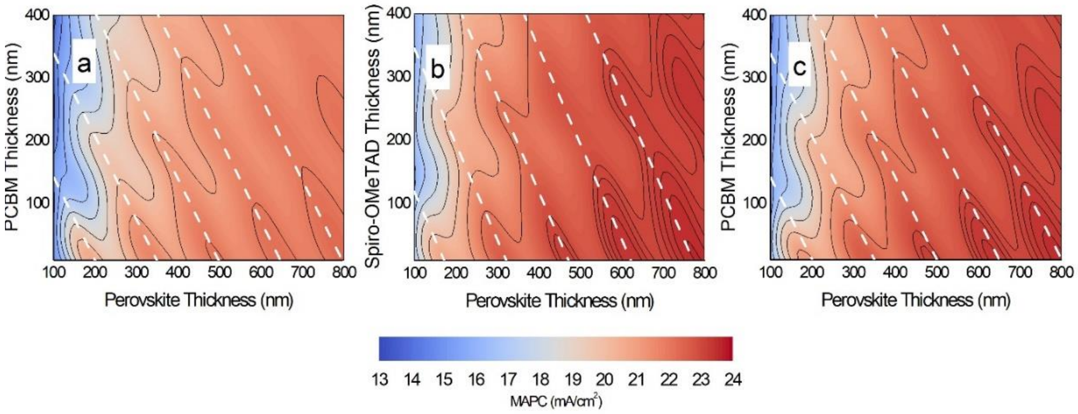

Figure 22 MAPCs varied with perovskite and RTL thicknesses (a, b and c), for PEDOT:PSS, TiO_2 and NiO_x FTLs, respectively.

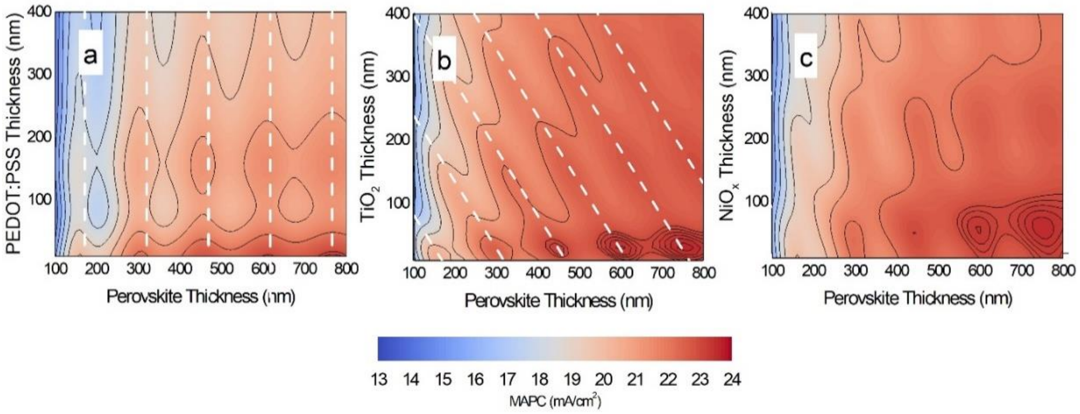

Figure 23 MAPCs varied with perovskite and FTL thicknesses (a, b and c) for PEDOT:PSS, TiO_2 and NiO_x FTLs, respectively.

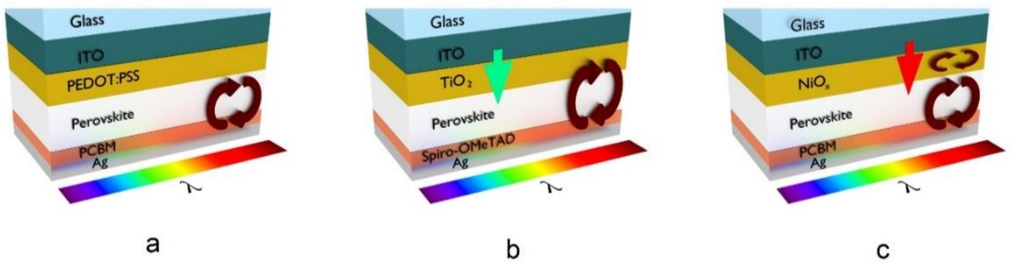

Figure 24 Light trapping (circular arrows) and ARC (vertical arrows) mechanisms in perovskite solar cells are presented for PEDOT:PSS (a), TiO_2 (b) and NiO_x FTLs (c).

The optimum thicknesses of perovskite ($t_{perovskite}$) and RTL (t_{RTL}) that yield local maxima in MAPC presented by the dashed lines in Figure 22a and Figure 23a are described by the following linear formula for PEDOT:PSS FTL:

$$t_{perovskite} \cong 50 + 150m - (n_{RTL}/n_{perovskite})t_{RTL} \quad \text{Equation 54}$$

where n_{RTL} and t_{RTL} are the refractive index and thickness of the RTL and m is an integer, representing the interference order. The constructive interference patterns arise at every 150 nm of the perovskite thickness supporting the HWOT behavior at the 770 nm wavelength as presented in Figure 22a and Figure 23a. Refractive indices of n_{RTL} and $n_{perovskite}$ are chosen at 730 nm (for m=3), which is near the central wavelength of the strong interference region occurring in the perovskite layer. Considering the fact that the interference region onset shifts due to the perovskite thickness as shown in Figure 20, a slightly shorter (~685 nm) or a longer central wavelength (~780 nm) can be chosen for m=1 or m>3, respectively. The RTL acts as a phase shifter (delayer) which is illustrated by the perfect fit of Equation 54 with the maxima in MAPC shown in Figure 22a. Thus, the increased phase shift defined with increasing the RTL drives the optimal thickness of the perovskite layer for each interference order to shift to smaller values as presented in Figure 22a.

Considering the contiguous refractive indices of PEDOT:PSS, ITO, and glass in the interference dominant region, the optimal PEDOT:PSS and perovskite thicknesses are optically decoupled from each other (Figure 23a). Hence, the result of having a transparent front window for the mentioned wavelength region, the back-reflected photons from perovskite into PEDOT:PSS are transmitted to the glass, escapes from the structure through the PEDOT:PSS/ITO and ITO/glass interfaces. Therefore, interferences in the perovskite solar cell at long wavelengths occur amid perovskite/PEDOT:PSS and PCBM/Ag interfaces as shown in Figure 24a.

In the case of TiO_2 FTL, a lateral shift of the dashed lines in Figure 22b – in comparison with Figure 22a - and a pronounced inclination of the dashed lines towards the y-axis in Figure 23b is found. The level of the shift and the slope of the inclination can be defined by subtracting the term $t_{FTL}(n_{FTL}/n_{perovskite})$ from Equation 54. The subsequent equation is expressed in Equation 55.

$$t_{perovskite} \cong 50 + 150m - (n_{RTL}/n_{perovskite})t_{RTL} - (n_{FTL}/n_{perovskite})t_{FTL} \quad \text{Equation 55}$$

It is noteworthy that, in the case of TiO_2 FTL, the shift is almost equivalent to the TiO_2 physical thickness due to the fact that n_{TiO2} is similar to $n_{perovskite}$ at wavelengths longer than 475 nm where there exists a greater photon flux in the AM 1.5G spectrum. Accordingly, the slope of the inclination is almost 45° which indicates optically both of the layers have equivalent shares in interference mechanisms. Local maxima in MAPC occur as continuous lines presenting that interferences in these configurations happen between TiO_2/ITO and PCBM/Ag interfaces as shown in Figure 24b. A local maximum at the 25 nm-thick TiO_2 leads to a greater ARC performance within the TiO_2 layer at short wavelengths, as shown in Figure 24b by the straight arrow, as illustrated in Figure 16b, in Figure 17a and also appears in Figure 23b.

Similar to TiO_2, in the case NiO_x FTL, a horizontal change of the local maxima of MAPC with the thicknesses of PCBM and perovskite happens (Figure 22c vs. Figure 22a). The NiO_x refractive index in the interference dominant region is different from that of both ITO and perovskite unlike PEDOT:PSS and TiO_2. Thus, interferences taking place within the perovskite layer - happens when the thickness of perovskite follows Equation 54 - can be supported or canceled out when the thickness of NiO_x equals to $m\lambda/2n_{NiOx}$ or $(2m+1)\lambda/2n_{NiOx}$, respectively, as shown in Figure 24c. Consequently, maxima in MAPC can be attained when both interference mechanisms happen constructively as illustrated in Figure 22c. Yet, the highest values of MAPC occur not in the absence of NiO_x but when the thickness of NiO_x is around 60 nm thanks to the greater ARC performance, in particular at longer wavelengths, as illustrated in Figure 17b and Figure 16c when a sufficiently thick perovskite (>700 nm or m>5) is utilized. A thinner NiO_x supports a better ARC performance for thinner perovskite layers, in which the IR light cannot be absorbed efficiently, presented as the green arrow in Figure 25c. The thickness of NiO_x follows the QWOT condition, 95 nm, at long wavelengths provides the optimum ARC performance ($\lambda/4n_{NiOx}$) for light reflected from the rear metal electrode (Figure 122, see Appendix C). Thus, a relatively high MAPC can be obtained irrespective of the NiO_x thickness between 0 and 100 nm as shown in Figure 23c.

Local maxima regions in MAPC for different interference orders are presented in Figure 25 (black squares). Local maxima regions predicted using Equation 54 and Equation 55 are shown by solid blue and red lines. Green arrows in Figure 25b and Figure 25c indicates the optimum TiO_2 and NiO_x thicknesses in terms of ARC efficiency. Green band in Figure 25c indicates NiO_x thickness range providing QWOT condition hindering occurrence of interference in perovskite solar cell.

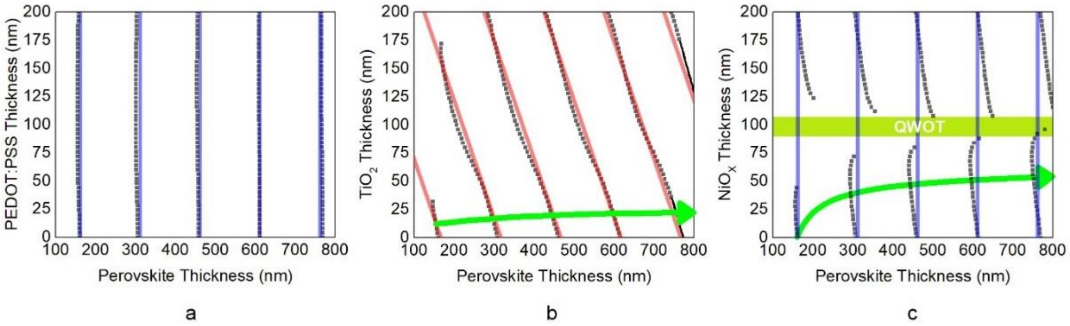

Figure 25 Local maxima regions in MAPC for different interference orders when (a) PEDOT:PSS, (b) TiO_2 and (c) NiO_x is used as FTL (black squares). Local maxima regions predicted using Equation 54 and Equation 55 are shown by solid blue and red lines. Green arrows in (b) and (c) indicated the optimum TiO_2 and NiO_x thicknesses in terms of ARC efficiency. Green band in (c) indicates NiO_x thickness range providing QWOT condition hindering occurrence of interference in perovskite solar cell.

As previously discussed through Figure 22, Equation 54 or Equation 55 can be followed if the interferences happen among the perovskite/FTL and RTL/Ag interfaces or in between the FTL/ITO and RTL/Ag interfaces, respectively. It is noteworthy to discuss the correctness of Equation 54 and Equation 55 in predicting perovskite and transport layers thicknesses to accomplish local maxima in MAPC, and the validity of the proposed equations with respect to n_{FTL}, n_{TCO}, and $n_{perovskite}$. Equation 54 and Equation 55 are precise within a few nanometers compared to the TMM simulations and previously documented experimental studies for PEDOT:PSS and TiO_2 as shown in Figure 25a and Figure 25b, respectively.[41,42,66] Figure 26 manifests that, with a constant n_{FTL} assumption, Equation 54 and Equation 55 are valid when n_{FTL} is below and above 2.1, respectively. It should be noted that the FTL extinction coefficient is taken as zero over the spectrum of interest in Figure 26. The aberration in the optimum thickness of the perovskite layer from what is predicted by both equations is the largest at the transition refractive index (i.e. n_{FTL} = 2.1), as presented in Figure 26.

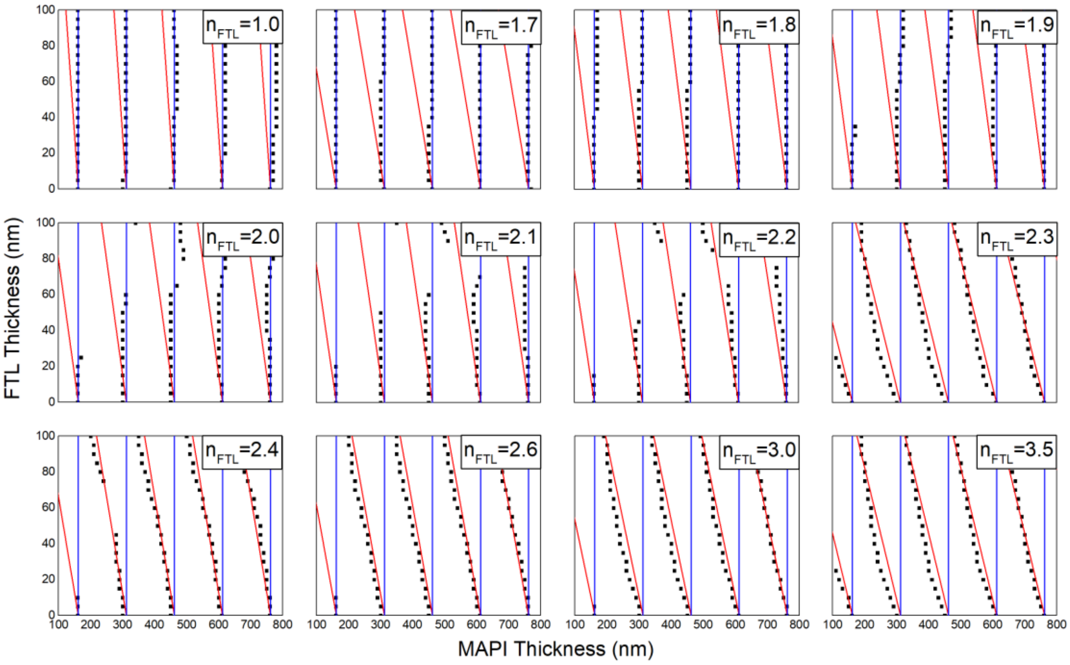

Figure 26 Computed maximal trends in MAPC for various interference orders for hypothetical FTLs with refractive indices between 1.0 and 3.5 and with no extinction coefficient. Maximal trends predicted using Equation 54 and Equation 55 are shown by solid blue and red lines.

While the optimum thickness of the NiO_x FTL decreases with perovskite thickness, TiO_2 thickness does not vary considerably, as discussed through Figure 23b and c. Furthermore, the optimum thickness of PEDOT:PSS should be zero or as thin as possible regardless of the perovskite thickness. Accordingly, the effect of n_{FTL} on the optimum FTL thickness, and consequently on Equation 54 is elaborate. The optimum FTL thickness versus its refractive index for various thicknesses of perovskite, satisfying constructive interference at long wavelengths when RTL thickness is zero is shown in Figure 27. The highlighted regions in Figure 27 specify the range of the FTL thickness at which the MAPC varies no more than 1% from its maxima at the computed n_{FTL} (shown by square symbols). Equation 56 is an empirical fit to Figure 27 for n_{FTL} larger than $n_{cut\text{-}off}$, supporting the optimum thickness of FTL when the thicknesses of perovskite and RTL satisfy Equation 54 or Equation 55, for interference orders larger than or equal to 2, as illustrated by the solid red line in Figure 27. The deviation between the simulated optimum FTL thickness and Equation 55 estimates is less than 0.6 nm. The optimum FTL thickness is zero in the case of thin perovskite layers, which have the interference order of 1, as illustrated in Figure 27a. The transition refractive index, $n_{cut\text{-}off}$, is defined as the refractive index which the optimum thickness of the FTL is no longer zero.

$$t_{FTL} = (t_{semi-inf} - t_0 \times exp(-t_{perovskite}/t_1)) \times exp(-(n_{FTL} - n_{cut-off}) \times C) \qquad \text{Equation 56}$$

where $t_{semi\text{-}inf}$ = 118.80 nm, $C=C_0 + C_1\exp(-t_{perovskite}/t_2)$, t_0= 167.65 nm, t_1= 361.85 nm, C_0=1.71, C_1= 4.04, t_2=170.77 nm. $t_{semi\text{-}inf}$ is the optimum FTL thickness in the case of perovskite thickness is semi-infinite and n_{FTL} is $n_{cut\text{-}off}$, which equals to 1.95, 1.85, 1.80 and 1.75 for perovskite interference orders of 2, 3, 4 and >= 5, respectively.

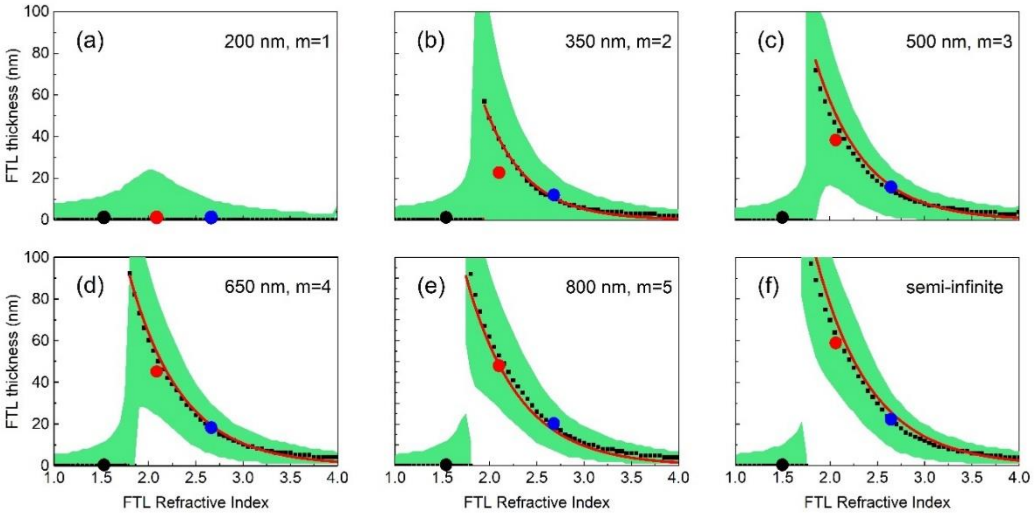

Figure 27 The optimum FTL thickness with respect to FTL refractive index for interference orders of (a) 1, (b) 2, (c) 3, (d) 4, (e) 5 and for semi-infinite perovskite. The RTL thickness is set to zero. Black, red and blue dots indicate the optimum FTL thickness of PEDOT:PSS, NiO_x and TiO2 obtained using their experimental refractive index and extinction coefficients, respectively. The solid red line shows the optimum thickness prediction of Equation 56.

The n_{FTL} value can be chosen from 450 nm wavelength. However, n_{FTL} chosen at a shorter wavelength presents a better estimate for the thickness of FTL for materials whose refractive index decreases with wavelength. Furthermore, a smaller FTL thickness should be targeted when FTLs with a large extinction coefficient are used which might be inevitable for large refractive index materials, $n_{FTL} > 2.5$. However, deviations of the optimum thickness for NiO_x and TiO_2 FTLs from what is predicted by Equation 56 yield less than 1% variations in MAPC from its maxima at the calculated n_{FTL} as illustrated in Figure 27.

It is noteworthy that contiguous refractive indices of ITO and glass at long wavelengths hinder the formation of interferences within the ITO layers hence the thickness of ITO is not accounted in Equation 54 and Equation 55. In other words, the optimum perovskite thicknesses in which local maxima in MAPC for various interference orders occur, do not vary with the ITO thickness as presented in Figure 28. This mechanism is generalizable for other common TCO materials such as FTO

(Fluorine-doped Indium Oxide) and AZO (Aluminum-doped Zinc Oxide) as illustrated in Figure 29.

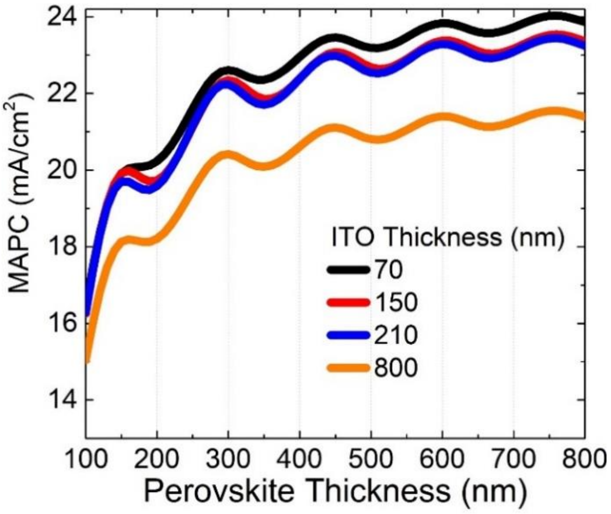

Figure 28 Variation of MAPC with perovskite thickness for various ITO thicknesses, NiO_x and PCBM thicknesses are taken as 30 nm and 50 nm, respectively. MAPC decreases with the thickness and the extinction coefficient (Figure 116, see Appendix B) of TCO due to enhanced parasitic absorption.

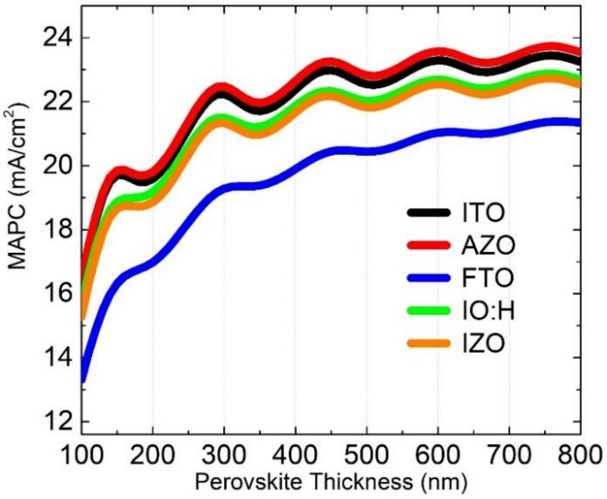

Figure 29 Variation of MAPC with perovskite thickness for different TCO materials with 210 nm thickness.[37,39] *NiO_x and PCBM thicknesses are taken as 30 nm and 50 nm, respectively. The extensive parasitic loss in FTO smooths out MAPC variation with perovskite thickness.*[38,40]

Moreover, the differences in optimum perovskite thicknesses fall in a range of 10 nm when different perovskite are employed, employing the refractive index and extinction coefficient spectra of various reported perovskites, as illustrated in Figure 30.

However, the magnitude of MAPC changes regarding different extinction coefficients.

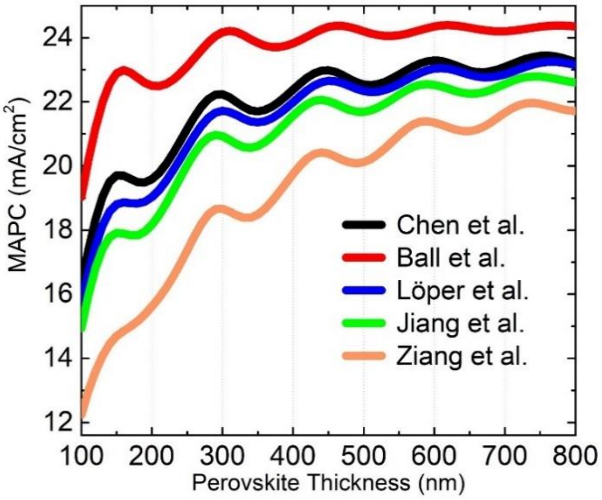

Figure 30 Variation of MAPC with perovskite thickness for various perovskites.[37] *NiO$_x$ and PCBM thicknesses are taken as 30 nm and 50 nm, respectively. The variations in optimum perovskite thicknesses are within a range of 10 nm for various perovskites.*

In this chapter, a guideline to predict the optimal thicknesses of the layers in perovskite solar cells (TCO, FTL, perovskite, and RTL) is proposed when the refractive indices of FTL (both at 450 nm and 730 nm) and RTL (at 730 nm) are known. The required equation sets to present a guideline are given in Table 2.

Table 2 Summary of equations that needs to be used when calculating the t_{FTL}, $t_{perovskite}$ and t_{RTL} for various n_{FTL} ranges. The values of refractive indices should be taken for λ=450 nm in Equation 56 and λ=730 nm in Equation 54 and 55.

n_{FTL} range	t_{FTL}	$t_{perovskite}$ & t_{RTL}
< 1.8	~ 0 nm	Equation 54
1.8 - 2.1	Equation 56	Equation 54
2.1 - 2.8	Equation 56	Equation 55
2.8 <	~ 0 nm	Equation 55

The optical engineering of perovskite solar cells can be briefly summarized as follows (also a decision tree is given in Figure 31):

- Use an FTL with a refractive index between 1.8 and 2.8 (at λ = 450 nm). Else, use as thin FTL as possible. Next, the thicknesses of perovskite and RTL can be calculated using Equation 54 or 55 if n_{FTL}<2.1 or n_{FTL}>2.1 at 730 nm wavelength, respectively. Note that a thinner RTL is superior if its extinction coefficient is non-zero.

- Calculate the approximate thicknesses of perovskite-based on the thickness of the RTL using Equation 54. Consider that there is about 150 nm perovskite thickness difference in between two following constructive interferences. Choose the thickness of FTL using Equation 56 based on its refractive index (at $\lambda = 450$ nm) and $t_{perovskite}$. Recalculate $t_{perovskite}$ taking into account t_{FTL} using Equation 55 if n_{FTL} is above 2.1 (at $\lambda = 730$ nm). Superior t_{FTL} and $t_{perovskite}$ values can be found by iterating Equation 56 and 55. It should be considered that the optimum FTL thickness for very thin perovskite layers with the interference order of 1 is zero. Table 12 and Table 13 (see Appendix C) provide the optimum FTL and MAPI thicknesses calculated using the proposed guideline and reported in the literature.
- The optically optimum thickness of the ITO layer is about 60 nm. MAPC reduces monotonously with TCO thickness as a result of the parasitic absorption in this layer. Hence, the TCO thickness should be decided mainly by taking the area of the solar cell into account.
- Approximately 100 nm MgF_2 ARC on glass can provide an additional enhancement of 0.4 mA/cm^2 in MAPC as presented in Figure 32.
- An RMS roughness of 15 nm does not affect the optimum thicknesses but can result in about 0.1 mA/cm^2 reduction in MAPC as shown in Figure 32.

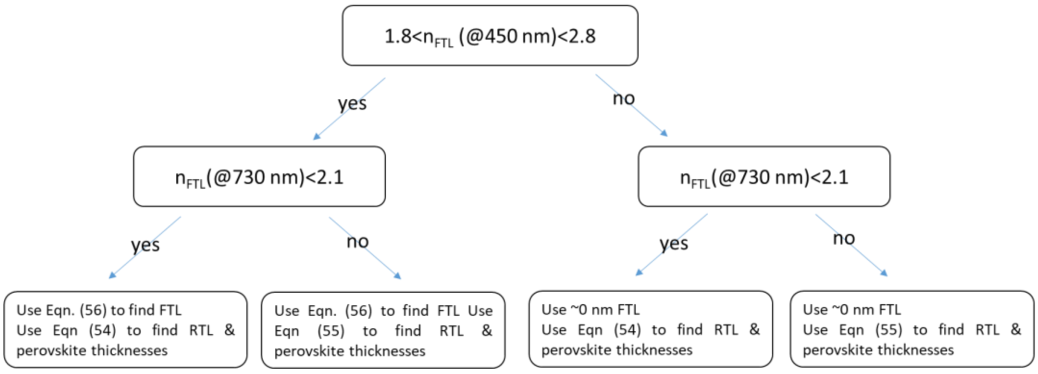

Figure 31 Decision tree for the thickness optimization guideline of FTL, perovskite, and RTL to achieve maximum MAPC.

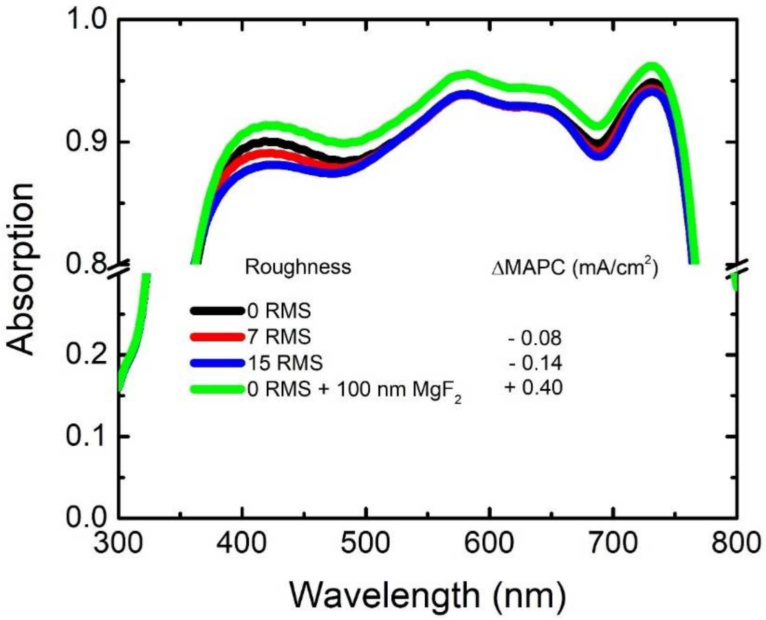

Figure 32 Absorption spectra of a perovskite solar cell with 50 nm NiO_x, 445 nm Perovskite and 50 nm RTL, and with no roughness (black), 7 nm RMS roughness (red) and 15 nm RMS roughness (blue). Roughness slightly reduces absorption in perovskite primarily in the UV part of the spectrum where scattering is more significant and therefore leads to an optical path length increase and parasitic absorption losses in FTL with relatively large extinction coefficients such as NiO_x and TiO_2. The absorption spectrum of a perovskite solar cells with the same thicknesses of layers having no roughness but a 100 nm-thick MgF_2 ARC on glass (green line).

The validity of the guidelines proposed in this work was examined experimentally in device structures with 33 nm-thick NiO_x as FTL, 115 nm-thick ITO, 25 nm-thick C_{60}/7 nm-thick BCP as ETL and 100 nm-thick Ag. The refractive index spectra of ITO, C_{60}, $NiO_{x,}$ and perovskite were successively measured by spectroscopic ellipsometry following the fabrication sequence. The measured spectra are given in Figure 110-114 (see Appendix B). The refractive index of BCP were acquired from literature for simplicity.[67] Co-evaporation method was used to precisely control the thickness of the perovskite.[36,68] The cross-sectional SEM images of the fabricated devices are shown in the inset of Figure 33a. The interferences in the 370 nm-thick perovskite are destructive while those in 310 nm and 460 nm-thick perovskite layers are constructive at long wavelengths based on the guideline given in this article. This is examined by replacing A(λ) by 1-R(λ) in Equation 8 to calculate the total photocurrent presented in Figure 33a. Since the complete solar cell device is used in the reflection (R) measurements, the comparison between the simulation and experimental results are provided based on 1-R(λ). Figure 33b manifests the experimentally measured 1-R(λ) spectra for the mentioned thicknesses of perovskite. They are similar in the range of λ = 300-550 nm and diverge in the interference region of λ = 550-800 nm as presented in Figure 33b. Constructive and destructive interferences for the optimum and non-optimum thicknesses are prominent as predicted. For example, lower 1-R(λ) values are obtained in the case of the device with 370 nm-thick perovskite. In total, the calculated MAPC and measured 1-R(λ) values are in good agreement for the chosen thicknesses of perovskite according to Figure 33. Similarly, measured and simulated reflection spectra for 310 and 460 nm-thick perovskite models are presented in Figure 34.

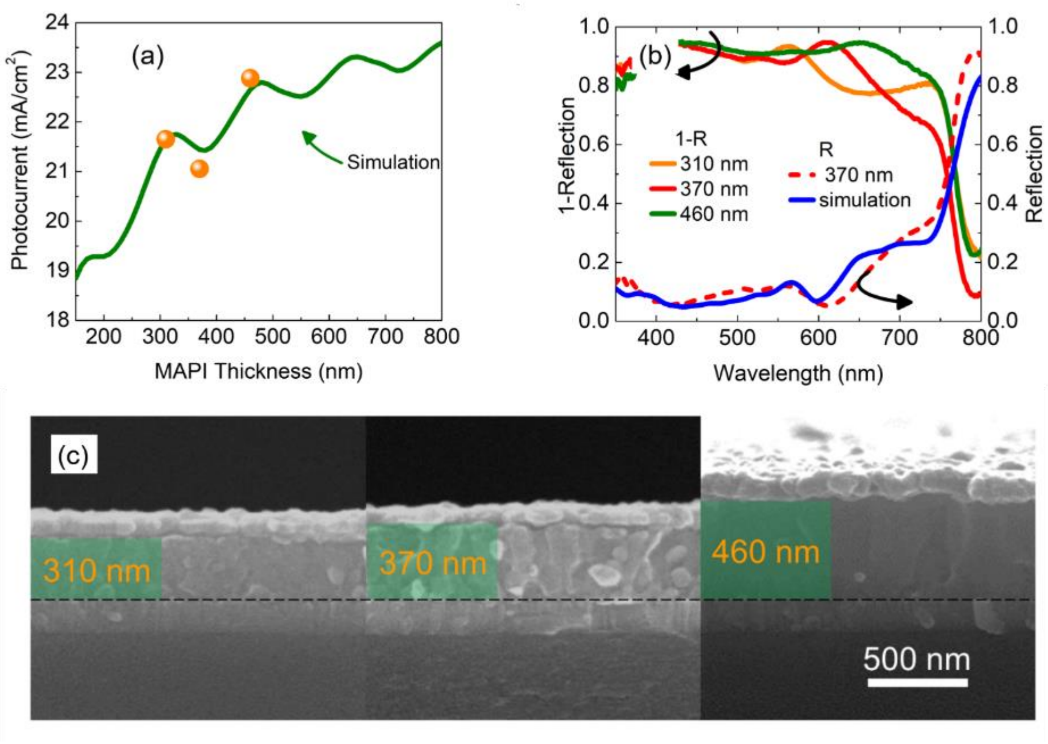

Figure 33 (a) Available photocurrent (in wavelengths between 350 and 800 nm) calculated using Equation 1 where A is replaced by 1-R as a function of perovskite thicknesses for a perovskite solar cell with 115 nm ITO, 33 nm NiO_x, 25 nm C_{60}, 7 nm BCP and 100 nm Ag. Orange circles, extracted from 1-reflection measurements, are the total available photocurrent of fabricated solar cells with perovskite thicknesses of 310, 370 and 460 nm. (b) Measured 1-Reflection spectra for perovskite solar cells with thicknesses of 310, 370 and 460 nm, and measured and simulated reflection spectrum for the perovskite solar cell with a thickness of 370 nm. (c) Cross-section SEM images of fabricated solar cells.

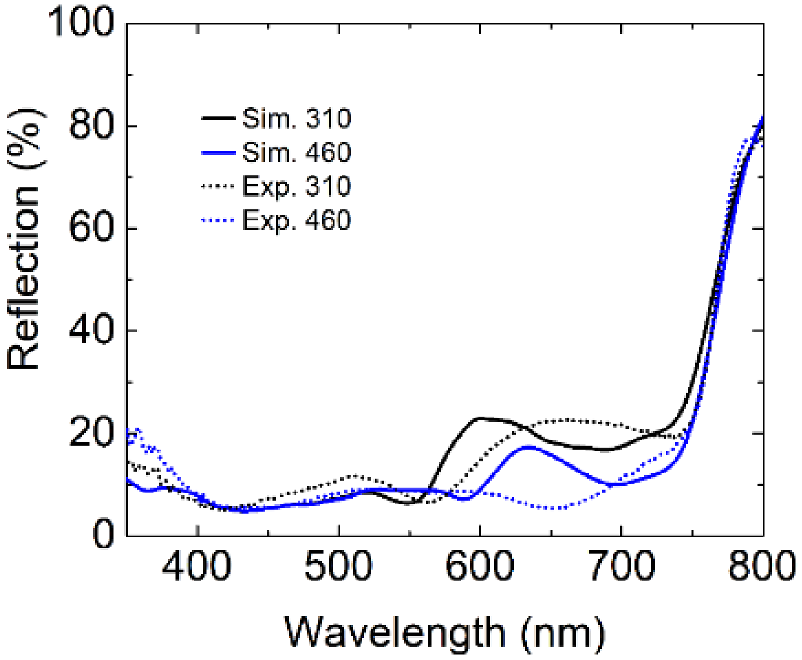

Figure 34 Measured and simulated reflection spectrum for the perovskite solar cells with thicknesses of 310 nm and 460 nm.

MAPC, and reflection and parasitic absorption losses are summarized in Figure 35a for the cases of A) non-optimum thicknesses of perovskite, FTL and ITO, (B) optimum thicknesses of perovskite and FTL but the non-optimum thickness of ITO and C) optimum perovskite, FTL and ITO thicknesses are used. Additionally, Figure 35b demonstrates the layer thicknesses establishing the perovskite solar cell for cases A, B and C and for the three FTL materials. To guarantee that no light is transmitted, the Ag layer thickness is set as 100 nm. Also, an RTL thickness of 50 nm is assumed. It is possible to attain a 1.8 mA/cm^2 higher MAPC by reducing the PEDOT:PSS and perovskite thicknesses from 85 nm to 25 nm and from 520 nm to 455 nm, respectively, which in turn lower the reflection and parasitic absorption losses. Also, the perovskite solar cell can possess an additional MAPC of 0.62 mA/cm^2 with the utilization of a thinner ITO (60 nm vs. 210 nm) which in turn further reduces the reflection and parasitic losses. Likewise, it is possible to boost MAPC by 1.85 mA/cm^2 by reducing the TiO_2 and perovskite thicknesses from 90 nm to 20 nm and from 585 nm to 445 nm, respectively, and using the optimum ITO thickness of 60 nm. Lastly, the MAPC is enhanced by 1.07 mA/cm^2 by reducing the perovskite thickness from 520 nm to 445 nm and increasing NiO$_x$ thickness from 10 nm to 50 nm together with the utilization of the optimum ITO thickness.

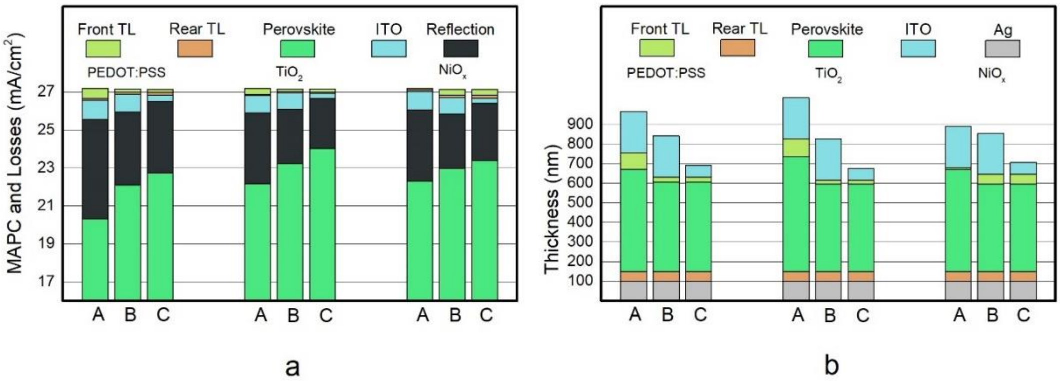

Figure 35 MAPC, and reflection and parasitic absorption losses are given in mA/cm^2 units for perovskite solar cells utilizing PEDOT:PSS, NiO$_x$ and TiO$_2$ as FTL (a) and corresponding layer thicknesses are given in (b). A denotes the non-optimum perovskite, FTL and ITO thicknesses, B denotes the optimum perovskite and FTL thicknesses but non-optimum ITO thickness and C denotes the optimum perovskite, FTL and ITO thicknesses.

The proposed guideline for MAPI type perovskites can be extended to other widely-used perovskites with various halide and cation combinations. Equation 54 and Equation 55 can be re-written as

$$t_{ABX3} \cong \begin{cases} t_{offset} + (\lambda_o/2n_{ABX3})m - (n_{RTL}/n_{ABX3})t_{RTL}, & n_{FTL} < n_{transition} \\ t_{offset} + (\lambda_o/2n_{ABX3})m - (n_{RTL}/n_{ABX3})t_{RTL} - (n_{FTL}/n_{ABX3})t_{FTL}, & n_{FTL} \geq n_{transition} \end{cases} \qquad \text{Equation 57}$$

where λ_o is slightly below the absorption onset wavelength of perovskite, t_{offset} is the fitted offset thickness, n_{ABX3} is the refractive index of perovskite and n_{FTL} is the refractive index of FTL at λ_o, and $n_{transition}$ is the transition refractive index where condition switches between cases. Values of λ_o, $n_{transition}$, and t_{offset} for various perovskite types are provided in Table 3.

Table 3 Generalized optimum thicknesses of ABX_3 (B=Pb), RTL and FTL prediction formula parameters.

A	X_3	$\lambda_{abs.onset}$ (nm)	t_{offset} (nm)	λ_o (nm)	$n_{threshold}$	Ref.
MA	I	790	50	775	2.1	Chen et al.[66]
MA	I	795	50	770	2.1	Ball et al.[42]
MA	I	780	50	750	2.1	Lin et al.[41]
MA	I	790	50	770	2.1	Löper et al.[69]
MA	I	779	50	750	2.1	Ziang et al.[70]
MA	I	776	50	750	2.1	Jiang et al.[71]
MA	I	795	50	770	2.1	Ndione et al.[72]
MA	I	780	50	770	2.1	Xing et al.[73]
FA	I	827	40	780	1.8	Ndione et al.[72]
$Cs_{0.15}FA_{0.85}$	I	821	40	780	1.8	Ndione et al.[72]
$Cs_{0.17}FA_{0.83}$	$Br_{0.17}I_{0.83}$	761	40	750	2.1	Manzoor et al.[74]
$Cs_{0.25}FA_{0.75}$	$Br_{0.20}I_{0.80}$	739	40	710	2.2	Manzoor et al.[74]
MA	Br	539	50	530	1.8	Ndione et al.[72]
FA	Br	554	50	530	1.8	Ndione et al.[72]

The accuracy of Equation 57 by comparing the optimal thicknesses of perovskite simulated by TMM simulations for various perovskite types (Table 4) is tested. Perovskite and FTL thicknesses, predicted by Equation 57 and computed through TMM simulations, leading to a maximum in MAPC are presented in Figure 26 for MAPI, Figure 119 for $Cs_{0.15}FA_{0.85}PbI_3$ (see Appendix C), Figure 120 for $FAPbI_3$ (see Appendix C), and Figure 121 for $Cs_{0.17}FA_{0.83}Pb(Br_{0.17}I_{0.83})_3$ (see Appendix C). Yet, further experimental verification of Equation 57 is still required for perovskites other than MAPI as the verification is only done for MAPI in this chapter.

Table 4 Accuracy comparison of generalized Equation 57 for various perovskites (i.e. ABX_3, B=Pb) for various FTL thicknesses for the interference order of 3. Δt_{error} is calculated by averaging the differences between the optimal perovskite thicknesses found using Equation 57 and calculated through TMM simulations over various FTL thicknesses. The thickness difference can be seen in Figure 26 for MAPI, Figure 121 for $Cs_{0.17}FA_{0.83}Pb(Br_{0.17}I_{0.83})_3$, Figure 119 for $Cs_{0.15}FA_{0.85}Pb(Br_{0.17}I_{0.83})_3$, and Figure 120 for $FAPbI_3$.

		Δt_{error} (nm)			
A	X_3	$n_{FTL}<n_{threshold}$	$n_{FTL}=n_{threshold}$	$n_{FTL}>n_{threshold}$	Ref.
MA	I	5.23	10.81	5.07	Chen *et al.*[66]
FA	I	18.64	19.65	4.39	Ndione *et al.*[72]
MA	Br	9.78	10.18	10.45	Ndione *et al.*[72]
FA	Br	8.89	10.43	22.57	Ndione *et al.*[72]
$Cs_{0.17}FA_{0.83}$	$Br_{0.17}I_{0.83}$	4.84	16.32	8.99	Manzoor *et al.*[74]

3.2. **Organic Solar Cells: A Case Study PTB7:PCBM Absorbers**

In this part, the two-step analysis method, which is previously discussed in the perovskite solar cell chapter, is extended for organic solar cells. For a case study, an organic solar cell comprised of ITO coated glass as superstrate, PEDOT:PSS as the FTL, PTB7:PCBM (1:1.5) as the absorber layer, LiF as the electron blocking layer in place of the RTL in Figure 9, and Al as the metal electrode is investigated. As previously discussed, strong absorber-based solar cells benefit more from interference driven MAPC enhancement in the thin-film structures. Typically, the absorption mechanism in organics solar cells functions similarly to direct-band absorption. Instead of a band structure, molecular orbitals of the active material are responsible for the generation of the energy level difference which yields photovoltage. In organic solar cells, light absorption generates a strongly bound electron-hole pair, which is called an exciton. One of the main challenges for charge collection is the separation of strong excitonic pairs which makes the thickness of the active layer constrained in conjunction with fabrication limitations. Hence, previously proposed optical optimization guidelines are applied to organic solar cells. The optical effects of the individual layers of cell structure are discussed in detail.

As a first step of the two-step analysis method, MAPC with varying the refractive index and thickness of the FTL atop the semi-infinite PTB7:PCBM layer is presented in Figure 36. ITO is used with a 70 nm thickness in coherence with optical optimization of perovskite solar cells. The division of MAPC results into three distinct regions with different behaviors is also valid for the PTB7:PCBM absorber. High MAPC zones for the thin FTL region are prominent. In the second region, where the high MAPCs are obtained irrespective of FTL thickness, it is found that the optimum window range is 1.8-2.3.

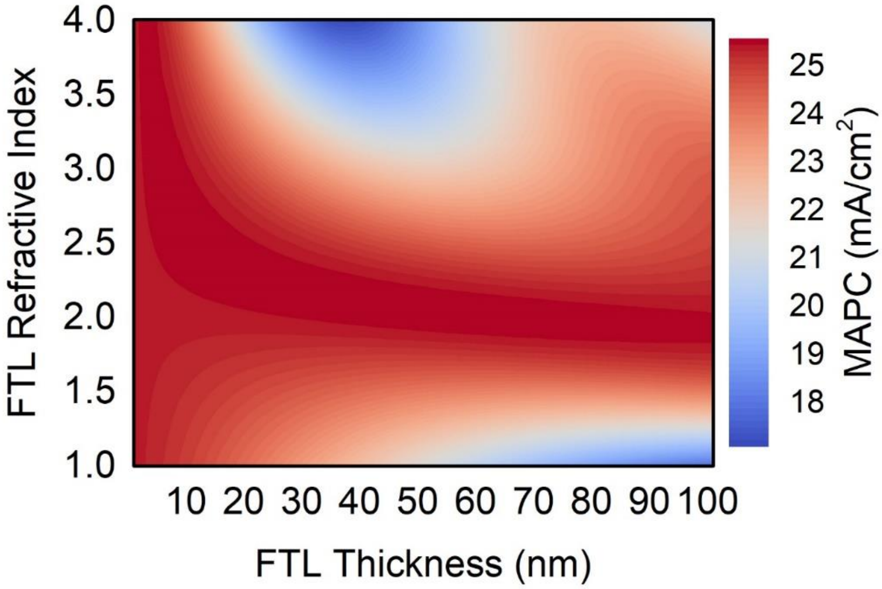

Figure 36 MAPC as a function of the refractive index and thickness of the front transport layer. PTB7:PCBM is used with a thickness of 400 µm and no RTL and metal layers are used.

The single-pass absorption spectra of PTB7:PCBM for its various thicknesses are shown in Figure 37. It can be seen that incident photons are almost fully absorbed up to 700 nm wavelength for an absorber thickness of 700 nm. The single-pass absorption decreases considerably with decreasing the thickness which leads to pronounced interferences. Since the device parameters (i.e. recombination and carrier lifetime) constraints the thickness of PTB7:PCBM, the interference is crucial for a PTB7:PCBM layer thinner than 500 nm.

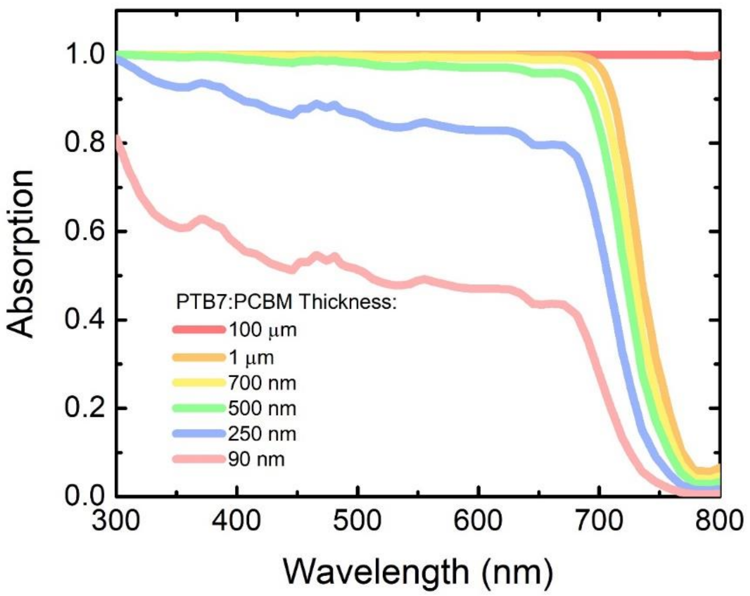

Figure 37 Single-Pass absorption spectra of PTB7:PCBM for various thicknesses.

MAPC as a function of ITO and PTB7:PCBM thicknesses are presented in Figure 38. Al and LiF layers are used with 150 and 5 nm thicknesses, respectively. The PEDOT:PSS layer is omitted to isolate the interdependency of ITO and PTB7:PCBM. Notably, 90, 240, 400, 600 and 780 nm thicknesses of PTB7:PCBM present local maxima which are not changing with ITO thicknesses. Two thicknesses of PTB7:PCBM, 90 and 240 nm, are selected due to practical thickness limitations. When PTB7:PCBM is used with a 90 nm thickness, the optimum ITO thickness is 130 nm. When it is used with a 240 nm thickness, an additional local maximum of MAPC is obtained at the 40 nm-thick ITO. Optimum ITO thicknesses can be explained with the following the consecutive QWOT values of ITO.

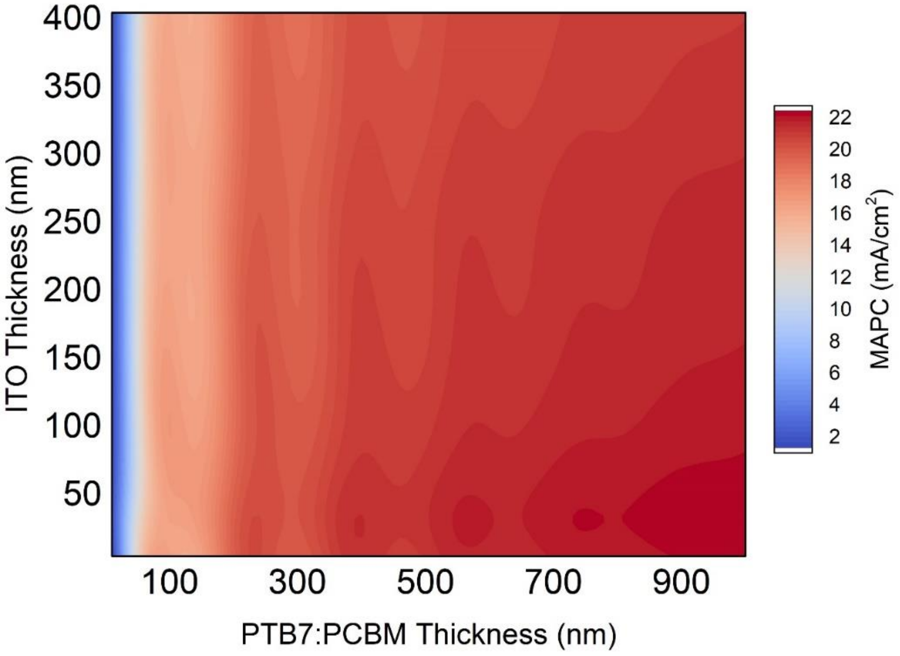

Figure 38 MAPC as a function of ITO and the active layer thicknesses.

The normalized MAPC as a function of ITO and PEDOT:PSS thicknesses for PTB7:PCBM with 90 nm (a), 240 nm (b), 400 nm (c) and semi-infinite (100 µm) (d) thicknesses are shown in Figure 39. Except for the 90 nm-thick PTB7:PCBM, optimum ITO and PEDOT:PSS thicknesses are 40 and 0 nm, respectively. When a 90 nm-thick PTB7:PCBM is used, high MAPCs are found in a broader ITO and PEDOT:PSS thickness range. While the maximum MAPC is obtained with 130 nm-thick ITO and 20 nm-thick PEDOT:PSS. Optimum thickness pairs present a decline towards the y-axis which indicates that optimum ITO thickness changes with increasing the PEDOT:PSS layer thickness. It can be attributed to their similar refractive indices in longer wavelengths of the spectrum of interest (Figure 116, see Appendix B).

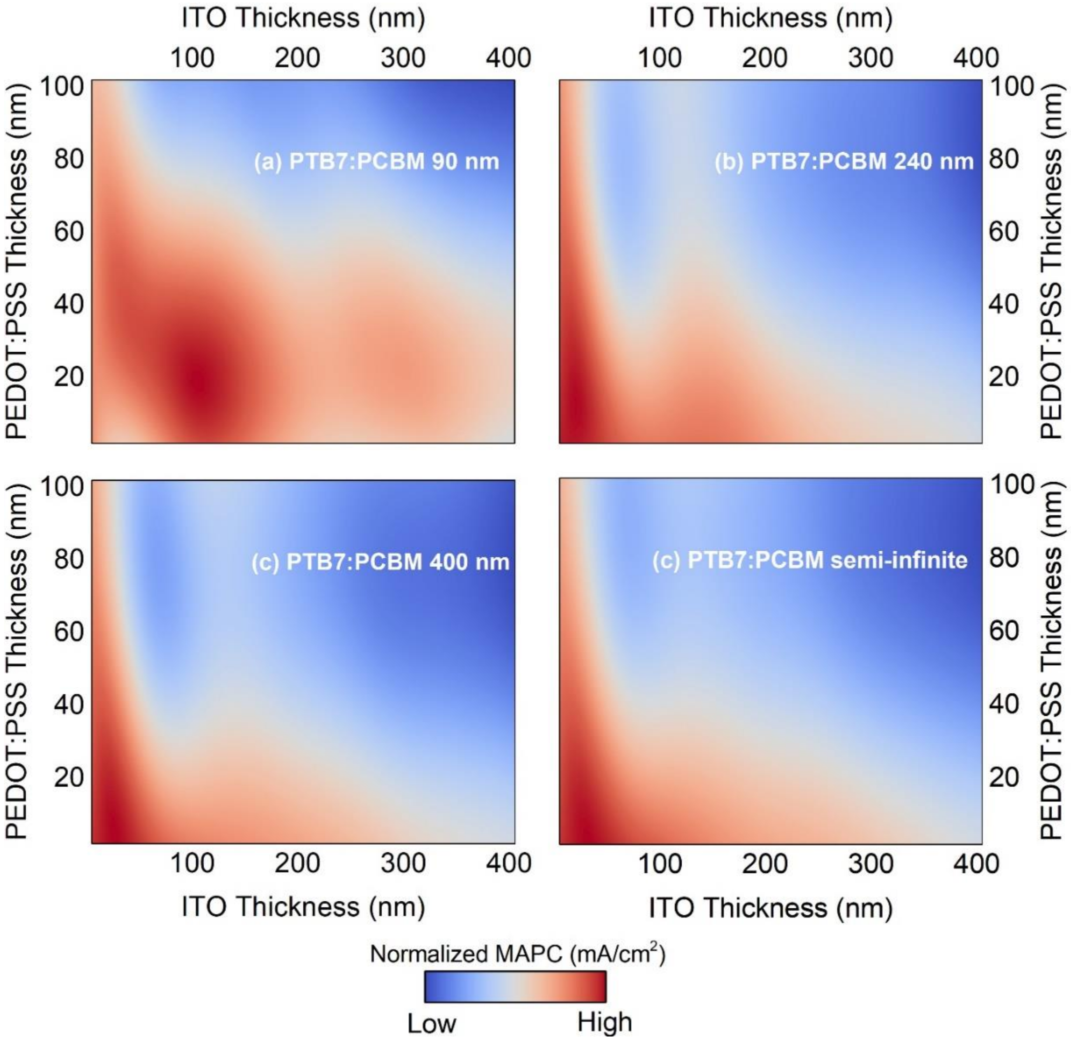

Figure 39 Normalized MAPC as a function of ITO and PEDOT:PSS thicknesses for 90 nm, 240 nm, 400 nm, and 100 µm PTB7:PCBM layer thicknesses.

MAPC as a function of the PEDOT:PSS layer thickness is presented in Figure 40 for various PTB7:PCBM and ITO thickness combinations. Thickness pairs are selected from the local maxima regions of Figure 38. The optimum PEDOT:PSS thickness is found as thin as possible for the 240 nm-thick PTB7:PCBM. For the 90 nm-thick PTB7:PCBM, optimum PEDOT:PSS thickness is found approximately as 20 nm.

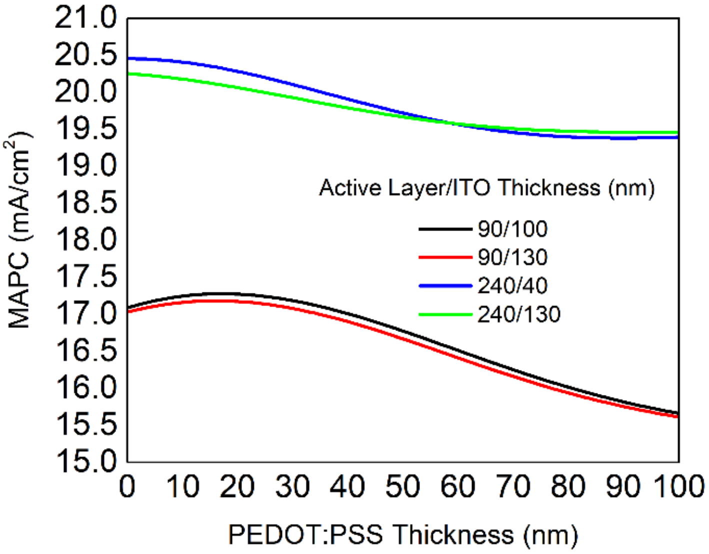

Figure 40 MAPC as a function of PEDOT:PSS thickness for various active layer and ITO combinations

MAPC as a function of the ITO thickness for 90 nm-thick PTB7:PCBM is presented in Figure 41. The PEDOT:PSS layer thickness is fixed to 20 nm to simplify the optimization problem. Considering the optical losses, and electrical transport properties, a selection of the ITO thickness within the 200-300 nm range is not favorable (highlighted red). Instead, the 100-200 nm thickness range is optically more advantageous (highlighted green). The local maximum of MAPC is obtained with a 100 nm-thick ITO. To lower the sheet resistance, ITO layer thickness either can be increased up to 200 nm or it can be selected 300 nm or larger.

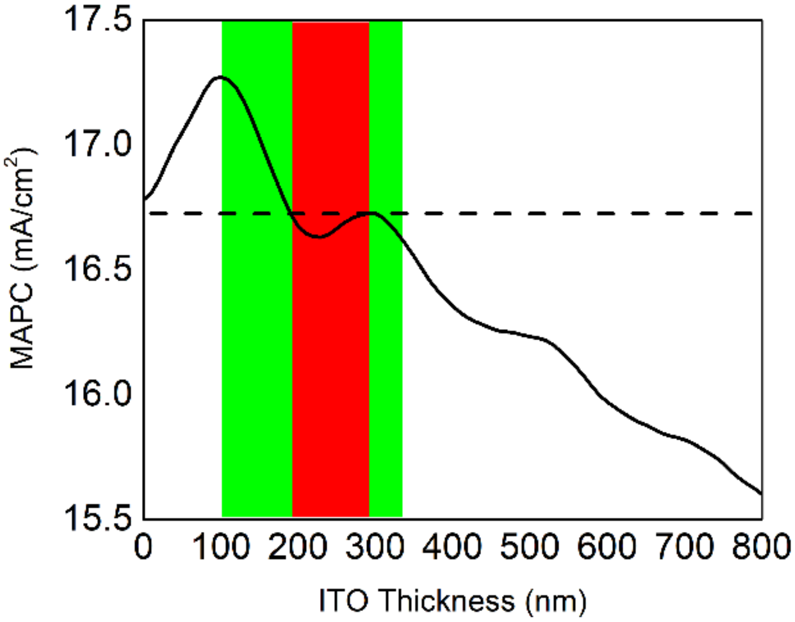

Figure 41 MAPC as a function of ITO thickness for a 90 nm-thick active layer. Recommended (green) and non-recommended regions (red) are highlighted

MAPC as a function of the ITO layer thickness for the 240 nm-thick PTB7:PCBM and 20 nm-thick PEDOT:PSS layers are demonstrated in Figure 42. Similar to Figure 41, favorable and unfavorable ITO thicknesses are shaded with green and red regions, respectively. ITO thicknesses up to 50 nm are recommended for superior optical transparency and anti-reflective behavior. Besides, ITO thicknesses larger than 130 nm can be selected to provide better electrical transport without having a considerable transparency penalty.

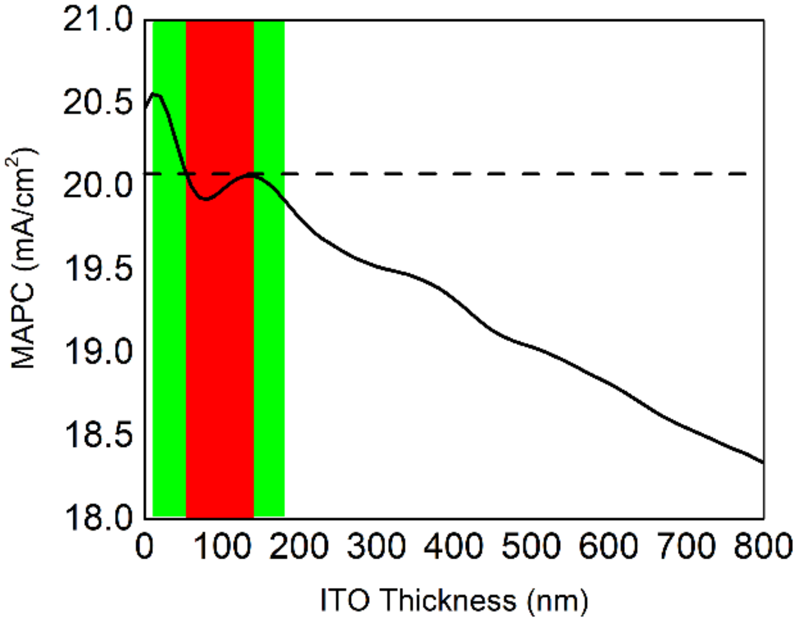

Figure 42 MAPC as a function of ITO thickness for a 240 nm-thick active layer. Recommended (green) and non-recommended regions (red) are highlighted

The absorption spectra of the optimized structures are shown in Figure 43. The effect of the ARC layer is also demonstrated. A 90 nm-thick MgF_2 is used as the ARC layer. The structure with 240 nm-thick PTB7:PCBM demonstrates a superior absorption throughout the spectrum of interest. MAPC is computed as 17.3 mA/cm^2 for the 90 nm-thick PTB7:PCBM and the ARC utilization boosts it to 17.8 mA/cm^2. For the 240 nm-thick PTB7:PCBM, MAPCs are found as 20.1 mA/cm^2 and as 20.7 mA/cm^2 with ARC.

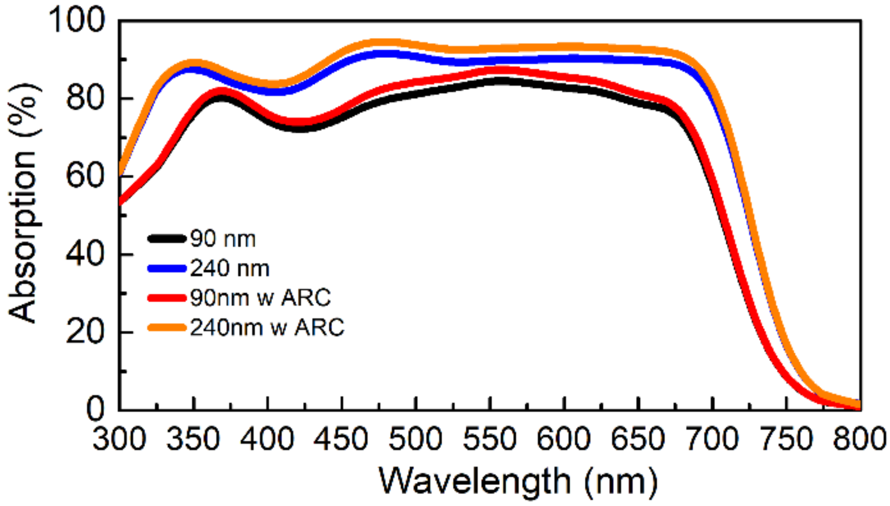

Figure 43 Absorption spectra of optimized structures for active layers 90 and 240 nm with and without the ARC layer. ITO and PEDOT:PSS are used as 130 and 20 nm.

Optimized structures with various thickness combinations of ITO and PTB7:PCBM are compared with reference structures. The thicknesses of the reference (A), optimized with thin ITO (B), and thick ITO (C) structures are presented in Figure 44. Corresponding MAPC and optical losses are presented in Figure 45. The reference structures are taken from the simulation study of Singh et al, which have the PTB7:PCBM layer thicknesses of 135 and 300 nm, and ITO and PEDOT:PSS layers are used as 180 and 45 nm, respectively.[75] MAPC increases by 2.25 mA/cm^2 for the 90 nm-thick PTB7:PCBM with a 100 nm-thick ITO and it is 1.71 mA/cm^2 with 300 nm-thick ITO compared to the thin reference structure (135 nm). When an ARC layer atop the glass superstrate is utilized, MAPC increases by 2.77 and 2.17 mA/cm^2 with 100 and 300 nm ITO layers, respectively. Compared to the thick reference structure (300 nm), MAPC improvements in the optimized structures are 1.69 and 1.47 mA/cm^2 for 40 and 130 nm thick ITO layers, respectively. When the ARC is employed, MAPC improvements are computed as 2.32 and 2.09 mA/cm^2 for 40 and 130 nm thick ITO layers, respectively.

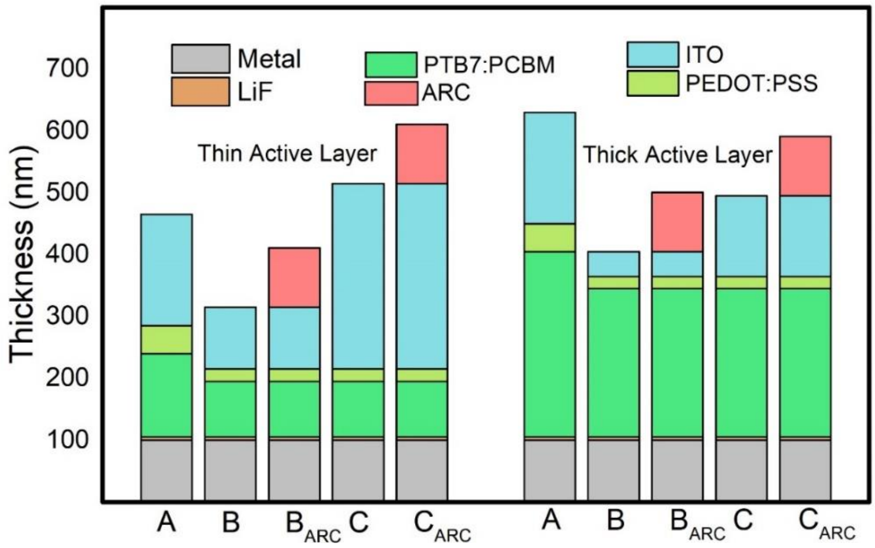

Figure 44 Thickness values of the reference (A), optimized using optically best ITO (B) and optimized using optically favorable ITO with low sheet resistance structures for the thin and thick active layer cases along with ARC coated.

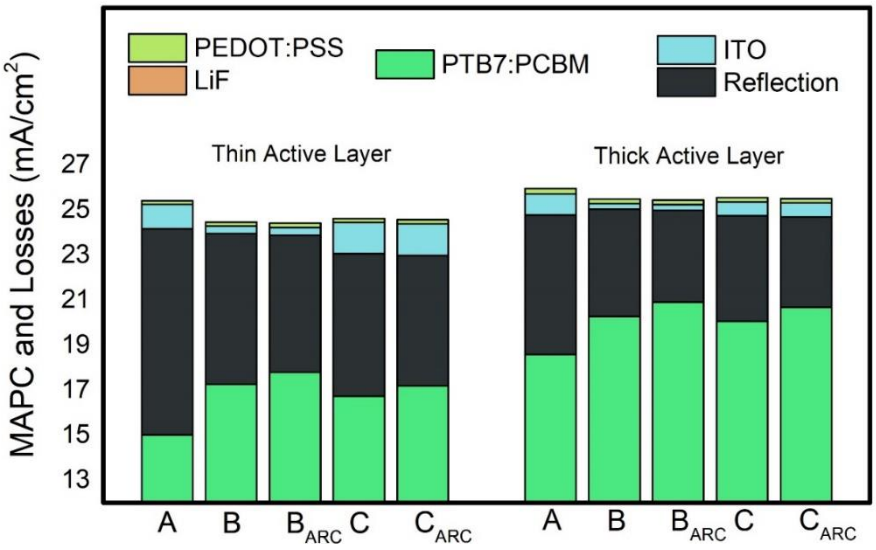

Figure 45 MAPCs and losses of the reference (A), optimized with the optically best ITO (B) and optimized with optically favorable and low sheet resistance layer for the thin and thick active layer cases and along with the ARC coated structures.

3.3. **Anti-Reflective Trends of Window Layers in CdTe Solar Cells**

CdTe is among the most suitable solar materials for the utilization of the provided light management approach. Thickness selection is constrained result of fabrication limitations, hence they are typically utilized with a thickness range of 0.5-3.0 μm.[76] Large absorption coefficient of CdTe in conjunction with the utilized thicknesses yield to single-pass dominant absorptions. Therefore, the anti-reflective behavior of the window layers is of great importance. Figure 46 presents MAPC as a function of the refractive index and thickness of the FTL. CdTe is used as semi-infinite in Figure 46a and it has a 3 μm thickness in Figure 46b. ITO is used as 70 nm for both CdTe thicknesses. For the 3μm-thick CdTe, 5 nm-thick MoO_x is employed as RTL, and 150 nm-thick Ag is utilized as the metal layer. MAPC trends are not changing with the CdTe thickness as expected while the MAPC decreases only 2 percent in cells with 3 μm in thickness.

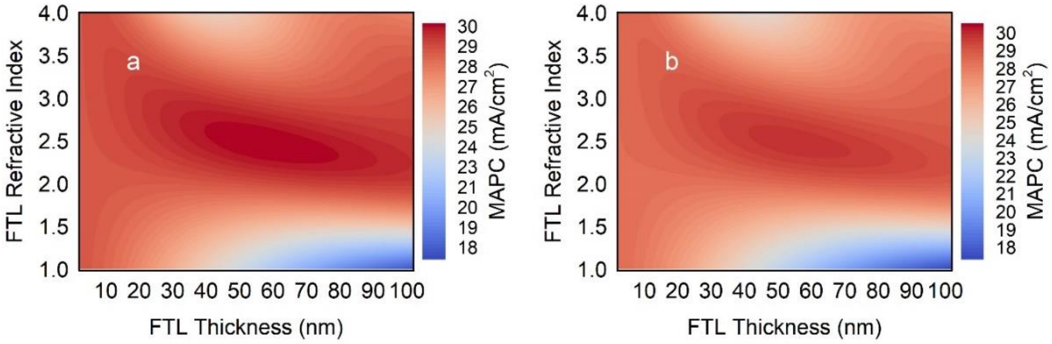

Figure 46 MAPC as a function of refractive index and thickness of FTL for (a) semi-infinite, and (b) 3 μm-thick CdTe layers. ITO is used as 70 nm, 5 nm-thick MoO_x is used as RTL and Ag thickness is 150 nm.

MAPC trends can be explained with three distinct regions similar to the perovskite and organics solar cells, as shown in Figure 11 and Figure 36, respectively. High MAPC zones for refractive index insensitive thin FTL region are fall into 0-20 nm region. Optimum refractive index window is found as 2-2.9 which is a higher index range compared to the perovskite solar cell results and can be attributed to the higher refractive index of CdTe (Figure 116, see Appendix B). A more detailed analysis of CdTe based solar cells is provided in Chapter 5.

3.4. **Investigation of the Optoelectronic Effects of TCO Layers**

In the previous section, a generalized guideline for the optimization of individual layers in perovskite solar cells is presented (see **Chapter 3.1.**). ITO thickness is chosen within practical limits to fulfill the criteria for low sheet resistance. It is presented that ITO thickness presents solely parasitic behavior for thickness larger than 50-60 nm range. Yet, there is still room for improvement for ITO thickness optimization taking both optical and electrical constraints into account.

In this subchapter, the optimum thickness of the ITO layer is discussed in terms of optical absorption and series resistance. The optoelectronic effects of the TCO layer are investigated for an exemplary perovskite solar cell structure formed from glass/ITO/NiO_x/perovskite/PCBM/Ag layers. Along with ITO, the effect of the different TCO materials are also discussed.

It should also be noted that the typically electric transport performance of the transport layers, PCBM and NiO_x, improves with decreasing layer thickness. Thus, NiO_x and PCBM layers are selected with thicknesses of 5 and 30 nm respectively and the perovskite layer is fixed at 465 nm which is the optimum value for the 400-500 nm thickness range. The Ag layer is used as 100 nm. Selecting a thin NiO_x layer helps to remove the effect of the interdependency between NiO_x and ITO layers and keeps the focus of the investigation exclusively on the ITO layer thickness. It is important to recall that we showed in Figure 11 that there is a negligible optical difference in the absorption spectra of perovskite with very thin front transport layers for different materials.

MAPC as a function of ITO thickness is demonstrated in Figure 47 for the described structure. The highest MAPC can be achieved with an ITO thickness around 50 nm – corresponds to the QWOT for the 400-500 nm wavelength range – as discussed for perovskite solar cells (see **Chapter 3.1.**). The obtained optimum thickness range is based on the integrated effect of refractive index spectra of the materials, parasitic absorption within the ITO layer, and AM1.5G flux. The refractive index spectrum of ITO has a gradual declining trend towards the longer wavelengths in the interested spectrum (Figure 116, see Appendix B). Thus, the refractive index contrast between glass and ITO layer reduces at longer wavelengths, meaning that the AR performance of ITO is more pronounced at shorter wavelengths.

MAPC reduces with increasing the ITO thickness due to parasitic absorption which hinders the effect of interferences. The improvements in MAPC exploiting interferences are more dominant in the 0-50 nm ITO thickness region, while the parasitic absorption in the ITO layer is weaker. In the ITO thickness region of 50-100 nm, ITO does not behave as an AR layer result of having HWOT while parasitic absorption is pronounced more. Hence, low MAPCs are computed in the mentioned region. The parasitic absorption losses are smeared out when ITO thickness approaching 150 nm since it is a consecutive QWOT value. MAPC benefits from interference-driven AR behavior which cancels loss caused by the parasitic absorption in 150-250 nm range, thus a flat region is computed in this thickness range. Beyond this value, the parasitic absorption dominates, and oscillations in MAPC due to interferences are overshadowed.

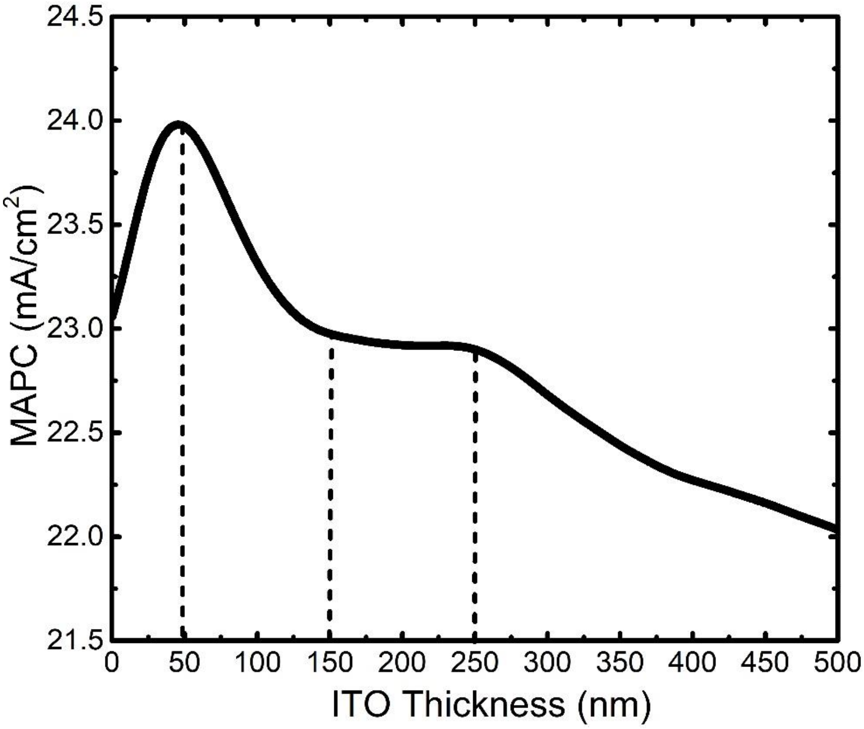

Figure 47 MAPC for various ITO thicknesses. The dashed lines indicated ITO thicknesses of 50, 150, and 250 nm, used in electrical and optical optimizations.

The ITO layer can act as a SLARC in perovskite solar cells regarding its favorable refractive index profile and utilization of a thin FTL which is practically invisible to incident light. In this sense, the optimum ITO thickness values can be described with odd multiples of QW optical thicknesses for the wavelength with the highest photon flux. ITO thicknesses corresponding to these AR behaviors for the interested spectrum are presented in Figure 48a. It demonstrates corresponding QW and HW optical thicknesses as a function of the refractive index of ITO and the wavelength of the incident light. The intersections in the vertical lines correspond to the consecutive interferences for the same wavelength, while the intersections at the horizontal line present intermittent QW and HW behaviors at different wavelengths at that thickness. For instance, the horizontal dotted line at 250 nm of ITO thickness intersects three QW lines at wavelengths of 310, 400, and 600 nm which results in relatively lower reflections, and three HW lines at wavelengths of 359, 480 and 800 nm that present relatively higher reflections for these wavelengths. Likewise, the vertical dashed line at 400 nm wavelength intersects four different ITO thicknesses, 50,150, 250, and 350 nm, corresponding to AR behavior.

A 50 nm-thick ITO layer demonstrates a superior and broadband AR behavior for a wavelength range of 300 to 525 nm. This is well described by the black line AR line in Figure 48a which corresponds to the first interference order. The low steepness observed for the first interference line enables AR behavior in a broad spectrum. The reflection spectrum of the optimized solar cell stack with selected ITO thicknesses are presented in Figure 48b. The broadband AR behavior of the 50 nm-thick ITO layer is demonstrated. The ITO layer with 250 nm thickness presents the AR behavior for 320, 400, and 600 nm wavelengths as predicted in Figure 48a. Similarly, The ITO with 150 nm thickness, demonstrates AR behavior for 400 nm but has a higher reflection in 600 nm wavelength. The constructive interference of the reflection by the 150 nm-thick ITO layer causes relatively a higher reflection at 600 nm wavelength since it is adjacent to the half-wave optical thickness for the same wavelength. Computation results, presented in Figure 48b-d, are in good agreement with single-layer AR criteria as demonstrated in Figure 48a. The reflection spectra of models with three ITO thicknesses are shown in Figure 48b-d. The interference within the ITO layer gets pronounced as its thickness increases which results in an oscillatory absorption profile in Figure 48c and, especially, in Figure 48d. This undulation is the result of having more frequent interference order, thus more destructive and constructive interferences can be supported by thicker layers. A superior AR performance with 50 nm-thick ITO is obtained through all spectrum except for a very limited wavelength range, 690-705 nm. The AR behavior of 250 nm-thick ITO at 600 nm wavelength is prominent. Therefore, when the absorption is considered along with AM 1.5G photon flux, both cases demonstrate very close MAPC values even though their ITO thicknesses are significantly different.

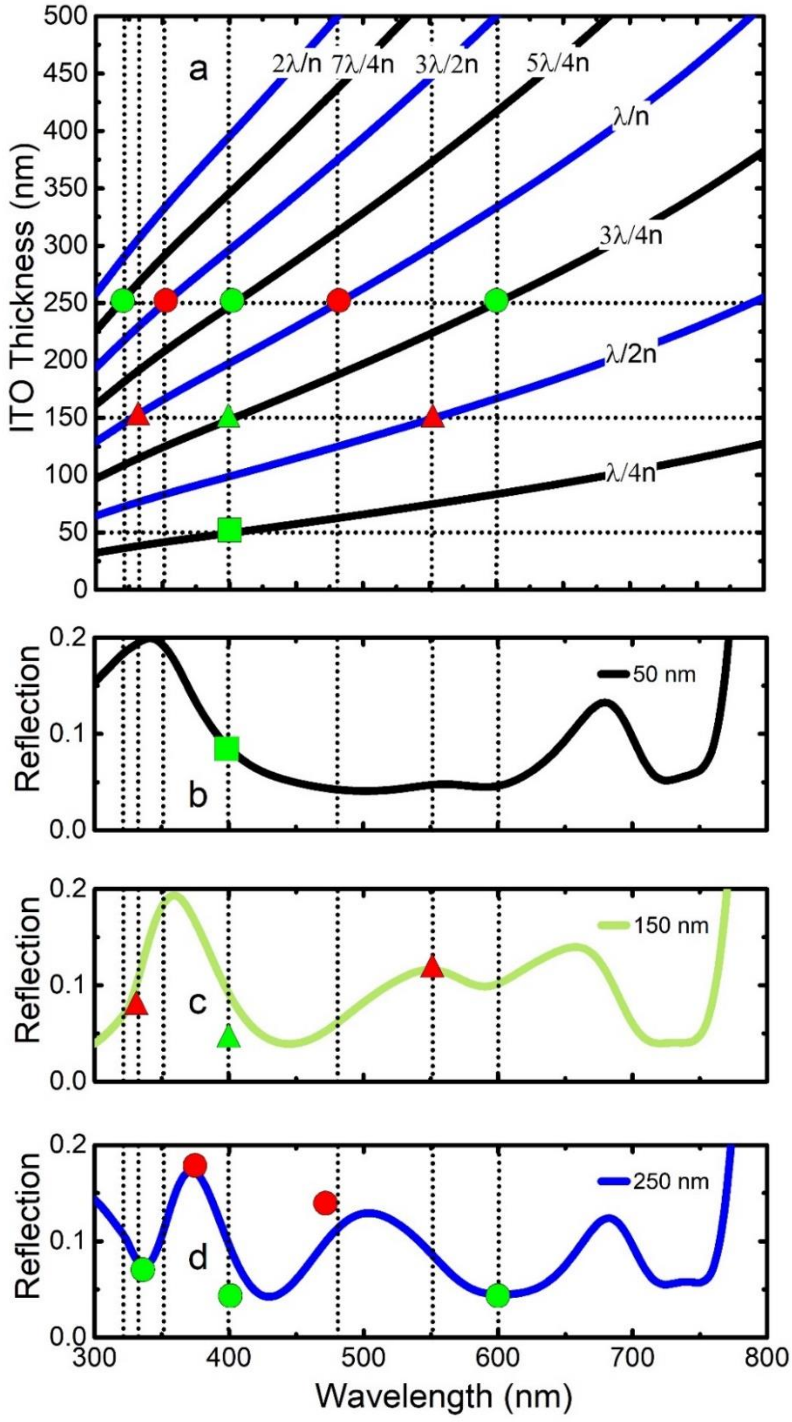

Figure 48 ITO thickness corresponding to QW and HW anti-reflection lines regarding the refractive index spectrum as a function of wavelength (a). Reflection spectra of 50 nm (b), 150 nm (c), and 250 nm thick ITO layer (d). Anti-reflective (green) and reflective (red) trends in line with (a) are presented for 50 nm (square), 150 nm (triangle), and 250 nm(circle).

Moreover, the sheet resistance of the ITO layer depends on its thickness. The optical transparency of the ITO layer decreases gradually with increasing thickness of the ITO due to parasitic absorption, while the electrical transport properties of this layer improve with increasing thickness. Hence, the trade-off between electrical and optical properties is investigated by combined optical-electrical simulations. On account of the aforementioned requirements, three sets of ITO thicknesses are chosen (highlighted on Figure 47) as 50 nm, 150 nm, and 250 nm with the following characteristics to be investigated in the full stack of the solar cell:

- Very thin ITO (50 nm, and $R_{sheet} = 40.5\ \Omega/\square$)
- Common ITO thickness (150 nm, and $R_{sheet} = 13.5\ \Omega/\square$)
- Thicker ITO (250 nm, and $R_{sheet} = 8.1\ \Omega/\square$)

where R_{sheet} is the resistivity (ρ) per thickness of the ITO layer. The resistivity of the ITO layer is adopted from the literature.[77] Note that various combinations of the abovementioned thicknesses of 150 nm and 250 nm are commonly used in the literature.[78–82]

Reflection and parasitic absorption losses, in terms of the photocurrent, and absorption in perovskite, calculated in terms of MAPC, for models with selected ITO thicknesses are given in Table 5. The highest MAPC can be achieved with a 50 nm-thick ITO which yields the lowest reflection and parasitic absorption. The ability of the 250 nm-thick ITO layer to sustain multiple QWOTs leads to a lower reflection compared to the structure with a 150 nm-thick ITO despite having a parasitic absorption penalty. Hence, 150 nm and 250 nm-thick structures have very comparable MAPC values while their sheet resistances differ significantly.

Table 5 Reflection, parasitic losses in ITO, NiO_x, PCBM, and Ag layers and absorption in perovskite layer (in units of mA/cm^2) with three ITO thicknesses.

	ITO Thickness (nm)		
	50	150	250
		mA/cm2	
Reflection	2.83	3.37	3.08
Parasitic absorption in ITO	0.24	0.70	1.07
Parasitic absorption in NiOx	0.03	0.03	0.03
Parasitic absorption in PCBM	0.06	0.06	0.06
Parasitic absorption in Ag	0.14	0.13	0.13
MAPC	23.97	22.98	22.90

3.4.1. **Electrical Simulations and Sheet Resistance Analysis**

Lab- and industry-scale cell structures are investigated to determine the optimum ITO thickness. The lab-scale cell is typically a single cell, while industry-scale cells are an array of cells connected in series. The one-diode model is used to calculate solar cell efficiencies with 50, 150, and 250 nm-thick ITO layers in terms of MAPC and the effective series resistance (R_S) are investigated using[83]

$$J = J_o * e^{\left(\frac{q(V-JR_S)}{nk_BT}-1\right)} + \frac{V-JR_S}{R_{sh}} - MAPC \qquad \text{Equation 58}$$

where J is the current density, $MAPC$ is the photogenerated current flux, V is the voltage, J_0 is the dark current density, n is the ideality factor, and R_{sh} is the shunt resistance. R_s is the effective series resistance of the device that scales with the cell geometry.[84] For simplicity, the effect of R_{sh} is omitted by setting its value to infinity in this analysis. For the lab-scale cells, the lateral charge spreading in ITO considerably reduces the effective sheet resistance, therefore the effective series resistance. An example illustration of the lab-scale solar cell is given in Figure 49. The lateral spreading of the generated electrons is also demonstrated. The effective series resistances of the lab-scale cells are calculated elsewhere and adopted in this analysis.[85]

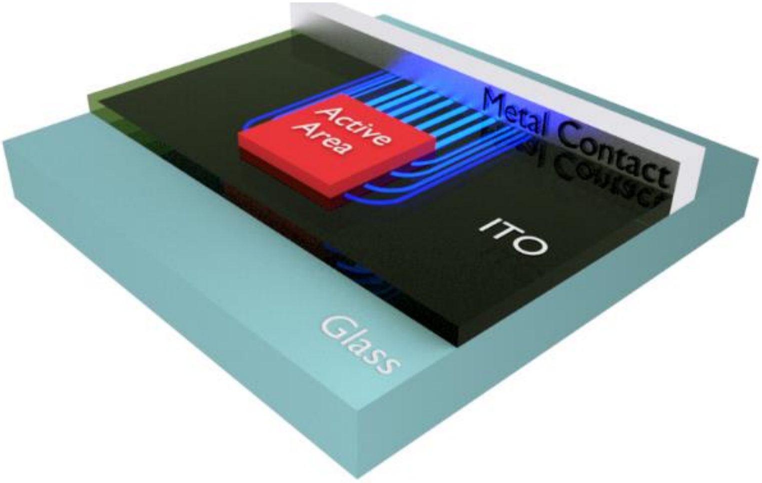

Figure 49 Illustration of the photogenerated charge collection in a lab-type perovskite solar cell with the current spreading phenomenon.

The J-V curves are computed for ITO thicknesses of 50, 150, and 250 nm, and cell areas of 1x1, 4x4, 7x7, and 10x10 mm^2. Resistivity, ρ, is taken as 2.025×10^{-4} Ω.cm[77] while J_0 and n are assumed to be 2.8×10^{-11} mA/cm^2 and 1.5, respectively.[86] The efficiency of solar cells with various ITO thicknesses and cell areas is shown in Figure 50. The 50 nm-thick ITO layer leads a superior optoelectronic performance over the thicker ITO layers for cell areas smaller than 5x5 mm^2. On increasing the cell area from 1x1 to 10x10 mm^2, the efficiency of the structure with 50 nm-thick ITO, drops about 3.5 % from its initial value, but the loss is mere, 1% with the ones with 150 nm and 250 nm thicknesses. Even though the cell with a 250 nm-thick ITO layer has considerable higher parasitic absorption, its efficiency outperforms the one with a 150 nm-thick ITO layer when the solar cell area exceeds 5x5 mm^2.

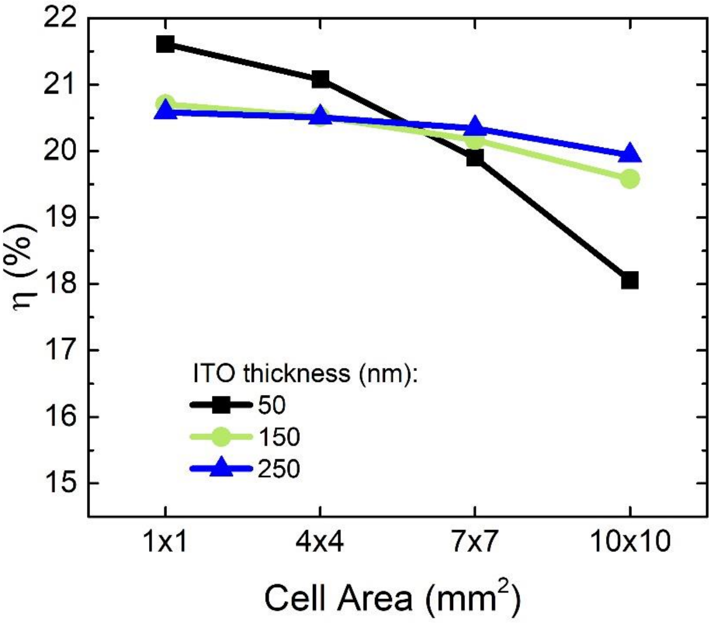

Figure 50 Variation of lab-type solar cell efficiency as a function of the cell length with 50, 150, and 250 nm thick ITO layers. J_o, n, ρ, R_{sh} *are assumed to have values of* 2.8×10^{-11} *mA/cm*^{2}, *1.5,* 2.025×10^{-4} *Ω.cm, and infinity, respectively.*

3.4.1.1. Industry-Scale Perovskite Solar Cells

The scheme of an example industry-scale solar cell design is presented in Figure 51. Cells can have any width-length ratio, while the effective series resistance is solely defined by the metal finger opening as[84]

$$R_s \cong \frac{\rho}{t}\frac{L^2}{3} \qquad \text{Equation 59}$$

where ρ represents the resistivity and t is the thickness of ITO, and L is the metal finger opening in the solar cell, respectively. Since there is no lateral spreading in industry-scale solar cells, typically their effective series resistances are larger. The metal fingers cause shadowing at the active area which in turn decreases the overall performance. In this study, the metal finger width is assumed as 50 μm, which corresponds to 5%, 1.25%, 0.7%, and 0.5% absolute performance drops for 1, 4, 7, and 10 mm finger openings result of the shadowing, respectively. The efficiency results with and without including these shadowing losses are also provided to give a theoretical limit.

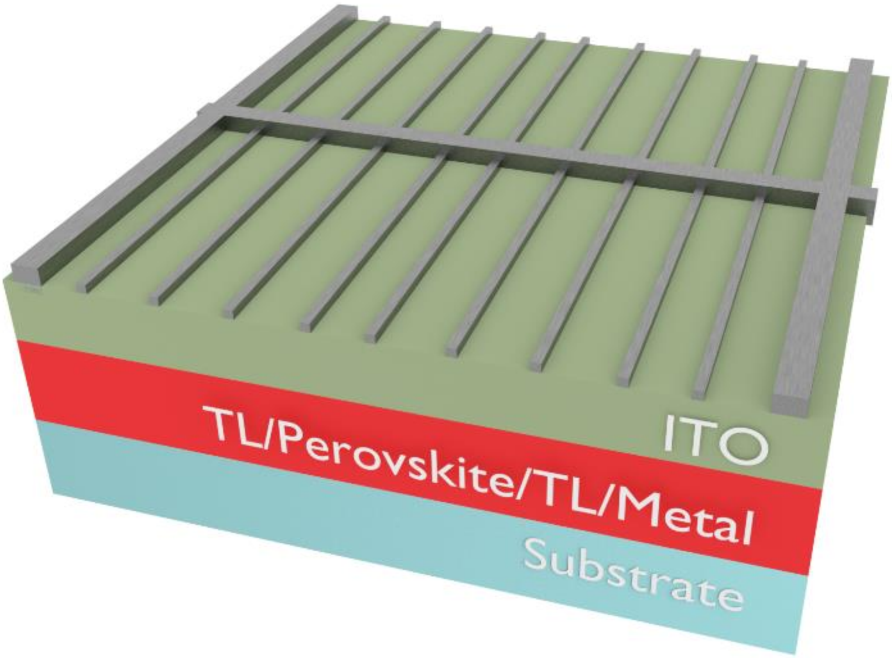

Figure 51 Scheme of the industrial type module design with metal grid network atop the ITO layer.

The efficiency of the designed perovskite solar cell as a function of the metal finger opening for the industry-scale design is shown in Figure 52. ITO with a 50 nm thickness is a better alternative for opening values up to 4 mm. Below this value of metal finger openings, cells with 150 nm and 250 nm thick ITO layers perform identical, however, the 250 nm-thick ITO becomes a more preferable with further increasing the finger opening value.

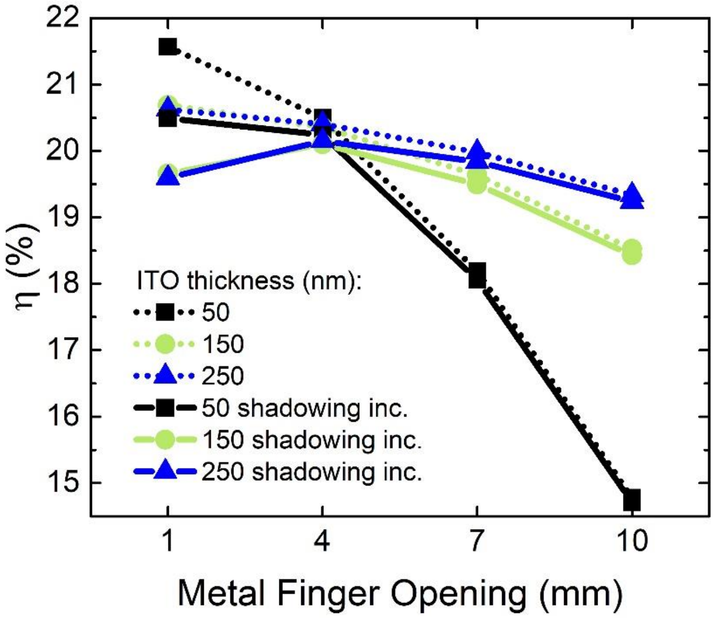

Figure 52 Efficiency of the industry-scale solar cell as a function of the metal finger opening with 50, 150, and 250 nm thick ITO layers. J_o, n, ρ, R_{sh} are assumed to have values of 2.8×10^{-11} mA/cm^2, 1.5, 2.025×10^{-4} Ω.cm, and infinity, respectively. Results are presented with (solid) and without (dot) the effect of metal finger shadowing.

3.5. **Conclusions**

An optical design guideline for the thickness optimization of perovskite solar cells by systematically investigating the contributions of layers to the antireflection and light-trapping performance is provided. An optimum n_{FTL} range (i.e. $1.8 < n_{FTL} < 2.8$) providing superior ARC efficiency is identified. Additionally, the interferences appearing at long wavelengths can be engineered to trap the light within the perovskite layer are demonstrated by controlling thicknesses of FTL, perovskite, and RTL or those of perovskite and RTL if n_{FTL} is larger or smaller than 2.1. In a guideline framework, the set of equations to determine the optimum thicknesses of FTL, perovskite, and RTL of a perovskite solar cell to achieve the maxima in MAPC within an error less than 1% for the given n_{FTL} and n_{RTL} and approximate thickness of perovskite are provided. Additionally, it is demonstrated that the trends in MAPC with perovskite layer thicknesses are independent of the commonly used TCO materials.

The perovskite guideline, experimentally-validated for MAPI, is generalized, to commonly-used perovskites such as FAPI, MAPBr, and $Cs_{0.17}FA_{0.83}Pb(Br_{0.17}I_{0.83})_3$. The proposed framework is applicable to other strong absorbers (e.g. direct bandgap materials) based devices such as Cadmium Telluride (CdTe), Copper Indium Gallium Sulfide (CIGS), and Copper Zinc Tin Sulfide (CZTS).

The thickness of ITO plays a key role in constructive interference and the resultant absorption oscillatory patterns. The optical optimization in this study was shown particularly useful to bypass both optical and electrical constraints in the case of large-area/scale perovskite solar cells. The results were shown viable regardless of the perovskite processing conditions and the employed TCO.

Manufacturing PSCs with longer than 1 cm cell lengths can provide ease of fabrication. In particular, large solar cell modules would benefit from less processing stages such as masking and TCO scribing steps. Besides, larger active area solar cells can be realized without power loss due to the cell length. Therefore, an ITO layer with 250 nm thickness can be a more industrially favored thickness than 50 and 150 nm.

When an FTL material with distinct refractive index profile such PEDOT:PSS is used instead of NiO_x, MAPC differs as much as 0.15 mA/cm^2. Therefore, optoelectronic discussions are presented with an FTL material independent perspective.

For the organic solar cell investigations, it is shown that since the refractive index profile is ordered as high-low-high for a structure of ITO-PEDOT:PSS-PTB7:PCBM, the PEDOT:PSS layer should be as thin as possible for thick PTB7:PCBM layers. An alternative to that, replacing PEDOT:PSS with a higher refractive index FTL for thicker PTB7:PCBM layers can be considered. Due to electrical properties, i.e. recombination, carrier lifetime, the fabricated thickness of PTB7:PCBM is limited. As a result, interference becomes important for thicknesses smaller than 700 nm. For instance, 37% of incident light reaches the rear metal cathode for a 120 nm thick PTB7:PCBM, while this number is 1% for a 625 nm-thick PTB7:PCBM. To sum, the interference is important for a PTB7:PCBM layer thinner than 650 nm, there is room for optimization of the refractive index order, PTB7:PCBM, HTL and TCO thickness optimization can be done.

CHAPTER 4

AEROGEL REAR REFLECTORS

Silicon solar technology has the largest share among the industrial solar cells. After the first introduction in 1954,[2] they still attract researchers regarding the fact that they have a mature technology, robust stabilities, the broad availability of the fabrication infrastructure, and outstanding efficiencies.[3] Currently, one of the solutions to reduce the fabrication cost of silicon solar cells is reducing the amount of silicon by using thinner wafers. However, reducing the silicon wafer thickness yields two major challenges: (i) optical absorption reduces, and (ii) parasitic absorption in the metal layer increases. The former one typically addressed with surface texturing at both sides of the cell structures. However, rear side surface texturing can also yield more pronounced metal parasitic absorptions. Considering this, both challenges should be addressed concurrently. Utilizing a rear reflector layer between textured silicon surface and the metal layer can simultaneously improve parasitic absorption while enabling the utilization of surface texturing. To optimize the rear reflector layer, the internal reflections at the interfaces should be quantized, especially, more pronounced metal absorptions with decreasing the wafer thickness.

The screen-printed Al metal layer is widely utilized in the PV industry with its ease-of fabrication and low-cost. Considering its large surface roughness and the large extinction coefficient of Al, its parasitic absorption, especially for wavelengths longer than 900 nm is significantly pronounced. This calls for the requirement of a highly reflective rear reflector layer.

Combinations of SiN_x and SiO_2 are typically utilized as the rear reflector layer. Both materials are widely used in silicon solar cell technologies regarding being a silicon compound and their multi-functions in the solar cells such as passivation. SiO_2 with its ~1.4 refractive index in the near IR part of the spectrum provides an index contrast at the silicon-metal interface and increases the overall reflection. However, the index contrast still is not enough to effectively confine light within the silicon substrate. Alternative solutions such as distributed Bragg reflectors are utilized as rear reflector layers to increase overall reflection.[87] However, regarding their complex fabrication processes, costs and additional losses introduced at the interfaces limit their usage as a rear reflector. Silicon nanoparticles are one of the promising approaches for minimizing the parasitic absorption regarding their low refractive index result of high porosity. Boccard *et al.* showed that further decreasing the refractive index can improve overall reflection in their theoretical study.[88] However, experimental results presented reduced reflections by further increasing the porosity of the rear reflector layer contradicting the theoretical study which is attributed to the increased metal surface roughness with the interdiffusion of evaporated metal. Yet, available simulation algorithms are not capable of modeling this pronounced metal absorption.

Absorption takes place in various locations in a solar cell such as the absorber, and metal, transport, transparent conductive electrode layers parasitic absorptions. Absorption in the absorber layer can be band to band as well as via free carriers. Regardless of the mechanism, the absorption in the active regions mainly depends on their absorption coefficient and the optical path of the incident light. The optical path is related to the angle of incidence (AOI), the refractive index of the medium, the thickness of the layer, and light trapping features. The absorption coefficient of silicon reduces gradually with wavelength. In other words, absorption length increases with wavelength. Thus, the light travels further within the substrate before being fully attenuated at longer wavelengths. Depending on the thickness of the silicon absorber, absorption can be classified into two distinct regimes: the strong absorption and interference. The strong absorption regime is described for the wavelength range where absorber has a thickness larger than $5/\alpha$.[89] In this regime, more than 99.33% of the incident photons (possessing wavelengths of 300-940 nm for a thickness of 200 μm) are absorbed before reaching the rear electrode. Within this regime, the main optical loss mechanism is reflection. In the interference regime, the incident light makes multiple internal reflections that call for employing light-trapping schemes to maximize these internal reflections. Within the light trapping framework, there exist several improvement approaches such as rear scatterers, rear reflectors, and textured interfaces. Among them, the rear reflector can not only mitigate the metal parasitic absorption but also improve the light-trapping with increased reflections and yet passivate the silicon surface.

Photons with a wavelength of 1200 nm are used as an indication of parasitic loss at the rear metal since silicon band to band absorption is zero and free carrier absorption is minimum at this wavelength. It is presented that it is possible to obtain over 95% reflections at 1200 nm wavelength with silicon nanoporous materials when they are used as the rear reflector layers,[88] however, experimentally obtained reflections do not follow this suggestion which is attributed to the pronounced parasitic loss at the rear metal.

In this chapter, after quantizing the loss mechanisms in planar and double-side textured silicon layers, the usage of an optimal rear reflector is evaluated based on its refractive index and the adjacent metallization schemes. For this purpose, silica aerogel as a rear reflector is proposed. The effect of various metals (i.e. Al and Ag) and deposition techniques (i.e. screen printing and thermal evaporation) are investigated. The investigated structure consists of anti-reflective coating (ARC), c-Si, rear reflector (RR), and metal, as shown in Figure 53. SiN_x is among the most widely used ARCs and RR materials. In this chapter, the performance of SiN_x as RR is taken as a benchmark. Reflection at the 1200 nm wavelength is used as a performance monitor and it is denoted as the rear reflection in this chapter. The effects of metal layer roughness and aerogel surface planarization are discussed in detail. This approach confers way-outs to mitigate metal parasitic absorption, which leads to a band-to-band silicon IR absorption. A hybrid approach based on the combination of wave and ray optics is developed to compute electromagnetic interactions in the silicon solar cell stack used herein.

4.1. Results and Discussions

Structures with planar, front-side textured, and double-side textured silicon substrates investigated in this analysis are presented in Figure 53. Silicon pyramid textures are used to have a face angle of 54.7 degrees regarding <111> etch-stop. A 75 nm-thick anti-reflective coating (ARC), SiN_x, is assumed to be conformally deposited atop the front surface.

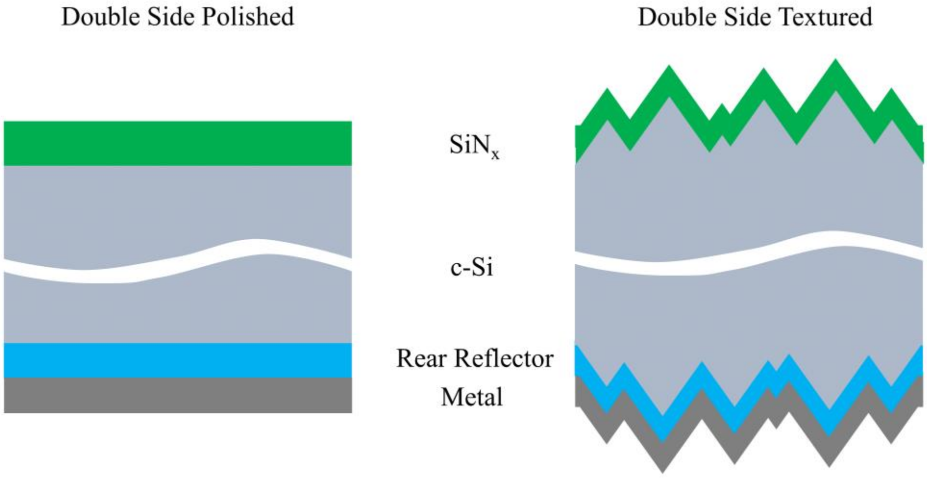

Figure 53 Illustrations of double-side polished and textured structures and used in this investigation.

The absorption coefficient of silicon (Figure 54a) has a gradually decreasing trend towards longer wavelengths which in turn increases the absorption length (attenuation length). Figure 54b shows the single-pass absorbance of 50, 120, 180, and 200 µm-thick silicon substrates. The threshold wavelengths where strong absorption changes to interference regime are computed as 800, 895, 931, and 940 nm for 50, 120, 180, and 200 µm silicon layers, respectively. The main loss mechanism for photons shorter than this threshold value is reflection since they cannot reach the rear interface. The 180 µm silicon layer is utilized in this study for the rest of this chapter due to common utilization in the silicon industry. Considering photons with wavelengths longer than 931 nm, the internal reflections gain importance. In particular, the metal interface is of great importance regarding the large extinction coefficient of metal (Figure 117, see Appendix B).

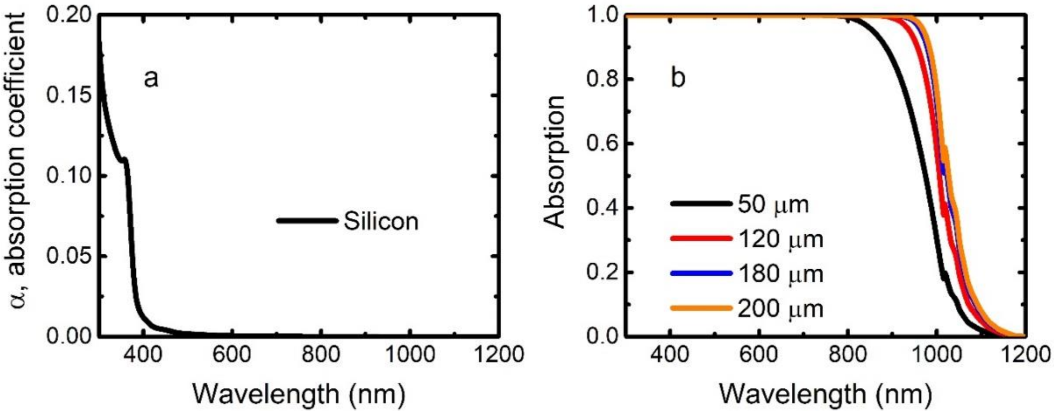

Figure 54 Absorption coefficient of silicon (a). Single-pass absorption spectra of 50, 120, 180, and 200 μm-thick silicon (b).

The integrated metal absorptions for various correlation lengths and RMS values are shown in Figure 55 to demonstrate the effect of the metal layer absorption. Surface morphologies are swept for; (i) RMS values of 25, 50, 100, and 200 nm which depicts vertical variations, (ii) correlation lengths of 25, 50, and 100 nm, which characterizes the horizontal variations on the metal surface. Simulation models are illustrated in Figure 56. The integrated metal absorption of a planar Ag surface is computed as 0.05. The medium of incidence is taken as silicon and it is assumed at a normal incidence. Since the majority of the photons with wavelengths shorter than 950 nm cannot reach the metal layer in a 180 μm-thick silicon layer (Figure 54b), absorption is calculated for a wavelength range of 950-1200 nm. It is noticeable that the lower the correlation length, the higher the metal absorption. This trend is more prominent for RMS values above 10 nm. When the metal surface has an RMS value of 10 nm, roughness is almost invisible to the incident light at the computed spectrum.

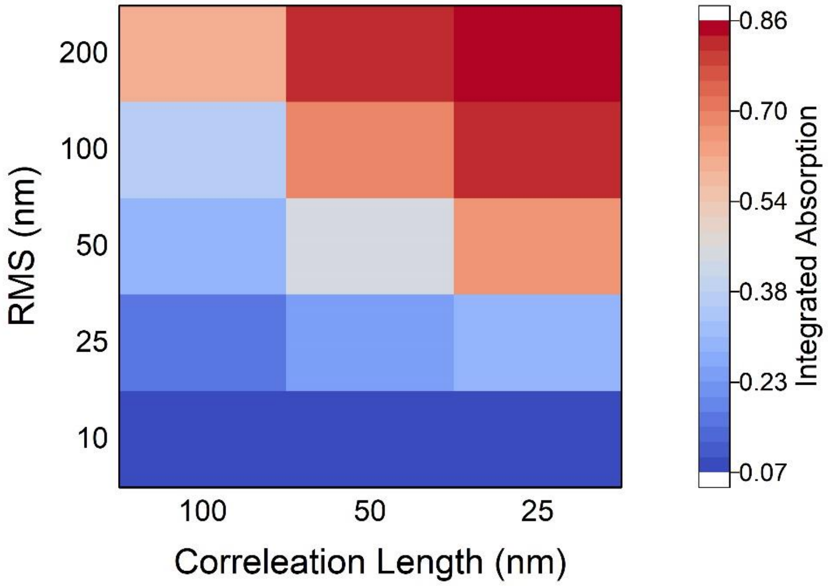

Figure 55 Normalized metal absorption spectra for various correlation length and RMS values of the metal surface roughness

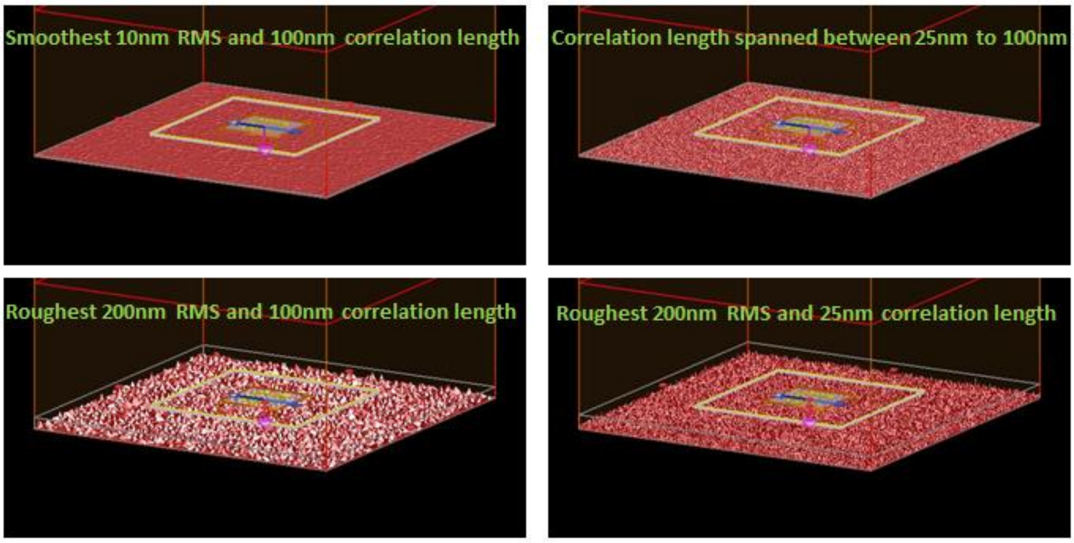

Figure 56 Illustration of metal surfaces with various roughness types.

Aerogel has a high porosity which decreases its effective refractive index. The low-index enables higher contrast at the silicon-RR interface, which in turn increases the reflection. The spectroscopic ellipsometry measurement and fitted data of the fabricated aerogel, SiO_2, and SiN_x layers on polished silicon substrates are presented in Figure 89-94 (Appendix A). The spectral dispersion of the indices is low, in particular, they are almost constant for wavelengths longer than 500 nm. Their measured extinction coefficients are negligibly small (Figure 107-111 Appendix B).

The effect of the porosity on the aerogel layer is investigated using 3D optical simulations. The aerogel structures used in the optical simulations are illustrated in Figure 57. Utilized porosity fractions are 98.40, 88.20, 67.20, 44.30, 30.00, and 23.10 %, which correspond to refractive indices of 1.01, 1.05, 1.14, 1.25, 1.32, and 1.35, respectively.

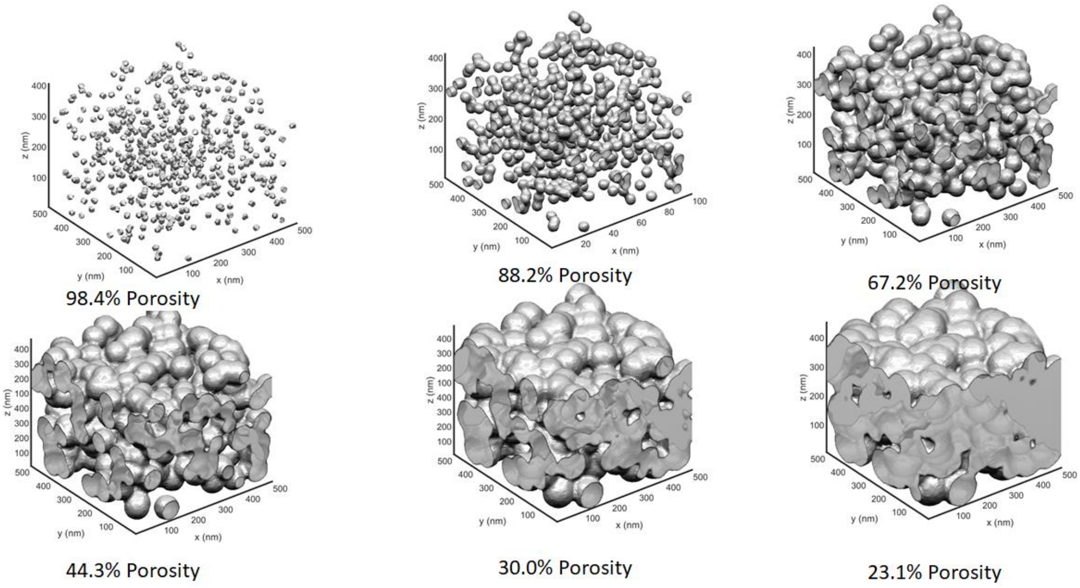
98.4% Porosity

88.2% Porosity

67.2% Porosity

44.3% Porosity

30.0% Porosity

23.1% Porosity

Figure 57 Illustration of aerogel layers with various porosities used in 3D optical computations.

The measured reflection spectra of aerogel layers with measured refractive indices of 1.10, 1.16, 1.17, and 1.20 are presented in Figure 58a. According to 3D optical simulations and the effective medium approach, the corresponding porosity fractions are 79.34, 73.07, 60.35, and 58.34% for measured refractive indices 1.10, 1.16, 1.17, and 1.20, respectively. Figure 58b shows the reflection spectra of SiO_2 nanoparticles with various porosities calculated with 3D optical simulations along with planar reflection spectra calculated with the TMM method. As the porosity fraction decreases, the interaction of the incident light with the scattering medium starts to converge to that of a thin-film regarding an increased effective refractive index. Figure 58c shows a comparison of the two approaches, 3D optical simulations (using many-body SiO_2 particles and porosity) and the Bruggeman EMA with the TMM method. It is evident that both approaches are in good agreement; therefore, EMA can be utilized for the sake of simplicity in the full device calculations when the rear interface is assumed as planar.

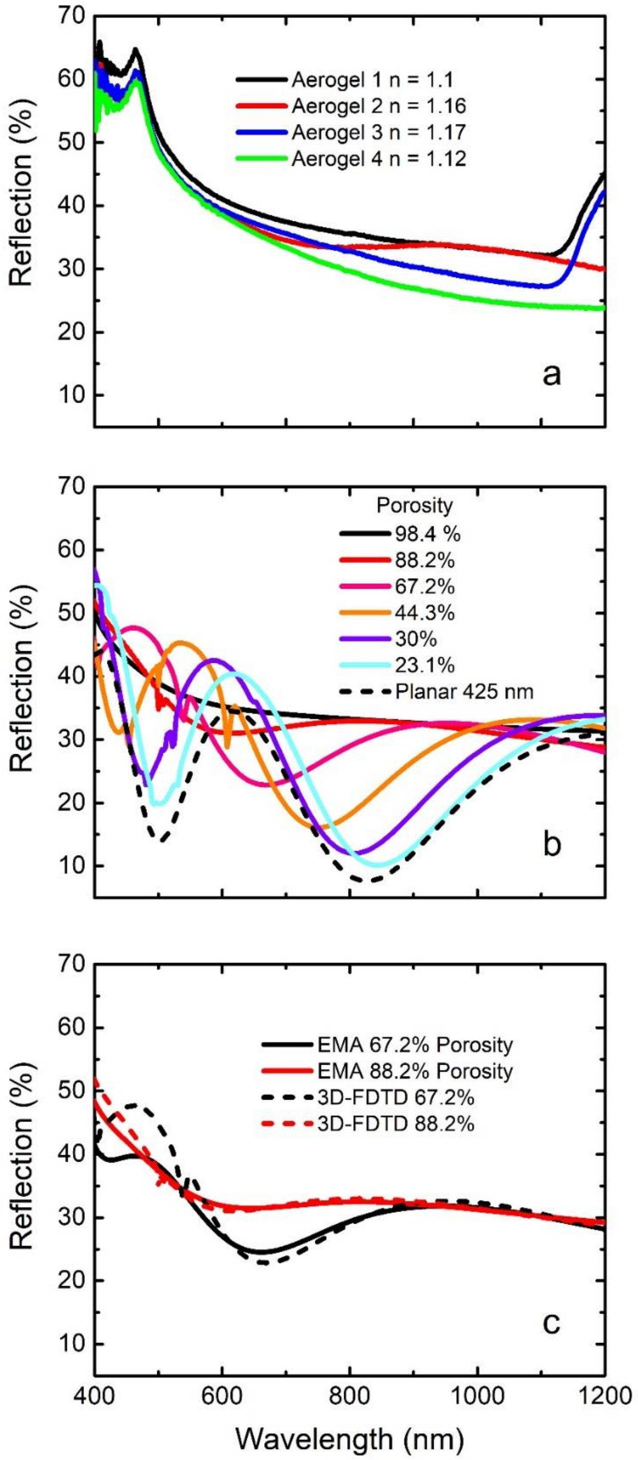

Figure 58 Measured reflection spectra of fabricated aerogel layers on a planar silicon substrate (a). Reflection spectra of aerogel layers for various porosities using 3D optical simulation (b). Comparison of selected porosity fractions using Bruggeman effective medium theory and 3D optical simulations.

Simulated reflection, silicon and metal absorption spectra of the double-side polished (DSP) silicon substrate with 120 nm SiN_x (red), and 250 nm aerogel RR layers (blue), along with no RR layer (black) are presented in Figure 59. Designs consist of SiN_x and aerogel as the RRs, and Al and Ag as the metal layers. A planar metal interface is assumed for the calculations. SiN_x ARC and the metal electrode are taken as 75 nm and 150 nm, respectively. Approximately a 95% rear reflection is obtained when there is no RR layer. The total metal parasitic absorption is around 5%. In the case of the SiN_x RR, the rear reflection is 98% and the metal absorption is 2%. Therefore, the SiN_x RR layer suppresses the metal absorption. The alteration of the silicon absorption spectrum is negligible with the SiN_x RR. Similar to the SiN_x RR, the variation in the absorption spectrum of the silicon layer is negligible for aerogel RR. The metal parasitic absorption is suppressed to as low as 0.6% and the rear reflection is 99%. This is attributed to the higher refractive index discrepancy in the case of aerogel. The obtained results are in good agreement with the literature.[88]

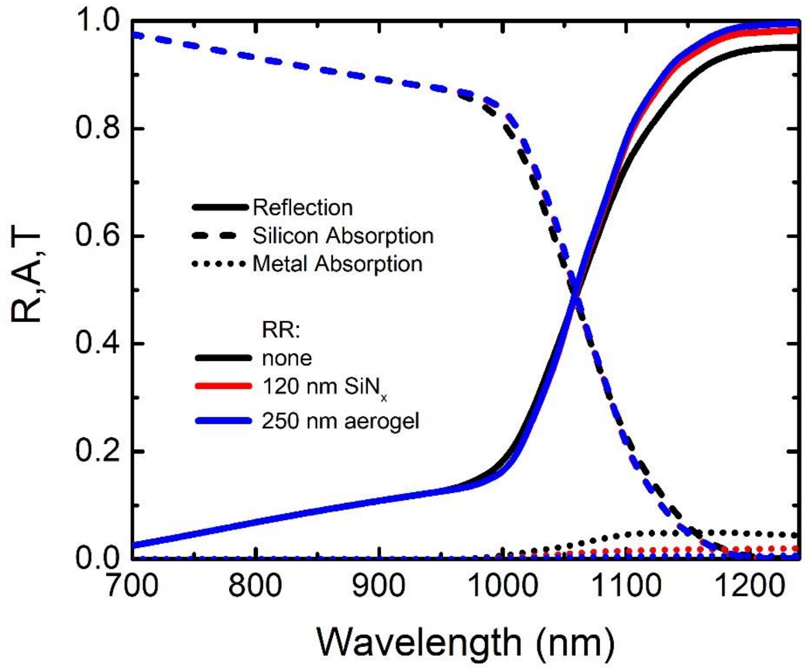

Figure 59 Reflection, and silicon and metal absorption spectra of DSP silicon substrate with various RR combinations (none, 120 nm SiN_x and 250 nm aerogel). Ag is used as the metal electrode.

The effect of the thickness and refractive index of the RR layer on the rear reflection at the normal incidence is presented in Figure 60. The reflectance increases with decreasing the refractive index as a result of the higher refractive index contrast. In addition to this, interferences can cancel out the reflection at the rear interface which in turn increases the parasitic absorption in the metal layer as can be seen in dark regions in Figure 60. The optimum thicknesses for an index of 2.5 can be documented as 100 nm which gradually increases to 250 nm for an index of 1.1. It should be noted that these thicknesses are calculated for the normal incidence and the DSP silicon substrates, hence they follow the optical thickness of the RR layer.

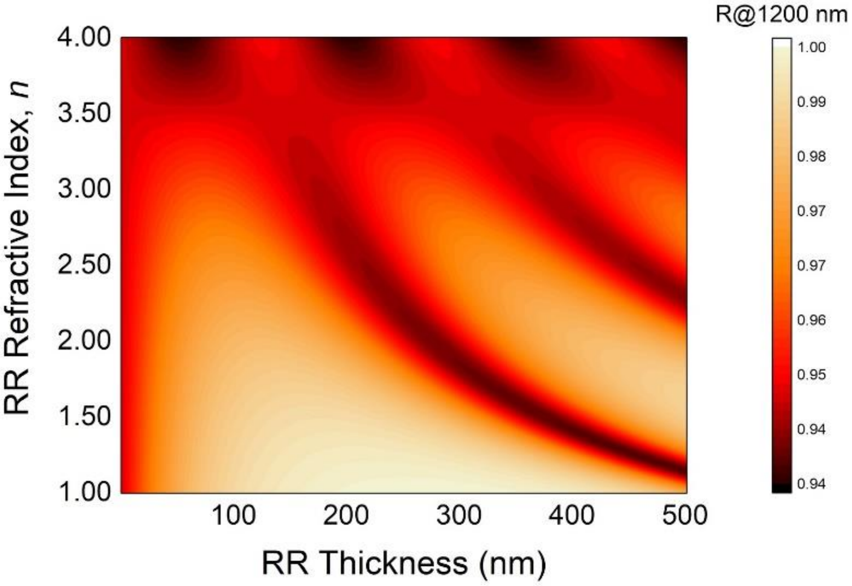

Figure 60 Internal reflectance at the rear interface at 1200 nm wavelength as a function of the RR refractive index and thickness.

A widespread way to reduce reflection losses and enhance the absorption is to use silicon substrates with double-side pyramid textures. To model the propagation of trapped photons within the silicon layer, a Phong scattering profile is assumed which can be expressed as:[90,91]

$$R(\Theta) = R_o(\cos\Theta)^{\alpha}$$ Equation 60

where R_0 is the specular reflection, Θ is the scattering angle defined as the angular deviation of the outgoing light from the specular reflection angle, and α is the Phong exponent. In the case of $\alpha=1$, the scattering profile can be described as a Lambertian one. Unlike the specular propagation, which is the case for planar structures, trapping the incident light significantly improves with the scattering model. This can be attributed to the oblique refraction angles that cause the total internal reflection (TIR). For the light to present a TIR, the incidence angle must be larger than or equal to the critical angle which can be defined as:

$$\Theta_c = \sin^{-1}\frac{n_{RR}}{n_{Si}}$$ Equation 61

where n_{RR} and n_{Si} are refractive indices of the RR and silicon layers, respectively. The TIR condition strongly depends on the refractive index of the RR layer. Decreasing the refractive index of the RR layer enhances the absorption of the silicon layer with two mechanisms; (i) the reflectance increases with higher refractive index contrast which is the case for all substrate types irrespective of the surface morphology, (ii) larger refractive index contrast at the rear interface yields a larger portion of the incident light to be reflected totally regarding the surface features and the TIR. To demonstrate this effect, the percentage of the TIR at 1200 nm wavelength and the normal incidence as a function of the refractive index of the RR layer and the Phong exponent is presented in Figure 61. It shows that the TIR percentage is over 70% for an RR layer with a refractive index of 1, which drops linearly with increasing the refractive index for the case with a Lambertian-type scattering profile. Increasing the Phong exponent, α, yields a decrease in the percentage of the TIR as the angular distribution of the scattering starts to narrow down. Since the light propagates specularly in the DSP silicon, the total internal reflection doesn't happen in the TIR fashion.

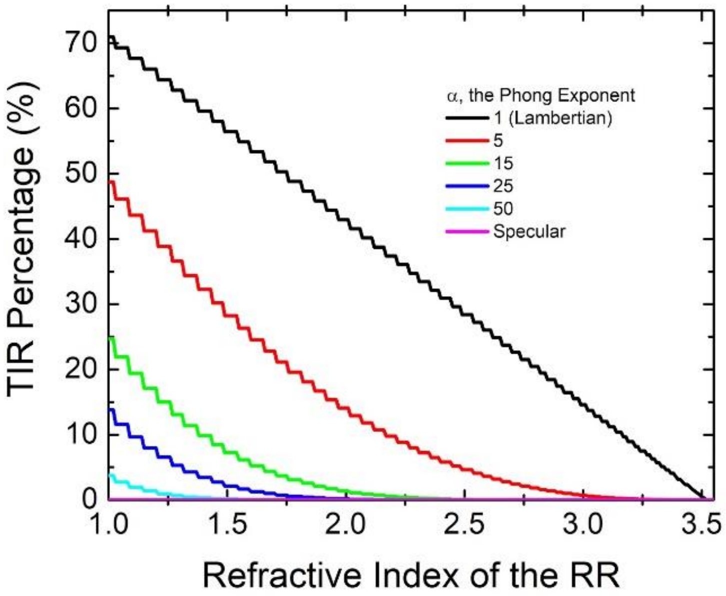

Figure 61 The percentage of the TIR as a function of the refractive index of the RR for various Phong exponents at normal incidence.

It should be noted that the incidence angle of the rear interface is defined by the scattering at the front and rear interfaces in the case of textured silicon substrates. To illustrate the effect of the incidence angle on TIR, the percentage of the TIR as a function of the RR refractive index and the central scattering angle is calculated as shown in Figure 62 and Figure 63. Figure 62 shows the effect of the refractive index of RR and the central scattering angle for a Lambertian scattering profile. It is calculated that a full TIR occurs for a central scattering angle larger than or equal to 50^o for a refractive index of 1 and gradually shifts to more oblique angles with increasing the refractive index. For instance, in the case of SiN_x, the TIR angular threshold becomes 60^o.

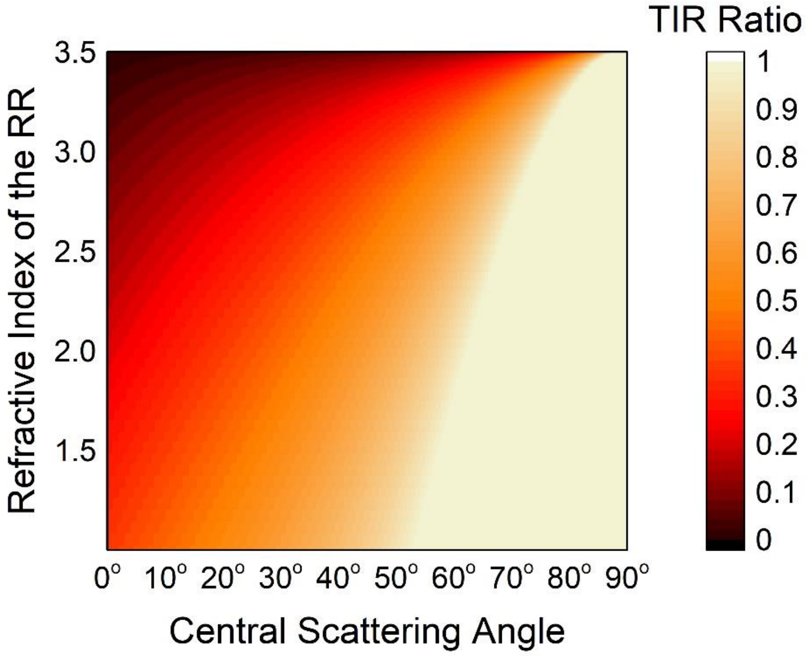

Figure 62 The ratio of the TIR as a function of the refractive index of the RR and the central scattering angle for the Lambertian scattering profile.

Figure 63 shows the TIR condition as a function of the central scattering angle and the refractive index of the RR for the Phong exponents of 5, 15, 25, and 50. As the Phong exponent increases, the TIR threshold angle approaches the critical angle calculated with Equation 61. This is because as the Phong exponent increases, the angular dispersion of the scattered photons becomes narrower, which decreases the number of photons with scattered angles smaller than the critical angle.

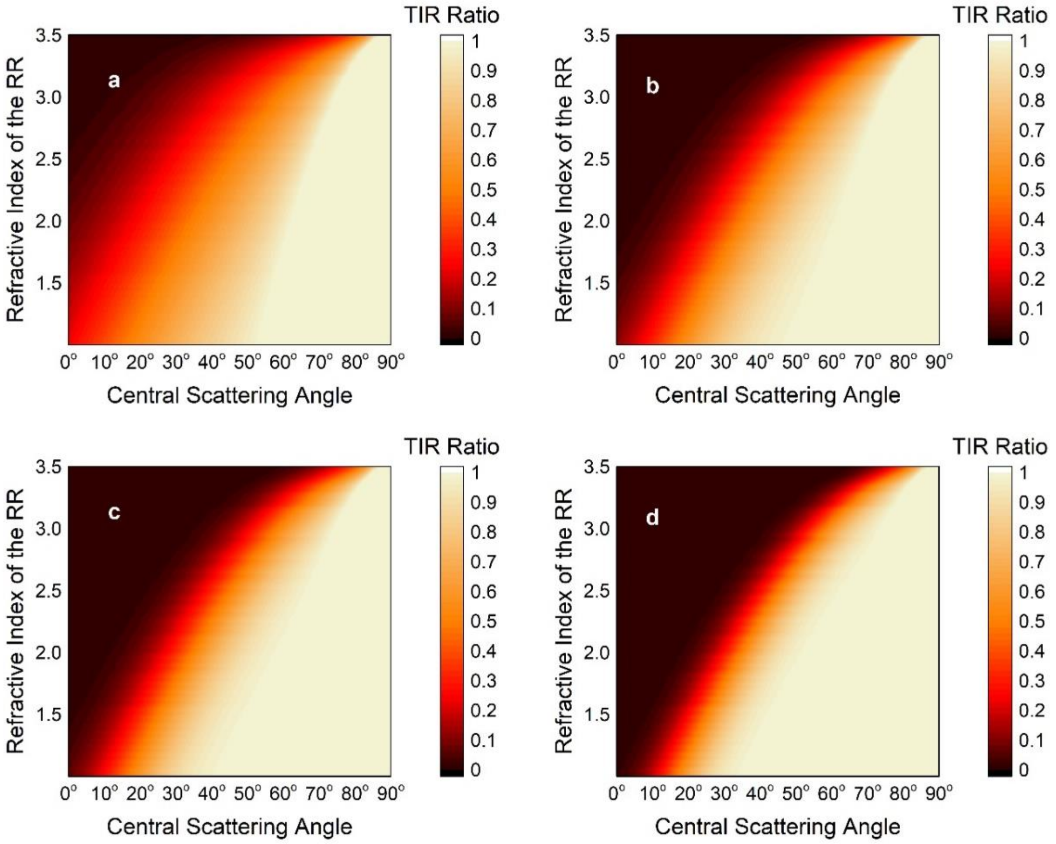

Figure 63 The ratio of the TIR as a function of the refractive index of the RR and the central scattering angle for various Phong exponents, 5 (a), 15 (b), 25 (c), and 50 (d).

The angular distribution of the Phong scattering for various Phong exponents is presented in Figure 64. As the Phong exponent increases, the angular distribution gets confined in a narrower range.

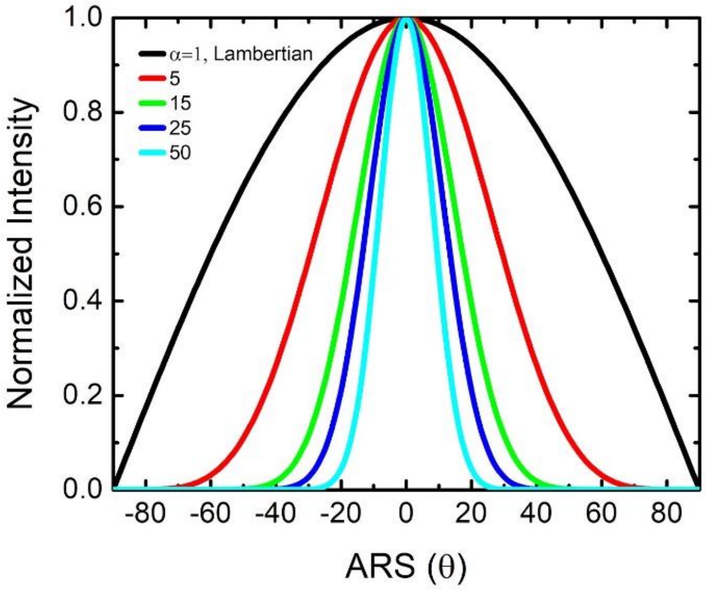

Figure 64 The angle-resolved spectroscopy of the Phong scattering for various Phong exponents.

The central scattering angle is the key parameter defining the degree of light-trapping for the textured silicon substrates. Figure 65 illustrates the optical paths in a textured silicon substrate and the corresponding scattering angles.

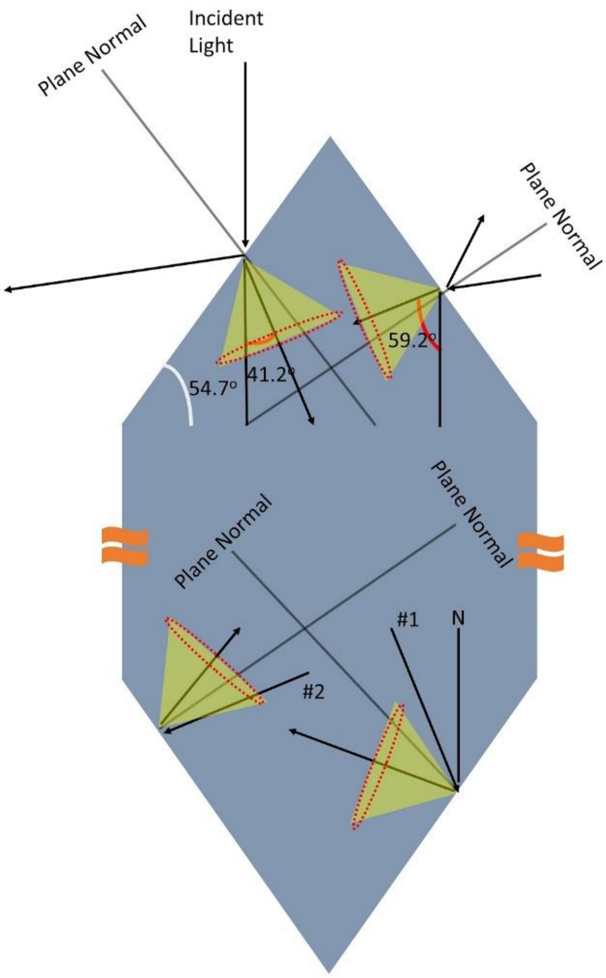

Figure 65 Illustration of the optical paths in the DST silicon substrates at the normal incidence for random distribution of pyramids.

The simulation is fitted to the experimental reflectance by varying Phong exponent to accurately model the measured scattering angles. Figure 66 shows the experimental measurement and simulation results of the random DST silicon substrate without RR and metal layers. The lowest level of mismatch is obtained for $\propto=1$ (Lambertian Scattering). Therefore $\propto$ is chosen accordingly unless otherwise stated.

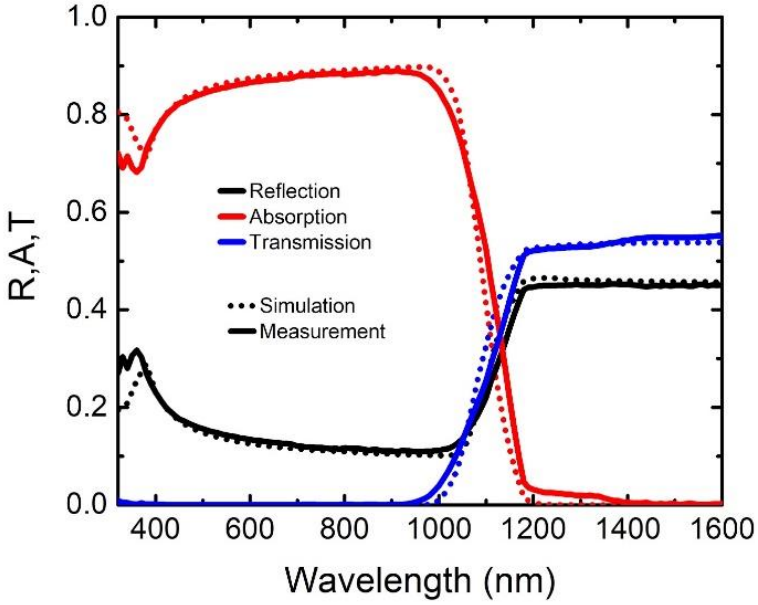

Figure 66 Reflection, absorption and transmission spectra of random DST silicon substrate with simulation (dotted line) and measurement (solid line).

The simulated and measured reflections when a conformal metal layer is coated at the rear surface are presented in Figure 67. The metal layer has a thickness of 300 nm. Subtracting the reflection from unity is a good approximation of the parasitic absorption in the metal layer. A significant enhancement in the silicon absorption is obtained with textured surfaces which can be attributed to the increased light-trapping and suppressed reflections compared with the DSP silicon substrate case. The simulation of DST silicon with the 300 nm-thick Ag metal layer presents a rear reflection of 80% while measured reflection data for the same structure manifests around 50%. The difference between both spectra can be explained with a measurement error of the characterization device and the enhanced parasitic absorption of the metal layer as a consequence of the introduced roughness to the interface, and variation of optical properties of the metal layer. At the time of writing this thesis, we have not been able to clarify this large discrepancy.

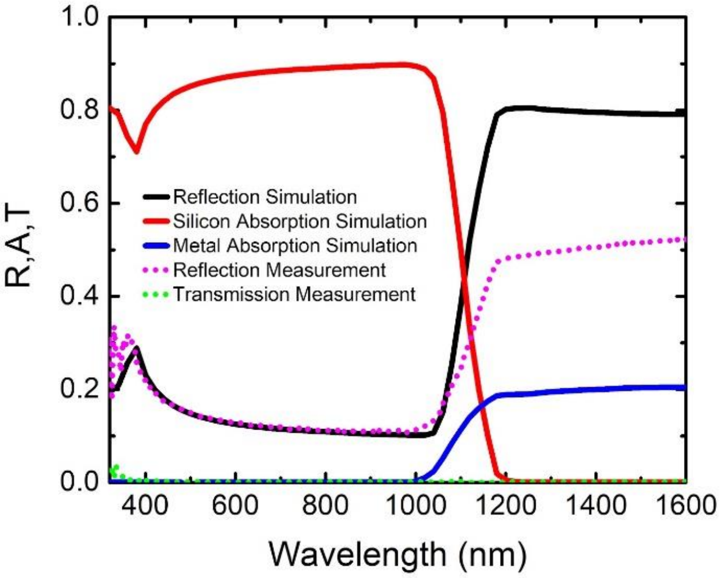

Figure 67 The measured reflection and transmission spectra (dotted line) of random DST silicon substrate with 300 nm-thick Ag metal layer along with simulated reflection, transmission, silicon and metal absorption spectra (solid lines).

The reflection spectrum of a 3.3 mm-thick protected silver mirror from ThorLabs is measured to investigate the measurement error. The measured reflection and the one provided by the datasheet for the reference sample are shown in Figure 68. In addition to the reference sample, the reflectance of 150 nm-thick Ag deposited on a DSP silicon by thermal evaporation is also presented. The measurement error can be seen in both reflection spectra. We believe that this difference is caused by the fact that the utilized diffuse reflector reference ($BaSO_4$) leads to very different reflection paths inside the integrating sphere than our specular reflectors.

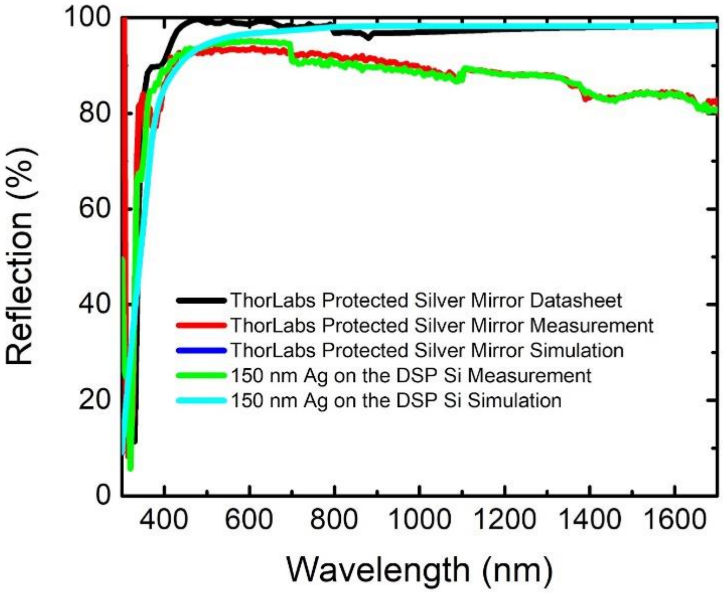

Figure 68 Measured and supplied reference reflection spectra of the protected silver coated mirror from ThorLabs and fabricated 150nm-thick Ag coated DSP silicon substrate. Along with the corresponding simulated reflection spectra.

The main advantage of using an RR layer at the rear interface is that when an interlayer is formed between the metal and silicon layers, only photons with an incident angle smaller or equal to the acceptance cone defined by refractive indices of both layers can transmit to the metal layer. For instance, the acceptance cones are 34.3° and 16.5° at 1200 nm wavelength for SiN_x and aerogel RR layers, respectively. For a Lambertian scattering profile, the ratio of photons corresponds to an incidence larger than the acceptance cone angle is around 30.8% and 46.1% for SiN_x and aerogel RR layers, respectively.

The path length enhancements of DSP and DST models at 1200 nm wavelength are presented in Figure 69. The incident light travels a pathlength that is almost 27 times the substrate thickness in the case of the DST silicon substrate. This can be attributed to the scattering of the incident light and the TIR which takes place at the interfaces due to the oblique incident angles and the refractive index contrast. Hence, the rear interface reflection becomes more important considering multiple bounces of the incident light to mitigate parasitic absorption. Since refractive indices of the utilized materials, silicon, aerogel, and SiN_x, differ inconsiderably for wavelengths longer than 900 nm (Figure 107-109 and Figure 117, see Appendix B), an increased reflection at the 1200 nm wavelengths is representative of a broader range (500-1200 nm). It is important to note that while the light-trapping and absorbance improve with enhanced path lengths, the free carrier absorption (FCA) in the silicon layer increases which in turn yields a decrease in photogeneration. The FCA is defined by the doping levels of the wafer. The utilized silicon substrate in this thesis has a resistivity of 1-3 Ω/cm^2 which corresponds to an FCA of 0.1% per single-pass.[92] Therefore, the FCA is neglected regarding the fact that a maximum of 2.7% absorption loss at 1200 nm wavelength can be obtained and this number decreases with shorter wavelengths.

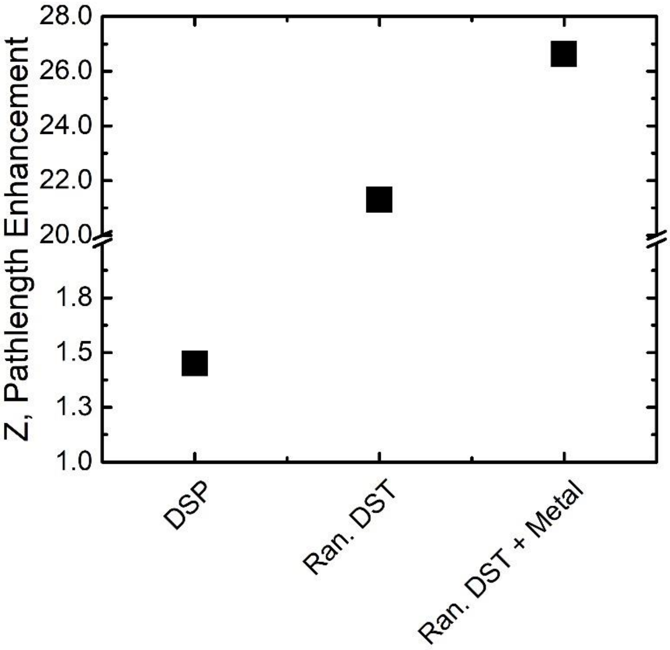

Figure 69 Path length enhancements for various front and rear surface morphologies at 1200 nm wavelength.

The simulated reflection, absorption, and transmission spectra of the double-side random textured silicon substrate are given in Figure 70. Considering the internal reflectance at the rear interface, the utilization of the aerogel and SiN_x layers significantly improves reflectance which in turn increases the absorption in the silicon layer for all the cases. As predicted, the rear interface reflectance improves with decreasing its refractive index.

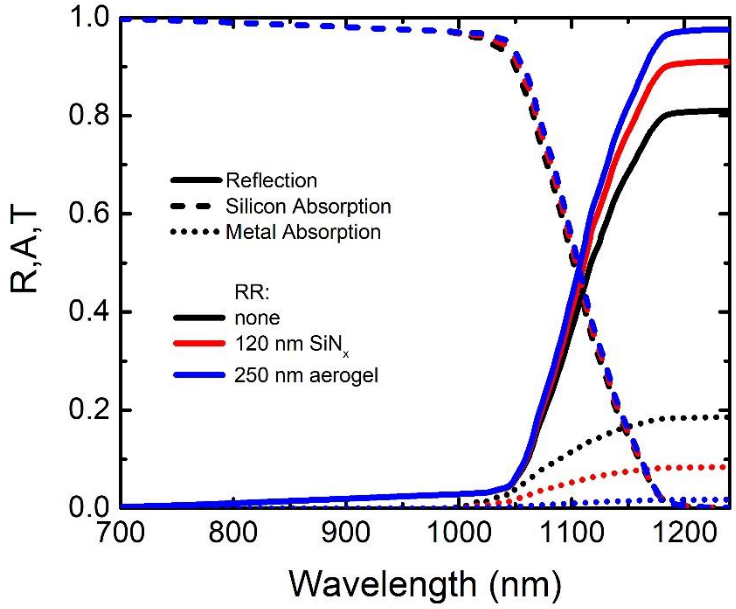

Figure 70 Reflection, and silicon and metal absorption spectra of random DST silicon substrate with various RR combinations (none, 120 nm SiN$_x$ and 250 nm aerogel). Ag is used as the metal electrode.

The reflection and absorption spectra are presented in Table 6 in the form of their photocurrent equivalents showing that the reflection is the main loss mechanism. The reflection loss is around 9 mA/cm^2 for all DSP cases and there is a slight increase with SiN$_x$ and aerogel RR introduction. As mentioned previously, a negligible absorption difference is presented for all DSP cases. The free carrier absorption is not accounted for the silicon layer, as a result, the loss is assumed to be due to the reflection and metal absorption. Since a 300 nm-thick metal electrode is used, zero transmissions are obtained with all the cases. Negligible parasitic absorption values are calculated in the ARC and RR layers. The introduction of the surface texturing boosts the silicon absorption by more than 5 mA/cm^2. However non-planar surface features cause increased parasitic absorption in the metal layer. In particular, the utilization of texturing at the rear surface results in 0.75 mA/cm^2 parasitic absorption. In all the cases, SiN_x and aerogel RR layers mitigate the metal parasitic absorption. Specifically, the aerogel RR can suppress the metal absorption effectively.

Table 6 Photocurrent equivalent of optical interaction mechanisms of DSP and DST substrates with SiN_x and aerogel RR layers. Results of DSP and DST substrates without an RR layer are also demonstrated.

	Reflection	Silicon Absorption	Metal Absorption
		mA/cm2	
DSP Si	8.93	37.23	0.30
DSP Si with SiNx RR	9.04	37.29	0.13
DSP Si with aerogel RR	9.10	37.31	0.04
DST ran. Si	3.30	42.38	0.75
DST ran. Si with SiNx RR	3.60	42.49	0.34
DST ran. Si with aerogel RR	3.79	42.57	0.07

4.1.1. The Quantization of the Metal Absorption in Practical Cases

The effect of the surface roughness of the RR-metal interface is investigated. A planarization step of the RR-metal interface is introduced and its optical effects are discussed. The aerogel layer is modeled as a 3D scattering medium and optical simulations are performed in this framework. Conflicting results of the simulation and experimental data which is first presented by Boccard et al. are quantized herein.[88] Since the aerogel layer is modeled using many-body SiO_2 particles with altered porosity fractions, it is predicted that the conformally coated metal surface has inevitable surface roughness considering the porosity of the aerogel layer. The EMA utilized in the previous chapter is demonstrative for the planar metal interfaces, so in this chapter, the internal reflections are computed using 3D optical simulations to account for the surface roughness. To improve the planarity of the aerogel layer, a 60 nm-thick spin-coated SiO_2 planarization layer is introduced and analyzed.

The effect of the planarization is investigated using various surface roughness RMS values while the correlation length is assumed as 150 nm. Figure 71 shows the rear reflection of the DSP silicon substrate with a planarized aerogel RR layer at the normal incidence. Reflection and metal absorption strongly vary with introduced surface roughness. The corresponding metal surfaces used in the simulations are also presented for illustrative purposes. As the surface roughness RMS values increase, more intense geometric features start to occur at the metal surface.

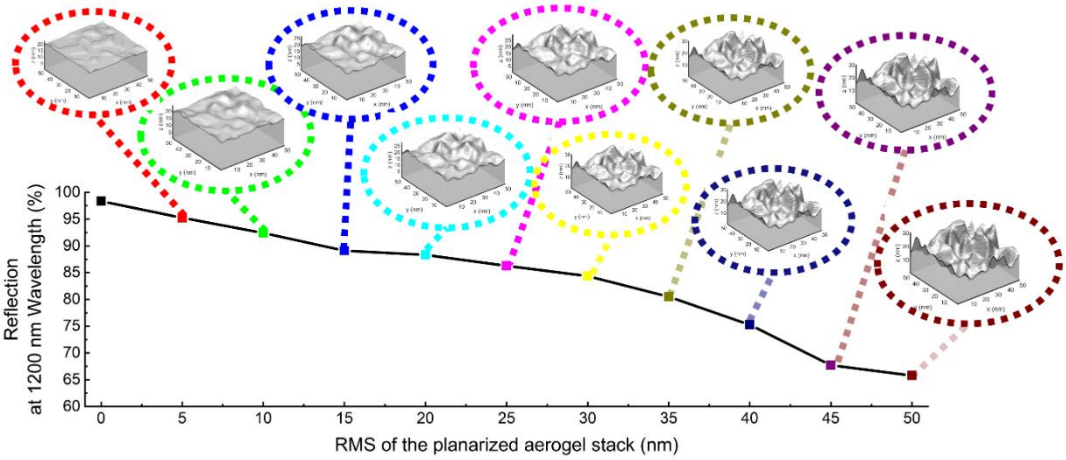

Figure 71 The internal reflection of the planarized aerogel RR layer and the Ag metal for various surface roughness values at the normal incidence at 1200 nm wavelength. Illustration of the metal surface is given as inset.

Figure 72a shows the AFM measurement of a 60 nm-thick SiO_2 planarization layer/250 nm-thick aerogel RR/ silicon substrate stack. Figure 72b shows the height map of the mentioned structure. The RMS value and the correlation length of the surface are calculated as 40 nm and 250 nm, respectively. The morphology data measured by AFM is imported to the 3D optical simulation environment. The internal reflections and parasitic absorptions are calculated and imported to the developed combined wave optics and ray-tracing algorithm. The internal reflection at the rear interface is calculated as 91.76% for the unpolarized light which yields an overall rear reflection of 91.98% for the DSP silicon substrate at the normal incidence. It should be noted that the reflection is calculated as 75% for the same RMS value with a correlation length of 150 nm, however, according to the AFM measurements, the correlation length is 250 nm which is an equally important parameter to define the surface roughness as presented in Figure 55.

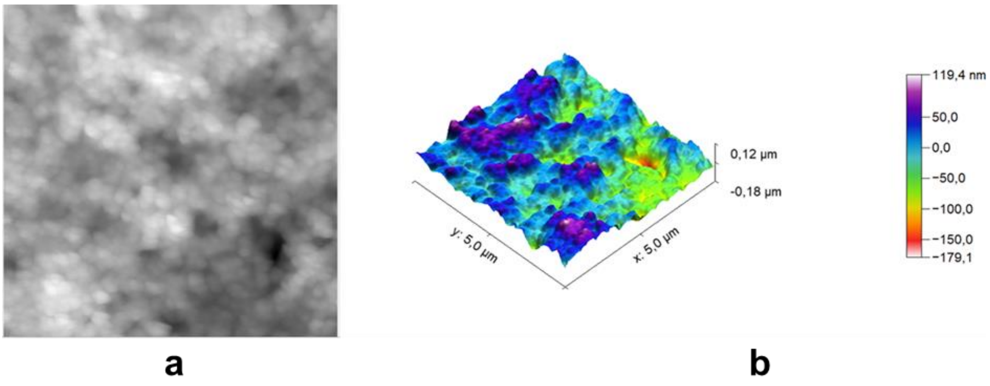

Figure 72 Illustration of AFM surface measurement of the planarized aerogel coated rear interface (a). The height map of the measured surface (b).

Figure 73 presents the corresponding simulation model of AFM surface measurement when a 60 nm-thick SiO_2 planarization layer is inserted between the aerogel RR layer and the evaporated metal layer.

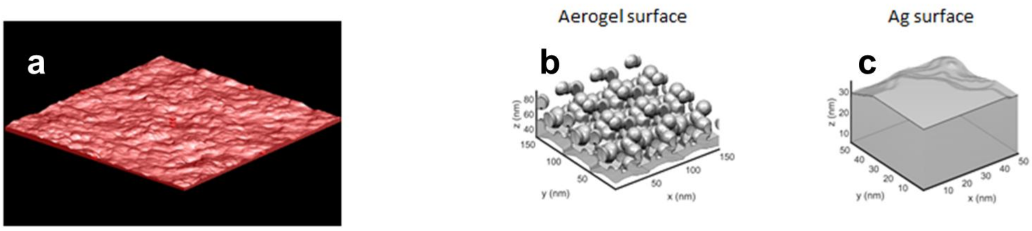

Figure 73 Corresponding simulation model of AFM surface (a) at the rear interface of planarized aerogel RR (b) and conformally coated Ag layer (c).

The effect of the surface roughness of the metal layer on the rear reflection can be seen in Figure 74. The measurement and simulation results of the DSP silicon with various RR combinations are demonstrated. Figure 74a shows the measured reflection spectra of DSP with no RR, 35 nm- and 110 nm-thick SiN_x RR layers along with corresponding simulation data. Since SiN_x and Ag layers are deposited by sputtering and thermal evaporation methods, yielding conformal coating, the surface roughness is neglected in the optical simulations. Overall, the experimental and simulation data are in good agreement, in particular for the wavelengths shorter than 1100 nm. However, there is an offset at wavelengths longer than 1200 nm in all the experimental-simulation pairs which is attributed to the measurement error as shown in Figure 17b.

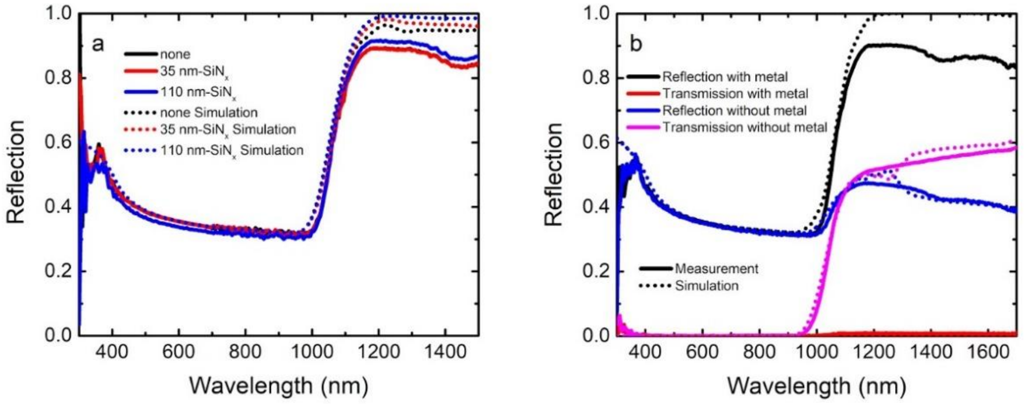

Figure 74 Measured and simulated reflection spectra of the DSP silicon with 35 and 110 nm thick SiN_x RR layer, and without an RR layer (a). Measured and simulated reflection and transmission spectra of the DSP silicon with a planarized aerogel RR layer with and without the Ag layer (b).

Figure 74b shows the reflection spectra of the DSP silicon with a planarized aerogel RR layer with and without an Ag layer. The rear interface reflections are simulated in a 3D framework to account for the porosity of the aerogel layer and the interdiffusion of the evaporated metal layer. The simulation results are in good agreement with the measurement in the case without the Ag layer. However, in the case of models with rear metal, reflection spectra of the simulation and measurement differ which arises from the measurement error explained previously in Figure 17b.

To compare the rear reflection performance of different evaporated metals, the simulated reflection, and silicon and metal absorption spectra of the DST silicon substrate are presented in Figure 75a. When there is no RR layer, there exists a noticeable reflection difference between the cases with Al and Ag which is explained by the higher extinction coefficient of Al compared to Ag (Figure 117, see Appendix B). The difference in rear reflections is 20% and it decreases to 7% with the utilization of 120 nm-thick SiN_x RR layer. However, when the aerogel RR layer is employed, the difference between rear reflections diminishes as it is 97% for Ag and 95% for Al.

Reflection, and silicon and metal absorption spectra of the DST silicon with various metal, RR layer, and metal interface combinations are presented in Figure 75. Surface roughness is adapted from the AFM measurements. The simulated rear reflections are 69% and 74% for Al and Ag metal layers with planarized aerogel RR layers, respectively. A comparison of reflection, and silicon and metal absorptions of various metals, RR layers and metal interfaces in the form of current flux is given in Table 7. When metal is selected as Al, a higher metal absorption is calculated as predicted. The utilization of the RR layer almost completely mitigates this parasitic absorption, especially in the case of the planar aerogel RR layer. When the porosity induced surface roughness of the metal layer is considered, the aerogel RR layer is detrimental in the case of Ag, however, an almost 10% improvement is computed with Al.

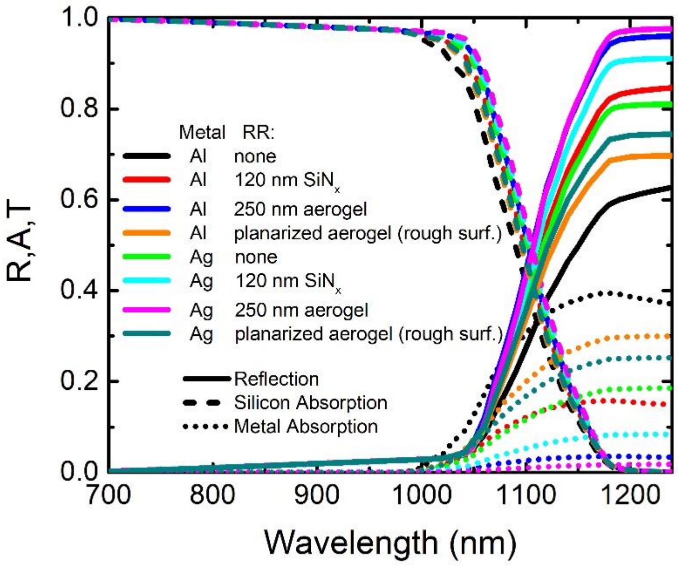

Figure 75 Reflection and absorption spectra of the DST silicon substrate with various RR and metal layer combinations (a).

Table 7 Photocurrent equivalent of optical interaction mechanisms of DST substrate with none, SiN_x, and with aerogel RR layers for Ag and Al metal layers without surface roughness effects.

RR	Metal	Metal Surface	Reflection	Silicon Absorption mA/cm^2	Metal Absorption
none	Ag	planar	3.30	42.38	0.75
SiN_x	Ag	planar	3.60	42.49	0.34
aerogel	Ag	planar	3.79	42.57	0.07
planarized aerogel	Ag	rough	3.13	41.67	1.04
none	Al	planar	2.62	41.54	1.85
SiN_x	Al	planar	3.36	41.91	0.73
aerogel	Al	planar	3.74	42.10	0.16
planarized aerogel	Al	rough	2.99	41.62	1.24
aerogel	Al	planar	3.74	42.10	0.16
planarized aerogel	Al	rough	2.99	41.62	1.24

Finally, reflection, silicon absorption, and metal absorption spectra with a screen-printed Al metal layer are calculated. The screen-printing is modeled as agglomerated Al microparticles according to the SEM measurements from the literature.[93] Although the screen-printed Al layer introduces strong parasitic absorption regarding its wavelength-scale feature size, a reflection of 57% is achieved with the planarized aerogel RR layer. The simulation results for the DST silicon with the screen-printed Al metal layer and different RR layers are presented in Figure 76. It can be seen that the reflectance of the planarized aerogel RR layer is at least 10% higher than the one of the SiN_x RR layer.

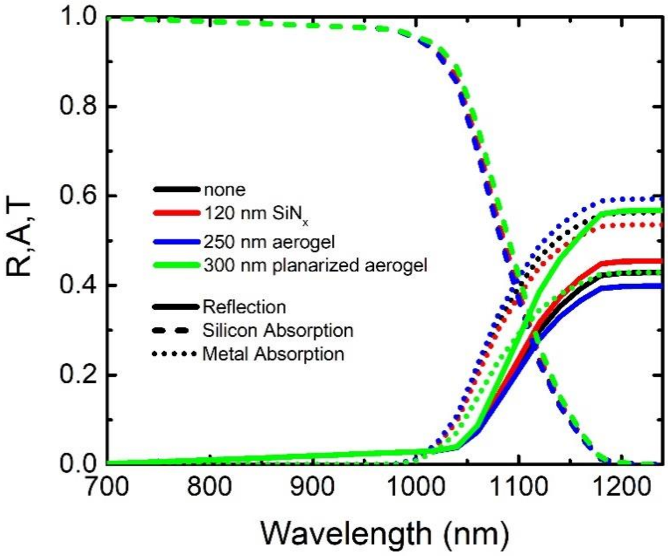

Figure 76 Reflection, and silicon and metal absorption spectra of the DST silicon substrates with various RR combinations for the screen-printed Al layer.

4.2. **Conclusions**

Utilization of a low index material as an RR improves the rear reflection by establishing a higher index contrast and a larger TIR rate. Aerogel with its low refractive index is a proper candidate for the RR. However, if porosity induced rough metal surface is not addressed, the mitigation of the metal parasitic absorption is limited. To address this problem and block the interdiffusion of metal, a planarization layer based on spin-coated SiO_2 film is introduced. The planarized aerogel has a significantly smoother surface hence it presents an improved rear reflection. The advantage of using an aerogel RR is more prominent with the screen-printed Al. More than 10% rear reflection difference is computed with planarized aerogel compared to state-of-the-art SiN_x RR layers.

CHAPTER 5

COMBINED OPTICAL-ELECTRICAL OPTIMIZATION OF CZT/SILICON TANDEM SOLAR CELLS

In this section, an optical and electrical optimization is performed, in line with the SQ limit, to extract the maximum photocurrents with $C_{1-x}Z_xT$/Si tandem cells. In accordance, the main optical and electrical performance drawbacks including parasitic absorption, energy level mismatches, and low transparency of the top cell for wavelengths longer than its absorption onset are addressed.

Part of the material presented in this chapter has been published in *Materials* **2020**, *13*(8), 1860.[8]

5.1. Introduction

Year by year, new record-high efficiencies have been announced in many photovoltaic (PV) technologies (i.e. Silicon, CdTe, CIGS, Perovskite, organic, etc.).[3,94] Performance improvements of different solar cell types started to slow down while approaching their fundamental limits, referred also as the Shockley-Queisser (SQ) limit. Since the SQ limit only considers radiative recombination losses, the SQ limit may be remote, whereas the performance is still diminished by electrical and optical losses. Alternatively, tandem solar cell configurations can exceed the SQ limits of single-junction solar cells. For the two-junction tandem solar cells having a rear cell with a bandgap of 1.12 eV, the SQ limit reaches a maximum when a top cell with a bandgap of 1.81 eV is used.[5] A two-terminal (2T) connection based tandem solar cells requires, a tunnel-junction, continuous device fabrication and processing, and current matching of the subcells, each of which has challenges. For instance, the thermal stability of a subcell must be sufficiently high. The current matching constraint requires refinement of the subcell parameters, which drives deductions in cell properties. Alternatively, a four-terminal (4T) tandem cell would have fewer fabrication considerations as it is based on joining one cell on top of another with a transparent interlayer, by enabling each cell to be fabricated and operate separately in terms of their PV operates. Furthermore, the degree of freedom of the top cell bandgap improves compared to the 2T tandem structures.[95]

Both perovskite and III-V solar cells have been researched as a top cell counterpart to silicon recently. It is documented that more than 25% conversion efficiencies are achievable with various technologies such as conformal top cell coating on the textured silicon rear cell and the tuning of the bandgap of the top cell.[96–100] The most prominent device performance was documented by Essig et al. considering III-V/Si tandem cells, where ~30% efficiency is achieved in 4T structure using a ~18% GaInP top cell and ~12% Si rear cell in the tandem device.[101] However, both of these top cells have their drawbacks, for instance, the perovskite cells still suffer from instability while they are far from matching the lifetime of silicon cells, and the III-V cells are fabricated only at small scales which in turn increases the cost. Instead, the developed CdTe thin-film technology can provide substantial pluses, having a proven long carrier lifetime and relatively inexpensive fabrication costs with noteworthy performance.

5.2. **Results and Discussions**

5.2.1. **Optical Optimizations**

In order to perform optical simulations of the full device, CdS is assumed as the electron transport layer (ETL) for the top cell for most of tandem configurations, as of being the conventional associate of the CdTe absorber. Furthermore, magnesium zinc oxide (MZO) is used as an alternative ETL. MoO_x is considered as the hole transport layer (HTL) for the top cell. ITO is employed as the transparent conducting oxide (TCO) on both sides of the top cell regarding its good optical and charge transport properties. The IBC Si cell with a 25.2% conversion efficiency is assumed as the rear cell. The index-matching glue is assumed between the two cells with a constant refractive index of 1.6 and zero extinction coefficient. Silicon nitride (SiN_x) is employed as the ARC for the IBC Si cell. Finally, EVA is used as the encapsulant material at both sides. The schematics of the optically simulated structures are shown in Figure 77. The maximum achievable photocurrent (MAPC) is used to quantify the absorption in the cell.

Light interacts with the top cell layers ($C_{1-x}Z_xT$, ETL, HTL, and TCO layers) in the specular domain, which is caused by the planar interfaces. Alternatively, the Lambertian scattering is assumed for the silicon interface. Transmission, reflection, absorption, and external quantum efficiency (EQE) spectra of the IBC Si cell are calculated following the study of Smith et al.[102]

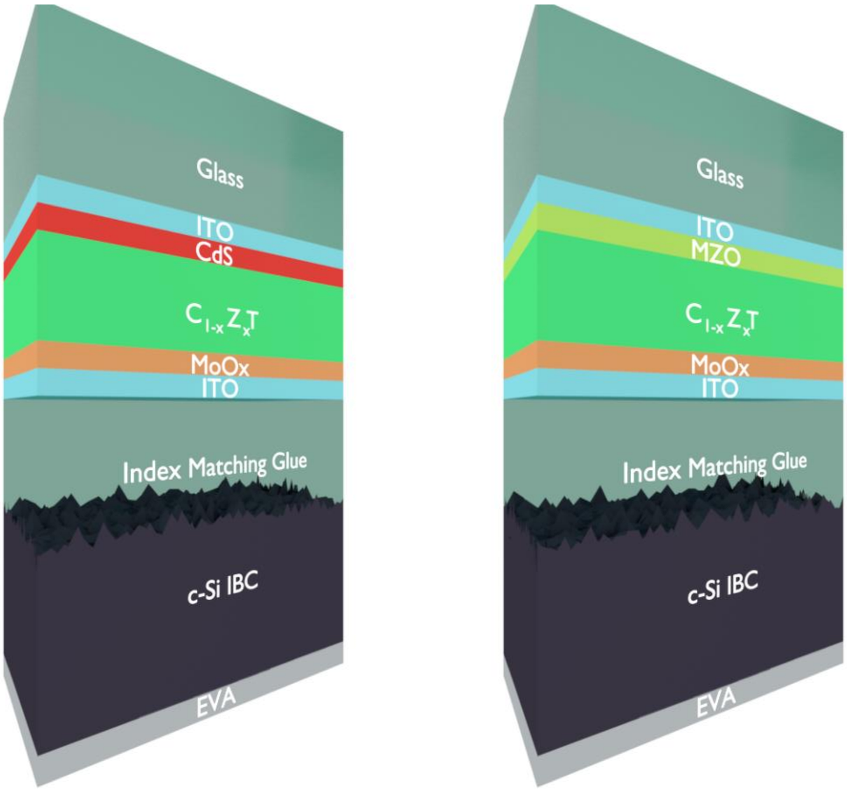

*Figure 77 Schematic of $C_{1-x}Z_xT$/c-Si interdigitated back contact (IBC) tandem cells with top cell electron transport layers (ETLs) of CdS (**LEFT**) and $Mg_{0.23}Zn_{0.77}O$ (**RIGHT**).*

Most of the incident light is absorbed within a single-pass due to the fact that the practical thickness range of the CdTe layer for an efficient CdTe cell is 0.5 to 3.0 μm

(Figure 78).[76] Therefore, the interference of light due to the CdTe absorber is negligable.

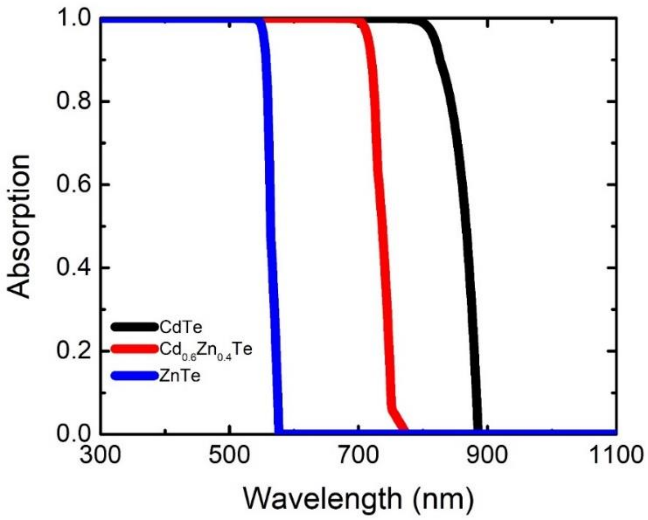

Figure 78 Single-pass absorption spectra for 3 µm thick top cell active absorber (CdTe, $C_{0.6}Z_{0.4}T$ and ZnTe) obeying the Beer-Lambert Law for the incident light as a function of wavelength are given.

Figure 79a,b shows the effect of the thicknesses of the front layers, CdS, and ITO, on the MAPCs of CdTe and IBC Si cells, respectively. A sufficiently thick (3 µm) CdTe and no rear ITO are used to examine the effects of the front layers solely. A local maximum at around 55 nm thick front ITO layers is computed for the MAPC of the CdTe cell (Figure 79a), where the MAPC of the IBC Si cell reduces with increasing the thickness of the front ITO result of the parasitic loss within this layer (Figure 79b).[7] The strong free carrier absorption and low refractive index of the ITO layer at the long wavelengths where incident light reaches the IBC Si cell yield this drop in the MAPC with ITO thickness. The adverse effects of the CdS layer on the MAPC of the CdTe cell, regarding its nonzero extinction coefficient in the UV and visible parts of the spectrum (Figure 118, see Appendix B), are prominent, while a local maxima in the MAPC of IBC Si cell at odd integer multiples thickness values of 105 nm are computed for the CdS layer. These distinct thicknesses support the quarter-wave optical thicknesses (QWOT) of the CdS layer at a central wavelength of 900 nm. The central wavelength corresponds to the absorption onset of the CdTe absorber, which incident light flux peaks for the rear cell.

The MAPCs of the CdTe and Si IBC cells as a function of front ITO, CdS, CdTe, and rear ITO thicknesses are presented in Figure 79c,e,g, and Figure 79d,f,h, respectively. The optimum front ITO thickness for the MAPC of the CdTe cell is calculated as 55 nm regardless of the thickness of CdTe (Figure 79c), while it yields lower silicon absorption due to the parasitic absorption in the IBC Si cell for any thickness of the CdTe layer, as shown in Figure 79d. Correspondingly, the detrimental behavior of the CdS layer on the CdTe cell and the optimum thickness of the CdS (i.e., QWOT condition) to attain a local maximum in the MAPC of the IBC Si cell are valid at various CdTe thicknesses, as presented in Figure 79e,f. Finally, the rear ITO leads to parasitic loss in MAPC of the IBC Si cell, although the MAPC of the CdTe cell is independent from it, as shown in Figure 79g,h. The parasitic loss caused by the rear ITO, analogous to the front ITO, is attributable to its nonzero extinction coefficient in the near-infrared (IR) due to the high free carrier concentration (Figure 118, see Appendix B).

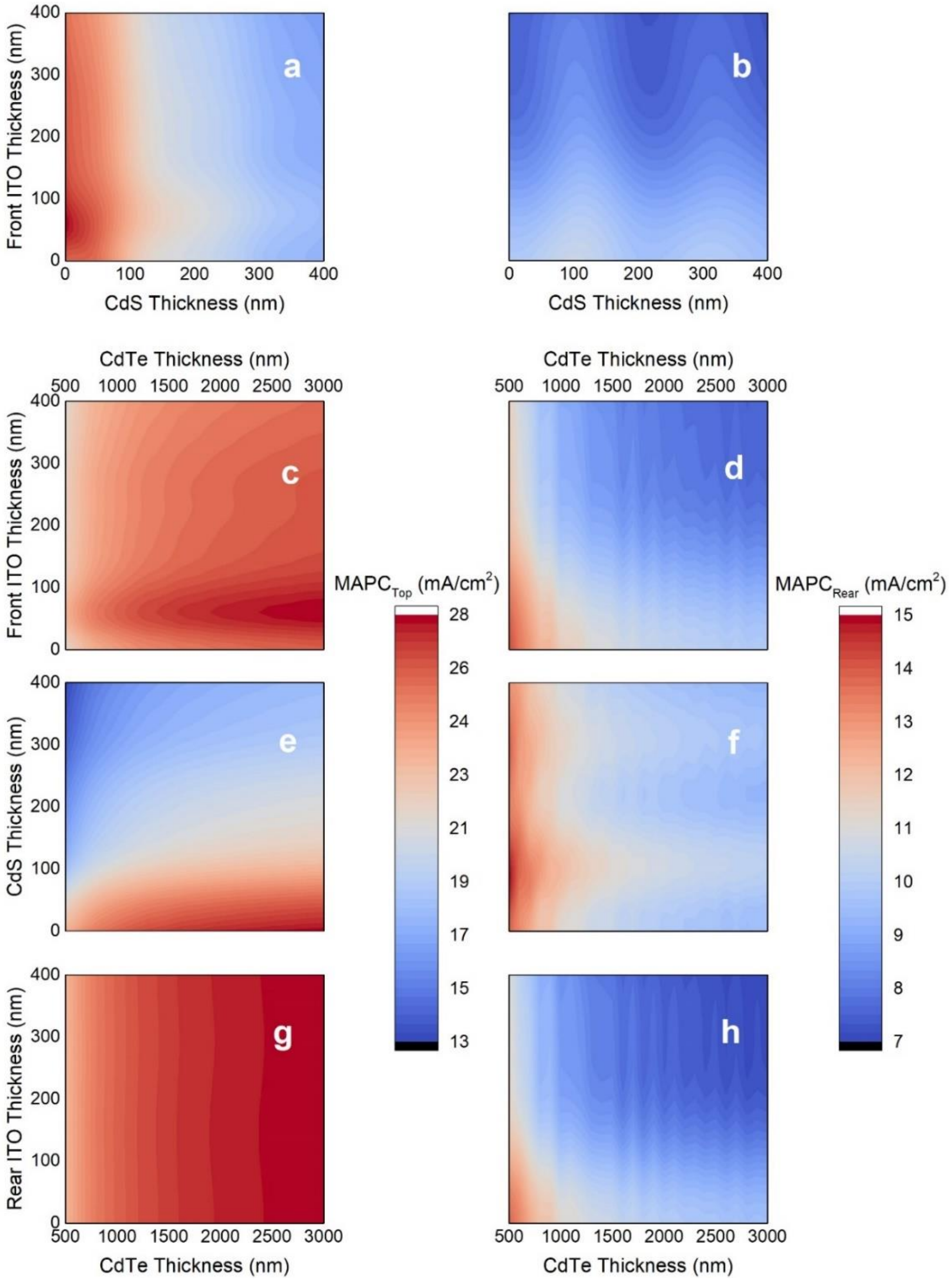

*Figure 79 The maximum achievable photocurrent (MAPC) of CdTe and IBC Si cells for various front indium-tin-oxide (ITO) and CdS thicknesses for a constant CdTe thickness of 3000 nm, assuming no rear ITO layer is present (**a**,**b**); for various front ITO and CdTe thicknesses, assuming no CdS and rear ITO layers are present (**c**,**d**); for various CdS and CdTe thicknesses, assuming a front ITO layer thickness of 55 nm and no rear ITO is present (**e**,**f**); and for various rear ITO and CdTe thicknesses, assuming a front ITO layer thickness of 55 nm and no CdS layer is present (**g**,**h**), respectively.*

The optimum front ITO thickness of 55 nm obtained for the CdTe top cell is also valid for $C_{1-x}Z_xT$ absorbers independent from the Zn content (Figure 80a). Note that both front and rear ITO layers have parasitic absorption in the near IR and consequently lower the MAPC of the Si IBC cell which is independent from the $C_{1-x}Z_xT$ composition. Although parasitic absorption in the CdS layer results as the MAPC of the $C_{1-x}Z_xT$ cell to decrease, the QWOT condition that yields local maximum at the MAPC of the IBC Si cell is also valid for any Zn content. Evidently, the thickness of the CdS layer that corresponds to the QWOT value decreases with increasing Zn content as the absorption onset shifts to shorter wavelengths (Figure 80b).

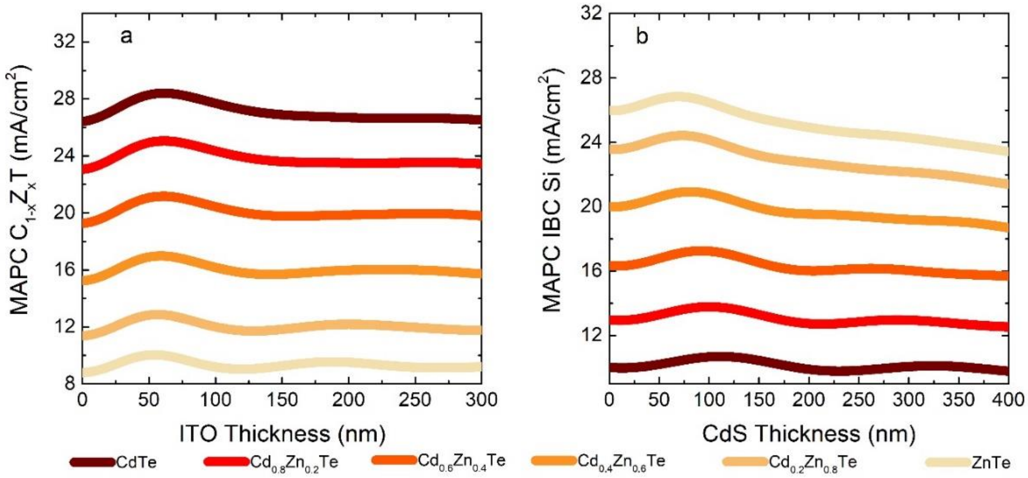

*Figure 80 The MAPC of $C_{1-x}Z_xT$ (**a**) and IBC Si (**b**) cells for various x values and $C_{1-x}Z_xT$ thickness of 3 µm. In panel (a), the front ITO thickness is varied with no CdS and no rear ITO layers employed, whereas in panel (b), the CdS thickness is varied with 55 nm front ITO and no rear ITO layer employed.*

Frequently, $Mg_xZn_{1-x}O$ ($0 < x < 0.4$) is utilized as a replacement for CdS to improve the photocurrent of CdTe solar cells[103–105] due to its much smaller and spectrally limited extinction coefficient (Figure 118, see Appendix B). Figure 81 shows the MAPCs of CdTe, $C_{0.6}Z_{0.4}T$, and ZnTe top cells and IBC Si rear cell as a function of ITO and MZO thicknesses in the case of the MZO ($Mg_{0.23}Zn_{0.77}O$) ETL. The MAPC of the top cell presents local maxima for total thicknesses of front ITO (t_{ITO}) and MZO (t_{MZO}) layers (i.e. $t_{ITO} + t_{MZO} \approx 60$ nm) as a result of the adjacent refractive indices of MZO and ITO in the visible part of the spectrum. In addition to that, MAPCs of CdTe and $C_{0.6}Z_{0.4}T$ cases demonstrate local maxima regions for odd integer multiples of MZO thickness of ~100 nm (Figure 81a,b). This thickness satisfies the QWOT condition at the 700–800 nm wavelength region of the spectrum. The consolidated thickness behavior is no longer effective, therefore the interference of incident light is exclusively determined by MZO thickness since the refractive index of ITO is contiguous to that of glass in the mentioned spectrum range. Since the absorption onset wavelength shifts to thinner values with increasing Zn content, observed anti-reflective trends with odd multiples of MZO thicknesses move to thinner values (Figure 81b). As the Zn content of $C_{1-x}Z_xT$ increases, the local maxima when the condition of odd multiples of $t_{ITO} + t_{MZO}$ dominates. Thus, Figure 81c shows inclined high MAPC lines for ZnTe that correspond to local maxima. The MAPC of the IBC Si cell manifests local maxima regarding constructive interferences in the MZO layers like the case of CdS ETL (Figure 81b). For an approximately 120 nm-thick MZO corresponding to the QWOT value, the MAPC of the IBC Si cell presents local maxima regions (Figure 81d), which shifts to thinner values with increasing Zn content as shown in Figure 81e,f.

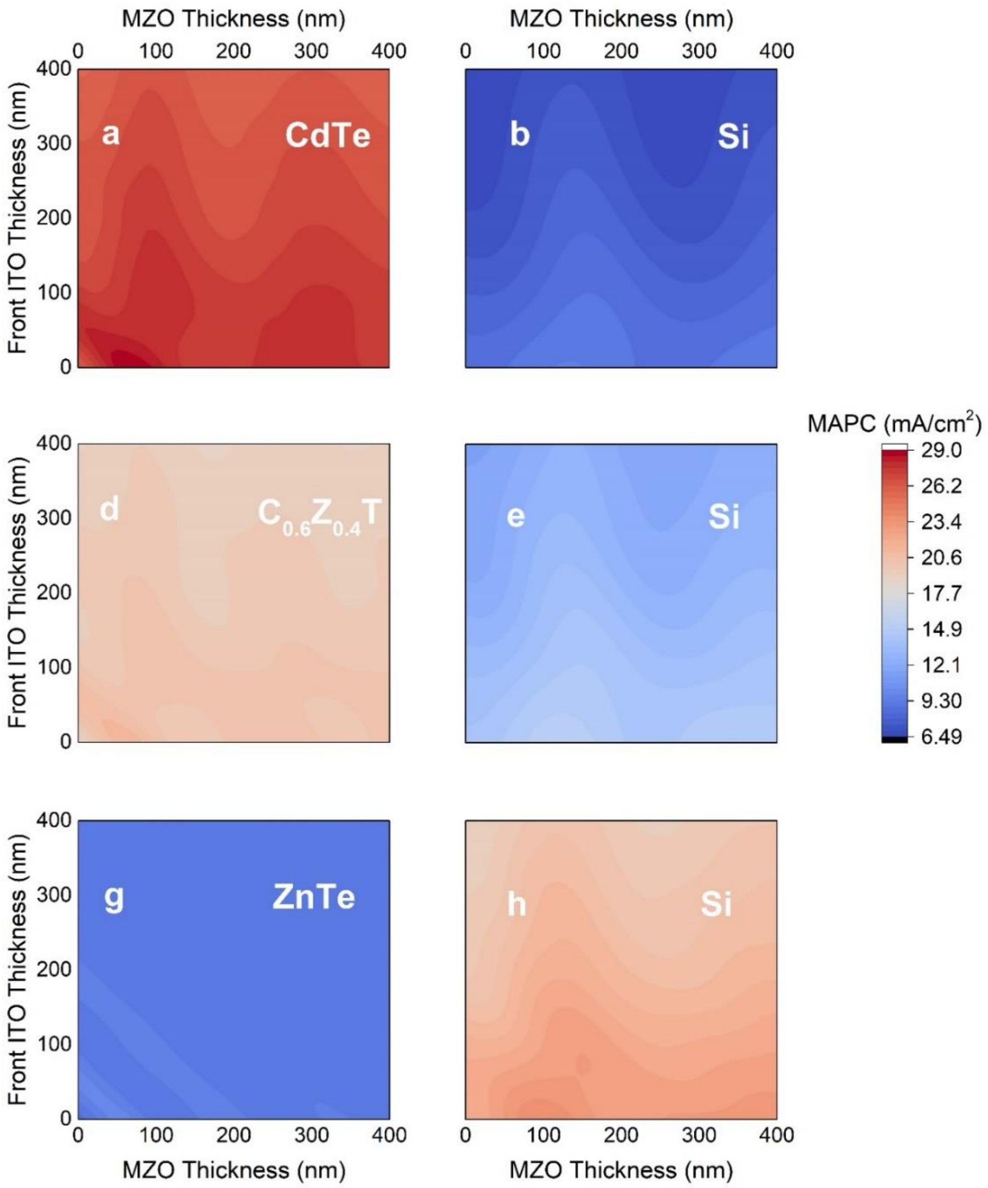

*Figure 81 MAPC of CdTe (**a**), $C_{0.6}Z_{0.4}T$ (**b**), and ZnTe (**c**) top cells, along with the corresponding IBC Si cells (**d–f**) as a function of front ITO and MZO thicknesses. In all cases, $C_{1-x}Z_xT$ = 3 μm, HTL (MoO_x) = 5 nm, and no rear ITO is used to isolate the effect of the front ITO and MZO layers.*

The parasitic absorption in the CdS layer can also be eradicated by flipping the $C_{1-x}Z_xT$ solar cell upside down. To simulate this proposed inverted structure, the top cell is protected with a humidity-blocking encapsulant (e.g., EVA), as shown in Figure 82. The inverted structure can remove the parasitic absorption of the CdS layer since CdS has almost zero extinction coefficient for wavelengths longer than 550 nm where the incident photons within this wavelength window are almost completely absorbed by the $C_{1-x}Z_xT$ layer within a single-pass (Figure 78). Furthermore, the CdS layer can be used with a QWOT without any parasitic effect on the top cell.

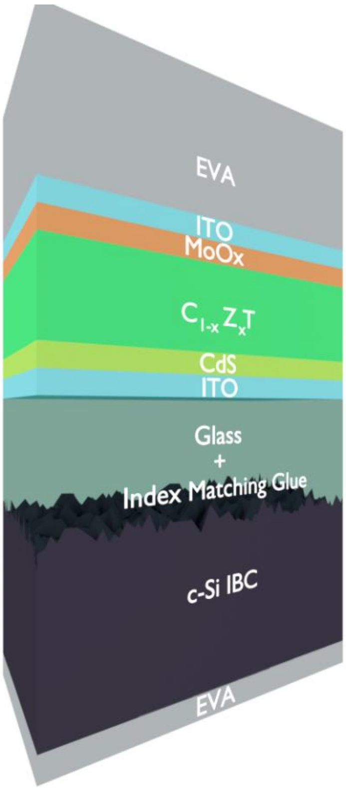

Figure 82 Schematic of the inverted structure. Front and rear TCO is ITO, ETL is CdS, HTL is MoO_x, index matching glue is employed between two cells. EVA is used to protect IBC Si cell contacts; glass is employed as the substrate.

Figure 83a–c shows the absorption spectra of the optimized normal top cell structure with a CdS or $Mg_{0.23}Zn_{0.77}O$ window ETL and the inverted design with a CdS rear ETL. Table 8 presents the calculated MAPCs for top and rear cells. Note that a 110 nm thick MgF_2 at the front is utilized as an anti-reflective coating (ARC) atop the glass. When the MZO is used in place of CdS, substantial increases in the MAPC of the top cell can be attained. For instance, in the CdTe case, 1.78 mA/cm^2 higher MAPC of the top cell is calculated with MZO compared with CdS having the same thickness (50 nm). For the inverted structure with QWOT ETL, improvement in the MAPC of the CdTe cell is 1.69 mA/cm^2. The MAPC increase is 2.08 mA/cm^2 for the MZO replacement in the normal configuration relative to the CdS as ETL and 1.79 mA/cm^2 for the inverted design in the case of the $C_{0.6}Z_{0.4}T$ cell. Lastly, the enhancement in the top cell MAPC is 1.74 mA/cm^2 for the MZO replacement relative to the CdS as window ETL and 2.36 mA/cm^2 for the inverted design in the case of the ZnTe top cell. The difference in the MAPC of the IBC Si cell is a drop of almost 0.6 mA/cm^2 with the MZO replacement for all cases. This drop can be attributed to the more preferable refractive index of CdS. Less than 0.35 mA/cm^2 increase in the MAPC of the rear cell is found with the utilization of the CdS layer with QWOT value; however, it triggers more than 3 mA/cm^2 MAPC drop at the top cell. Meanwhile, in the inverted structure cases, MAPC of the rear cell improves more than 1 mA/cm^2.

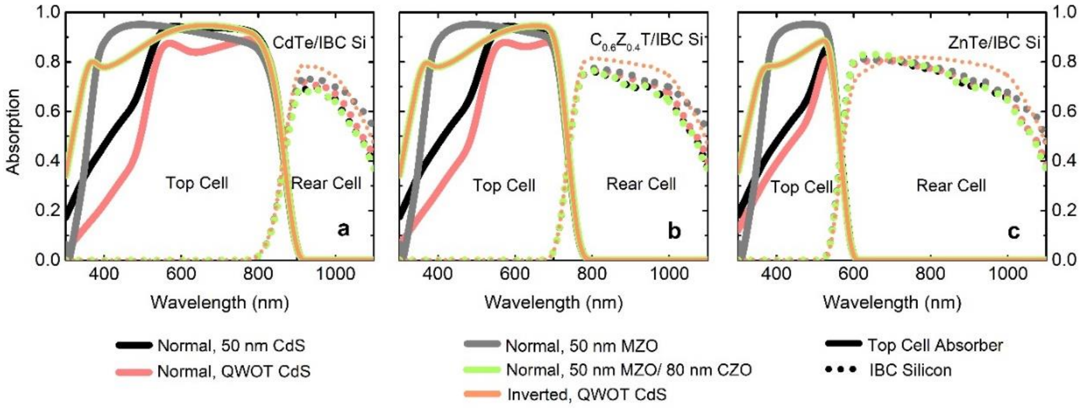

*Figure 83 Absorption spectra of CdTe (**a**), $C_{0.6}Z_{0.4}T$ (**b**), and ZnTe (**c**) top cells (solid lines), along with the corresponding IBC Si rear cell absorption spectra (dotted lines); in the normal configuration with 50 nm CdS (black), QWOT CdS (red), 50 nm MZO (blue), 50 nm MZO, and 80 nm CZO as rear TCO (cyan) and in the inverted configuration with QWOT CdS (green). In all cases, $C_{1-x}Z_xT$ = 3 μm, MoO_x = 5 nm, front ITO = 55 nm, and rear TCO (ITO or CZO) = 100 nm. QWOT CdS values are 105 nm for CdTe, 95 nm for $C_{0.6}Z_{0.4}T$, and 65 nm for ZnTe top cells.*

Table 8 The MAPC (mA/cm^2) of the top and rear cells for the optimized normal design, with CdS and $Mg_{0.23}Zn_{0.77}O$ ETL window layers, and the ITO and CZO rear TCO layers and the proposed inverted design. CdS QWOT thicknesses are 105, 90, and 65 nm for CdTe, $C_{0.6}Z_{0.4}T$, and ZnTe, respectively; 110 nm MgF_2 is used as an anti-reflective coating (ARC). Thicknesses of top cell absorber and rear TCO are set to 3 µm and 80 nm, respectively.

Cell Structure TL/Thickness Rear TCO	Normal CdS/50 nm ITO	Normal CdS/QWOT ITO	Normal MZO/50 nm ITO	Normal MZO/50 nm CZO	Inverted CdS/QWOT ITO
Top Cell 1-CdTe	26.4	23.3	28.2	28.1	28.1
Rear Cell-Si	9.7	10.1	9.1	10.3	10.2
Top Cell 2-C0.6Z0.4T	18.8	16.5	20.6	20.5	20.8
Rear Cell 2-Si	16.4	16.9	15.8	17.4	16.9
Top Cell 3-ZnTe	7.3	6.6	9.1	9.1	9.7
Rear Cell 3-Si	27.1	27.3	26.5	27.4	27.3

The low transmission of the incident light to the rear cell lowers MAPCs. As the wavelength increases, the transmitted light reduces as a result of the unfavorable refractive index alignment for long wavelengths and the free carrier absorption in the front and rear ITO layers, which are caused by the high-doping concentration in the ITO. Replacing ITO with a material with a higher refractive index for long wavelengths ($\lambda > 800$ nm) and lower free carrier concentration can efficiently reduce this parasitic loss without any optical trade-off since the rear ITO acts parasitic for the rear cell and does not change the top cell MAPC. $Cd_{0.9}Zn_{0.1}O$ (CZO), for instance, meets both criteria, with its higher refractive index of ~2.12 for $\lambda > 800$ nm and a smaller extinction coefficient for the same region compared to ITO. Figure 83 shows the absorption spectra of the selected top cell absorbers with the MZO ETL and CZO rear TCO. Evidently, the absorption spectra of the rear cell in both cases improve significantly. This is attributed to the optically well-aligned refractive index profile and diminished parasitic absorption within the CZO layer. The combined utilization of MZO and CZO in place of CdS and ITO can lead to 1.77 mA/cm^2 greater MAPC in the rear cell.

5.2.2. **Electrical Simulations**

Table 9 presents device simulation results for the normal configuration with 55 nm front ITO, 50 nm CdS ETL, and 3 µm $C_{1-x}Z_xT$, as a function of the Zn ratio. The optically-simulated spatial photoelectron generation profile, which is calculated in the optical calculation section, is employed in the electrical simulations. To match the loss mechanisms happening in the practical devices within a polycrystalline absorber based solar cell, defect mechanisms are modeled in electrical simulations, such as surface and bulk recombinations in the top cell absorber and transport layers in agreement with experimental results.[10–12] A lifetime of 10 ns is assumed for MZO and CdS ETL. The minority carrier lifetime is assumed to be 5 ns in top cell absorbers, and the surface recombination velocity at the ETL/top cell absorber interface is used as 500 cm/s. Series and shunt resistances are assumed to be as 2 and 2000 Ω/cm^2, respectively. The highest tandem cell efficiency of $C_{1-x}Z_xT$ is computed with considering $x = 0.2$, as 22.9%. The top cell efficiency of 16.9% is considerably lower than the recent record for CdTe solar cells, 22.1%. The inferior performance of the top cell is caused primarily by (i) the significant parasitic absorption in the CdS layer as discussed through the optical calculations, causing a 2 mA/cm^2 MAPC loss, and (ii) the reduced V_{OC} induced by the intensified recombination because of the detrimental band alignment at the $CdS/C_{1-x}Z_xT$ interface.[104,106] More transparent ETLs, such as $Mg_xZn_{1-x}O$, and Se alloying of the CdTe absorber to reduce the bandgap towards 1.35 eV, are employed for the record efficiency cells, which improves the collected charges at short and long wavelengths, respectively. Furthermore, the band alignment between the ETL/absorber can be tailored by the Mg and Se content in the respective layers, which overcomes the interfacial recombination, thus increases the Voc. Likewise, the corresponding IBC Si cell conversion efficiency, 6.61%, is below the standard. The inferior performance is mainly caused by the weak transmittance of photons with long-wavelength to the IBC Si cell.

Table 9 Electrical and optical device simulation data for a normal top cell structure with 50 nm CdS ETL, and the corresponding IBC Si rear and tandem cell results as a function of the Zn content in $C_{1-x}Z_xT$. Series and shunt resistances are used as 2 and 2 $k\Omega/cm^2$. Minority carrier lifetime is assumed to be 5 ns in top cell absorbers and surface recombination velocity at the ETL/top cell absorber interface is taken as 500 cm/s.

$C_{1-x}Z_xT$ (x)	E_g (meV)	MAPC (mA/cm^2)	J_{SC} (mA/cm^2)	V_{OC} (mV)	FF (%)	η (%)	$J_{SC\text{-}Si}$ (mA/cm^2)	$V_{OC\text{-}Si}$ (mV)	FF_{Si} (%)	η_{Si} (%)	η_{Tandem} (%)
0	1450	26.4	23.8	902	77.8	16.9	8.35	696	82.1	4.8	21.7
0.2	1550	22.8	20.6	996	79.2	16.3	11.43	704	82.2	6.6	22.9
0.4	1700	18.8	17.2	1038	74.1	13.2	15.02	711	82.3	8.8	22.0
0.6	1860	14.4	13.0	1025	74.0	9.8	19.04	717	82.4	11.3	21.1
0.8	2040	10.2	9.2	1008	73.5	6.8	22.93	722	82.5	13.7	20.4
1	2200	7.3	6.6	991	72.5	4.8	25.65	725	82.5	15.3	20.1

Figure 84 shows the CdTe/IBC Si tandem cell efficiencies as a function of minority carrier lifetime for three different surface recombination velocities: 10, 50, and 500 cm/s. Minority carrier lifetime increased from 1 to 100 ns leads to a 0.55% efficiency improvement while 0.20% more tandem efficiency is obtained with decreasing the surface recombination velocity from 500 to 10 cm/s. However, this improvement is not a sufficient one for the CdTe/IBC Si tandem cell to exceed the IBC Si single-junction cell efficiency.

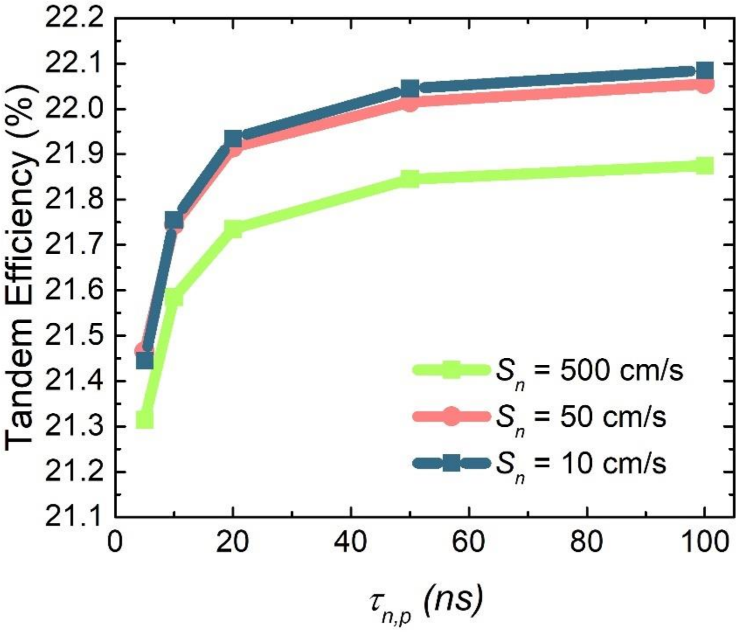

Figure 84 CdTe/IBC Si tandem efficiency as a function of lifetime for three surface recombination velocities (10, 50 and 500 cm/s) for a 3 µm CdTe absorber. CdS is used as the ETL.

Table 10 shows the device simulation results for the MZO ETL case. The same thicknesses with the previous case are used. The spatial photoelectron generation profile is optically-computed similar to the CdS ETL model. The most prominent outcome is that the highest tandem conversion efficiency becomes 24.9%, which is 2.9% higher than the CdS ETL case with the same thickness parameters. This performance improvement is exclusive for the top cell conversion efficiency as projected since the CdS layer acts parasitic solely for the top cell. for the champion cell, The V_{OC} improvement is 86 mV, which utilizes a $C_{0.6}Z_{0.4}T$ top cell absorber.

Table 10 Electrical and optical device simulation data for a normal top cell structure with 50 nm $Mg_{0.23}Zn_{0.77}O$ as ETL, and the corresponding IBC Si rear and tandem cell structures as a function of the Zn concentration in $C_{1-x}Z_xT$. Series and shunt resistances are used as 2 and 2000 Ω/cm^2. The minority carrier lifetime is assumed to be 5 ns in top cell absorbers and surface recombination velocity at the ETL/top cell absorber interface is taken as 500 cm/s.

$C_{1-x}Z_xT$ (x)	E_g (meV)	MAPC (mA/cm^2)	J_{SC} (mA/cm^2)	V_{OC} (mV)	FF (%)	η (%)	J_{SC-Si} (mA/cm^2)	V_{OC-Si} (mV)	FF_{Si} (%)	η_{Si} (%)	η_{Tandem} (%)
0	1450	28.2	25.1	904	78.7	17.9	7.9	694	82.1	4.5	22.4
0.2	1550	24.7	22.4	1000	80.7	18.1	11.0	703	82.2	6.4	24.5
0.4	1700	20.6	19.0	1124	76.1	16.3	14.6	710	82.3	8.6	24.9
0.6	1860	16.2	14.7	1136	74.7	12.5	18.7	716	82.4	11.0	23.5
0.8	2040	11.9	10.9	1122	74.4	9.1	22.6	721	82.5	13.5	22.6
1	2200	9.1	8.4	1109	73.8	6.8	25.3	724	82.5	15.1	21.9

Figure 85 shows the spectral external quantum efficiency (EQE) response of the $C_{1-x}Z_xT$ top cell for different absorber compositions and 50 nm CdS and MZO ETLs. The cut-off at the long-wavelengths that corresponds to the bandgap of the absorber layer, leads to a gradual narrowing of the response bandwidth and experiences a blue shift from ~850 nm to ~550 nm with increasing Zn content. It is seen that the MZO ETL case yields a much superior UV response compared to the CdS case since the short-wavelength response is dominated by the ETL absorption.

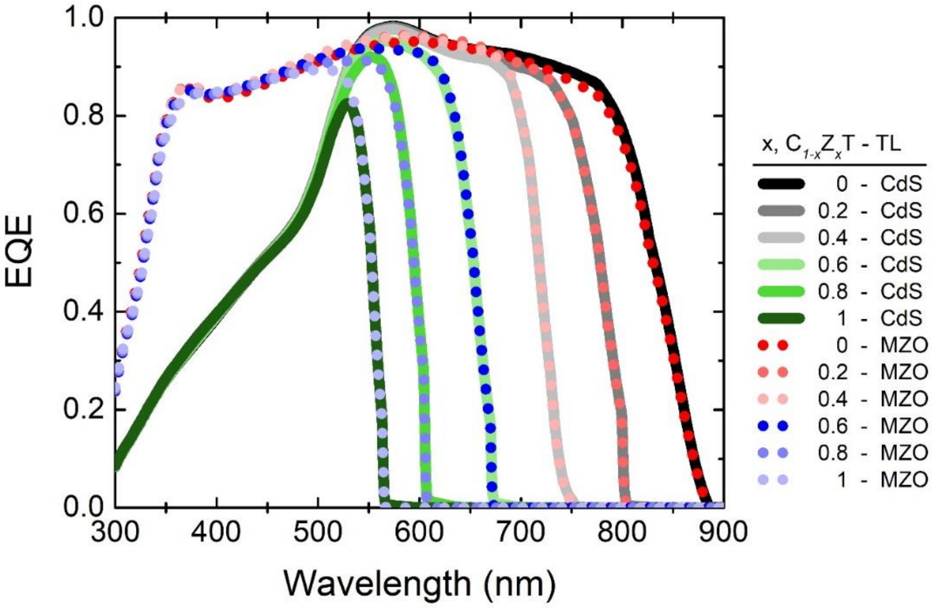

Figure 85 Calculated external quantum efficiency (EQE) spectra for the $C_{1-x}Z_xT$ top cell as a function of the absorber composition (x = 0, 0.2, 0.4, 0.6, 0.8, and 1) at 3 µm thickness with 50 nm ETL of CdS and MZO.

Figure 86 illustrates the effect of the absorber thickness on the EQE spectrum for the $C_{0.6}Z_{0.4}T$ absorber. The response at the wavelengths longer than 500 nm becomes weaker with decreasing the thickness, in particular at 1 µm thickness, triggering considerable photocurrent losses.

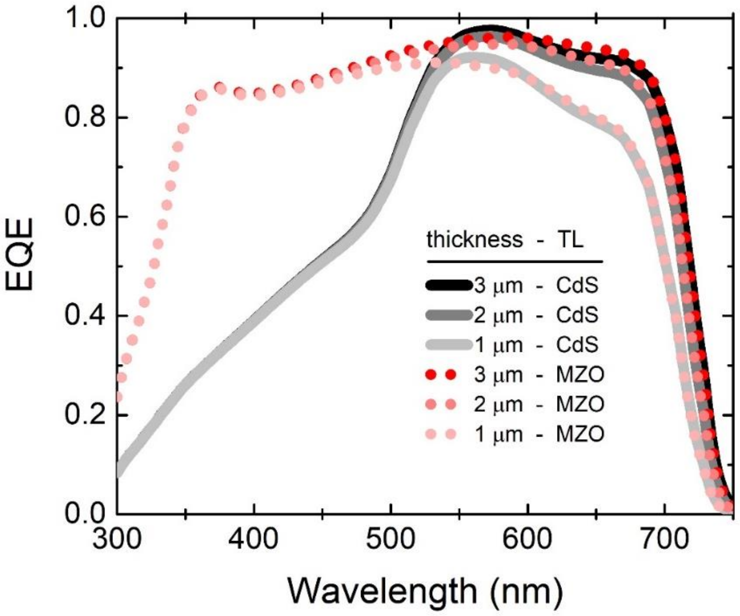

Figure 86 Calculated external quantum efficiency (EQE) spectra for the $C_{1-x}Z_xT$ top cell as a function of the absorber thickness (1, 2, and 3 μm) at x = 0.6 with 50 nm ETL of CdS and MZO.

Figure 87 presents the $C_{1-x}Z_xT$/IBC Si tandem cell efficiencies with different defect mechanisms and device parameters combinations, in addition to different ETL/rear TCO configurations. The single-junction efficiency of the IBC Si solar cell, 25.2% (horizontal line), is also given as a reference point. The Zn content which provides maximum tandem cell efficiency shifts from 0.2 to 0.4 with the replacement of the MZO-CdS (curves 1–6). improving defect mechanisms enhances the tandem cell efficiency while trends for maximum tandem cell efficiency does not alter. It is shown that cases that exceed the IBC Si cell single-junction efficiency have the MZO ETL, a 20 ns minority carrier lifetime and a 50 cm/s surface recombination velocity. CdTe, $C_{0.8}Z_{0.2}T$, $C_{0.6}Z_{0.4}T$, and $C_{0.4}Z_{0.6}T$ top cells can outperform the IBC Si cell with utilizing the CZO as the rear TCO, while $C_{0.8}Z_{0.2}T$ and $C_{0.6}Z_{0.4}T$ are the ones in the case of ITO as the rear TCO.

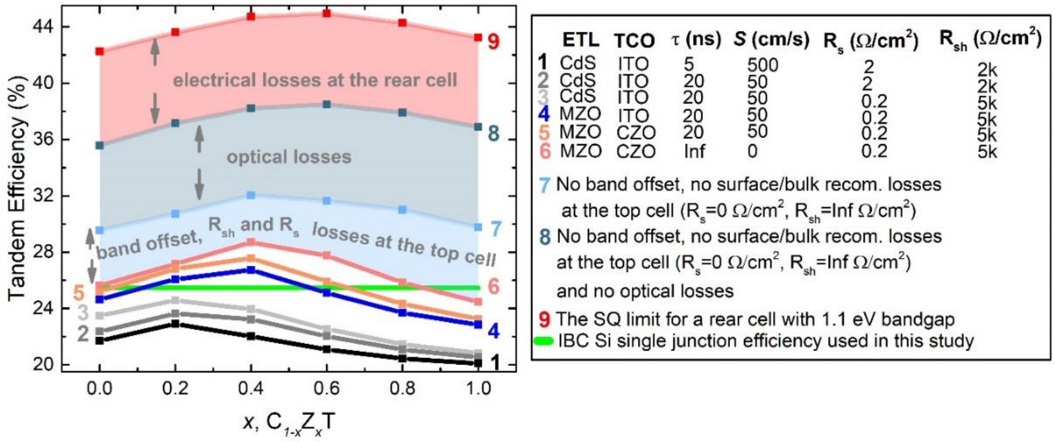

Figure 87 $C_{1-x}Z_xT$/IBC Si tandem efficiency as a function of various x values for different ETL (CdS and MZO) and rear TCO (ITO and CZO) combinations, along with different shunt-series resistances (2000–2 and 5000–0.2 Ω/cm²), minority carrier lifetimes (5 and 20 ns), and surface recombination velocities (50 and 500 cm/s): Curves 1–5. Curve 6 is the case for the eliminated bulk and surface recombination at the top cell with MZO ETL and CZO rear TCO for R_s = 0.2 and R_{sh} = 5 kΩ/cm². The single-junction efficiency of IBC Si cell, 25.2 %, is illustrated as a reference (horizontal green line). The estimated share of efficiency losses with respect to the SQ limit. Curve 7 represents the most ideal electrical case for the top cell with no series/shunt resistance losses and no energy band offset at interfaces, tailored for each absorber composition. Curve 8 represents the ideal electrical case for the top cell and eliminated optical losses, parasitic absorptions, reflection, and transmission for both cells. Curve 9 is the SQ limit for the double-junction tandem solar cell with a rear cell with 1.1 eV bandgap.

The estimated share of efficiency losses with respect to the SQ limit are also presented in Figure 87. Electrically-calculated idealized cases (curves 7 and 8) and the SQ limit (with no optical or electrical losses, curve 9) are compared. The Zn content that leads the maximum tandem cell efficiency does not change with the electrical idealization of the top cell (curve 7), while an offset performance increase is computed for both CZO and ITO as rear TCO cases. The Zn content that gives the maximum tandem cell efficiency shifts to 0.6 in the case of eliminated optical losses (curve 8). When assuming perfect energy alignment of CB and VB levels, perfect front and rear contact energy alignment and no bulk and surface defects and no series and shunt resistance limitations (curve 7), the only loss due to the top cell is the optical ones, i.e., parasitic absorption and reflection losses. The best tandem performance is computed as ~11% lower than the SQ limit. The shortage with respect to the SQ limit decreases to ~6%

when the optical losses due to the top cell are also removed (curve 8), which should account for losses due to the IBC Si rear cell.

Table 11 presents the device simulation results with an 80 nm thick CZO as a rear TCO in place of ITO, where all other parameters are kept as same. Evidently, almost 1% further conversion efficiency improvement is calculated with this replacement. As predicted, this improvement is exclusive for the IBC Si cell.

Table 11 Electrical and optical device simulation data for a normal top cell structure with 50 nm $Mg_{0.23}Zn_{0.77}O$ *as ETL and 80 nm* $Cd_{0.9}Zn_{0.1}O$ *as rear TCO, and the corresponding IBC rear and tandem cell structures as a function of the Zn content in* $C_{1-x}Z_xT$*. Series and shunt resistances are used as 2 and 2000 Ω/cm*^{2}*. Minority carrier lifetime is assumed to be 5 ns in top cell absorbers and surface recombination velocity at the ETL/top cell absorber interface is taken as 500 cm/s.*

$C_{1-x}Z_xT$ (x)	E_g (meV)	E_g (eV)	MAPC (mA/cm^2)	J_{SC} (mA/cm^2)	V_{OC} (mV)	FF (%)	η (%)	J_{SC-Si} (mA/cm^2)	V_{OC-Si} (mV)	FF_{Si} (%)	η_{Si} (%)	η_{Tandem} (%)
0	1450	1.45	28.1	25.1	904	78.7	17.9	8.9	697	82.1	5.1	23.0
0.2	1550	1.55	24.6	22.4	1000	80.7	18.1	12.3	706	82.2	7.1	25.2
0.4	1700	1.7	20.5	19.0	1124	76.1	16.2	16.0	712	82.3	9.4	25.6
0.6	1860	1.86	16.1	14.7	1136	74.7	12.5	20.0	718	82.4	11.8	24.3
0.8	2040	2.04	11.9	10.9	1121	74.4	9.1	23.6	723	82.5	14.1	23.2
1	2200	2.2	9.1	8.4	1109	73.8	6.8	25.9	725	82.5	15.5	22.3

Figure 88 presents the J–V curves of the selected $C_{1-x}Z_xT$ cases, x = 0.4 and 0.6, from Table 9 and Table 10.

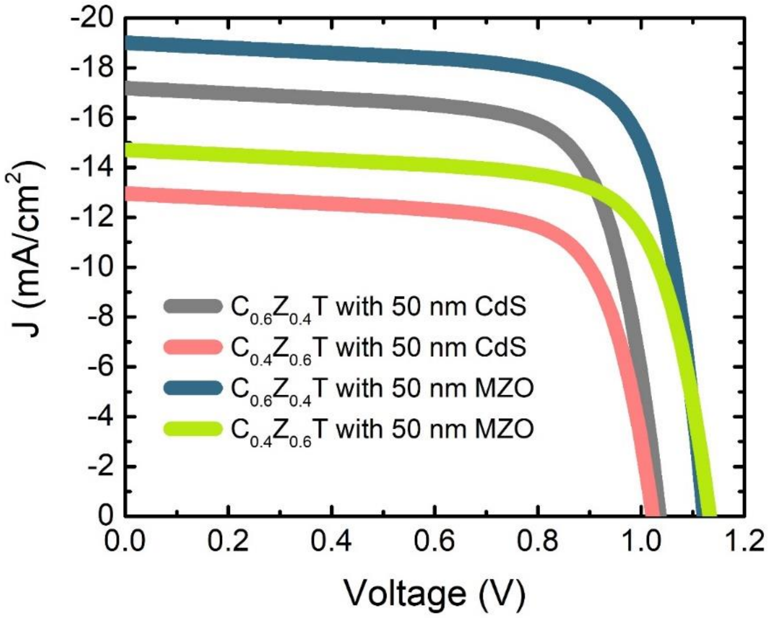

Figure 88 Top cell J-V curves of selected $C_{1-x}Z_xT$ cases (x = 0.4, 0.6) with 50 nm ETL (CdS and MZO).

The difference between the SQ limit and the electrical device simulations (Figure 87) is dominated by electrical and optical losses in the top cell as well as losses due to the rear IBC Si cell, which was not designed for a better IR response. To reduce this difference, reducing the parasitic absorption at the functional layers (TL and TCO), and reflection losses are still required. Alternatively, the utilization of a bifacial silicon solar cell can improve the efficiency, in particular, when high bifacial degrees and albedo values are achieved. Moreover, if light-trapping schemes (additional to use of the MgF_2 AR layer) can be introduced to the top cell, additional improvements in the tandem cell efficiency can be attained. For instance, the conformal fabrication of the top cell over the textured IBC Si rear cell can boost tandem efficiency through eliminated reflection losses, in particular at the near IR, and enhanced optical paths of the incident photons. The enhanced optical paths would allow the utilization of thinner active layers without an optical trade-off in the top cell, which leads to the improved optical and electrical properties, while reduced IR reflections would enhance the IBC Si rear cell absorption.

It can be seen from the outcomes of the combined optical and electrical simulations that it is possible to exceed the IBC Si single junction efficiency using a $C_{1-x}Z_xT$ top cell in tandem. c-Si solar cell is a mature technology that allows adaptability to the tandem application. The four-terminal connection has the advantages of independent fabrication and operation of subcells without the need of a tunneling (recombination) layer and current matching condition. Still, the up-to-date $C_{1-x}Z_xT$ solar cells must be reviewed to tackle feasibility and potential issues with the fabrication of high-performance $C_{1-x}Z_xT$ top cell. The $C_{1-x}Z_xT$ compositions with $x = 0.2–0.6$ are the most favorable (see Figure 87), and CdTe is less promising regarding its bandgap.

5.3. Conclusions

Integrated optical and electrical simulations are carried out to evaluate the potential and limitations of $C_{1-x}Z_xT$/c-Si tandem solar cells in the 4T structure. Cell parameters including variable absorber band gaps and transport layers in the top cell are investigated to exceed the efficiency limits.

Followings are the major outcomes:

- The usage of the CdS layer as a transparent electron transport layer in the normal top cell structure is hindered by the large extinction coefficient of CdS in the UV and visible part of the spectrum.
- Considerable top and tandem cell efficiency enhancements are obtained with the application of MZO instead of CdS. J_{SC} and V_{OC} enhancements are provided by smaller and less dispersed extinction coefficient and the favorable energy level alignment. Hitherto, there are still areas for continued development. For example, replacing MZO with a higher refractive index material, where MZO has a refractive index (n) of ~1.9 in the UV–visible regions, can considerably increase the MAPC of the top cell.
- it is manifested that the optical performance of the tandem cell can be improved by reversing the fabrication sequence while utilizing an intrinsic top cell absorber instead of the substitution of the CdS ETL. the proposed inverted

configuration mainly benefits from (i) the eradicated CdS parasitic absorption in the top cell and (ii) more pronounced enhancements of the MAPC of IBC Si cell caused by the interferences taking place within the CdS layer.

- Transparent conducting electrodes (TCEs) with higher IR transparency should be used to increase the MAPC of IBC Si cell. For example, $Cd_{0.9}Zn_{0.1}O$ is proposed regarding its higher IR transparency in place of the rear ITO to demonstrate the effect. A smoother transition towards the rear cell, and consequently 4.33% higher tandem efficiency is achievable result of the higher refractive index of $Cd_{0.9}Zn_{0.1}O$.

The front and rear ITO or the front ITO and CdS ETL, in terms of MAPC of the $C_{1-x}Z_xT$ cell, are optically independent from each other. A declining trend with the thickness of the front ITO is obtained for the MAPC of IBC Si cell, regarding the more pronounced reflection and free-carrier absorption. MAPC shows local maxima around the distinct CdS thickness satisfying the QWOT values at a wavelength corresponding to the absorption onset of the top cell absorber. The parasitic absorption of the CdS layer can be eliminated with the proposed inverted configuration. Moreover, CdS can function as an anti-reflective coating without any parasitic absorption since it has zero extinction coefficient for the interested part of the spectrum for the IBC Si cell. Rear ITO does not affect the MAPC of the $C_{1-x}Z_xT$ cell while it behaves as a parasitic absorber for the IBC Si cell. MAPC of the rear and tandem cells can be improved considerably by employing a TCO with a higher refractive index and lower extinction coefficient at the long wavelengths. Overall, this chapter heralds the high-efficiency CZT/c-Si tandem solar cells.

CHAPTER 6

CONCLUSIONS AND FUTURE LOOKS

In this thesis, various light management methods are discussed for thin-film, silicon, and tandem solar cells, accordingly, beneficial guidelines for optical optimizations are provided. The vertical-cavity approach is employed for thin-film solar cells. Textured front and rear surfaces combined with a scattering medium in the light trapping framework are employed to design the silicon solar cells. Finally, a combination of surface texturing and vertical-cavity approach is employed to study tandem solar cells. Moreover, in order to enhance the photocurrent of solar cells, general guidelines and formulas are developed and supplementary analytical discussions are provided in a material independent approach which is also presentable for current and future studies.

A two-step optimization methodology is presented to improve computational efficiency with engineering the anti-reflection trends of front layers atop a semi-infinite absorber and later carefully adjusting the refractive index and thickness of each layer to improve absorption. This methodology provides a better understanding and control of light management mechanisms based on the vertical-cavity approach within thin-film solar cells. Simple analytical equations for reflection in a multi-layered structure are provided to present a material-independent approach. A good agreement with simulation and developed analytical equations are demonstrated. Since FTL can also serve as an anti-reflection coating and considering the broad range of availability of different FTL materials, a generalized refractive index and thickness guideline independent of material is developed for thin-film solar cells. Three distinct MAPC behaviors are computed as a function of thickness and refractive index. For the thin FTL region, high MAPC values can be achievable irrespective of the refractive index of the FTL. It is recommended to use this region when an FTL with an unfavorable refractive index spectrum is employed. In the second region, irrespective of the FTL thickness, high MAPCs are computed within an optimum refractive index window. Lastly, alternating high and low MAPCs are found which are extremely sensitive to the refractive index and thickness of the FTL. The values of optimum thickness and index ranges are discussed in the light of provided analytical equations and for various thin-film solar cell technologies. The proposed methodology is also demonstrated to be useful for PTB7:PCBM based organic and CdTe solar cells.

Practical FTL materials, PEDOT:PSS, $TiO_{2,}$ and NiO_x are discussed in detail for perovskite solar cells within the presented distinct MAPC regions. Individual optimization criteria are presented for each FTL material. Furthermore, semi-empirical equations for predictions of FTL, perovskite, and RTL thicknesses to replace full optical simulations are demonstrated. Guidelines developed in this thesis are experimentally validated for MAPI type perovskites. The effects of different TCOs and perovskites are also discussed theoretically and high accuracy with predictions is obtained. Optimum thicknesses of RTL, FTL, and perovskite layers are predicted with a high accuracy using the 3-level decision algorithm. While required inputs are as simple as the refractive indices of FTL and perovskite at two distinct wavelengths and refractive index of RTL at a single wavelength. Considering the lack of availability of optical simulation or characterization tools, the 3-level decision algorithm is expected to support and boost experimental researches due to its ease of use, practicality, material independence, and high precision.

Optical optimizations show that it is possible to achieve more than 2 mA/cm^2 MAPC improvements with PTB7:PCBM organic solar cells compared to widely used designs. Two different thickness options are investigated to present alternative solutions while taking fabrication and electron transport challenges into account. Typically, the thinner option is superior regarding the suppressed bulk recombinations. However, for some instances, this range can be impractical such as coating quality or thickness limitations. In addition to that, two ITO thickness options are provided to address low-sheet resistance requirements if needed.

Optoelectronic effects of TCOs are also discussed. It is shown that a 50 nm-thick ITO presents superior optical transparency and anti-reflective behavior, and its relatively higher sheet resistance can be tolerated with proper cell dimensions. Up to 5x5 mm^2 cell areas, 50 nm-thick ITO present higher efficiency than 150 and 250 nm thick ITO layers for a lab-scale device. For the industry-type solar cells with a metal grid, 50 nm-thick ITO is a better choice up to 4 mm finger openings. It is possible to achieve more than 1% efficiency increase with this optimization compared to the 150 nm-thick ITO which is the most widely used value among the literature.[78] For larger sized solar cells either it is a lab- or an industry-type, 250 nm-thick ITO is recommended instead of the one with 150 nm thickness. Although ITO is investigated as a case study, the optoelectronic discussions can be extended to other TCO materials.

For silicon solar cells, aerogel is introduced as an RR layer. Considering its low refractive index, ease of fabrication, compatibility with silicon solar cells, and high rear reflection, it is a superior alternative to the state-of-the-art SiN_x RR layers. It is demonstrated that the solution to surpass SiN_x RR layers is by introducing a planarization layer between metal and aerogel layers to block metal interdiffusion and establish a planar metal interface. The aerogel RR is the most efficient when screen-printed Al is used as the metal. A 10% more rear reflection can be achieved compared to the SiN_x RR layer. Testing aerogel in standard silicon fabrication can be realized as a part of future studies. For these computations, a hybrid optical simulation environment is developed including a combination of FDTD, TMM, and ray-tracing method. Absorption, reflection, and transmission, and as well as loss mechanisms within a randomly textured silicon solar cell are quantized. Results are validated with experimental measurements. Developed simulation setup can be applied to multi-junction solar cells without any computational constraints.

$C_{1-x}Z_xT$/c-Si tandem solar cells are optimized using a combination of electrical and optical simulations. Optical loss mechanisms are elucidated and addressed with various approaches such as replacing with alternative materials and changing the fabrication order. CdS substantially limits $C_{1-x}Z_xT$ solar cell performance both electrically and optically. One way of dealing with its optical losses is by using CdS layer as thin as possible to suppress its parasitic absorption. However, this solution depends on various parameters such as fabrication limitations, deposition quality, and $C_{1-x}Z_xT$ crystallinity. As an alternative way, we propose an inverted fabrication order which can result in simultaneous improvement of the absorption of both cells. This can be generalized to different rear cells when they are coupled with $C_{1-x}Z_xT$ top cells in tandem configuration. With careful adjustment of CdS thickness (or other FTLs), its anti-reflection effect can be tailored to meet their absorption spectra. However, the band offset induced electrical losses should still be addressed for both solutions based on employing CdS. MZO replacement of CdS is becoming popular among researchers. Its considerably smaller and less dispersed extinction coefficient and favorable energy level alignment address optical and electrical losses caused by employing CdS, and it can enable superior $C_{1-x}Z_xT$ cells. CZO with its higher refractive index and lower free-carrier absorption in the IR part of the spectrum compared to ITO as an alternative material of rear TCO is investigated. The tandem efficiency is improved with employing the CZO and MZO up to 4.33%. CZO is selected as of being a Cd compound which can alleviate the fabrication constraints, however, guidelines can be generalized for other IR transparent TCEs. The optimum bandgap of $C_{1-x}Z_xT$ in the tandem configuration is elucidated by varying Zn content in terms of optical and electrical losses, and the SQ limit. Optimum Zn content is found as 0.2 when CdS and ITO are used, and it shifts to 0.4 with MZO and CZO replacements. It is shown that the optimum Zn content does not vary with improving device parameters. When optical losses are completely eliminated, the optimum Zn content is found to be 0.6 in agreement with the SQ limit. Hence, two mature solar cell technologies, silicon, and CdTe, are integrated in a tandem environment with careful optical/electrical optimization to surpass the single-junction efficiency of recent best-performing silicon solar cells. Even though calculated tandem cell efficiencies are not as attractive as recently documented efficiencies of perovskite/c-Si tandem cells,[107] it should be noted that CdTe and silicon solar cells have robust stability and a long lifetime.

Light trapping in tandem solar cells by texturing the top cell and the use of a conformally coated top cell following the silicon surface can be considered. Both solutions can yield enhancements in the absorptions of both cells. Moreover, bifacial silicon solar cells can be utilized to enhance the overall efficiency when high albedo and bifacial degrees are achieved. Narrower band absorbers can be combined with $C_{1-x}Z_xT$ and silicon for multi-junction cells which can improve the UV response of overall tandem structure where $C_{1-x}Z_xT$ has a relatively poor response. Silicon solar cells with a better IR response irrespective of its UV-visible one can be utilized in place of high-performance silicon solar cells. It can reduce the cost of tandem configuration while improving overall efficiency if a better IR response is obtained. Fabrication of high-efficiency $C_{1-x}Z_xT$ with CZO and MZO can be realized in the light of provided optimization recipes presented here in this work by deposition of high-quality $C_{1-x}Z_xT$ layer.

REFERENCES

1. National Geophysical Data Center. U.S. standard atmosphere (1976). *Planetary and Space Science* (1992) doi:10.1016/0032-0633(92)90203-Z.
2. Chapin, D. M., Fuller, C. S. & Pearson, G. L. A new silicon p-n junction photocell for converting solar radiation into electrical power. *Journal of Applied Physics* (1954) doi:10.1063/1.1721711.
3. Research Cell Record Efficiency Chart. https://www.nrel.gov/pv/assets/images/efficiency-chart.png.
4. Würfel, P. *Physics of Solar Cells: From Principles to New Concepts*. *Physics of Solar Cells: From Principles to New Concepts* (2007). doi:10.1002/9783527618545.
5. Shockley, W. & Queisser, H. J. Detailed balance limit of efficiency of p-n junction solar cells. *J. Appl. Phys.* (1961) doi:10.1063/1.1736034.
6. Fresnel, A. Mémoire sur la Diffraction de la Lumière. *Verdet al., op. cit.(12), i* (1818).
7. Koç, M., Soltanpoor, W., Bektaş, G., Bolink, H. J. & Yerci, S. Guideline for Optical Optimization of Planar Perovskite Solar Cells. *Adv. Opt. Mater.* (2019) doi:10.1002/adom.201900944.
8. Koc, M., Kartopu, G. & Yerci, S. Combined Optical-Electrical Optimization of Cd1−xZnxTe/Silicon Tandem Solar Cells. *Materials (Basel).* (2020) doi:10.3390/ma13081860.
9. Chen, C.-W. *et al.* Optical properties of organometal halide perovskite thin films and general device structure design rules for perovskite single and tandem solar cells. *J. Mater. Chem. A* **3**, 9152–9159 (2015).
10. Kartopu, G. *et al.* Photovoltaic performance of CdS/CdTe junctions on ZnO nanorod arrays. *Sol. Energy Mater. Sol. Cells* (2018) doi:10.1016/j.solmat.2017.11.036.
11. Kartopu, G. *et al.* Progression of metalorganic chemical vapour-deposited CdTe thin-film PV devices towards modules. *Prog. Photovoltaics Res. Appl.* (2016) doi:10.1002/pip.2668.
12. Kartopu, G. *et al.* Enhancement of the photocurrent and efficiency of CdTe solar cells suppressing the front contact reflection using a highly-resistive ZnO buffer layer. *Sol. Energy Mater. Sol. Cells* (2019) doi:10.1016/j.solmat.2018.11.002.

13. Born, M. & Wolf, E. *Principles of Optics Electromagnetic Theory of Propagation INterference and Diffraction of Light 2nd edition by Max Born Emil Wolf New York NY Pergamon Press 1964* (1999).

14. Pedrotti, F. L., Pedrotti, L. M. & Pedrotti, L. S. *Introduction to Optics*. *Introduction to Optics* (2017). doi:10.1017/9781108552493.

15. Yee, K. S. Numerical Solution of Initial Boundary Value Problems Involving Maxwell's Equations in Isotropic Media. *IEEE Transactions on Antennas and Propagation* (1966) doi:10.1109/TAP.1966.1138693.

16. FDTD from LUMERICAL Tools. https://www.lumerical.com/tcad-products/fdtd/.

17. Burgelman, M., Nollet, P. & Degrave, S. Modelling polycrystalline semiconductor solar cells. *Thin Solid Films* (2000) doi:10.1016/S0040-6090(99)00825-1.

18. Arfken, G. & Mathews, J. Mathematical Methods for Physicists. *Am. J. Phys.* (1972) doi:10.1119/1.1988084.

19. Malitson, I. H. Interspecimen Comparison of the Refractive Index of Fused Silica*,†. *J. Opt. Soc. Am.* **55**, 1205 (1965).

20. Siefke, T. *et al.* Materials Pushing the Application Limits of Wire Grid Polarizers further into the Deep Ultraviolet Spectral Range. *Adv. Opt. Mater.* (2016) doi:10.1002/adom.201600250.

21. Palik, E. D. *Handbook of optical constants of solids*. *Handbook of Optical Constants of Solids* (2012). doi:10.1016/C2009-0-20920-2.

22. Hedley, G. J. *et al.* Determining the optimum morphology in high-performance polymer-fullerene organic photovoltaic cells. *Nat. Commun.* (2013) doi:10.1038/ncomms3867.

23. Alomairy, S. E. *et al.* Morphological and optical characterization of Mg-ZnO thin films deposited by co-magnetron sputtering technique. *Dig. J. Nanomater. Biostructures* (2017).

24. Paulson, P. D., McCandless, B. E. & Birkmire, R. W. Optical properties of Cd 1-xZn xTe films in a device structure using variable angle spectroscopic ellipsometry. *J. Appl. Phys.* (2004) doi:10.1063/1.1646437.

25. Vogt, M. R. *et al.* Optical Constants of UV Transparent EVA and the Impact on the PV Module Output Power under Realistic Irradiation. in *Energy Procedia* (2016). doi:10.1016/j.egypro.2016.07.136.

26. Aguilar, O., de Castro, S., Godoy, M. P. F. & Rebello Sousa Dias, M. Optoelectronic characterization of Zn 1-x Cd x O thin films as an alternative to

photonic crystals in organic solar cells . *Opt. Mater. Express* (2019) doi:10.1364/ome.9.003638.

27. Koirala, P. *et al.* Through-the-glass spectroscopic ellipsometry for analysis of CdTe thin-film solar cells in the superstrate configuration. *Prog. Photovoltaics Res. Appl.* (2016) doi:10.1002/pip.2759.

28. Jackson, J. D. Jackson - Classical Electrodynamics. *John wiley & sons* (1962) doi:10.1119/1.19136.

29. Fujiwara, H. *Spectroscopic Ellipsometry: Principles and Applications*. *Spectroscopic Ellipsometry: Principles and Applications* (2007). doi:10.1002/9780470060193.

30. Tauc, J., Grigorovici, R. & Vancu, A. Optical Properties and Electronic Structure of Amorphous Germanium. *Phys. status solidi* (1966) doi:10.1002/pssb.19660150224.

31. Boor, C. de. *A Practical Guide to Splines - Revised Edition*. *Springer-Verlag, New York* (2001).

32. Jellison, G. E. & Modine, F. A. Parameterization of the optical functions of amorphous materials in the interband region. *Appl. Phys. Lett.* (1996) doi:10.1063/1.118064.

33. Abdellaoui, T., Bennaceur, J. & Chtourou, R. Effect of nanostructured porous n GaAs substrates on the energy band gap of nanocrystalline TiO2 thin films analyzed by spectroscopic ellipsometry. *Phys. E Low-Dimensional Syst. Nanostructures* (2010) doi:10.1016/j.physe.2010.07.014.

34. Forouhi, A. R. & Bloomer, I. Optical dispersion relations for amorphous semiconductors and amorphous dielectrics. *Phys. Rev. B* (1986) doi:10.1103/PhysRevB.34.7018.

35. Forouhi, A. R. & Bloomer, I. Optical properties of crystalline semiconductors and dielectrics. *Phys. Rev. B* (1988) doi:10.1103/PhysRevB.38.1865.

36. Pérez-Del-Rey, D., Boix, P. P., Sessolo, M., Hadipour, A. & Bolink, H. J. Interfacial Modification for High-Efficiency Vapor-Phase-Deposited Perovskite Solar Cells Based on a Metal Oxide Buffer Layer. *J. Phys. Chem. Lett.* (2018) doi:10.1021/acs.jpclett.7b03361.

37. Green, M. A., Ho-Baillie, A. & Snaith, H. J. The emergence of perovskite solar cells. *Nat. Photonics* **8**, 506–514 (2014).

38. Yang, W. S. *et al.* Iodide management in formamidinium-lead-halide-based perovskite layers for efficient solar cells. *Science (80-.).* **356**, 1376–1379 (2017).

39. Roldán-Carmona, C. *et al.* High efficiency methylammonium lead triiodide

perovskite solar cells: The relevance of non-stoichiometric precursors. *Energy Environ. Sci.* (2015) doi:10.1039/c5ee02555a.

40. Malinkiewicz, O. *et al.* Perovskite solar cells employing organic charge-transport layers. *Nat. Photonics* **8**, 128–132 (2014).

41. Lin, Q., Armin, A., Nagiri, R. C. R., Burn, P. L. & Meredith, P. Electro-optics of perovskite solar cells. *Nat Phot.* **9**, 106–112 (2015).

42. Ball, J. M. *et al.* Optical properties and limiting photocurrent of thin-film perovskite solar cells. *Energy Environ. Sci.* **8**, 602–609 (2015).

43. Albrecht, S. *et al.* Towards optical optimization of planar monolithic perovskite / silicon-heterojunction tandem solar cells. *J. Opt.* **18**, 1–10 (2016).

44. Santbergen, R. *et al.* Minimizing optical losses in monolithic perovskite/c-Si tandem solar cells with a flat top cell. *Opt. Express* **24**, A1288 (2016).

45. Jiang, Y. *et al.* Optical analysis of perovskite/silicon tandem solar cells. *J. Mater. Chem. C* **4**, 5679–5689 (2016).

46. Grant, D. T., Catchpole, K. R., Weber, K. J. & White, T. P. Design guidelines for perovskite/silicon 2-terminal tandem solar cells: an optical study. *Opt. Express* **24**, A1454 (2016).

47. Kaminski, P. M., Isherwood, P. J. M., Womack, G. & Walls, J. M. Optical Optimization of Perovskite Solar Cell Structure for Maximum Current Collection. *Energy Procedia* **102**, 11–18 (2016).

48. Long, M. *et al.* Ultrathin efficient perovskite solar cells employing a periodic structure of a composite hole conductor for elevated plasmonic light harvesting and hole collection. *Nanoscale* **8**, 6290–6299 (2016).

49. Shalan, A. E. *et al.* Versatile plasmonic-effects at the interface of inverted perovskite solar cells. *Nanoscale* **9**, 1229–1236 (2017).

50. Shen, T., Siontas, S. & Pacifici, D. Plasmon-Enhanced Thin-Film Perovskite Solar Cells. *J. Phys. Chem. C* acs.jpcc.8b07063 (2018) doi:10.1021/acs.jpcc.8b07063.

51. Santbergen, R. *et al.* Minimizing optical losses in monolithic perovskite/c-Si tandem solar cells with a flat top cell. *Opt. Express* **24**, A1288 (2016).

52. Ramírez Quiroz, C. O. *et al.* Correction: Balancing electrical and optical losses for efficient 4-terminal Si-perovskite solar cells with solution processed percolation electrodes (Journal of Materials Chemistry A (2018) 6 (3583-3592) DOI: 10.1039/C7TA10945H). *J. Mater. Chem. A* **6**, 10149 (2018).

53. Pazos-Outón, L. M. *et al.* Photon recycling in lead iodide perovskite solar cells. *Science (80-.).* (2016) doi:10.1126/science.aaf1168.

54. Richter, J. M. *et al.* Enhancing photoluminescence yields in lead halide perovskites by photon recycling and light out-coupling. *Nat. Commun.* **7**, (2016).

55. Wang, D.-L. *et al.* Highly efficient light management for perovskite solar cells. *Sci. Rep.* **6**, 18922 (2016).

56. Wei, J. *et al.* Enhanced Light Harvesting in Perovskite Solar Cells by a Bioinspired Nanostructured Back Electrode. *Adv. Energy Mater.* **7**, 1–7 (2017).

57. Ramos, F. J. *et al.* Nanocolumnar 1-dimensional TiO $_2$ photoanodes deposited by PVD-OAD for perovskite solar cell fabrication. *J. Mater. Chem. A* **3**, 13291–13298 (2015).

58. Du, Q. G., Shen, G. & John, S. Light-trapping in perovskite solar cells. *AIP Adv.* **6**, (2016).

59. Hörantner, M. T., Zhang, W., Saliba, M., Wojciechowski, K. & Snaith, H. J. Templated microstructural growth of perovskite thin films via colloidal monolayer lithography. *Energy Environ. Sci.* **8**, 2041–2047 (2015).

60. Kang, S. M. *et al.* Moth-Eye TiO $_2$ Layer for Improving Light Harvesting Efficiency in Perovskite Solar Cells. *Small* **12**, 2443–2449 (2016).

61. Tavakoli, M. M. *et al.* Efficient, flexible and mechanically robust perovskite solar cells on inverted nanocone plastic substrates. *Nanoscale* **8**, 4276–4283 (2016).

62. Shi, B. *et al.* Enhanced light absorption of thin perovskite solar cells using textured substrates. *Sol. Energy Mater. Sol. Cells* **168**, 214–220 (2017).

63. Yang, Y. *et al.* Low-temperature solution-processed perovskite solar cells with high efficiency and flexibility. *ACS Nano* **8**, 1674–1680 (2014).

64. Ke, W. *et al.* Perovskite solar cell with an efficient TiO2compact film. *ACS Appl. Mater. Interfaces* **6**, 15959–15965 (2014).

65. Jeng, J. Y. *et al.* Nickel oxide electrode interlayer in CH3NH3PbI 3 perovskite/PCBM planar-heterojunction hybrid solar cells. *Adv. Mater.* **26**, 4107–4113 (2014).

66. Chen, C.-W. *et al.* Optical properties of organometal halide perovskite thin films and general device structure design rules for perovskite single and tandem solar cells. *J. Mater. Chem. A* **3**, 9152–9159 (2015).

67. Chiu, T. L., Mandal, H., Zhang, M., Yang, S. P. & Chuang, Y. T. Effects of anodic buffer layer in top-illuminated organic solar cell with silver electrodes. *Int. J. Photoenergy* (2013) doi:10.1155/2013/131984.

68. Momblona, C. *et al.* Efficient vacuum deposited p-i-n and n-i-p perovskite solar

cells employing doped charge transport layers. *Energy Environ. Sci.* (2016) doi:10.1039/c6ee02100j.

69. Löper, P. *et al.* Complex Refractive Index Spectra of CH $_3$ NH $_3$ PbI $_3$ Perovskite Thin Films Determined by Spectroscopic Ellipsometry and Spectrophotometry. *J. Phys. Chem. Lett.* **6**, 66–71 (2015).

70. Ziang, X. *et al.* Refractive index and extinction coefficient of CH_3NH_3PbI_3 studied by spectroscopic ellipsometry. *Opt. Mater. Express* **5**, 29 (2014).

71. Jiang, Y. *et al.* Optical analysis of perovskite/silicon tandem solar cells. *J. Mater. Chem. C* **4**, 5679–5689 (2016).

72. Ndione, P. F., Li, Z. & Zhu, K. Effects of alloying on the optical properties of organic-inorganic lead halide perovskite thin films. *J. Mater. Chem. C* (2016) doi:10.1039/c6tc02135b.

73. Xing, G. *et al.* Low-temperature solution-processed wavelength-tunable perovskites for lasing. *Nat. Mater.* **13**, 476–480 (2014).

74. Manzoor, S. *et al.* Optical modeling of wide-bandgap perovskite and perovskite/silicon tandem solar cells using complex refractive indices for arbitrary-bandgap perovskite absorbers. *Opt. Express* (2018) doi:10.1364/oe.26.027441.

75. Ompong, D., Narayan, M. & Singh, J. Optimization of photocurrent in bulk heterojunction organic solar cells using optical admittance analysis method. *J. Mater. Sci. Mater. Electron.* (2017) doi:10.1007/s10854-017-6491-8.

76. Clayton, A. J. *et al.* MOCVD of Cd (1-x)Zn (x)S/CdTe PV cells using an ultra-thin absorber layer. *Sol. Energy Mater. Sol. Cells* (2012) doi:10.1016/j.solmat.2012.02.018.

77. Li, F. *et al.* Semitransparent inverted polymer solar cells employing a sol-gel-derived TiO2 electron-selective layer on FTO and MoO3/Ag/MoO3 transparent electrode. *Nanoscale Res. Lett.* **9**, 579 (2014).

78. Zhang, H. *et al.* Improved high-efficiency perovskite planar heterojunction solar cells via incorporation of a polyelectrolyte interlayer. *Chem. Mater.* **26**, 5190–5193 (2014).

79. Chen, L.-C., Chen, J.-C., Chen, C.-C. & Wu, C.-G. Fabrication and Properties of High-Efficiency Perovskite/PCBM Organic Solar Cells. *Nanoscale Res. Lett.* **10**, 1020 (2015).

80. Chen, L.-C., Tseng, Z.-L. & Huang, J.-K. A Study of Inverted-Type Perovskite Solar Cells with Various Composition Ratios of (FAPbI3)1−x(MAPbBr3)x. *Nanomaterials* **6**, 183 (2016).

81. Xi, J. *et al.* Controlled thickness and morphology for highly efficient inverted

planar heterojunction perovskite solar cells. *Nanoscale* **7**, 10699–10707 (2015).

82. De Bastiani, M. *et al.* Ion migration and the role of preconditioning cycles in the stabilization of the J-V characteristics of inverted hybrid perovskite solar cells. *Adv. Energy Mater.* **6**, 1–9 (2016).

83. Gray, J. L. The Physics of the Solar Cell. in *Handbook of Photovoltaic Science and Engineering* (2011). doi:10.1002/9780470974704.ch3.

84. Chopra, K. L. & Das, S. R. Thin film solar cells. *Springer US* (1983) doi:10.1007/978-1-4899-0418-8.

85. Koç, M. *et al. Optoelectonic Effects of TCOs (In-preperation).*

86. Huanping, Z. *et al.* Interface engineering of highly efficient perovskite solar cells. *Science (80-.).* **345**, 542–546 (2014).

87. Ingenito, A. *et al.* Optimized back reflectors for rear diffused c-Si solar cells. in *Energy Procedia* (2014). doi:10.1016/j.egypro.2014.08.085.

88. Boccard, M. *et al.* Low-refractive-index nanoparticle interlayers to reduce parasitic absorption in metallic rear reflectors of solar cells. *Phys. Status Solidi Appl. Mater. Sci.* (2017) doi:10.1002/pssa.201700179.

89. Wakagi, M., Fujiwara, H. & Collins, R. W. Real time spectroscopic ellipsometry for characterization of the crystallization of amorphous silicon by thermal annealing. *Thin Solid Films* (1998) doi:10.1016/S0040-6090(97)00865-1.

90. Lambert, J. Photometria, sive de mensura et gradinus luminis, colorum et umbrae. *Ann. der Phys. und Chemie* (1760).

91. Phong, B. T. Illumination for Computer Generated Pictures. *Commun. ACM* (1975) doi:10.1145/360825.360839.

92. Baker-Finch, S. C., McIntosh, K. R., Yan, D., Fong, K. C. & Kho, T. C. Near-infrared free carrier absorption in heavily doped silicon. *J. Appl. Phys.* (2014) doi:10.1063/1.4893176.

93. Bryan, J. L. *et al.* Inserting a Low-Refractive-Index Dielectric Rear Reflector into PERC Cells: Challenges and Opportunities. in *Conference Record of the IEEE Photovoltaic Specialists Conference* (2019). doi:10.1109/PVSC40753.2019.8980513.

94. Green, M. A. *et al.* Solar cell efficiency tables (Version 55). *Prog. Photovoltaics Res. Appl.* (2020) doi:10.1002/pip.3228.

95. Essig, S. *et al.* Progress Towards a 30% Efficient GaInP/Si Tandem Solar Cell. in *Energy Procedia* (2015). doi:10.1016/j.egypro.2015.07.066.

96. Sahli, F. *et al.* Fully textured monolithic perovskite/silicon tandem solar cells with 25.2% power conversion efficiency. *Nat. Mater.* (2018) doi:10.1038/s41563-018-0115-4.

97. Mazzarella, L. *et al.* Infrared Light Management Using a Nanocrystalline Silicon Oxide Interlayer in Monolithic Perovskite/Silicon Heterojunction Tandem Solar Cells with Efficiency above 25%. *Adv. Energy Mater.* (2019) doi:10.1002/aenm.201803241.

98. Chen, B. *et al.* Grain Engineering for Perovskite/Silicon Monolithic Tandem Solar Cells with Efficiency of 25.4%. *Joule* (2019) doi:10.1016/j.joule.2018.10.003.

99. Jošt, M. *et al.* Textured interfaces in monolithic perovskite/silicon tandem solar cells: Advanced light management for improved efficiency and energy yield. *Energy Environ. Sci.* (2018) doi:10.1039/c8ee02469c.

100. oxford pv. https://www.oxfordpv.com/news/oxford-pv-perovskite-solar-cell-achieves-28-efficiency.

101. Essig, S. *et al.* Realization of GaInP/Si Dual-Junction Solar Cells with 29.8% 1-Sun Efficiency. *IEEE J. Photovoltaics* (2016) doi:10.1109/JPHOTOV.2016.2549746.

102. Smith, D. D. *et al.* Silicon solar cells with total area efficiency above 25 %. in *Conference Record of the IEEE Photovoltaic Specialists Conference* (2016). doi:10.1109/PVSC.2016.7750287.

103. Munshi, A. H. *et al.* Polycrystalline CdTe photovoltaics with efficiency over 18% through improved absorber passivation and current collection. *Sol. Energy Mater. Sol. Cells* (2018) doi:10.1016/j.solmat.2017.11.031.

104. Kephart, J. M. *et al.* Band alignment of front contact layers for high-efficiency CdTe solar cells. *Sol. Energy Mater. Sol. Cells* (2016) doi:10.1016/j.solmat.2016.05.050.

105. Li, D. B. *et al.* Eliminating S-Kink to Maximize the Performance of MgZnO/CdTe Solar Cells. *ACS Appl. Energy Mater.* (2019) doi:10.1021/acsaem.9b00233.

106. Chen, Y. *et al.* The Influence of Conduction Band Offset on CdTe Solar Cells. *J. Electron. Mater.* (2018) doi:10.1007/s11664-017-5850-9.

107. World Record: Efficiency of perovskite silicon tandem solar cell jumps to 29.15 per cent. https://www.helmholtz-berlin.de/pubbin/news_seite?nid=21020;sprache=en;seitenid=1.

108. Ball, J. M. *et al.* Optical properties and limiting photocurrent of thin-film perovskite solar cells. *Energy Environ. Sci.* **8**, 602–609 (2015).

109. Lin, Q., Armin, A., Nagiri, R. C. R., Burn, P. L. & Meredith, P. Electro-optics of perovskite solar cells. *Nat. Photonics* **9**, 106–112 (2014).

110. Chen, C.-W. *et al.* Optical properties of organometal halide perovskite thin films and general device structure design rules for perovskite single and tandem solar cells. *J. Mater. Chem. A* **3**, 9152–9159 (2015).

APPENDICES

A. ELLIPSOMETRY FITTINGS

The Forouhi-Bloomer oscillator model is used as a dispersion law for aerogel samples and a fit accuracy (root-mean-square error) of 98.95% is achieved. Fitted and measured tan(ψ) and cos (Δ) data of aerogel are presented in Figure 89 and Figure 90, respectively.

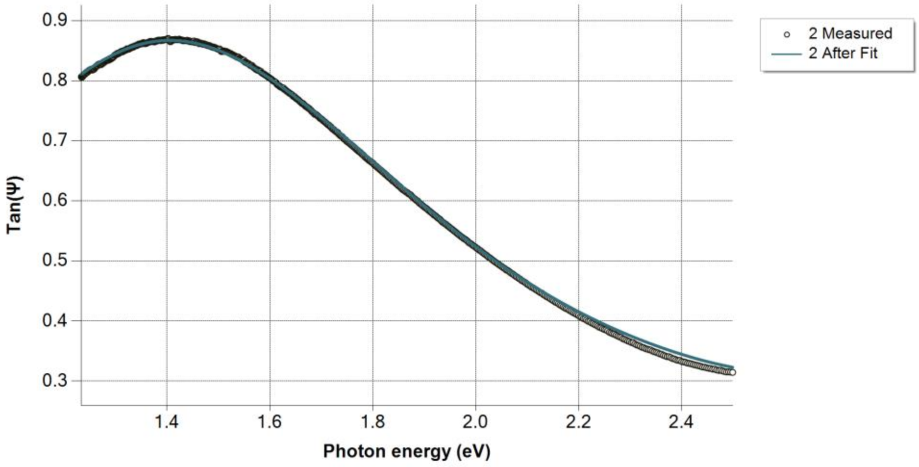

Figure 89 Fitted and measured tan (ψ) data of aerogel.

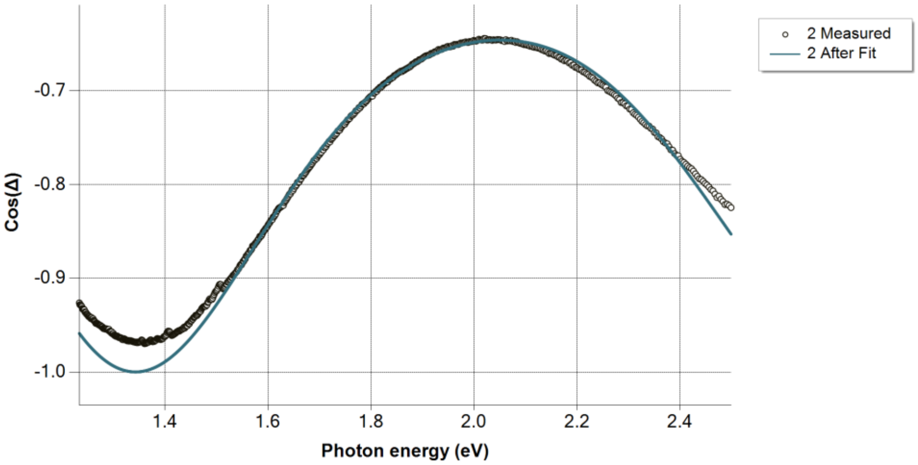

Figure 90 Fitted and measured cos (Δ) data of aerogel.

The Cauchy model is employed as a dispersion law for the spin-coated SiO_2 layer and obtaining a fit accuracy of 98.86%. Fitted and measured tan(ψ) and cos (Δ) data of SiO_2 are presented in Figure 91 and Figure 92, respectively.

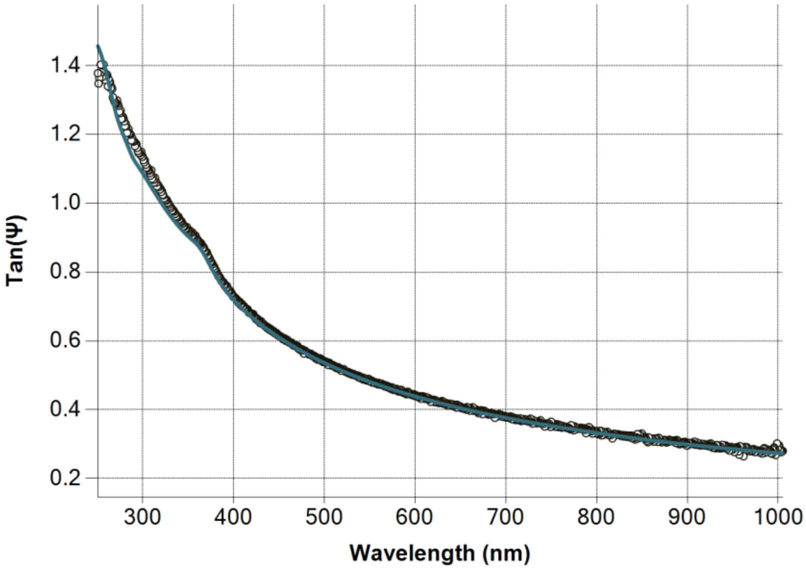

Figure 91 Fitted (line) and measured (dots) tan(ψ) data of SiO_2.

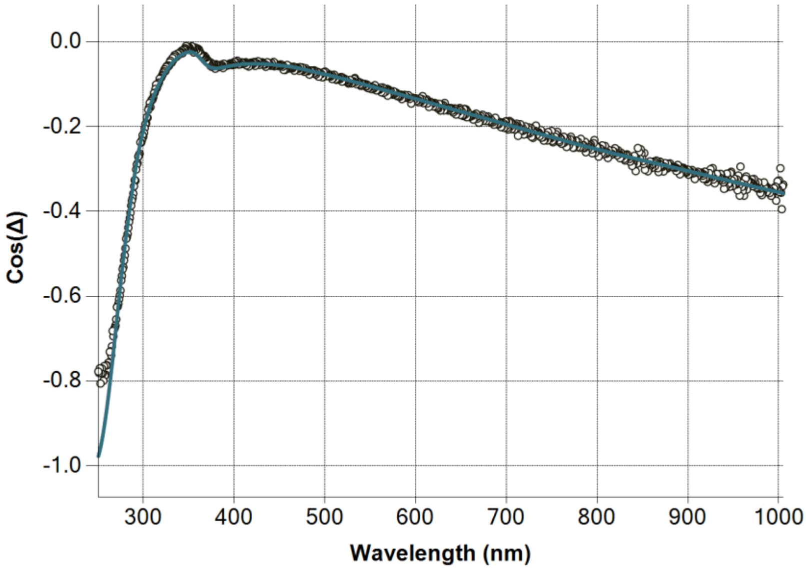

Figure 92 Fitted (line) and measured (dots) cos (Δ) data of SiO_2.

The Tauc-Lorentz model is employed as the dispersion law for the SiN_x layer and the obtained fit accuracy is 99.88%. Fitted and measured tan(ψ) and cos (Δ) data of SiN_x are presented in Figure 93 and Figure 94, respectively.

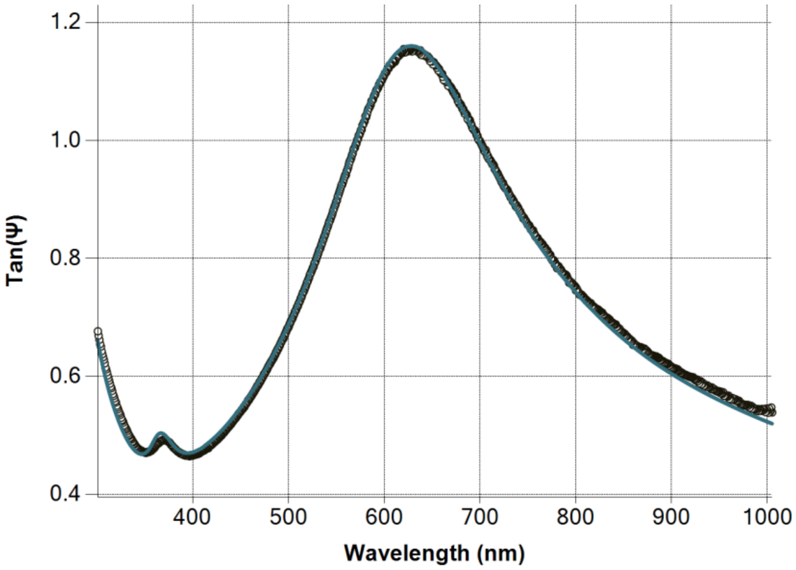

Figure 93 Fitted (line) and measured (dots) tan(ψ) data of SiN_x.

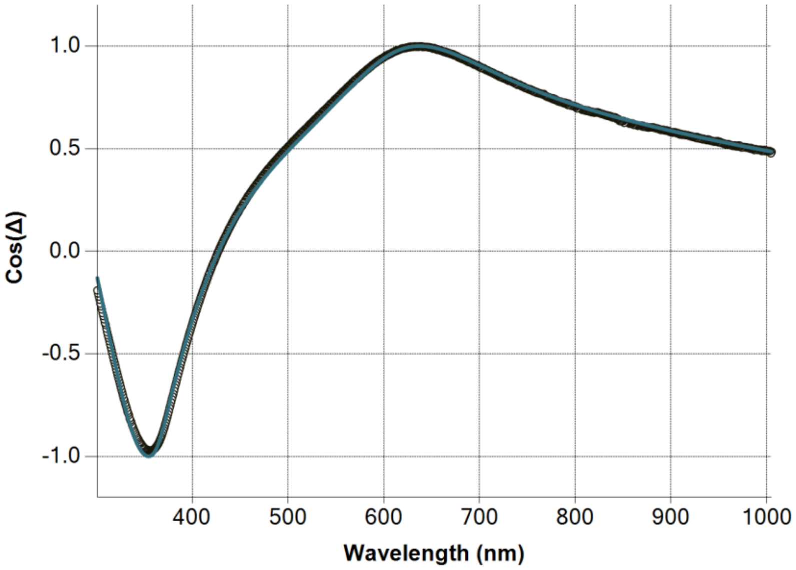

Figure 94 Fitted (line) and measured (dots) cos (Δ) data of SiN_x.

Three Forouhi-Bloomer oscillators are used to fit tan (ψ) and cos (Δ) spectra of MAPI in spectroscopic ellipsometry measurements. A fit accuracy of 98.58% is obtained. Fitted and measured tan(ψ) and cos (Δ) data for MAPI are presented in Figure 95 and Figure 96, respectively.

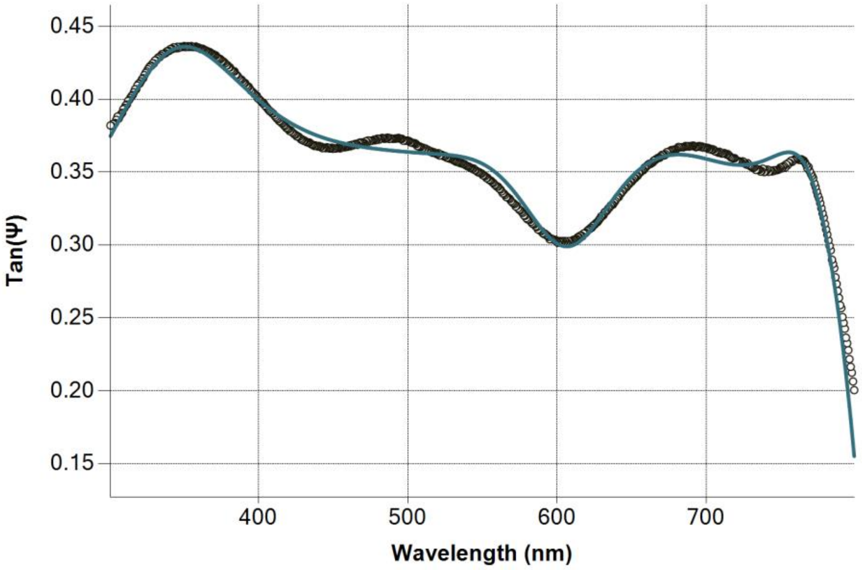

Figure 95 Fitted (line) and measured (dots) tan (ψ) data of MAPI.

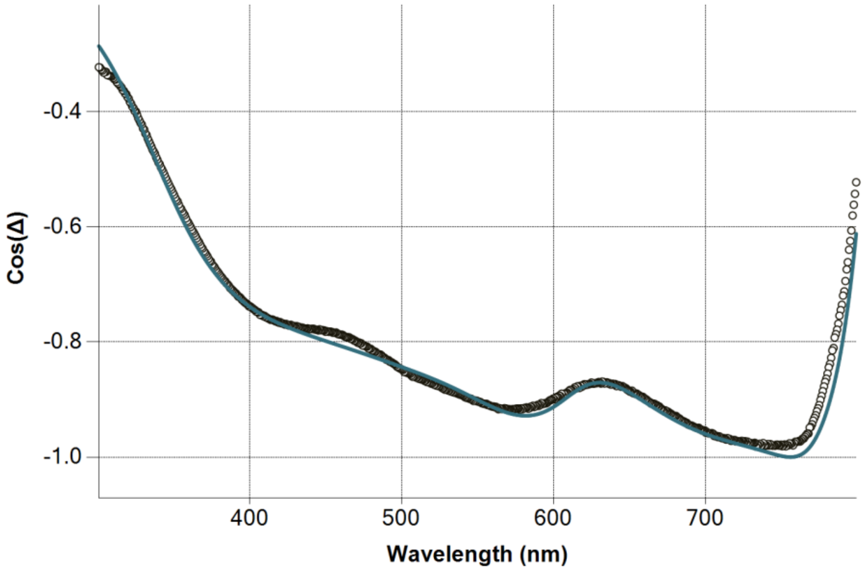

Figure 96 Fitted (line) and measured (dots) cos (Δ) data of MAPI.

The Tauc-Lorentz model is used as the dispersion law for NiO_x films. Obtained fit accuracy is 99.90%. Fit and measurement spectra of tan(ψ) and cos (Δ) values of NiO_x are presented in Figure 91 and Figure 92, respectively.

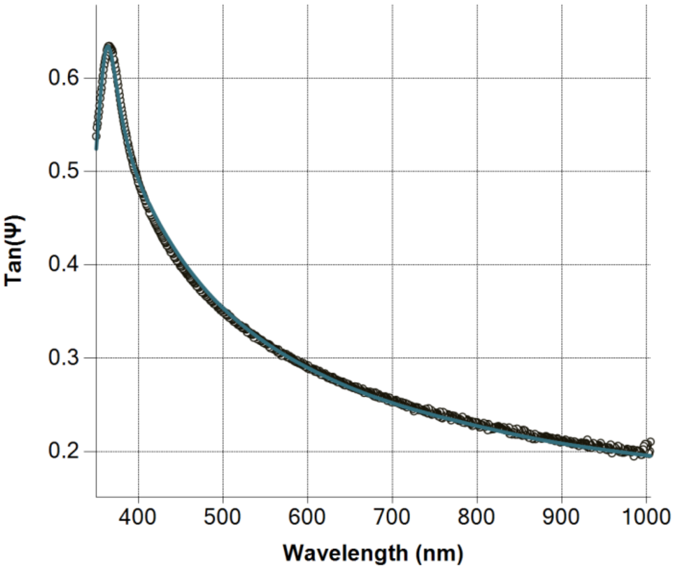

Figure 97 tan(ψ) spectra of NiO_x according to fitted dispersion law (line) and measurement (dots).

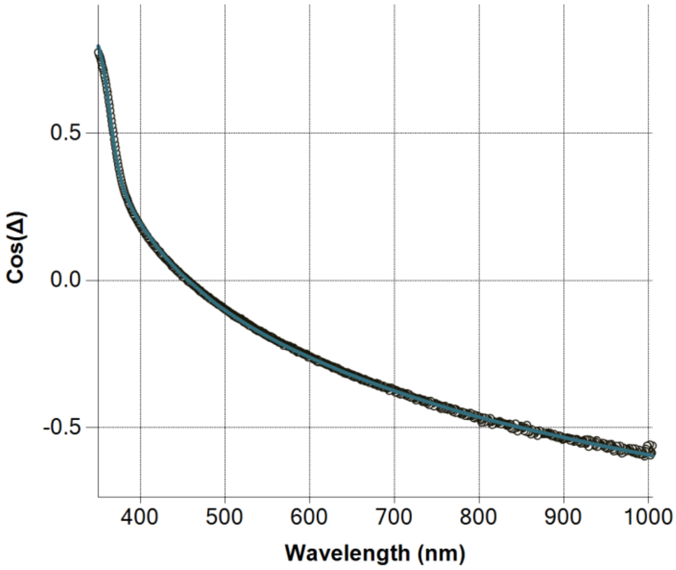

Figure 98 cos (Δ) spectra of NiO_x according to fitted dispersion law (line) and measurement (dots).

Lorentz and Drude dispersion laws are employed in ITO spectroscopic ellipsometry characterizations and fit accuracy is calculated as 98.93%. Measured and fitted tan ψ spectra are given in Figure 99. Ones corresponding to cos (Δ) are given in Figure 100.

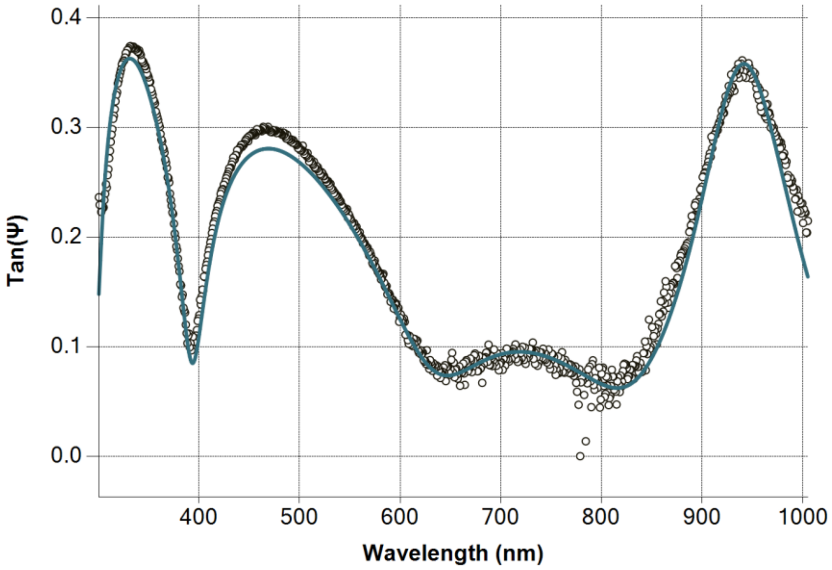

Figure 99 tan (ψ) spectra of ITO with fitted dispersion law (line) and measurement (dots).

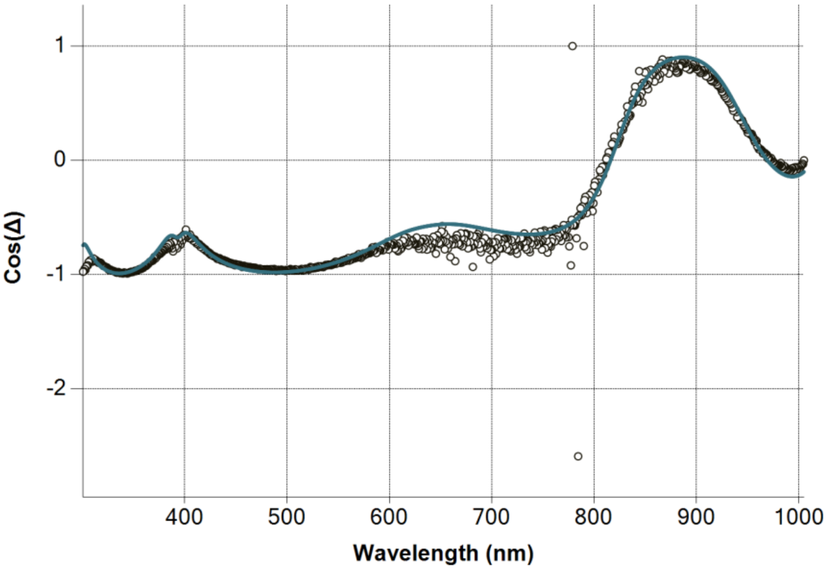

Figure 100 cos (Δ) spectra of ITO with fitted dispersion law (line) and measurement (dots).

Cauchy as the dispersion law is used to model dielectric properties of MoO_x. Fit accuracy is found as 99.07%. Measured and fitted tan (ψ) and cos (Δ) spectra are presented in Figure 101 and Figure 102, respectively.

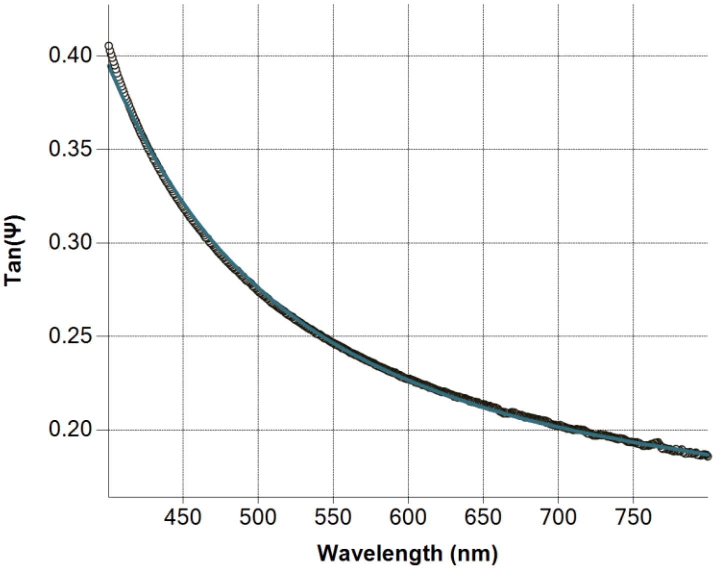

Figure 101 tan (ψ) spectra of ITO with fitted dispersion law (line) and measurement (dots).

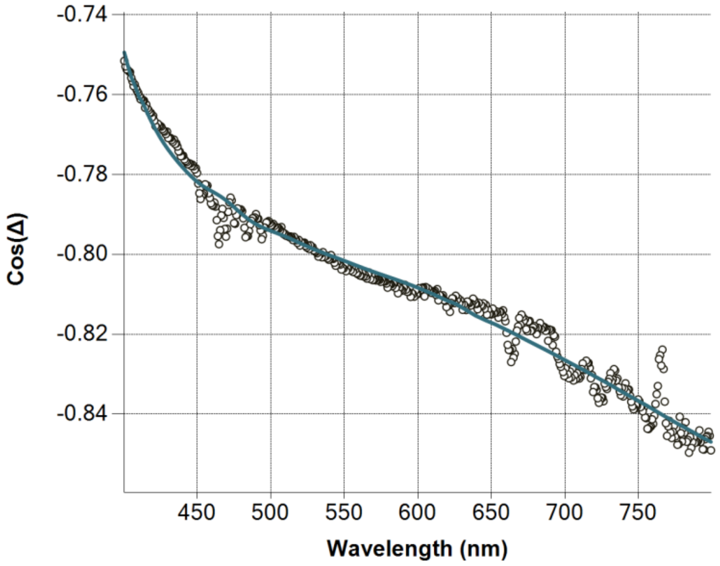

Figure 102 cos (Δ) spectra of ITO with fitted dispersion law (line) and measurement (dots).

The Cauchy dispersion law is used to model MgF_2 samples. Measured and fitted tan (ψ) and cos (Δ) spectra are manifested in Figure 103 and Figure 104, respectively. Obtained fit accuracy is 99.96%.

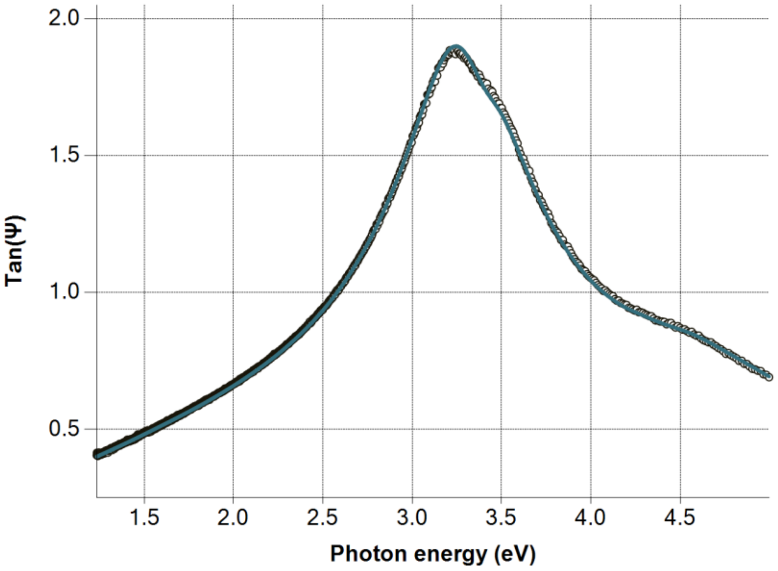

Figure 103 tan (ψ) spectra of MgF_2 with fitted dispersion law (line) and measurement (dots).

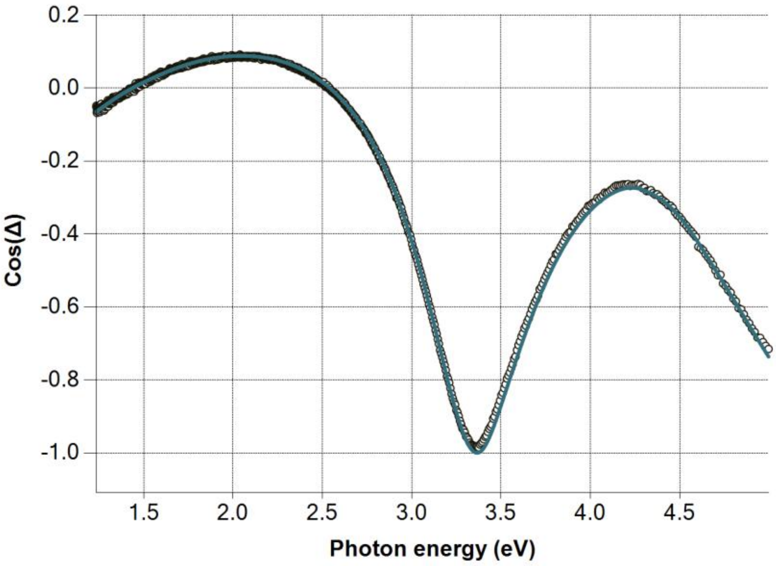

Figure 104 cos (Δ) spectra of MgF_2 with fitted dispersion law (line) and measurement (dots).

Cauchy with Urbach tail, Tauc-Lorentz, and Gauss dispersion laws are used for C_{60} with a fit accuracy of 98.05%. Measured and modelled tan (ψ) and cos (Δ) spectra are presented in

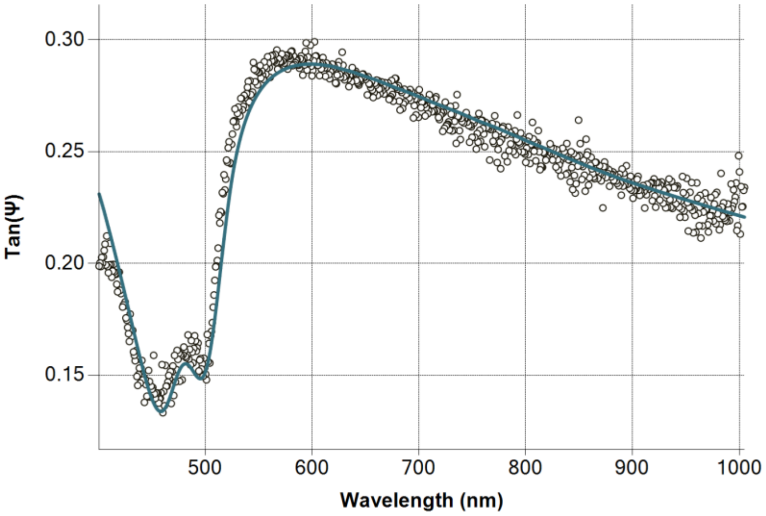

Figure 105 tan (ψ) spectra of C_{60} with fitted dispersion law (line) and measurement (dots).

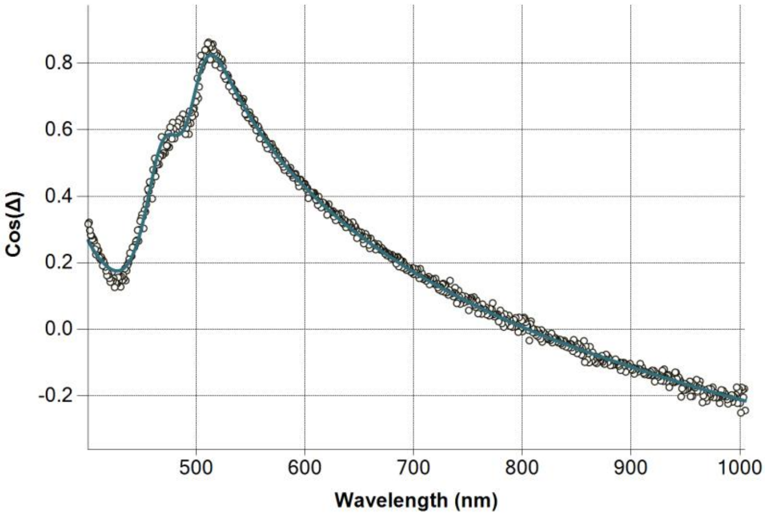

Figure 106 cos (Δ) spectra of C_{60} with fitted dispersion law (line) and measurement (dots).

B. OPTICAL CONSTANTS

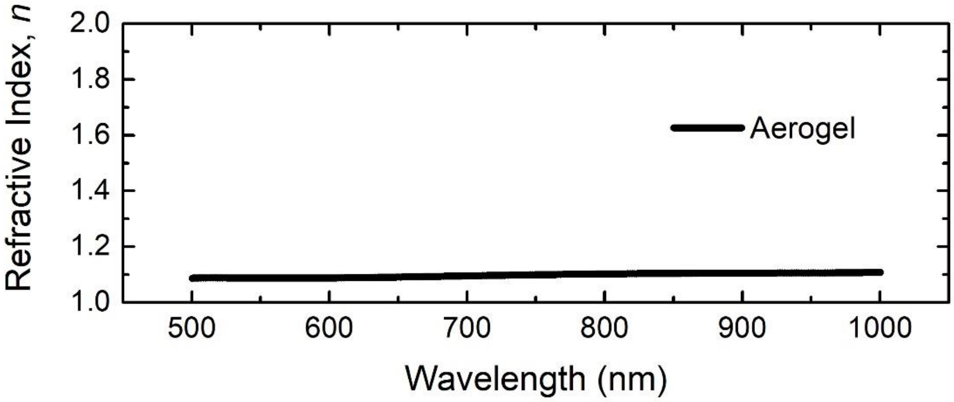

Figure 107 Measured refractive index spectra of aerogel.

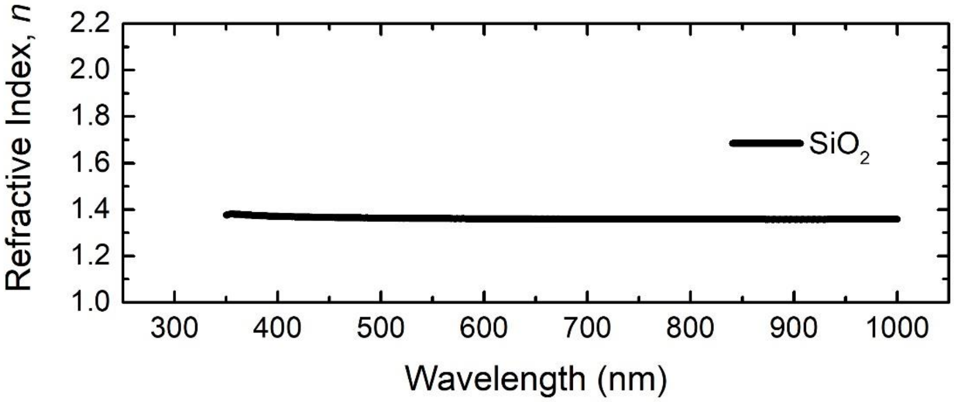

Figure 108 Measured refractive index spectra of SiO_2.

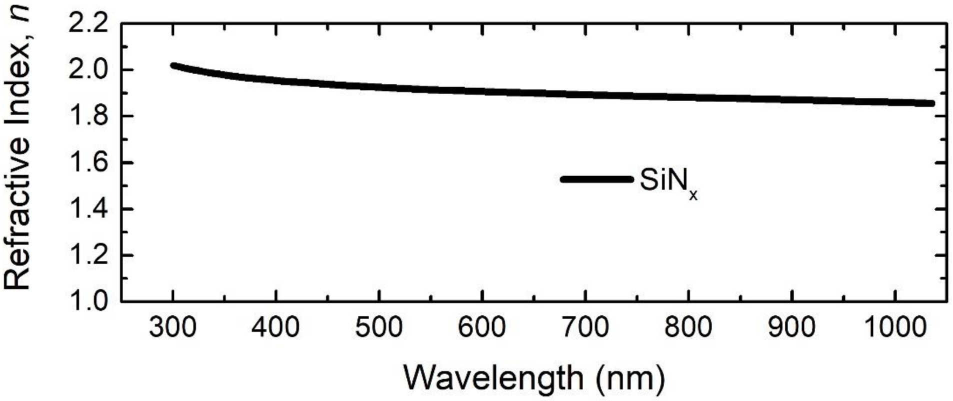

Figure 109 Measured refractive index spectra of SiN$_x$.

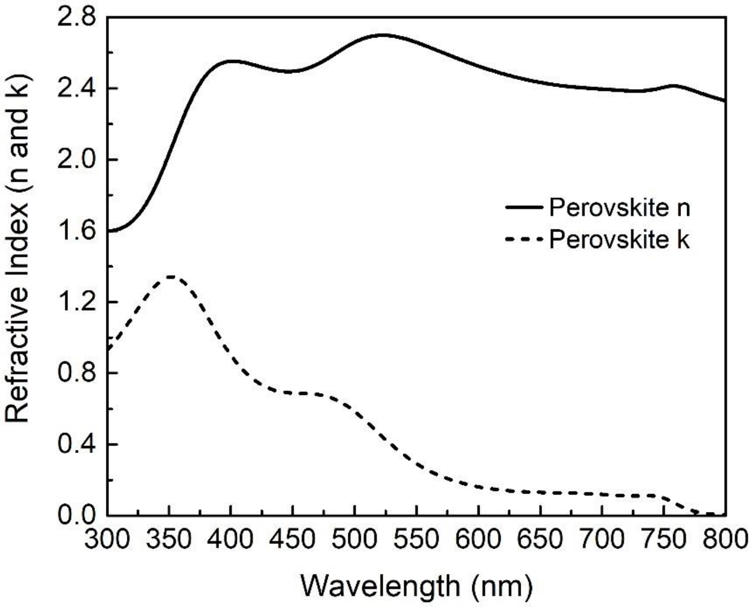

Figure 110 Measured refractive index spectra of MAPI.

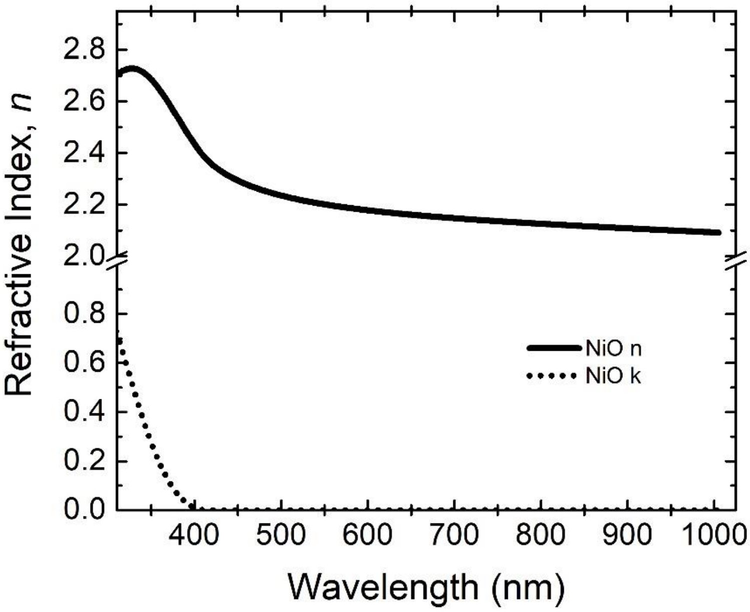

Figure 111 Measured refractive index spectra of NiO$_x$.

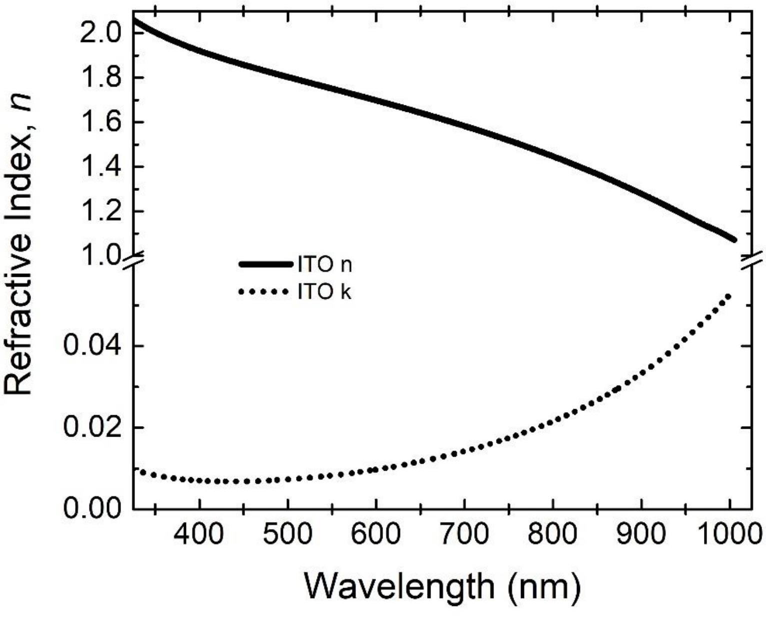

Figure 112 Measured refractive index spectra of ITO.

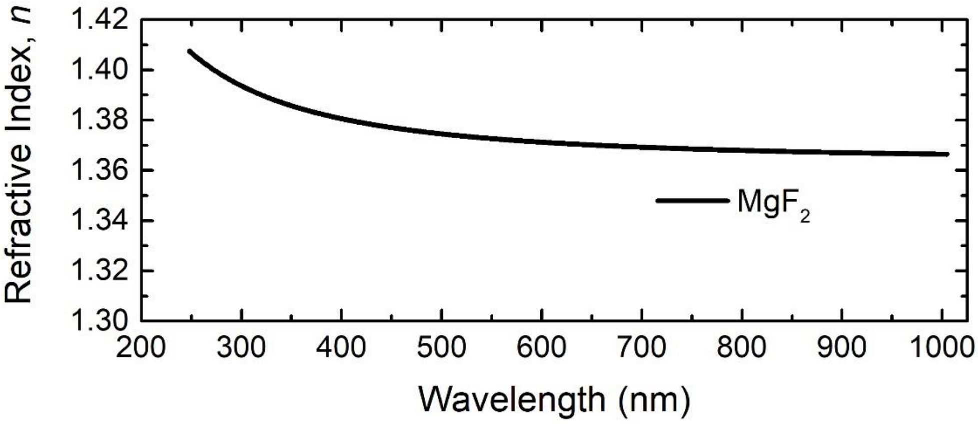

Figure 113 Measured refractive index spectra of MgF_2.

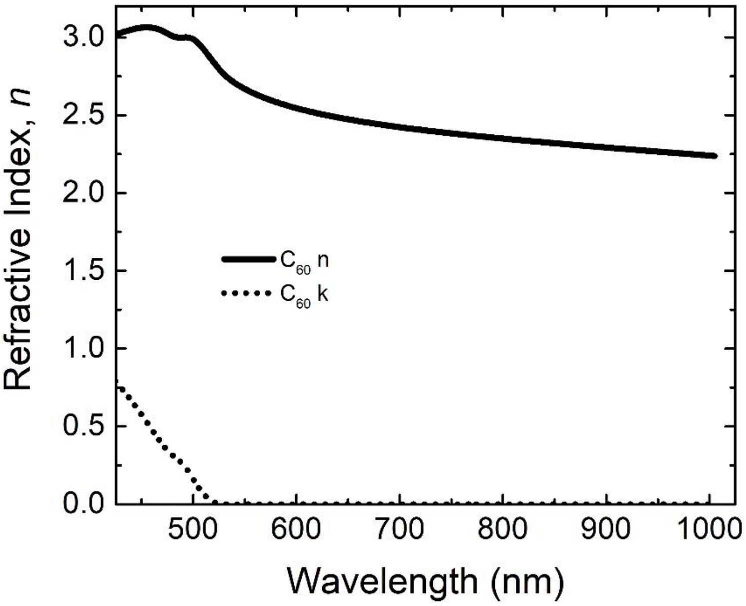

Figure 114 Measured refractive index spectra of C_{60}.

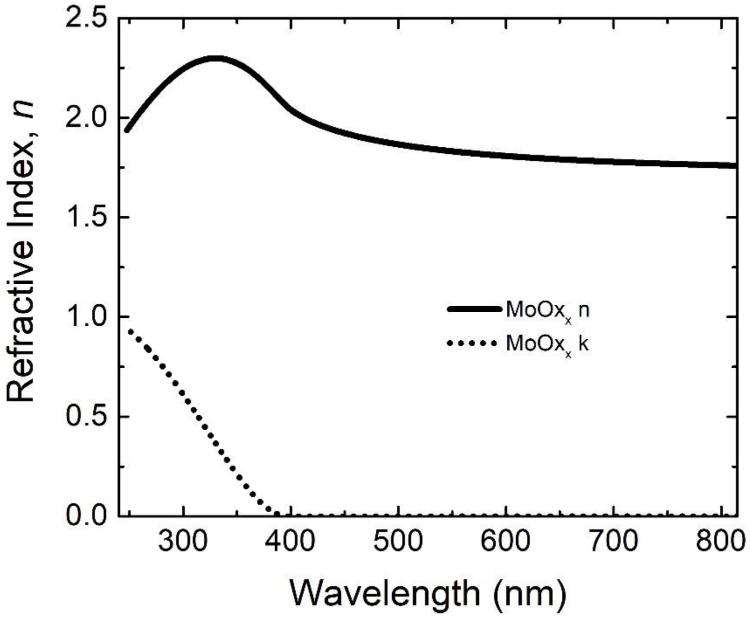

Figure 115 Measured refractive index spectra of MoOx.

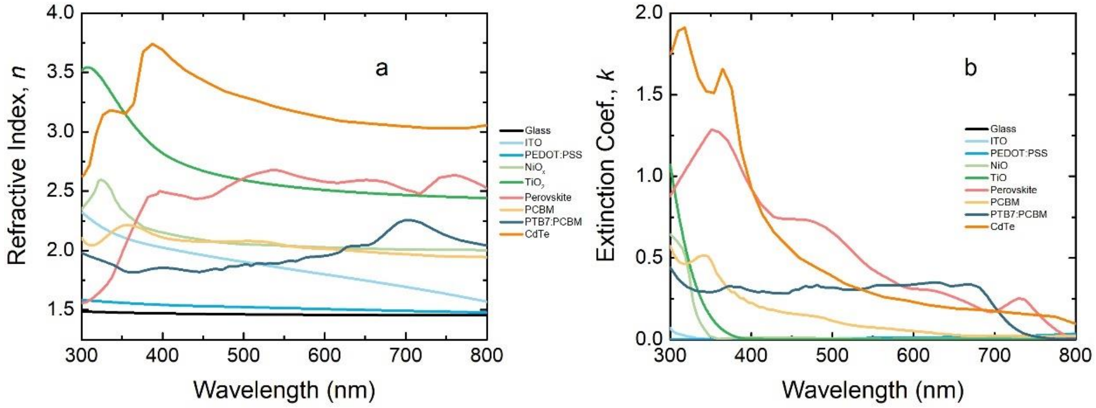

Figure 116 Refractive index (a) and extinction coefficient (b) spectra of adopted materials used in Chapter 3.

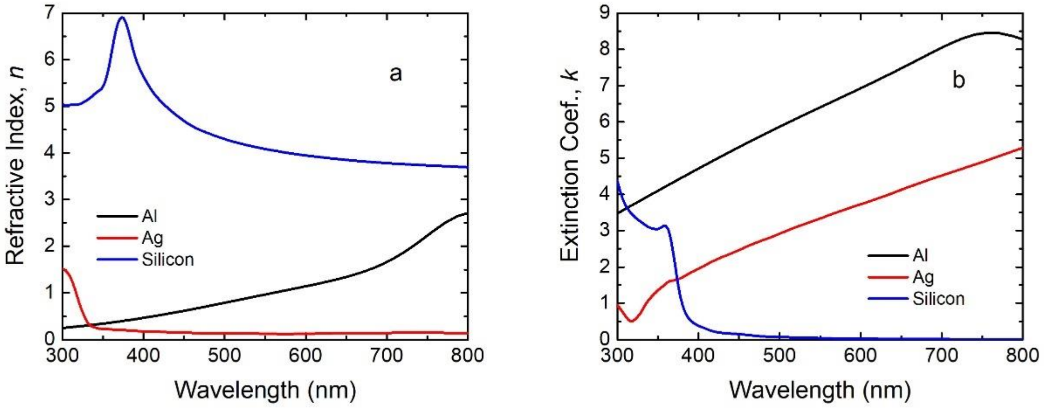

Figure 117 Adopted refractive index (a) and extinction coefficient (b) spectra of Al, Ag, and silicon used in Chapter 4.

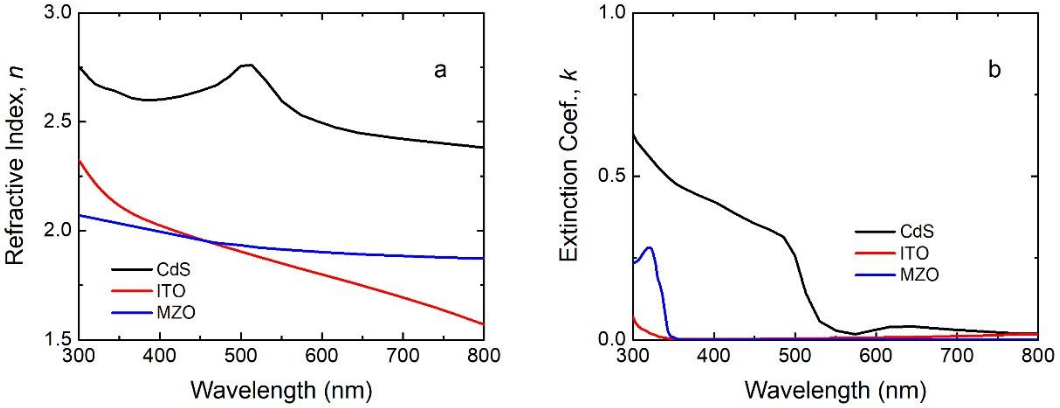

Figure 118 Adopted refractive index (a) and extinction coefficient (b) spectra of CdS, ITO, and MZO used in Chapter 5.

C. SUPPLEMENTARY MATERIAL

Table 12 TCO, FTL, RTL material information, refractive indices of FTL (both at 450 nm and 770 nm), MAPI (at 770 nm) and RTL (at 770 nm), and estimated interference order and cut-off FTL refractive index acquired from publications of Ball et al.,[108] Lin et al.[109] and Chen et al.[110]

	Ball(1)	Ball(2)	Lin	Chen(1)	Chen(2)
TCO	FTO	FTO	ITO	ITO	ITO
FTL	TiO_2	TiO_2	PEDOT:PSS/PCDTBT	ZnO	PEDOT:PSS
RTL	Spiro.	Spiro.	PCBM	Spiro.	PCBM
n_{FTL}@450nm	2.20	2.20	1.63	2.04	1.53
n_{FTL}@770nm	2.07	2.07	1.58	1.93	1.48
n_{MAPI}@770nm	2.59	2.59	2.82	2.61	2.61
m	4	5	2	4	3
$n_{cut\text{-}off}$	1.80	1.80	1.95	1.80	1.85

Table 13 Optimum FTL, MAPI and RTL thicknesses calculated via optical simulations by Ball et al., Lin et al. and Chen et al., and using Equation 54-56 following the guideline given in this article.

	FTL	MAPI	RTL (fixed)
Ball (1)	41	470	253
Our guideline	34	478	253
Ball (2)	41	630	253
Our guideline	39	628	253
Lin	15	350	10
Our guideline	0	343	10
Chen (1)	40 (fixed)	460	300
Our guideline	44	451	300
Chen (2)	40 (fixed)	435	100
Our guideline	0	424	100

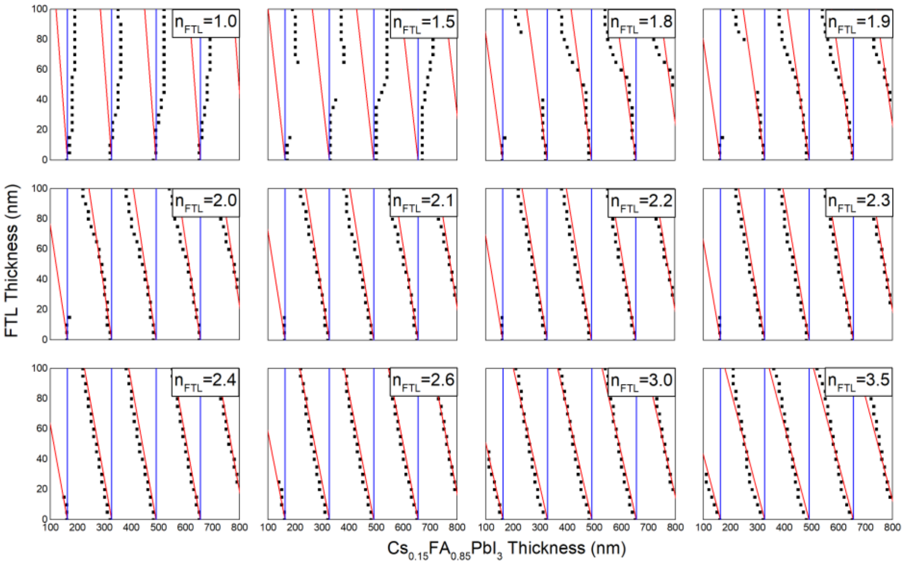

Figure 119 Maximal MAPC trends predicted with Equation 57 are shown as red and blue lines. Simulated maximal trends (black squares) for $Cs_{0.15}FA_{0.85}PbI_3$ in MAPC for various interference orders for hypothetical FTLs with refractive indices between 1.0 and 3.5 and with no extinction coefficient.

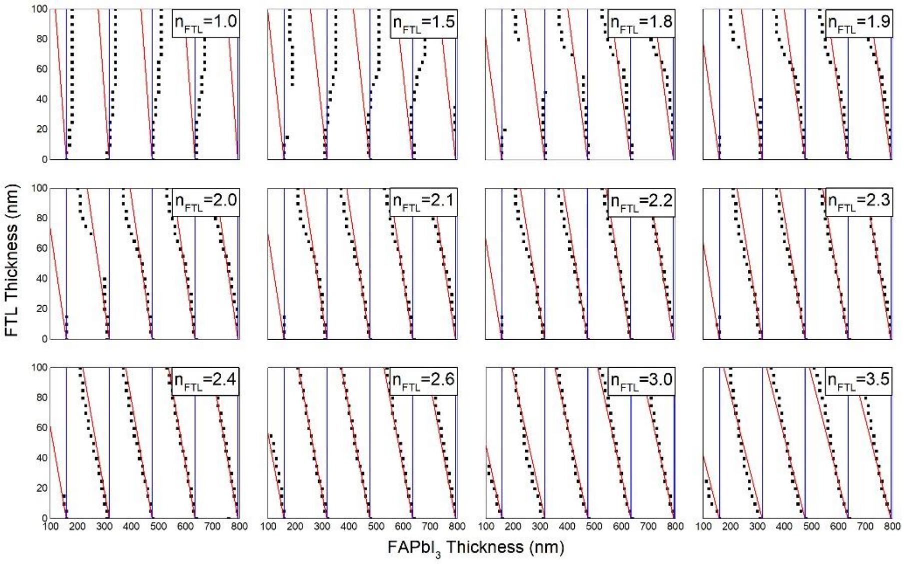

Figure 120 Maximal MAPC trends predicted with Equation 57 are shown as red and blue lines. Simulated maximal trends (black squares) for $FAPbI_3$ in MAPC for various interference orders for hypothetical FTLs with refractive indices between 1.0 and 3.5 and with no extinction coefficient.

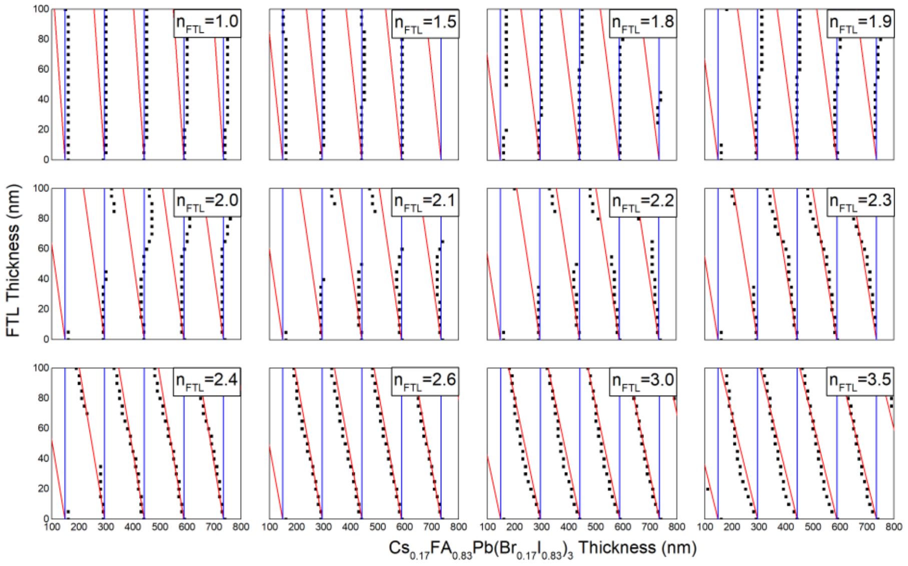

Figure 121 Maximal MAPC trends predicted with Equation 57 are shown as red and blue lines. Simulated maximal trends (black squares) for $Cs_{0.17}FA_{0.83}Pb(Br_{0.17}I_{0.83})_3$ in MAPC for various interference orders for hypothetical FTLs with refractive indices between 1.0 and 3.5 and with no extinction coefficient.

$$dR = \frac{(2Cn_2+2Dn_1-2n_0n_3(\frac{C}{n_2}+\frac{D}{n_1}))(C+n_0n_3(\frac{C}{n_2^2}-\frac{2\pi A t_2}{\lambda n_2}+\frac{2\pi B t_2}{\lambda n_1})+\frac{2\pi A n_2 t_2}{\lambda}-\frac{2\pi B n_1 t_2}{\lambda})-(2n_0(\frac{B}{n_1}+\frac{2\pi C t_2}{\lambda}+\frac{2\pi D n_2 t_2}{\lambda n_1})-2n_3(\frac{2\pi C t_2}{\lambda}-\frac{B n_1}{n_2^2}+\frac{2\pi D n_1 t_2}{\lambda n_2}))(n_0(A-\frac{B n_2}{n_1})-n_3(A-\frac{B n_1}{n_2}))}{(n_0(A-\frac{B n_2}{n_1})+n_3(A-\frac{B n_1}{n_2}))^2+(Cn_2+Dn_1+n_0n_3(\frac{C}{n_2}+\frac{D}{n_1}))^2}$$
$$-\frac{((n_0(A-\frac{B n_2}{n_1})-n_3(A-\frac{B n_1}{n_2}))^2+(Cn_2+Dn_1-n_0n_3(\frac{C}{n_2}+\frac{D}{n_1}))^2)((2Cn_2+2Dn_1+2n_0n_3(\frac{C}{n_2}+\frac{D}{n_1}))(C-n_0n_3(\frac{C}{n_2^2}-\frac{2\pi A t_2}{\lambda n_2}+\frac{2\pi B t_2}{\lambda n_1})+\frac{2\pi A n_2 t_2}{\lambda}-\frac{2\pi B n_1 t_2}{\lambda})-(2n_0(\frac{B}{n_1}+\frac{2\pi C t_2}{\lambda}+\frac{2\pi D n_2 t_2}{\lambda n_1})+2n_3(\frac{2\pi C t_2}{\lambda}-\frac{B n_1}{n_2^2}+\frac{2\pi D n_1 t_2}{\lambda n_2}))(n_0(A-\frac{B n_2}{n_1})+}{((n_0(A-\frac{B n_2}{n_1})+n_3(A-\frac{B n_1}{n_2}))^2+(Cn_2+Dn_1+n_0n_3(\frac{C}{n_2}+\frac{D}{n_1}))^2)^2}$$

Equation 62

Reflection spectra of perovskite solar cell with various ITO, NiO_x, and perovskite thickness combinations are presented in Figure 122. Two distinct interaction mechanisms are found in front layers highlighted as red and green. In the green zone, refractive indices of ITO and NiO_x are similar, therefore it leads to a joint behavior of two layers as can be seen in black, red, and cyan curves in the corresponding part of the spectrum. In the red zone, considerable difference in the refractive index spectra of ITO and NiO_x yields distinct behavior. Since the refractive index spectrum of ITO becomes closer to glass, NiO_x presents a single-layer reflection and it presents a low-reflection satisfying the QWOT condition. This can be seen at 720 nm wavelength where 90 nm-thick NiO_x eliminates the reflection. This wavelength region is in the proximity of the central wavelength of the interferences within the perovskite layer, hence leads to suppressed undulations.

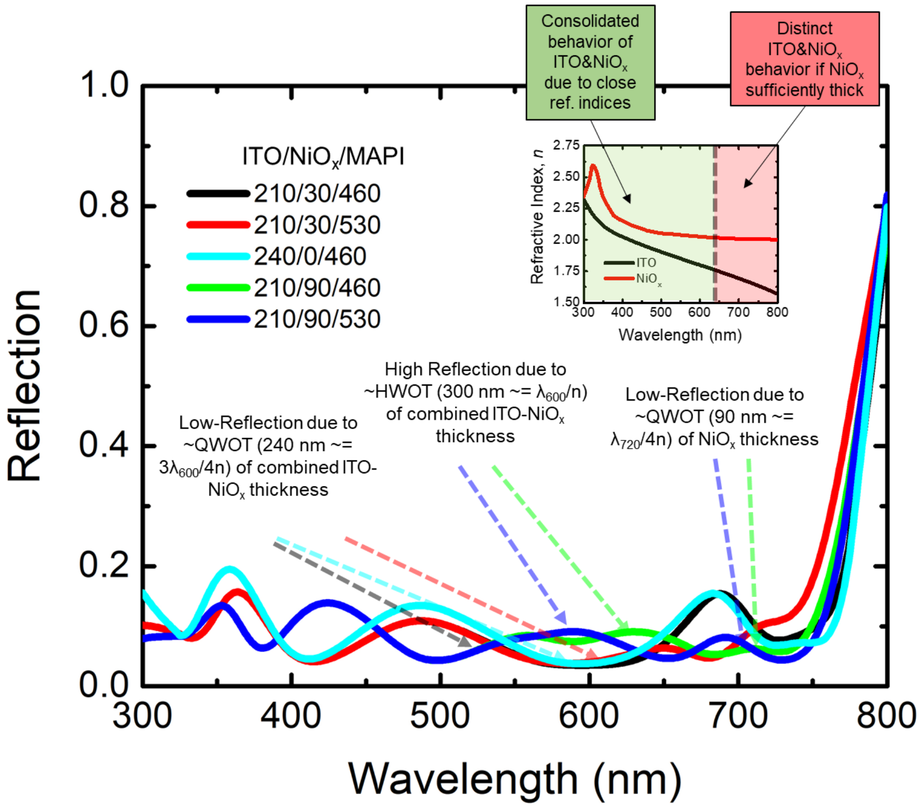

Figure 122 Reflection spectra of perovskite solar cell with various ITO, NiO_x, and perovskite thickness combinations. Inset: Refractive index spectra of ITO and NiO_x.

CURRICULUM VITAE

PERSONAL INFORMATION

Surname, Name	: Koç, Mehmet
Nationality	: Turkish (TC)
Date and Place of Birth	: 11 October 1988, Ankara
Phone	: +90 506 600 1900
E-mail	: mehmetkoc.ee@gmail.com

EDUCATION

Degree	**Institution**	**Year of Graduation**
MS	METU Micro and Nanotechnology	2013
BS	Bilkent U. Electrical-Electronics Eng.	2009
High School	Gazi Anadolu High School, Ankara	2005

WORK EXPERIENCE

Year	**Place**	**Enrollment**
2014-2020	AYBÜ Electrical-Electronics Eng.	Research Assistant

FOREIGN LANGUAGES

Advanced English, Basic French

PUBLICATIONS

1. **M Koç**, G Kartopu, S Yerci, “Combined Optical and Electrical Optimization of $C_{1-x}Z_xT$/Silicon Tandem Solar Cells”, *Materials* **2020**, *13*(8), 1860, https://doi.org/10.3390/ma13081860
2. **M Koç**, W Soltanpoor, G Bektaş, H J Bolink, S Yerci “Guideline for Optical Optimization of Planar Perovskite Solar Cells”, *Adv.Opt. Mat*, 2019, https://doi.org/10.1002/adom.201900944
3. **M Koç**, W Soltanpoor, D Turkay, K Tsoi, C Koroglu, S Yerci, “Optical and Electrical Investigation of Transparent Conductive Oxide Layer in Triple-Cation Perovskite Solar Cells” (in preparation)

4. **M Koç**, D Kocak, D Turkay, S Yerci, “Optical Investigation of Low Refractive Index Scattering Layer in Silicon Solar Cells as Rear Reflector” (in preparation)
5. **M Koç**, S Yerci, “A New Approach to Practical Limits of Single Junction and Tandem Solar Cells” (in preparation)
6. **M Koç**, M Codur, S Yerci, “Optical Filter Designs Using NiO Films with In situ Tunable Refractive Index” (in preparation)
7. **M Koç**, S Galioglu, D Toffoli, H Ustunel, and B Akata, “Understanding the Effects of Ion-Exchange in Titanosilicate ETS-10: A Joint Theoretical and Experimental Study”, *J. Phys. Chem. C*, 2014, 118 (47), pp 27281–27291
8. **M Koç**, S Galioglu, D Toffoli, H Üstünel, B Akata**,** “Effect of ion-exchange on Structural, Electronic, and Vibrational Properties of the -O-Ti-O-Ti-O- Quantum Wires in ETS-10”, MRS Proceedings (2014), 1704. doi:10.1557/opl.2014.796E
9. **M Koç**, Modelling and Experimental Study of Titanosilicate ETS-10: Application to Solar Cells. (2013)
10. S Galioğlu, M İşler, Z Demircioğlu, **M Koç**, F Vocanson, and N Destouches, "Photochromic behavior of silver nanoparticle incorporated titanosilicate ETS-10 films", https://doi.org/10.1016/j.micromeso.2014.05.009
11. **M Koç et al.**,” Maximization of Short Circuit Current in Perovskite Solar Cells by Optical Engineering”, PVSEC 2017, Amsterdam, Netherlands, 2017
12. **M Koç et al.**, “Maximization of Short Circuit Current in Perovskite Solar Cell”, EMRS 2017 Spring, Strasbourg, France, 2017
13. **M Koç et al.**, “Optimizing Layer thicknesses of Perovskite Based Thin Film Solar Cells by Optical Simulations”, EMRS 2016 Spring, Lille, France, 2016
14. **M Koç et al**., “Effect of Ion-Exchange on Structural, Electronic, and Vibrational Properties of the -O-Ti-O-Ti-O- Quantum Wires”, Invited Speaker, MRS 2014 Fall, Boston, MA, USA, 2013
15. **M Koç et al.**, “Theoretical Study of Effects of Exchangeable Cations on Electronic, Structural Properties of ETS-10”, IZC-17 International Zeolite Conference, Moscow, Russia, 2013

HOBBIES

Computer Games, Bicycle, Movies